



HAL
open science

Multicellular Tumour Spheroid (MCTS) model for evaluation of the efficiency of nanoparticle drug delivery

Saba Goodarzi

► **To cite this version:**

Saba Goodarzi. Multicellular Tumour Spheroid (MCTS) model for evaluation of the efficiency of nanoparticle drug delivery. Biological Physics [physics.bio-ph]. Université de Lyon, 2021. English. NNT : 2021LYSE1174 . tel-03526703

HAL Id: tel-03526703

<https://theses.hal.science/tel-03526703v1>

Submitted on 14 Jan 2022

HAL is a multi-disciplinary open access archive for the deposit and dissemination of scientific research documents, whether they are published or not. The documents may come from teaching and research institutions in France or abroad, or from public or private research centers.

L'archive ouverte pluridisciplinaire **HAL**, est destinée au dépôt et à la diffusion de documents scientifiques de niveau recherche, publiés ou non, émanant des établissements d'enseignement et de recherche français ou étrangers, des laboratoires publics ou privés.



N°d'ordre NNT : 2021LYSE1174

THESE de DOCTORAT DE L'UNIVERSITE DE LYON

opérée au sein de

l'Université Claude Bernard Lyon 1

École Doctorale ED 34 Matériaux

Spécialité de doctorat : Biophysique

Discipline : Physique

Soutenue prévu le 21/09/2021, par :

Saba Goodarzi

Multicellular Tumour Spheroid (MCTS) model for evaluation of the efficiency of nanoparticle drug delivery

Devant le jury composé de :

MERTANI, Hichem,

Maître de Conférence, Université Lyon 1

BARBERI-HEYOB, Muriel,

Professeure des Universités, Université de Lorraine

WILHELM Claire,

Directrice de Recherche, CNRS Paris

ROLS, Marie-Pierre,

Directrice de Recherche, CNRS Toulouse

Rivière, Charlotte,

Maître de conférences, Université Lyon 1

LUX, François,

Maître de conférences, Université Lyon 1

Favier Arnaud,

Chargé de Recherche, CNRS Lyon

Rodriguez-Lafrasse Claire,

Professeure des Universités, Université Lyon 1

Examineur

Rapporteure

Rapporteure

Présidente

Directrice de thèse

Co-directeur de thèse

Invité

Invitée

*To my parents for their endless love, support and
encouragement*

*To my love, without his support I could never have
accomplished this endeavor*

ACKNOWLEDGEMENT

The preparation and completion of this body of work could not have been possible without the guidance, support and leadership of many individuals. First and foremost, I would like to thank my supervisors: Dr. Charlotte Rivière and Dr. François Lux for providing me with this incredible opportunity. I do consider myself to be extremely privileged to have been their Ph.D student.

Charlotte deserves my heartfelt gratitude. I would not have expected a better supervisor than her; this dissertation would not have been possible without her unwavering support, guidance and encouragement. I was inspired to do my best during my Ph.D. because of her kindness and insights.

François, I'd like to express my heartfelt appreciation to him for his three years of encouragement, motivation, deep insights, and outstanding guidance and ideas that improved my Ph.D project and taught me valuable research skills.

My sincere gratitude also goes to the entire jury, Dr. Muriel Barberi-Heyob, Dr. Claire Wilhelm, Dr. Hichem Mertani, and Dr. Marie-Pierre Rols, for accepting to participate in my defense and taking time to review my thesis during their summer vacations and as well as for their insightful questions about my thesis.

Many thanks to the members of the thesis follow-up committee, Dr.Hichem Mertani, Dr. Loic vanel, and Dr.Laurent Bardotti, for their participation and suggestions for improving my Ph.D path.

I'd also like to thank the entire Biophysics team, including Hélène for her assistance with image analysis, Thomas for his assistance with my doctoral school examination, Sylvain for the friendly moments in the lab, Jean Paul, Christophe, Olivier, Maroun, and all PosDocs and Ph.Ds, Audrey, Anthony, Alexis, Marion, Malèke, Gucci, Adrien, Julie, Nasser, Gaëtan and Guillaume. I'd also like to thank the interns who have completed their internship in our lab over the last three years, Daiva, Gaëtan, Sara, and the team's newest members, Alpha and Kabir. I wish them all the best in their future endeavors.

Thank you to the members of the liquid and interface teams as well. Thank you for all of your pleasantries, Christmas dinners, and shared barbecues. Thank you, especially, Gilles, for being so accommodating in preparing plates for my experiments. Many thanks, especially, to Agnes for her kindness and help with my defense party. I'd also like to express my gratitude to Aderito for his kind-heartedness and friendship throughout my PhD.

I am also grateful to the members of the FENNEC team and NH TherAguix, Guillaume, Olivier, Paul, Tristan, and especially Fabien, who provided AGuIX® nanoparticles for my experiments.

I must also thank our Ph.D. collaborators, Dr. Arnaud Favier, for enabling me to use my Ph.D's 3D cellular model for another type of nanoparticle and for the opportunity of co-supervising Daiva during her M2 internship. I'd also like to thank Dr. Claire Rodriguez-Lafrasse and, in particular, her PhD student, Delphine, for her availability and participation in our irradiation experiments.

My journey was made more fulfilling by the friendship and support of my friends in Lyon, Narcisse, Ali, and Solmaz for all of the friendly moments we shared.

I am eternally grateful to Mr. François Corbi for all of the tennis activities and everything he taught me over the years. I'm grateful to Sabrina and Loïc for the wonderful cycling activities.

I'm also grateful to Dr. Hamid Omidvar, my undergraduate program professor, for getting me interested in research and for being supportive and encouraging all these years.

Special thanks to Dr. MohammadReza Samsam Shariat for his extremely valuable consultations, advice, and support in the weeks leading up to my defense.

I consider myself extremely fortunate to be unconditionally loved, nurtured, and guided by my family, whose optimism and boundless strength have inspired me to persevere and overcome obstacles. I'd like to thank my parents, brothers, and sisters from the bottom of my heart for everything they've done for me. Many thanks, especially, to my mother for instilling in me the desire to be a strong and successful woman since I was a child.

Finally, I'd like to express my heartfelt gratitude to my eternal love, my soulmate, for everything you've done for me. Thank you for teaching me to never be afraid of a challenge and to always persevere in the face of adversity. This achievement would not have been possible without everything you've taught me and your unwavering support.

RÉSUMÉ

Titre : Modèle de tumeur sphéroïde multicellulaire pour l'évaluation de l'efficacité de l'administration de médicaments à base de nanoparticules

Mots clés : modèle cellulaire 3D ; microsystèmes à base d'hydrogel ; nanoparticules ; Imagerie optique 3D ; radiothérapie

Le développement d'un modèle 3D in vitro standard pour le criblage des nanothérapies reste un défi. Plusieurs modèles de culture de tumeurs en 3D ont été développés, dont les sphéroïdes multicellulaires de tumeurs qui gagnent en popularité en raison de leur capacité à imiter certaines des caractéristiques des tumeurs naturelles. Les sphéroïdes peuvent être fabriqués de différentes manières, mais les méthodes traditionnelles présentent plusieurs inconvénients.

Dans cette étude, des micropuits à base d'agarose ont été utilisés pour la génération de sphéroïdes tumoraux multicellulaires uniformes d'une lignée de cancer colorectal (HCT-116). Selon les résultats de ce projet, la pénétration des nanoparticules AGuIX®- Cy5.5 dans les sphéroïdes dépend du temps et de la concentration. Alors que les nanoparticules ont été observées dans l'espace extracellulaire et intracellulaire des sphéroïdes, la localisation intracellulaire dominante des nanoparticules AGuIX®- Cy5.5 était dans les lysosomes ; les endosomes précoces et les mitochondries, par contre, ont montré une certaine colocalisation avec AGuIX®. Lorsque la localisation des nanoparticules AGuIX®- Cy5.5 dans les sphéroïdes et la culture cellulaire 2D a été comparée, la différence dans la localisation des nanoparticules en 2D et en 3D a mis en évidence les avantages de l'utilisation de ce modèle in vitro 3D pour le criblage des nanothérapies en raison de sa capacité à récapituler les caractéristiques tumorales influençant l'internalisation des nanoparticules et leur destin intracellulaire.

Le modèle in vitro 3D mis au point s'est avéré bénéfique pour l'évaluation de la thérapie associée à la radiothérapie, car les cellules en sphéroïdes (3D) ont montré une radiorésistance plus élevée que les cellules monocouches (2D), ce qui indique que ce modèle in vitro 3D peut être utilisé pour évaluer l'efficacité thérapeutique des nanothérapies dans une configuration plus réaliste. Le suivi de la croissance des sphéroïdes HCT-116 irradiés a révélé leur capacité à croître pour toutes les doses 6 jours après l'irradiation, contrairement au test classique de survie clonogénique, qui a révélé qu'ils étaient incapables de former des colonies aux doses plus élevées. Le meilleur effet radiosensibilisant d'AGuIX® a été observé à une irradiation de 2 Gy, selon l'analyse de la prolifération de cellules uniques dans les sphéroïdes.

ABSTRACT

Title: Multicellular Tumour Spheroid (MCTS) model for evaluation of the efficiency of nanoparticle drug delivery

Keywords: 3D cellular model; hydrogel-based microsystem; nanoparticles; 3D optical imaging; radiotherapy

Developing a standard 3D in vitro model for screening nanotherapeutics remains challenging. Several 3D tumor culture models have been developed, multicellular tumor spheroids among them are gaining popularity due to their ability to mimic some of the characteristics of natural tumors. Spheroids can be made in a variety of ways, but traditional methods have several drawbacks.

In this study, agarose-based microwells were used for generation of uniform multicellular tumor spheroids of a colorectal cancer line (HCT-116). According to the findings of this project, the penetration of AGuiX[®]- Cy5.5 nanoparticles within spheroids is time and concentration dependent. While nanoparticles were observed in both extracellular and intracellular space of spheroids, the dominant intracellular localization of AGuiX[®]- Cy5.5 nanoparticles was in lysosomes; early endosomes and mitochondria, on the other hand, showed some colocalization with AGuiX[®]. When the localization of AGuiX[®]- Cy5.5 nanoparticles in spheroids and 2D cell culture was compared, the difference in nanoparticle localization in 2D and 3D highlighted the advantages of using this 3D in vitro model for nanotherapeutics screening because of its ability to recapitulate tumor features influencing nanoparticle internalization and intracellular fate.

The developed 3D in vitro model has been shown to be beneficial in therapy assessment associated with radiotherapy, as cells in spheroids (3D) showed higher radioresistance than monolayer cells(2D), indicating that this 3D in vitro model can be used to assess therapeutic efficacy of nanotherapeutics in a more realistic set up. Growth monitoring of irradiated HCT-116 spheroids revealed their ability to grow for all doses, 6 days after irradiation, in contrast to the classical clonogenic survival assay, which revealed they were unable to form colonies at higher doses greater. The best radiosensitizing effect of AGuiX[®] was observed at 2 Gy irradiation, according to single cell proliferation analysis in spheroids.

Table of Contents

AKNOWLEDGEMENT	4
RÉSUMÉ	i
ABSTRACT	vii
ACRONYMS & ABBREVIATIONS	xii
PREFACE	x
Motivations and Objectives.....	1
Chapter 1. Introduction	4
1.1. Natural Tumor microenvironment	6
1.1.1 Cellular components of tumor microenvironment	6
1.1.2. Non-Cellular components of tumor microenvironment	8
1.1.3. Physical and chemical characteristics of TME	10
1.1.4. Role of tumor microenvironment in cancer pathobiology and therapy resistance.....	12
1.1.5 Summary.....	12
1.2. <i>In vitro</i> models seeking to reproduce tumor micro-environment	13
1.2.1. Scaffold-based 3D <i>in vitro</i> models.....	15
1.2.2. Bio-printed models.....	16
1.2.3. Organoids	17
1.2.4. Multicellular tumor spheroids.....	18
1.2.5. Summary.....	20
1.3. Spheroids preparation techniques	20
1.3.1. Liquid overlay methods	20
1.3.2. Hanging drop methods.....	22
1.3.3. Agitation-based approaches.....	22
1.3.4. Patterned surfaces and microfluidic devices.....	23
1.3.5. 3D <i>in vitro</i> platform used in my PhD	24
1.3.6. Summary.....	24
1.4. Tools for characterization of multicellular tumor spheroids.....	24
1.4.1. Drug screening assays	25
1.4.2. Biochemical assays	25
1.4.3. Western blot and qRT-PCR	26

1.4.4.	Flow cytometry.....	26
1.4.5.	Microscopy	27
1.4.6.	Optical clearing.....	31
1.5.	Cellular uptake of nanoparticles and application of MCTS model in nano-drug screening.....	32
1.5.1.	Cell-nanoparticles interactions.....	33
1.5.2.	Cellular uptake of nanoparticles	34
1.5.3.	Intracellular trafficking of nanoparticles	35
1.5.4.	MCTS as a predictive model for nanodrug screening.....	37
Chapter 2. Quantifying nanotherapeutics penetration using a hydrogel-based microsystem as a new 3D in vitro platform		39
1.	Introduction.....	41
1.1.	Spheroids Preparation.....	42
1.2.	Incubation with AGuIX®-Cy5.5 nanoparticles.....	44
1.3.	Three dimensional fluorescence microscopy	45
1.4.	Image analysis and quantification of fluorescence signals	48
1.5.	Quantification of Gd content internalized by cells in spheroids using ICP-MS techniques	50
1.6.	The compatibility with <i>in situ</i> immunostaining and quantification	51
2.	ABSTRACT	53
3.	CORPUS.....	54
4.	SUPPLEMENTARY MATERIALS	72
5.	Study the penetration of fluorescence polymer probes	88
6.	Study of the effect of nanoparticles on cell proliferation in multicellular tumor spheroids	92
7.	Conclusion and perspectives	93
Chapter 3. Evaluation of radiosensitization effect of AGuIX® nanoparticles using multicellular tumor spheroids		95
1.	INTRODUCTION	97
1.1.	Effect of spheroid size on cell proliferation.....	97
1.2.	The workflow of assessment of therapeutic efficacy of AGuIX® nanoparticles in radiotherapy using 3D in vitro model	99
2.	ABSTRACT	101
3.	CORPUS.....	102
	Introduction.....	102
	Materials and Methods	104

Results & Discussion	109
Conclusion	125
4. Supplementary Materials	126
5. Outlooks of this work	128
Chapter 4. Conclusion and Perspectives	130
General Conclusion	131
Perspectives.....	133
REFERENCES	134
APPENDIX I	160
APPENDIX II	161

ACRONYMS & ABBREVIATIONS

AP: Acid phosphatase

ATP: Adenosine triphosphate

CAF: cancer-associated fibroblast

CRC: Colorectal cancer

CSC: cancer stem cells

ECM: extracellular matrix

EMT: epithelial–mesenchymal transition

EPR: Enhanced Permeability and Retention

FDM: fused deposition modeling

GAG: glycosaminoglycans

Gd: Gadolinium

HA: Hyaluronic acid

HAS1–3: Hyaluronan synthases

HTS: high throughput screening

ICP-MS: Inductively Coupled Plasma-Mass Spectrometry

IFP: interstitial fluid pressure

LSFM: light-sheet-based fluorescence microscopy

MRI: Magnetic Resonance Imaging

MSCs: Mesenchymal stem cells

MCTS: Multicellular tumor spheroids

PC: Polymer chains

PCC: Pearson’s Correlation Coefficient

PDMS: poly(dimethyl siloxane)

PG: proteoglycan

PI: propidium iodide

PNP: Polymer nanoparticles

RAFT: reversible addition-fragmentation chain transfer

RI: Refractive index

RT: radiotherapy

SEM: scanning electron microscopy

SER: Sensitizer Enhancement Ratio

SL: Stereolithography

SLN: sentinel lymph node

SPIM: Selective plane illumination microscopy

TAM: Tumor-associated macrophage

TEM: transmission electron microscopy

TME: tumor microenvironment

ULA: Ultra low Adhesion

WB: Western Blot

2D: two-dimensional

3D: Three-dimensional

PREFACE

PhD Supervisor: Dr. Charlotte Rivière (Université Lyon 1)

Co-Supervisor : Dr. François Lux (Université Lyon 1)

PhD thesis : from 1/10/2018 to 30/12/2021

Context of the thesis:

My thesis was carried out at Université Lyon 1, Institute Lumière Matière (ILM), 69622, Villeurbanne, France

The thesis was supported by a Grant of the French government (Ministry of Higher Education and Research) attributed by the doctoral school of Materials (University of Lyon).



PUBLICATIONS:

Goodarzi S, Prunet A, Rossetti F, Bort G, Tillement O, Porcel E, Lacombe S, Wu TD, Guerquin-Kern JL, Delanoë-Ayari H, Lux F, Rivière Ch: Quantifying nanotherapeutic penetration using a hydrogel-based microsystem as a new 3D in vitro platform. Lab on a Chip. 2021. (published)

Ahmad A, Goodarzi S, Frindel C, Recher G, Riviere C, Rousseau D. Clearing spheroids for 3D fluorescent microscopy: combining safe and soft chemicals with deep convolutional neural network. bioRxiv. 2021 Jan 1. (Revised).

Motivations and Objectives

Cancer is a multifaceted pathology in which cellular and acellular factors interact to promote cancer progression and, in the worst-case scenario, metastasis. Replicating the tumor environment *in vitro* is an intriguing challenge for biologists and bioengineers trying to assess novel drugs and nanotherapeutics in preclinical studies (1).

Conventionally, two-dimensional (2D) *in vitro* cancer models and small *in vivo* animal models are utilized for drug testing and screening (2,3). However, due to the difficulties of reproducing the natural tumor microenvironment in 2D culture, as well as the cost and ethical questions associated with animal models, both approaches have become less attractive for routine drug testing. When compared to conventional methods, new three-dimensional (3D) *in vitro* cancer models have been developed as an alternative strategy and have demonstrated the potential to reproduce the natural microenvironment of tumors in a relatively simple and inexpensive manner (4–8).

In the pharmaceutical sector, cancer cells are commonly cultivated on 2D plastic substrates; however, certain signaling pathways that are critical in defining a cell's natural response in terms of growth, metabolism, and differentiation are lost in cancer cells growing on a 2D surface (9,10). Furthermore, poor penetration into tumors that might be an underlying reason for inefficient therapeutic effect of nanoparticle delivery systems (11), is not accessible to investigate in monolayer *in vitro* models (12).

Several 3D tumor culture models have been reported, including tumor tissue explant models, scaffold-based models, microfluidic models, 3D bioprinted models and multicellular tumor spheroids (MCTS) (13,14). MCTS models are particularly popular among them, many of the shortcomings identified in monolayer cultures are compensated in the multicellular tumor spheroid models. Spheroids on the scale of 200–500 μm create chemical gradients of oxygen, nutrients, and metabolites, as well as tumor-like physical and functional properties (15,16). As a result, when compared to monolayer cultures, assays relying on the MCTS model allow for the assessment of nanotherapeutics efficacy are more predictive of *in vivo* success (16,17).

MCTS can be produced using a variety of techniques that allow single cells to spontaneously self-assemble and eventually form multicellular aggregates (18). These approaches, on the other hand, produce spheroids with a broad distribution in size. As the cellular functions within spheroids are correlated to their size (19), spheroid size uniformity is critical for achieving a homogeneous and meaningful level of biological activity and obtaining highly reproducible nanotherapeutics screening results. Furthermore, several approaches have been linked to limited throughput and difficulty in extracting cells for analysis (20). Microfluidic technologies have been

developed to produce spheroids on-chip in order to address such issues associated with traditional techniques. However, the polymer materials frequently utilized for such devices (Polydimethylsiloxane -PDMS) have significant drawbacks, making them unsuitable for drug screening in physiological settings (21). On the other hand, microfluidic devices designed for spheroids are incapable of meeting all criteria required for high throughput screening (HTS) of nanotherapeutics using different kinds of biological assays and in particular assays based on optical microscopy such as long-term time-lapse analysis (i.e. compatibility with high-resolution video-microscopy, efficient medium and oxygen renewal, *in situ* immunostaining/drug application).

Innovative hydrogel-based microsystems have been designed in the Biophysics team of Institute of Light and Matter (ILM) to address these types of challenges connected with spheroids preparation, culture maintenance, and subsequent investigation (22).

The main goal of this project was to validate this microsystem for generation of uniform multicellular tumor spheroids, exploring various aspects of cell-nanoparticle interactions using optical microscopy characterizations, as well as the assessment of therapeutic efficacy of nanoparticles in such 3D *in vitro* model.

Ultra small and radiosensitizing nanoparticles named AGuIX[®] made of polysiloxane and gadolinium (Gd) chelates, which have been developed by the FENNEC team of Institute of Light and Matter ILM (23), were chosen for this proof of concept study. These nanoparticles are now in clinical trials for whole brain radiation therapy (NANORAD 2, Phase II, multicentric), brain metastasis (NANOBRAINMETS, Phase II, Harvard Medical School), Cervical cancer (NANOCOL, Phase Ib, Gustave Roussy), Pancreatic/Lung Cancer (NANOSMART, Phase I, Harvard Medical School) , Glioblastoma (NANO-GBM, phase I, Centre Jean Perrin), and for other irradiations (NANOREC, NANOPRO, NANORT-MSK, Phase I/II).

In this project, colorectal cancer cell lines, HCT-116 (capable of making coherent spheroids (24)) have been used for making spheroids in a hydrogel-based microsystem. The interaction of AGuIX[®] nanoparticles with these spheroids has been studied in different ways;

- (1) Cellular uptake of AGuIX[®] nanoparticles – Cy5.5, kinetics of penetration in HCT-116 spheroids and their transport within spheroids

Confocal fluorescence microscopy with subsequent image analysis using Matlab and ICP-MS technique were used for these experiments.

- (2) Extracellular and intracellular localization of AGuIX[®] – Cy5.5 nanoparticles in HCT-116 spheroids and comparing it with 2D cultured HCT-116 cells

The localization of AGuIX[®] – Cy5.5 nanoparticles were analyzed with confocal fluorescence microscopy and images were analyzed using a routine in Matlab

(3) The therapeutic efficacy of these AGuiX® – Cy5.5 nanoparticles for radiotherapy in HCT-116 spheroids

This part was carried out in collaboration with Delphine Vernos-Brichart, Ph.D. student of Dr. Claire Rodriguez-Lafrasse in the Laboratoire de Radiobiologie Cellulaire et Moléculaire, Faculté de Médecine Lyon Sud, and Dr. Olivier Tillement in FENNEC Team of ILM. Classical clonogenic survival assay, time-lapse optical microscopy and confocal fluorescence microscopy with subsequent image analysis were used to assess AGuiX® therapeutic efficacy.

This manuscript is divided into four chapters. **Chapter one** (Introduction) explains the complexity of the native tumor microenvironment and emphasizes the importance of developing more complicated *in vitro* models for evaluating different therapeutics in cancer research and making a first screening of new drugs before animal studies for further clinical translation. In subsequent part of this chapter, different 3D *in vitro* models, specifically MCTS, the techniques for generation and characterization of them and the importance of studying cell-nanoparticles interactions and the interest of using MCTS for such studies will be discussed. **Chapter two** contains the copy of the article that has already been published in Lab on a Chip - The Royal Society of Chemistry and presents the first set of results related to cell- AGuiX® – Cy5.5 nanoparticles interactions. The results of applying this methodology for screening distribution and localization of a type of polymer nanoparticles are also reported in this chapter. In **Chapter three**, the results related to therapeutic efficacy of AGuiX®– Cy5.5 nanoparticles in irradiation of HCT-116 spheroids are presented in the format of an article in preparation. **Chapter four** will be conclusions and perspectives of this PhD.

Chapter 1. Introduction

Contents

Chapter 1. Introduction.....	4
1.1. Natural Tumor microenvironment	6
1.1.1 Cellular components of tumor microenvironment	6
1.1.2. Non-Cellular components of tumor microenvironment	8
1.1.3. Physical and chemical characteristics of TME	10
1.1.4. Role of tumor microenvironment in cancer pathobiology and therapy resistance	12
1.1.5 Summary	12
1.2. <i>In vitro</i> models seeking to reproduce tumor micro-environment.....	13
1.2.1. Scaffold-based 3D <i>in vitro</i> models	15
1.2.2. Bio-printed models	16
1.2.3. Organoids.....	17
1.2.4. Multicellular tumor spheroids	18
1.2.5. Summary	20
1.3. Spheroids preparation techniques	20
1.3.1. Liquid overlay methods.....	20
1.3.2. Hanging drop methods	22
1.3.3. Agitation-based approaches	22
1.3.4. Patterned surfaces and microfluidic devices	23
1.3.5. 3D <i>in vitro</i> platform used in my PhD.....	24
1.3.6. Summary	24
1.4. Tools for characterization of multicellular tumor spheroids	24
1.4.1. Drug screening assays.....	25
1.4.2. Biochemical assays.....	25
1.4.3. Western blot and qRT-PCR.....	26
1.4.4. Flow cytometry	26
1.4.5. Microscopy.....	27
1.4.6. Optical clearing	31
1.5. Cellular uptake of nanoparticles and application of MCTS model in nano-drug screening.....	32
1.5.1. Cell-nanoparticles interactions	33
1.5.2. Cellular uptake of nanoparticles	34
1.5.3. Intracellular trafficking of nanoparticles.....	35
1.5.4. MCTS as a predictive model for nanodrug screening	37

1.1. Natural Tumor microenvironment

Cancers are more than just clusters of malignant cells; they are sophisticated villain organs that attract a variety of different cells that can be corrupted by transformed cells to aid the malignant progression. Cancer is distinguished by its multiplication, invasion, metastasis, apoptosis resistance, angiogenesis promotion, immunological evasion, genome instability and mutation (25,26).

Cancer cells with genetic or epigenetic instability activate signaling networks, which, in collaboration with adjacent cells and extracellular matrix (ECM) proteins, promote the establishment of a tumor microenvironment (TME) that is specifically supportive of tumor growth. The TME, in fact, plays a critical role in tumor differentiation, epigenetics, dissemination, and immune evasion (27). Oncologists have also discovered that a healthy microenvironment can help protect against cancer and invasion. In contrast, if TME is not in a healthy state meaning TME components are corrupted by cancer cells, it will become a collaborator in tumor progression (26).

The TME's various components combine to produce a complex network that precisely controls tumor fate and tumor cell interactions with other components(25). TME components are classified into two main categories: non-cellular components and cellular components. While communication can be mediated via cell–cell interactions, intact ECM macromolecules or some of their domains released by limited proteolysis and known as matrikines or matricryptins can also mediate it (28). Endothelial cells, stromal fibroblasts, infiltrating immune cells, adipocytes, and inflammatory cells also contribute in tumor growth and progression (29). In the following section, the main components and characteristics of TME will be discussed in more details.

1.1.1 Cellular components of tumor microenvironment

The tumor microenvironment contains a variety of cellular components (**Fig.1.1**), including cancer-associated fibroblasts (CAFs), immunological and inflammatory cells, blood and lymphatic vascular networks, adipose cells, and neuroendocrine cells (26).

Cancer-associated fibroblasts (CAFs)

Cancer-associated fibroblasts are a subpopulation of fibroblasts with a myofibroblastic phenotype found in cancerous wounds (CAFs). CAFs secrete matrix proteins that are distinct from those produced by normal tissues. CAFs influence cancer progression by altering ECM, generating angiogenesis, attracting inflammatory cells, and directly boosting cancer cell proliferation via growth factor release, immune suppressive cytokines, and mesenchymal-epithelial cell interactions (26,27,30).

Immune and inflammatory cells

Immune and inflammatory cells are another category of cells found in the tumor microenvironment. Immune cells in TME have low tumor detection and killing capability, despite their primary duty of tissue homeostasis surveillance. Tumors form when transformed cells escape immune control during the elimination phase; however, in the following stage called the equilibrium stage, tumor cells cannot be eliminated and only tumor progression is under control. As a result, cancer cells change their morphologies via mechanisms like EMT to acquire survival benefits and avoid immune system surveillance. In other words, the immunological microenvironment aids cancer cells in selecting the dominant cells, allowing the tumor to progress at the highest possible rate in a constrained environment (26,30). Tumor-associated macrophages (TAMs) are important cells in this category that support tumor growth. Studies have shown that there is a link between high TAMs density and a poor overall survival rate in individuals with a variety of cancer types(30,31).

Blood and lymphatic vascular networks

The blood and lymphatic vascular networks, like those in normal tissues, supply oxygen and nutrition while also removing carbon dioxide and metabolic wastes, allowing the neoplasm to continue to grow. Unlike healthy tissue, the vasculature surrounding tumors are inefficient, tortuous, or leaky in tumors, and the angiogenic switch stays active during carcinogenesis, resulting in ongoing proliferation of natural blood vessels. This network of blood and lymphatic vessels aids tumor cells in evading immune surveillance. Furthermore, lymphatic arteries around tumors provide a physical link between sentinel lymph nodes (SLNs) and the primary tumor, acting as a highway for tumor cells to migrate to other locations (26).

In addition to these cell types, other cells in subcategories reside in tumors, allowing them to escape immune surveillance and helping tumor progression (32–34).

The second category of tumor microenvironment components called non-cellular components, which primarily consists of extracellular matrix that will be discussed in more details in the following section.

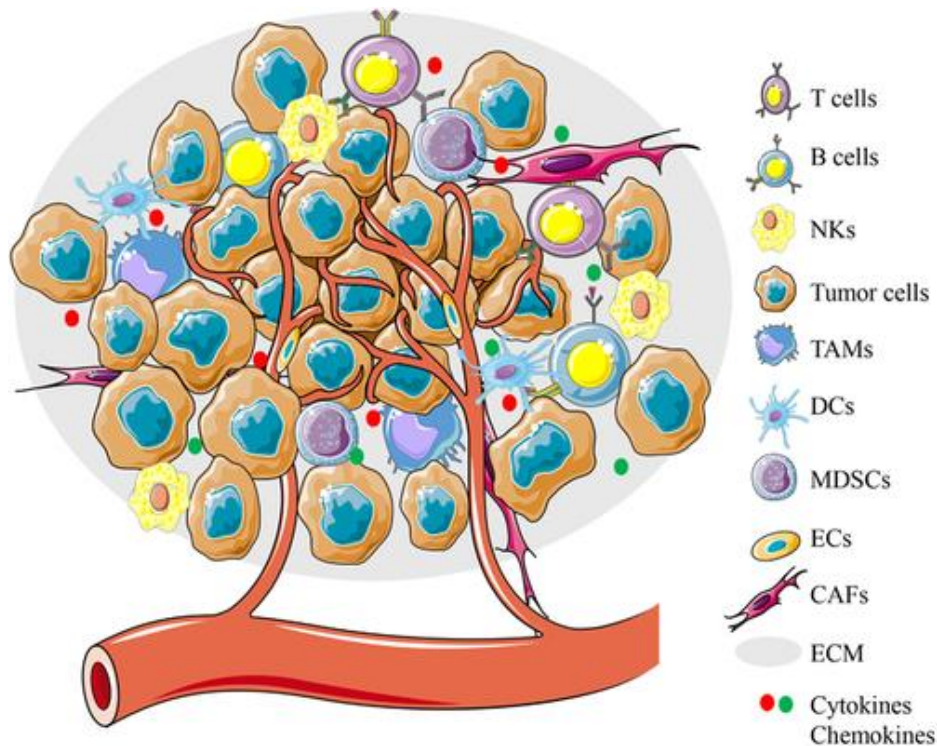


Figure 1.1. Cellular Components of TME. The TME consists of cellular and extracellular components. The cellular components are mainly composed of immune cells, resident stromal cells. ECM and cell-secreted proteins constitute the extracellular components. The interaction between these components regulates tumorigenesis and progression. Abbreviations: NKs, natural killers; TAMs, tumor-associated macrophages; DCs, dendritic cells; MDSCs, myeloid-derived suppressor; CAFs, cancer-associated fibroblasts; ECs, endothelial cells; ECM, extracellular matrix; From (35).

1.1.2. Non-Cellular components of tumor microenvironment

In addition to cellular components of TME, the non-cellular components in the character of extracellular matrix (ECM) also play a significant role in tumor growth. The extracellular matrix (ECM) is a complex network of fibrous proteins, glycosaminoglycans, and matricellular proteins that give structural support as well as biochemical and biomechanical cues to cancer cells (34). ECM is highly dynamic and participates in various cellular processes such as proliferation, cell migration and growth, thus the main function is providing structural support to maintain tissue architecture and nutritional support to the surrounding cells (36). Due to high levels of ECM molecule expression, ECM can account for up to 60% of the tumor mass in many cancers. These molecules are produced by tumor cells, but to a greater extent by the CAFs mentioned earlier. The tumor ECM, like all other components of TME, differs significantly from normal tissue ECM in terms of amount of deposition, composition, organization, and post-translational modification (37).

Here, the main components of ECM in tumor microenvironment will be discussed.

Collagens

Collagens are the most abundant proteins found in the animal kingdom being the major components of the ECM (38). The synthesis and maturation of collagens is a complex process. During tumor progression, many ECM proteins are significantly deregulated. The deposition of some proteoglycans and collagens is increased, leading to the reorganization of the tumor microenvironment. This ECM remodeling causes biochemical and biomechanical alterations that promote tumor metastatic progression. In this way, collagens can act as a scaffold, facilitating migration of invading cancer cells or stromal cells (39,40).

Proteoglycans

Similar to collagens, proteoglycans (PGs), also constituting an important part of the ECM, require enzymes for correct production and assembly. In many tumors, increased levels of PGs are observed, but the story seems to be more complex as the changes in PG content between normal and malignant tissue lie mainly in shifts between various PGs often between low- and high-molecular weight PGs (37).

Hyaluronic Acid

Hyaluronic acid (HA) is a glycosaminoglycan (GAG) that is not conjugated to peptides, and in contrast to the three others, it is not synthesized in the Golgi apparatus. HA production is increased in many cancers, most notably in pancreatic carcinomas (41,42) but also in breast cancers (43,44) CRC (45) prostate cancer (7), and even in brain tumors (46). Stromal cells, i.e., fibroblasts, are often identified histologically as the main source of HA in the tumor, and tumor cells can increase HA synthesis in cocultured fibroblasts (47). HA levels, and expression of HAS1–3, are correlated with poor prognosis (37,43,48).

Laminins

Laminins form a group of large heterotrimer glycoproteins. They represent the main non-collagenous proteins of basement membranes that constitute the extracellular matrix proteins and are involved in multiple important biological activities. They modulate several cellular homeostatic functions in normal cells which are often found deregulated in carcinomas (40,49–51). Laminins are also often stronger expressed in malignant tissue. Laminins were reported to promote tumor progression. (37,52).

The cellular and non-cellular components of TME that have been introduced give tumors unique properties. TME complexity emphasizes the need to better understand TME features in order to

design better *in vitro* models. In the next section, some features of solid tumors resulted from tumor heterogeneity will be discussed.

1.1.3. Physical and chemical characteristics of TME

The TME formed by the stromal, immunological, and malignant plays a role in tumor progression, provides a hostile environment and numerous obstacles to the cancer cells, including physical pressure, oxidative stress, nutrient deprivation and competition, hypoxia, and immunological surveillance (**Fig. 1.2**) (53–55). These variables are intricately linked to every stage of tumor development, metastasis, and metabolism.

Hypoxia

In addition to nutrition and waste, insufficient tissue coverage and aberrant tumor vasculature impede gas exchange and cause hypoxic zones. Tumor hypoxia is a well-known tumor microenvironment factor that contributes to cancer development and resistance to cancer treatment (56). Approximately 60% of human tumors exhibit distinct levels of hypoxia and even anoxia in tumor tissues. Adaptation to the hypoxia environment is said to be the foundation for cancer tissues' survival and growth (57).

There is a link between TME acidity and tumor hypoxia; accordingly, hypoxic regions of tumors are more likely to have a reduced supply of nutrients like glucose and critical amino acids. Tumor cells gain energy by glycolysis (the conversion of glucose into lactate to make ATP), which results in the generation of CO₂ and carbonic acid. A decrease in the clearance of these acidic metabolic products results in a low interstitial pH (53,58).

Extracellular pH (Tumor acidity)

Even when the oxygen supply is adequate, tumor cells can create a low pH environment by increasing glycolytic activity (known as the Warburg effect). Interactions between intrinsic metabolic networks and extrinsic(59) affectors result in a spectrum of cancer cells inside a tumor with varied properties and metabolic requirements (53). Tumor cells accumulate high levels of metabolism production and low glucose concentrations during this process(54). At the same time, many tumors exhibit pronounced extracellular acidity, with pH values as low as 6.5 which influences tumor metabolism and encourages local invasion (30).

Interstitial Fluid Pressure (IFP)

High cell density, increased vascular permeability, impaired venous or lymphatic drainage, and abnormal ECM are thought to cause elevated tumor interstitial fluid pressure (IFP) (60). Increased

IFP results in a positive pressure gradient, which acts as a driving force for connective transport back into capillaries or to low-IFP regions nearby (61). As a result of the drop in convection between the intravascular and extravascular spaces caused by the high IFP, drug delivery efficacy is greatly reduced, limiting drug distribution into the TME (62).

Tumor Fibrosis

Tumor fibrosis caused by an excess of crosslinked collagen matrix deposition by CAFs, MSCs, stellate cells, and fibrocytes (63). In summary, chronic inflammation leads to cancer fibrosis. When tissue is injured, a "nonhealing wound" is formed. Normal tissue fibrosis inhibits cancer initiation and spread. Cancer-related fibrosis, on the other hand, increases cancer cell interactions and advancement.

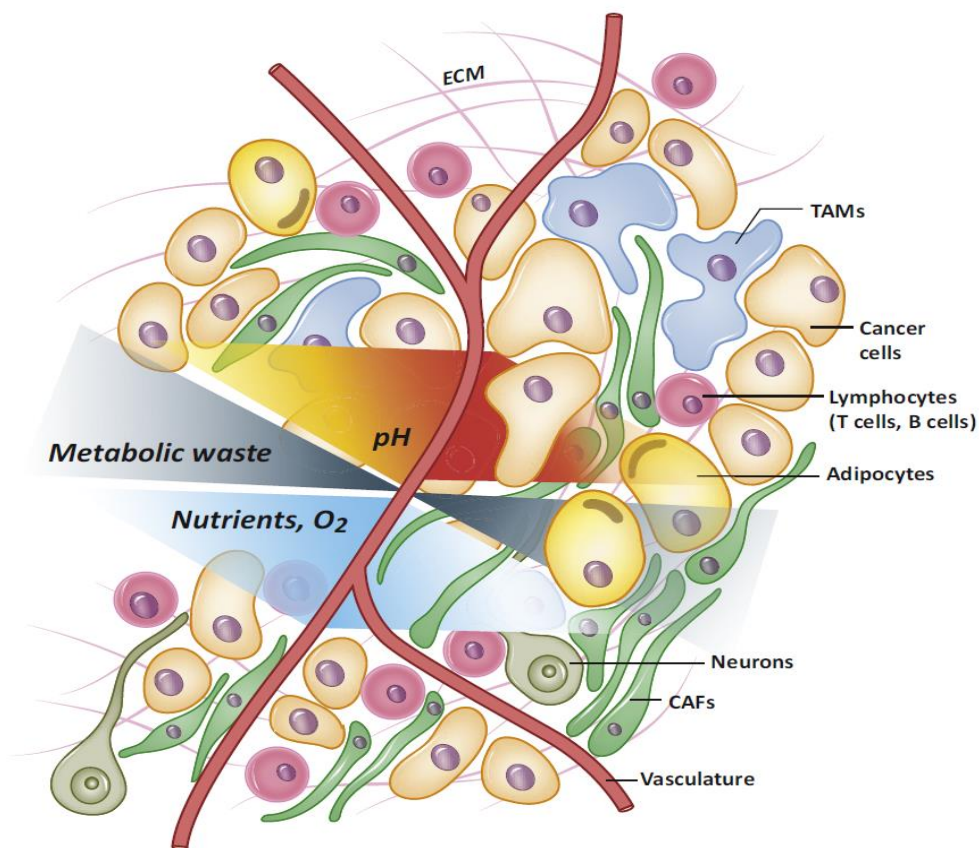


Figure 1.2. Features of the Tumor Microenvironment That Contribute to Metabolic Heterogeneity, gradients in pH, nutrients, oxygen and metabolic waste, From(53).

1.1.4. Role of tumor microenvironment in cancer pathobiology and therapy resistance

As introduced above, TME has a significant role in tumor destiny including promoting tumor formation, progression, metastasis and therapeutic response of solid tumors (25,27).

Cells in the tumor mass grow in a 3D tissue structure, with uneven oxygen exposure depending on their position within the tumor tissue. Because of increased tumor cell proliferation, cells in the tumor core are further away from the support blood arteries than cells in the outer layers of the tumor, resulting in a hypoxic microenvironment within the center that can contribute to variable treatment responses.

Tumor cells with p53 mutations or reduced p53 transcription can circumvent p53-mediated apoptosis pathways in hypoxic settings, resulting in the selection of tumor cell clones and the creation of apoptosis-resistant cells. Hypoxia also plays an important role in autophagy, which can lead to drug resistance (64). Chemotherapeutic resistance may also be caused by low extracellular pH (65). Tumor acidification has also been associated to apoptosis suppression in colon cancer cells, as well as a loss of function in p53 (57,66).

1.1.5 Summary

The research in recent decades has revealed to critical role of TME in cancer development and progression (67). As discussed earlier, cellular and non-cellular components of TME create a complex network with unique physiochemical properties in tumors. Moreover, tumor-associated stromal cells and ECM remodeling have been shown in studies to have both pro- and anti-tumorogenic effects. The failure of 2D cell cultures to address these complexities in TME highlights the need for improved *in vitro* models capable of recapitulating this complex environment in order to better understand the underlying molecular and cellular pathways, allowing for the identification of novel drugs that are more effective at combating drug resistance(57). Various 3D *in vitro* models, established in cancer research in recent decades for analyzing prospective therapy options, will be discussed in the next section.

1.2. *In vitro* models seeking to reproduce tumor micro-environment

Prior to clinical trials and FDA approval, the medicines and delivery system must be thoroughly studied to determine efficacy, toxicity, and safety. The initial step in this approach starts with *in vitro* testing of the drugs and subsequently by subcutaneous mouse xenograft cancer models (68,69). Such biology studies and disease models for drug screening and testing of delivery systems against target cells traditionally have been carried out in 2D, multi-well plate-based cell culture formats with the hypothesis that monolayer cells replicate some features of the physiology of native tissues (67,70,71), however, they lack predictive potential of *in vivo* and clinical outcome (69).

This method produces a well-controlled and uniform cell environment, which permits microscopic analysis and medium renewal while also sustaining cell growth in the majority of cell types. Considering their simplicity, 2D cancerous cell monolayers remain the most widely used model for assessing uptake and local drug delivery therapeutic efficacy. This is mostly owing to their ease of use and maintenance, as well as the ability to quickly evaluate combined therapies by adjusting several parameters (e.g., exposure time, concentrations, drug selection, and so on) (72).

However, cells in such a two-dimensional platform are normally exposed to a stiff solid surface on the basal side and a liquid on the apical side. Furthermore, studies have shown that due to the lack of cell–cell and cell–matrix interactions, as well as the loss of tissue-specific architecture, mechanical, and chemical cues that are essential for the unique functions of real tissues in the human body, two-dimensional cell culture cannot replicate real microenvironment and cell behaviors *in vivo*. That is, two-dimensional systems are not capable of providing a complex and dynamic microenvironment for cells, and consequently force cells to regulate to an artificial and rigid surface with cytoskeletal rearrangement, which may result in artificial polarity resulting in aberrant cell metabolism, gene and protein expression culminating in inaccurate findings (67,73,74). Consequently, the conclusions of these reductionist monolayer models are rarely in agreement with clinical trial outcomes (69,75).

Inefficiency of 2D cell culture models is widely understood from the standpoint of drug delivery due to a lack of suitable physiological barriers arranged in an acceptable shape in 2D cell culture. Therefore, to better predict drug effects and delivery mechanisms, *in vitro* models of relevant tissues that are more physiological than conventional 2D culture are required (71).

Additionally, a large number of studies have reported that cellular responses to drug treatments in 3D cultures are likely to give better *in vivo* predictions compared to 2D cultures (76–79). Most

of them show higher chemoresistance in 3D models, which is possibly a result of the limited drug diffusion through the tumor cell mass and to hypoxia (80,81).

Animal models, on the other hand, are used widely in cancer research to assess drug bioavailability, therapeutic efficacy, and dose-limiting toxicity (82). Prior to human clinical trials, all new drugs must undergo preclinical testing in animal models. These models, however, have a variety of drawbacks, including higher costs, species variations, restricted availability, and feasibility (83). Furthermore, ethical concerns about the use of animals in tumor research are widely contested. As a result, new *in vitro* cell culture models appear to be promising in terms of reducing the number of animals needed in cancer research and drug screening (84,85).

3D culture systems offer the unique opportunity to culture cancer cells in a spatially-relevant manner, together with the additional components of TME, mimicking native cell-cell and cell-matrix interactions and physico-chemical and mechanical properties (**Table 1.1**) (67,86–90).

Table 1.1. Key differences in cellular characteristics and process in 2D versus 3D

Cell features	2D	3D	Refs
Cell morphology	Altered shape, flat and elongated; loss of epithelial cell polarity	The natural cell shape and polarization is preserved; grow in 3D aggregates	(91)
Gene expression	Cell adhesion-, proliferation-, and survival-related genes are usually modified	Accurate representation of gene expression patterns	(9,92,93)
Cell interactions	Lack of cell-cell and cell-ECM interactions	Cell-cell junctions and cell communication	(94)
Access to nutrients and oxygen	all cells receive the same amount of nutrients and oxygen; inaccurate replication of the TME	Better approximation and representation of the TME; nutrients and oxygen are not equally supplied, hypoxic regions	(95,96)
Analysis and quantification	Easy interpretation of results; better long-term cultures	Difficult to analyze data, especially with multiple cell types or when in spheroid/organoid conformation	(5,95)
Cellular heterogeneity	Lack of sufficient heterogeneity to mimic natural tumor	heterogeneous cellular layers; proliferative, quiescent and necrotic zones similar to natural tumors in spheroids/organoids model	(53,95–97)

As indicated in the preceding section, TME exhibits distinct heterogeneity as a result of tumor associated cells and diverse molecular signals, which works as a fuel for potential therapy resistance. One of the main challenges in *in vitro* assessment of anti-cancer nano drugs is recapitulating such spatial and temporal heterogeneity. In recent decades, various 3D *in vitro* models have been developed and each of them are designed to fulfill one or more complexities of natural tumor microenvironment. Tumor-on-a-chip, patient-derived tumor organoids, tumor bioprinting, tumor spheroids, and scaffolds-based 3D models for tumor-like tissue growth are

examples of innovative tumor models aimed at better replicating the TME. Each of these models meets particular requirements of the TME that are depicted in four quadrants in **Fig.1.3**.

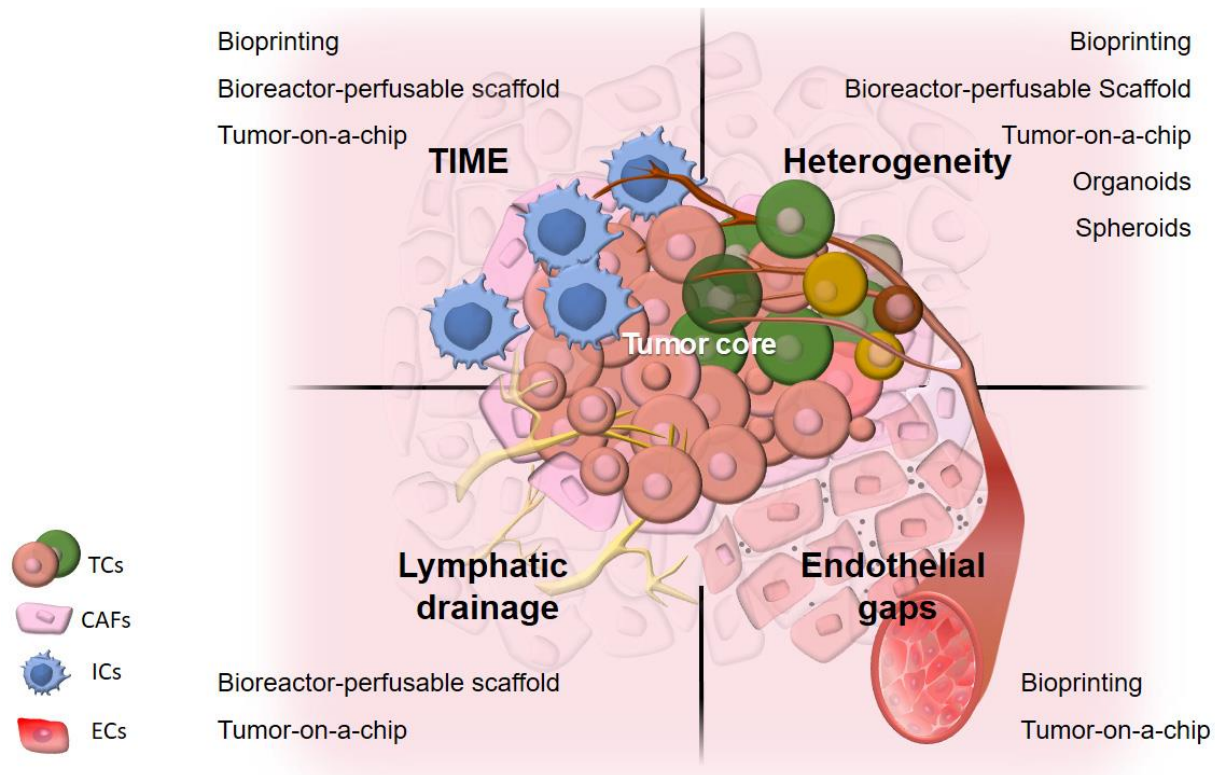


Figure 1.3. Comparison of Different innovative tumor models aiming to better mimic the TME, From (81)

1.2.1. Scaffold- based 3D *in vitro* models

Scaffold-based 3D tumor models rely on tumor cell attachment, proliferation, and migration to artificial 3D structures (72). Two main approaches for it includes: (a) cell seeding on an acellular 3D

artificial matrix (e.g., inserts, membranes, and sponges) and (b) dispersion of cells in a hydrogel often followed by its ionic cross-linking or radical polymerization (98–100). The artificial 3D scaffolds act as a mechanical support for cells, and their properties can be modified by employing adhesive molecules, modifications in surface charges, porosity, hydrophobicity, stiffness, and surface area to produce a 3D structure similar to natural ECM. (100,101). Bulk materials such as ceramics, glasses, polymers, and metals can be used to create artificial 3D structures. Polymers (natural or synthetic) are the most commonly used of these because of their ability to control their chemical and structural properties (101). The artificial 3D structures can be produced through various techniques, such as 3D printing, electrospinning, freeze-drying, foaming,

leaching, lithography, particulate molding, selective laser sintering, and solvent evaporation (102). Most of these methodologies are time-consuming and costly, as they necessitate high-tech equipment and techniques to create the artificial structure in a highly reproducible manner (102,103). Other drawbacks of scaffold based 3D cell culture models for drug screening include the formation of interactions between the materials and the drugs, which affect absorption and adhesion (10), and the difficulty in isolating/recovering cells or proteins from the structure for further assays (104).

1.2.2. Bio-printed models

3D bioprinting is the layer-by-layer deposition (additive manufacturing) of bioinks like cancer tissues, cancer cell pellets, microcarriers, decellularized ECM (dECM) components, and cell-laden hydrogels to mimic cancer initiation and progression and to explore cellular crosstalk or cellular morphogenesis (105–108).

The range of 3D bioprinting technologies available to biomedical researchers is broad. 3D bioprinting classified into different groups based on the working principle. These techniques that could be used alone or mixed-mode are fused deposition modeling (FDM), Stereolithography (SL), inkjet bioprinting, extrusion-based bioprinting, Laser-assisted bioprinting and Vat polymerization being introduced in review articles (108–110).

3D bioprinted tumors have been developed into a wide variety of structures ranging from fibers (111,112), microbeads (113), discs (114), grids (115), or multilayered grids (116,117), to sandwich structures (118), mini organs (119) and customized shapes (120). Moreover, 3D bioprinting has been used to enhance microfluidic devices (14,121) to enable modeling of cell migration and metastasis (122,123), endothelial barrier function (124), and vascularization (125). Current 3D bioprinting platforms have allowed the incorporation of multiple cell types, diverse ECM materials, and spatial and temporal introduction of signaling molecules and growth factors (126). Using this technique, 3D bioprinted models for different tumors, Breast cancer (127), Glioblastoma (111), Ovarian and cervical cancer (117,128), Lung cancer (129) and other types of cancers have been developed. These models have been useful for different pharmaceutical purposes and also testing immunomodulatory agents (130).

The major advantage of bioprinting is that it allows more realistic, accurate and facile 3D tumor modeling compared to the well-established 2D techniques (106). Despite the promising potential of 3D bioprinted models, challenges are still remained in terms of resolution, printing speed, biocompatibility, suitable bioink, bioprinting time, dimension of bioprinted tissues to mimic cancer tissue. The biocompatibility of 3D printing has been limited in cell viability and basic functions, and the effects on gene or protein levels have yet to be determined. In addition, to obtain large-scale tissue constructs, further studies are needed in both printing strategy and

bioink. Another limitation requiring extensive efforts is to develop appropriate technologies for real-time monitoring of cell functionality in the constructs.

Standardization and optimization of the printing process for the construction of effective models is essential which require intensive investigation of the relationship between the printing parameters and the characteristics of the obtained constructs. Therefore further development of bioink preparation and bioprinting process can significantly improve 3D bioprinted models for *in vitro* drug screening and evaluation of various therapies (105,106,131).

1.2.3. Organoids

Organoids are *in vitro* miniaturized and simplified model systems of organs that have gained enormous interest for modelling tissue development and disease, and for personalized medicine, drug screening and cell therapy (132). Compared with traditional 2D culture systems, 3D organoids better resemble the native organ in terms of gene and protein expression, metabolic function and microscale tissue architecture, moreover they can surpass 2D cell culture in structural resemblance to corresponding tissue and recapitulation of function such as producing mucus or absorbing and secreting biomolecules (133,134).

Organoids are widely used to model tissue development. Cancer organoids can be obtained from tumor biopsy samples such as gastrointestinal tract (135–137) breast (138), prostate (139,140), liver (141,142) and lung (143,144). These organoids capture the disease heterogeneity and present an excellent tool for personalized medicine to predict outcome of clinical treatments. They also allow mid-throughput to high-throughput screening of therapeutics and drug screening (134).

However, none of the established organoid systems reproduces the full functional repertoire of their respective organ and often lack key specialized cell types failing recapitulation of native organs. Another drawback of organoids is limited time span of maintaining them in culture, on the other hand optical monitoring of routinely used as readout providing little information about the functionality of organoids and the other techniques for *in situ* monitoring are technically challenging for organoids (134).

Organoid systems also suffer from considerable variability in organoid formation efficiency, end-point morphology and function, which is often inherent to the stochastic nature of *in vitro* self-organization and cell fate choices. These issues which limit the translatability of organoids are inherent to design of organoids, therefore design of organoids systems needs to be modified to increase the number of controllable parameters (134).

The growth environment of organoids is ill-defined which leads to high variability of resulting organoid phenotypes. Therefore, environments need to be designed for precise spatiotemporal modulation of bioactive cues to guide organoids growth. In addition, accurate and high throughput readouts are important for optimization of organoid models.

Although organoids can be made more robust and more physiologically relevant by using engineering approaches, they will probably never be as robust and reproducible as cell-line-based models, nor will they be able to fully reproduce the complexity of animal models. Therefore, to be able to choose appropriate models, a set of organoids with varying levels of complexity is required. The desired level of complexity should correlate with the scale of the process that needs to be modelled (134).

1.2.4. Multicellular tumor spheroids

3D tumor spheroids are self-assembled cultures of tumor cells that maintain strong cell-cell interactions (81). Multicellular tumor spheroids refer to the aggregates of single tumor cells or co-cultures with other types of suspended or embedded cells grown in scaffolds in a 3D environment (13,126).

Multicellular spheroids are the most common and versatile scaffold-free method for 3D cell culture (70). These micro-sized cell aggregates can be used to model many different tumors for *in vitro* studies (145,146) and, in particular, could represent a reference model for avascular tumor microregions (147,148). This model partly recapitulates *in vivo* tumor microenvironments (149). For example, larger MCTS sustain oxygen and nutrient gradients that often result in the formation of a necrotic core similar to those in poorly vascularized tumors (18).

Several literatures depict the genomic stability of multicellular spheroids, indicating the preservation of genomic profile of human malignant cells such as glioma in spheroid but lacks in monolayer (150,151). They have a well-defined spatial organization in which there is an actively proliferative outer layer due to the high availability of oxygen and nutrients, an intermediate layer composed of quiescent and senescent cells, and an inner apoptotic/necrotic core resulting from the limited distribution of nutrients and oxygen (96,148,152).

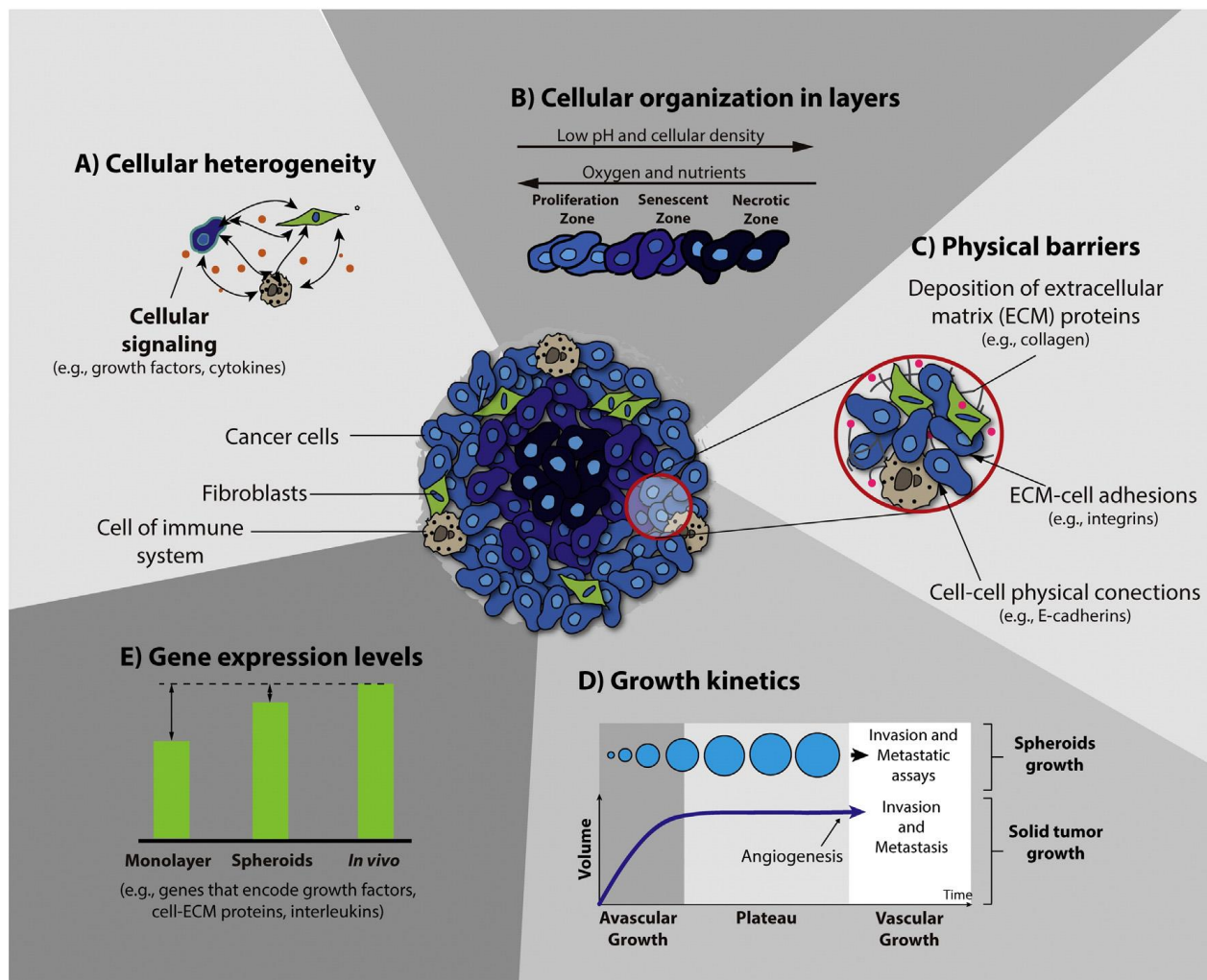


Figure 1.4. Schematic representation of the main characteristics of 3D spheroids that are crucial for their application in the screening of anticancer therapeutics, From (96)

Spheroids make excellent tools for tissue-based mechanistic assays, as well as for probing cell–cell and cell–matrix interactions. Spheroids have also been used as a tool to investigate the role of adhesion molecules in tumor biology. Multicellular tumor spheroids have greater chemotherapeutic resistance than the same cells in monolayer culture (24,149). Spheroids have been used in four main applications: (1) the study of cell function (e.g., cell proliferation, migration, and invasion) in an avascular tumor microenvironment, (2) the development of new therapies and drug screening, (3) the study of tumor angiogenesis, and (4) the study of tumor–immune cell interactions (16,149,153–156)

Yet, for drug screening purposes, they are commonly prepared out of immortalized cancer cell lines (157), which ensure the generation of standardized and reproducible models. They present several structural, physiological and biological features resembling the *in vivo* TME such as: (1) multicellular structure including proliferative, senescent and necrotic cancer cells; (2) the

formation of oxygen and nutrient gradients as they grow in size; (3) cell-cell signaling; (4) cell-matrix interactions; (5) gene expression; (6) stem-like properties (18,72,76). The features making spheroids an excellent *in vitro* model in cancer research were shown in **Fig.1.4**.

1.2.5. Summary

Different classes of developed 3D *in vitro* models try to recapitulate natural tumor microenvironment. Among them MCTS is an attractive model to recapitulate *in vivo* tumor features. Although spheroids have increased our understanding of tumor biology, there are certain limitations linked to reproducibility due to low size/morphology consistency, which impedes the establishment of standard models (151). Furthermore, some procedures have been linked to low throughput and difficulty in retrieving cells for analysis (20,151). Several techniques have been developed to generate spheroids trying to increase homogeneity of spheroids and throughput of experiments. The next section provides an overview of various approaches for generating spheroids.

1.3. Spheroids preparation techniques

There are varieties of spheroid construction processes available today (**Fig.1.5** and **Table 1.2**), each with their advantages and disadvantages(84), several of which have been improved for large-scale production under extremely repeatable conditions (96). They primarily include the application of cell attachment-resistant surfaces or physical pressures to stimulate cell-to-cell contacts and encourage the creation of 3D spheroid structures (158).

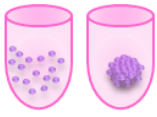
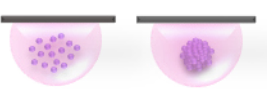
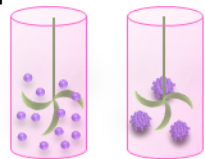
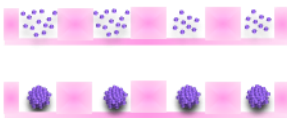
1.3.1. Liquid overlay methods

This method primarily employs non-adherent 96-well plates that have been coated with poly-2-hydroxyethyl methacrylate (poly-HEMA) (159–162) or agarose (163–166) to prevent cell attachment. This approach may be used to make mono- and hetero-type spheroids, with the size and morphology of the spheroids being carefully controlled by changing the amount of cells seeded in each well (167–170), with or without addition of diluted extracellular matrix such as Matrigel to provide cell-matrix adhesive cues.

Because of the enormous number of spheroids produced and the ease of handling, this method is suited to a variety of high-throughput experiments (167,170).

The time-consuming plate-coating phase, on the other hand, is a significant disadvantage. Although pre-coated low cell adhesion plates are commercially available (e.g., Corning® Ultra-low Attachment Surface; Sumitomo Bakelite Co. PrimeSurface low adhesion culture plate), their use raises overall expenses (171).

Table 1.2. A comparison of MCTS generation techniques.

Generation Methods	Advantages	Disadvantages	Ref
Liquid overlay methods 	Easy to operate Low shear stresses High yield Low cost	Labor intensive Variation in LCTS size and shape Inability to stimulate cell-ECM interactions	(172,173)
Hanging drop methods 	Easy to operate Good size control Low shear stresses Co-cultivation of multiple cells	Labor intensive Low yield Difficulties in mass production Difficult to change the medium Difficult to transfer the spheroid	(174,175)
Agitation-based approaches 	Mass generation Easy to operate Long-term culture Dynamic microenvironment Co-cultivation of multiple cells	High shear stresses Variation in MCSs size and shape Inconvenient to observe the generation process of the spheroid Inability to stimulate cell-ECM interactions	(176)
Patterned surfaces and microfluidic devices 	Realistic microenvironment High yield Long-term culture Good size control Low shear stresses High-throughput analysis Labor saving Dynamic microenvironment Generate aggregates of different shapes Co-cultivation of multiple cells Low reagent consumption Low cell usage	Requiring professional equipment Higher requirements for operation Higher cost	(177–182)

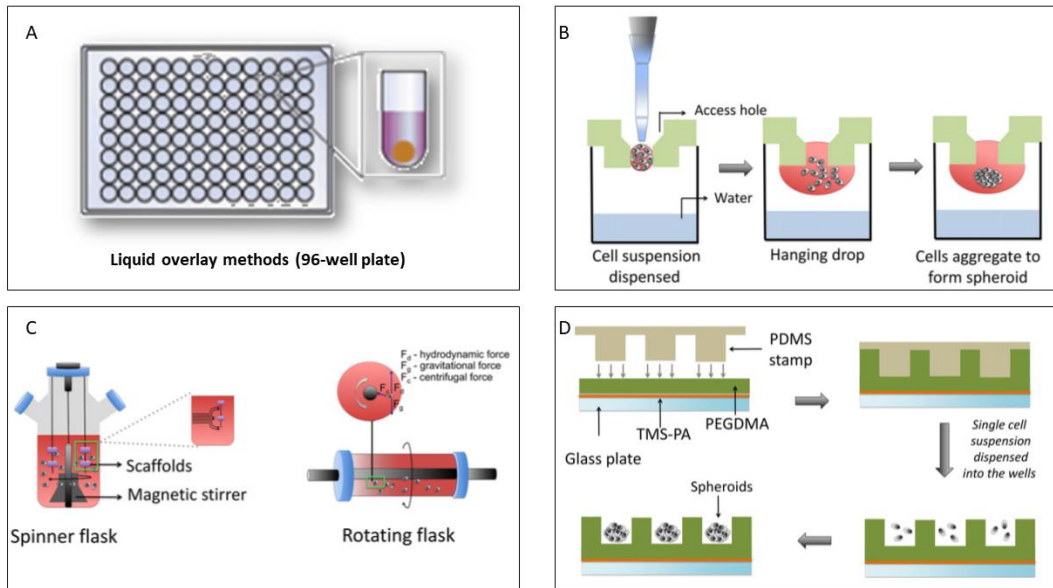


Figure 1.5. schematics of different approaches for spheroids formation (A) Liquid overlay methods (B) Hanging drop methods (C) Agitation-based approaches (D) Patterned surfaces and microfluidic devices. From (67)

1.3.2. Hanging drop methods

Surface tension is used to hang small cell suspension droplets (20-50 μL) on the underside of a tissue culture dish lid (155,170). Gravity then pushes cell accumulation at the drop's tip (liquid-air contact) and produces fast aggregation into a single spheroid (155,169). Control of spheroid size has been achieved with high reproducibility for various cell lines (171) in mono and co-cultures by adjusting cell density (183). The volume of the seeding suspension, on the other hand, is often limited and does not give adequate nutrients for a long-term culture (155,169).

As a result, once generated, spheroids must be moved to 96-well plates or embedded in polymer matrices for further investigation (184–187). Not only does such transfer influence the integrity of spheroids, but it also renders this procedure very labor intensive and time-consuming, prohibiting its widespread implementation (155,169,170). Commercially available systems (InSphero GravityPlusTM technology and 3D Biomatrix PERFECTA3DTM hanging drop plates) can minimize workload and enable high-throughput studies, albeit at a significant cost increase (158).

1.3.3. Agitation-based approaches

Spinner flasks and rotational culture systems (e.g., NASA Rotary Cell Culture System) are bioreactors in which cell aggregation and spheroid formation are mediated by continuous spinning that keeps a cell suspension in motion, allowing cell-to-cell interactions while preventing

cell attachment to the container wall (171). The mobility of the medium maintains the transit of nutrients and waste, allowing for (i) long-term culture and (ii) large-scale production.

Although it is possible to affect the average spheroid diameter by adjusting cell-seeding density, spinning rate, and culture time (155), overall control over the amount of cells per spheroid and their size is quite weak (169,171). As a result, prior to any additional testing (e.g., cytotoxicity, penetration, etc...), manual selection of similarly sized spheroids and their transfer in different supports are required (188,189). It should be emphasized that spinning flasks can only be used to culture cell lines that can endure significant shear stress (170,171).

1.3.4. Patterned surfaces and microfluidic devices

Patterned surfaces, in conjunction or not with microfluidics devices, have lately been developed, providing a new spectrum of advanced spheroid formation methodologies (171,190–193). Arrays of microwells manufactured with the micromolding or photolithography techniques, for example, have been used to create spheroids with defined size and composition (71,155,190,194–198). Non-adherent materials such as poly(dimethyl siloxane) (PDMS) with cell-repellent coatings (196,197,199) or agarose (198,200) or Pluronic® F-127 (201) have been used to achieve low adhesion surfaces. Microwell plates that are compatible with classic well plate formats and microscopes are ideal for high-throughput applications.

Similarly, the production of cellular aggregates in a controlled environment and with significant simplification of liquid handling methods has been achieved using microfluidic devices with various micro-sized chambers and channels (71,169,193).

Microfluidic technologies are defined by the advanced manipulation of tissue microenvironmental conditions and can include both tissue and micro-organ (individual or multiple tissue types) models. The unique experimental conditions that distinguish microfluidics from other research methodologies are the temporal manipulations of liquid movement and mechanical parameters through defined compartments (202). They are particularly appealing and convenient for drug screening applications since they require only a little amount of cells, medium, and chemicals and provides a unique control of cell environment. Yet, the inability to extract and fully characterize the generated spheroids is a general downside of these procedures (158,171,203). In addition there are issues associated with validation of models and standardization of materials and approaches (204,205).

1.3.5. 3D *in vitro* platform used in my PhD

3D *in vitro* model used in this project consists of a hydrogel-based microsystem for spheroids formation and culture. This microsystem with a pattern of microwells is made of agarose gel. The agarose gel as a hydrogel has interconnected pores allowing diffusion and transport of O₂, nutrients and metabolic wastes. As previously, discussed uniformity of spheroids plays a critical role in cellular response to treatments and reproducibility of results. This microsystem with microwells pattern, compatible with classical and available multi-well plates, enables generation of more than one hundred homogenous spheroids with single-step pipetting (**Fig.1** in article, **chapter 2**). Thanks to this agarose based microwells, all steps of experiments from cell seeding, treatment, fixation to immunostaining could be performed in classical multi-well plates without transferring spheroids. However, in case of requiring transfer of spheroids, microwell can be transferred easily and without manipulating spheroids. Another advantage of these microwells is their compatibility with high throughput optical microscopy techniques, biological assays or other analysis techniques (using either intact spheroids, either single cells after spheroid dissociation).

1.3.6. Summary

Recent interest in MCTS models has resulted in an ever-increasing number of novel solutions for the challenges of such 3D *in vitro* models. As a result, commercial and noncommercial techniques for the generation of spheroids were developed. In addition to forming spheroids and maintaining them in culture for longer periods, these techniques must be compatible with existing characterization techniques in order for researchers to analyze the effect of nanotherapeutics on cells in MCTS. In this regard, the most appropriate spheroids formation procedures are those that are compatible with nanotherapeutics characterization techniques.

1.4. Tools for characterization of multicellular tumor spheroids

Currently different techniques are employed to study 3D tumor spheroids characteristics including morphology, topography, size, cellular organization, protein and gene expression, invasive and metastatic potential of cancer cells. In addition these techniques are extensively used for evaluating anti-cancer treatment efficacy and changing tumor cell properties in response to these therapeutics (96). Below is a detailed description of the methodologies used for investigation of these properties (summarized in **Table 1.3**).

1.4.1. Drug screening assays

Colorimetric, fluorometric, and luminescent techniques are frequently used to analyze the activity of specific enzymes or the amount of metabolites that are connected with the state of health of the cells in 2D cell cultures.

Some of these methods, which were developed for 2D cultures, are now used to assess drug cytotoxicity in 3D models, but they can be a source of variability, and the data obtained must be carefully evaluated because the experimental procedures used are optimized for monolayer culture and are not always directly compatible with 3D models.

In fact, spheroids' compactness combined with limited mass transfer impedes the uniform distribution of solutes, particularly in the interior sections of the spheroids, resulting in incorrect results. Nonetheless, many of these assays have been used to evaluate therapy in tumor spheroids, including MTT (206), AlamarBlue® (207), Trypan Blue (208), and lactate dehydrogenase (206).

Due to the lack of a reference method, novel assays specially tailored for 3D spheroids and capable of giving rigorous data have been developed. CellTiterGlo 3D and Perfecta 3D cell viability assays (WST-1 assay) were developed specially for 3D culture and allow for improved reagent penetration into the compact mass of the spheroids, resulting in sensitive and reliable results (70).

1.4.2. Biochemical assays

The viability of MCTS is affected by poor O₂ delivery combined with metabolic waste accumulation. Acid phosphatase (AP) and resazurin are cell viability assays that are both sensitive and high-throughput compatible (75,152,209). The MCTS-produced acid phosphatase catalyzes the dephosphorylation of the phosphate group of p-nitrophenyl phosphate (AP substrate), resulting in a yellow-colored product that can be measured using a colorimeter. The degree of yellow color indicates acid phosphatase activity and thus serves as an indirect indicator of the number of living cells in MCTS.

The resazurin reduction assay is a fluorescence assay that determines viability based on the metabolic activity of living cells. Dehydrogenase enzymes generated by metabolically active cells convert the nonfluorescent blue substrate resazurin to fluorescent resorufin, the intensity of which could be read with a fluorescent plate reader. The number of metabolically active cells in MCTS is proportional to the number of relative fluorescence units (67).

1.4.3. Western blot and qRT-PCR

Standard cell biology techniques such as Western Blot (WB) and qRT-PCR, which are used to assess protein and gene expression fluctuation in 2D cultures, can also be employed in 3D spheroids. The approach utilized to harvest protein from the 3D culture is the fundamental difficulty with these approaches. In reality, the combination of chemical buffers containing detergents like SDS with mechanical pipetting or sonication, as well as prolonged incubation durations, is required to disrupt the spheroids' compact structure (208). The isolated proteins are then semi-quantified using normal WB analysis. Quantitative RT-PCR can also be used to assess gene expression in spheroids. Spheroid sample preparation for qRT-PCR analysis is very similar to that for Western blot analysis; namely cellular aggregation disruption and cellular homogenate preparation (210), but as with WB, a suitable lysis process is required to ensure that RNA is collected from all of the cells that comprise the spheroid. Although for these analysis, numerous spheroids need to be dissociated that is hard to achieve using standard ULA 96-well plates. Researchers employed these two methods in tandem to uncover distinct genes and proteins in spheroids that are important in tumor growth (211) and response to therapy (212).

1.4.4. Flow cytometry

Flow cytometry is a popular cell biology technique that can be used for quantification of cell viability, growth kinetics, apoptosis, and CSC phenotypic studies in MCTS. It is a highly effective method that provides quantitative and reliable data. Flow cytometry is commonly used to assess the cytostatic and/or cytotoxic effects of anticancer drugs in spheroids (213).

In flow cytometry, cells must be in suspension in order to be examined individually. As a result, spheroids in their natural condition are ineffective, and cellular disaggregation is required to generate a single-cell solution, thus, flow cytometry may not be the most efficient technique for assessment of drug penetration and localization within different layers of spheroids.

Spheroids are collected and processed using enzymes (e.g., trypsin) or enzyme mixtures (e.g., accutase[®] or accumax[®]) that induce cellular dissociation and damaging spheroids integrity and reduces cell survival in MCTS (12,214,215). Single cells are stained with calcein-AM and ethidium homodimer to represent live cells and cells with damaged membranes, respectively, for live/dead cell analyses. COPAS flow cytometers, but on the other hand, are a non-destructive technology that permits analysis of intact MCTS. They are a specially engineered fluidic system that permits measurement of particles ranging in size from 20 to 1500 μm . As a result, COPAS flow cytometers enable reliable viability determination and provide insightful knowledge about the cancer stem cell niche in MCTS (67,148).

1.4.5. Microscopy

Electron microscopy

Electron microscopy (scanning or transmission) enables for the capture of high magnification and resolution images of 3D spheroids (67). Electron microscopy can be used to see the ultra-structural changes that occur during apoptosis and necrosis (216,217).

Scanning electron microscopy produces high-resolution images of MCTS's superficial topography, whereas transmission electron microscopy produces high-resolution 3D images of large MCTS's interior structures (213).

The most frequent electron microscopy modality for 3D spheroid observation is high vacuum scanning electron microscopy (high vacuum SEM) (218,219). There are four key steps to sample preparation for this sort of microscopy: (1) fixation in which the spheroid structure is retained and stabilized), (2) dehydration (water in the sample is replaced by alcohols or acetone), (3) critical point drying (The sample is entirely dry; there is no ethanol or acetone in the sample) (4) sample sputter coating with gold to allow imaging (67) (**Fig. 1.6 D**).

Another electron microscopy technique that has been frequently used for 3D spheroid investigation is transmission electron microscopy (TEM). Spheroids are chemically fixed, then dehydrated and sectioned into thin slices for sample analysis. Specimen fractures may occur even though spheroid sectioning is normally done after immersion in resins (e.g., epoxy) (213).

The most typical application of TEM in spheroid analysis is the investigation of nanoparticle penetration and distribution within the spheroid (**Fig 1.6 E**) (220). Analysis of spheroids made in standard ULA 96-well plates with TEM is complicated as a large number of spheroids must be collected and pulled together before resin embedding. It is difficult to retrieve spheroid orientation and original shape. The agarose-base microsystems offer an easy sample preparation for electron microscopy. It was used in my PhD to prepare samples for analysis with nanoSIMS (**Fig.5** in article, **Chapter 2**).

Table 1.3. Summary of the main microscopy techniques and methodologies used to characterize the effect of anticancer therapeutics on 3D tumor spheroids.

Techniques	Parameter analyzed	Description	Ref
Optical and fluorescent microscopy	Size and growth Cellular organization Morphology Drug penetration Cellular death Proteins expression Invasion/metastasization of cancer cells	Monitoring of spheroid size, area or volume. Observation of live and dead cell distribution. Observation of spheroids labelled with antibodies. Observation of spheroids stained using simple histological protocols. Observation of spheroid shape and symmetry. Determination of the penetration and dispersion capacity of drugs. Assessment of the expression of proteins before and after drugs administration Visualization and determination of spheroid cell invasion/metastatic capacity.	(221,222) (219) (222) (218) (219,223) (198,224) (225) (226,227)
Scanning electron microscopy (SEM)	Topology Cellular death	Visualization of the spheroid surface and cell-cell physical Interactions Visualization of the superficial destruction of spheroids.	(219,224)
Transmission electron microscopy (TEM)	Cellular organization Drugs penetration Cellular death	Observation of specific characteristics of each spheroid Layer Visualization of cell-cell physical interactions Observation of modifications to spheroid structures.	(218) (228)
Flow cytometry	Drug penetration/uptake Cellular death Cell cycle Protein expression	Observation of mitochondrial status. Quantification of the percentage of proliferating and senescent cells. Quantification of the percentage of cells that express specific proteins.	12,185 213
Western blot and qPCR	Cellular death Protein expression	Analysis of the expression of cellular death biomarkers. Analysis of the expression of proteins	(215) (225)

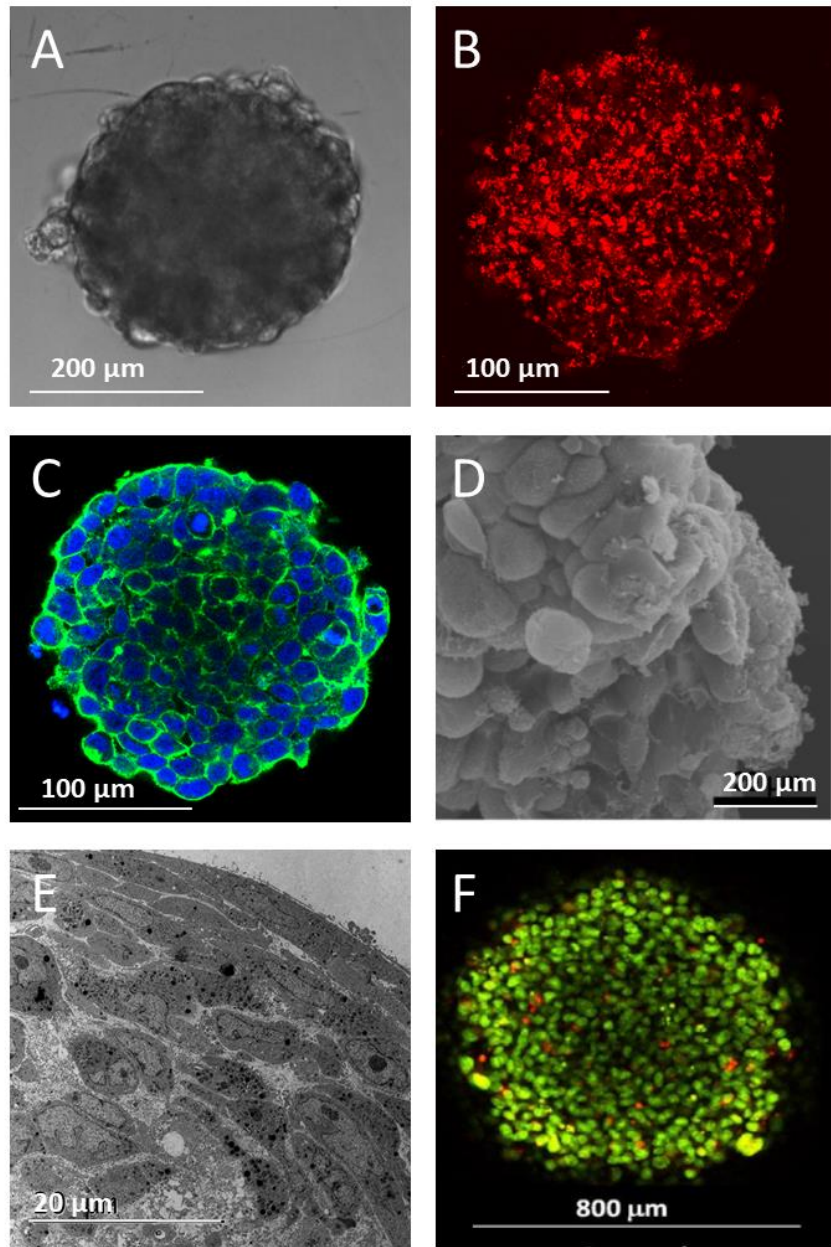


Figure 1.6. Samples of spheroids imaged acquired with different microscopy techniques; (A) Top view of SW-480 spheroids with phase contrast microscopy (24). (B) Maximal image project (MIP) of confocal fluorescence microscopy image of AGuIX®-Cy5.5 nanoparticles in HCT-116 spheroid [my PhD work]. (C) Confocal fluorescence microscopy image of slice of HCT-116 spheroid labelled for actin (green) and nuclei (blue) [my PhD work]. (D) Scanning electron microscopy (SEM) image of the MCF-7 spheroid surface (96). (E) Transmission electron microscopy (TEM) image of L-MSC spheroid (229). (F) Two-photon microscopy image of F-98 spheroids stained with Hoechst 33342 (green: live) and Ethidium Homodimer (red: dead) (230).

Optical microscopy

Conventional optical microscopy techniques combined with image-analysis software are extremely beneficial for studying the morphology, size, form, and structural organization of spheroids before and after anticancer therapeutics exposure. Growth evolution of spheroids may be observed for several days using a common phase-contrast microscope by evaluating several morphological parameters and modifications in their area, sphericity index, and volume (70,231) and analyzing them with appropriate software (**Fig. 1.6 A**) (212,232).

Light-sheet-based fluorescence microscopy (LSFM) and its variant, selective plane illumination microscopy (SPIM) generate high-contrast images of huge spheroids and enables live-cell division dynamics in spheroids to be monitored. The specimen is illuminated throughout a plane with a light sheet perpendicular to the microscope objective's axis. This allows for the specimen's focus sectioning to be done in a sequential manner, resulting in high-resolution images (233,234). SPIM is particularly beneficial for acquiring high-resolution images of the hypoxic core of spheroids, which is difficult to image using conventional light microscopy (96,235).

Two-photon or multiphoton microscopy is fundamentally different from traditional linear excitation microscopy. For contrast generation, multiphoton microscopy employs higher-order light-matter interactions involving several photons (236,237). Multiphoton microscopy, as a result, considerably improves depth penetration of photon. The biologic impacts of chemotherapeutics or nanomaterials on 3D tumor spheroids, previously undetected by standard light microscopy, may now be observed (**Fig 1.6 F**) (213).

Confocal images of spheroids reveal important details on cytoskeletal architecture and protein expression *in situ* (238). By staining MCTS cryosections with hematoxylin and eosin, the distinct biological zones (the outer proliferative rim, middle quiescent zone, and dark necrotic core) may be observed (213). ECM deposition can be seen in confocal and fluorescence microscopy pictures of MCTS immunostained with antibodies against fibronectin, laminin, collagen IV, tenascin, and other ECM proteins (225). Hoechst or DAPI staining, phalloidin, Ki-67, caspases, Annexin V, propidium iodide, and TUNEL staining can provide additional information regarding the morphology, cytoskeletal arrangement, proliferation, and live/dead state of cells in spheroids (**Fig. 1.6 B, C**) (216,239).

Imaging large spheroids using optical microscopy techniques is extremely difficult, owing to low light and antibody penetration, as well as attenuation of fluorescent signal by light scattering. Furthermore, the movement of spheroids in suspension makes imaging of living spheroids difficult (67).

1.4.6. Optical clearing

Due to the great thickness of 3D cell cultures, which causes a light scattering effect that limits light penetration, imaging them is extremely difficult. The light scattering is caused by mismatches in the refractive index (RI) of the cellular constituents, which cause the excitation light to disperse through the sample, limiting its penetration, or by reducing the amount of emitted light that reaches the detector (240). These RI mismatches cause variations in the speed and angle of light propagation (in the visible and near-infrared spectrum), i.e. light refraction from molecules, membranes, organelles, and cells (240). This effect promotes light refraction and is primarily responsible for tissue opacity. The fluorescence light emitted by the excited fluorophore, on the other hand, can be dispersed and hence may not reach the detector with high intensity or may indicate its origin incorrectly, resulting in images with poor contrast (241).

To bypass these constraints, sectioning processes or optical clearing processes can be applied. Both procedures necessitate spheroid fixation prior to analysis, making it difficult to analyze dynamic changes in spheroids in real-time or over time. Sectioning processes are time-consuming and require well-defined techniques as well in order to avoid sample fractures and morphological deformation (242), moreover they can permanently change spheroid initial structure (240,243,244).

Several clearing procedures are currently being employed to increase tissue transparency (245), reduce multiple refraction by homogenizing RI across the sample to allow for deep tissue visualization. This procedure creates transparent 3D biological samples, which improves light penetration, imaging depth, and contrast; that is, the majority of the light will reach the focus point and subsequently the majority of the fluorescence light will be detected without deviations in its course (**Fig. 1.7**) (240,244). However, depending on the clearing process utilized, moderate structural distortion in tissue structures may occur, as tissue shrinkage/expansion and labeling artifacts (245).

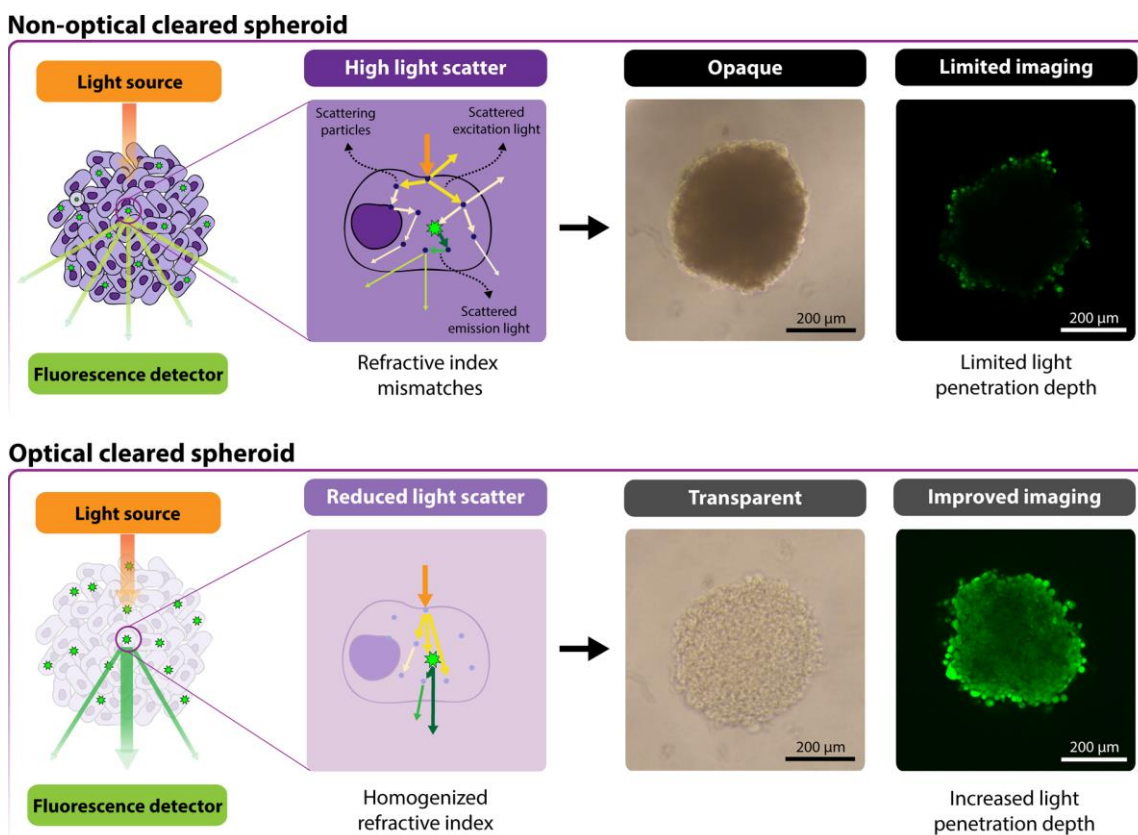


Figure 1.7. Representation of the light propagation in a non-cleared and cleared spheroid, From (246)

1.5. Cellular uptake of nanoparticles and application of MCTS model in nano-drug screening

Despite the promising potential of nanoparticles for targeted tumor therapy, difficulties associated with their journey through the biological environment have limited clinical translation success. There are various biological barriers in the efficient delivery of systemically administered nanoparticles to target tumors that stem from bio-interactions in the blood (247,248). and sequestrations in some organs such as the spleen and liver before reaching the tumor (249,250). Those nanoparticles that make it to the tumor encounter obstacles inside it. Interstitial pressure and tumor vasculature obstruct extravasation into tumors. Although the complexity of TME features discussed previously makes deep and uniform penetration of nanoparticles within tumors complicated (251), nanoparticle properties such as size, shape, and surface charge can influence intratumoral transport (252). Cell type, as well as the physiochemical properties of nanoparticles, influence cellular uptake and intracellular trafficking, which can affect bioavailability, drug release, and the overall functionality of the nanoparticles administered (253).

The complexities of nano-bio interactions emphasize the critical need for more relevant and complex preclinical models, such as tumor-on-chip devices capable of replicating many tumor features (254). Following that, some aspects of cell-nanoparticle interactions and the use of MCTS in such studies will be discussed.

1.5.1. Cell-nanoparticles interactions

Nanoparticles (NPs) are a diverse category of materials that include in particular inorganic metal and metal oxide nanoparticles, polymer particulate materials, and carbon-based nanomaterials in a variety of forms. NPs have distinct physicochemical features, including ultra-small size (1-100 nm), a significant surface area to mass ratio, strong reactivity and new properties appearing at the nanoscale size, that set them apart from bulk microscale materials of the same composition (255). There are several properties of NPs that influence their interactions with cells. These properties are summarized in **Fig. 1.8**. When engineered nanoparticles with specific physiochemical features reach the exterior membrane of the cells their cell-NPs interactions begin with NPs internalization.

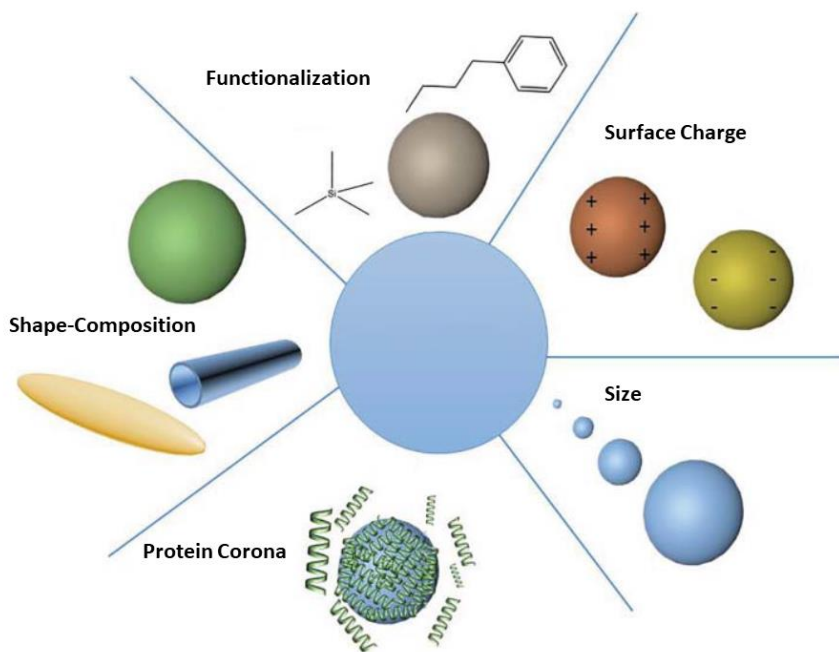


Figure 1.8. Factors influencing the interactions between NPs and cells. Factors influencing the interactions between NPs and cells. The main factors reported are: size of the nanosystem, surface charge, presence of functional groups on the surface, shape of the material, composition of the material, and composition of the protein corona formed upon incubation of the particles with biological media, From (256).

1.5.2. Cellular uptake of nanoparticles

Cellular uptake or internalization of nanoparticles is a highly regulated mechanism, in which biological membrane acts as a barrier for nanoparticles to enter cells. When nanoparticles reach the exterior membrane of the cells, they could interact with plasma membrane or ECM and enter the cells(257).

During *in vivo* and *in vitro* cell exposure, nanoparticles can pass the cell membrane by a variety of processes, the most frequent of which are subcategories of endocytosis. Endocytosis is the process by which NPs are engulfed in membrane invaginations, followed by their budding and pinching off to form endocytic vesicles, which are then transported to specialized intracellular sorting/trafficking compartments.

Endocytosis pathways can be classified in five distinct mechanism: (a) clathrin-dependent endocytosis; (b) caveolin-dependent endocytosis; (c) clathrin- and caveolin-independent endocytosis; (d) phagocytosis; and (e) macropinocytosis. Schematics of these pathways are shown in **Fig. 1.9**.

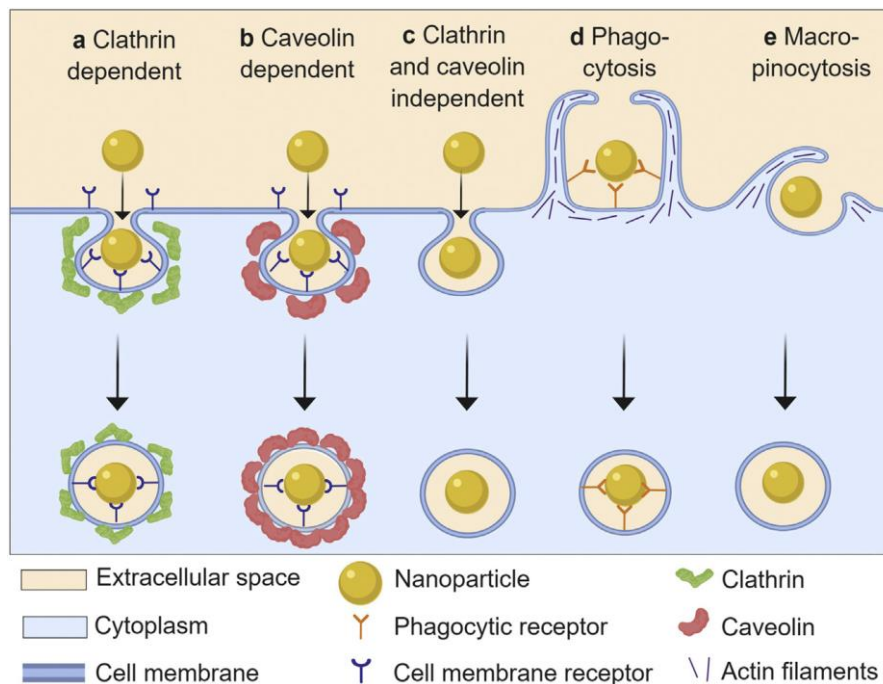


Figure 1.9. Schematic overview of nanoparticle uptake pathways via endocytosis. Multiple different pathways exist for cellular entry of nanoparticles via endocytosis mechanisms: (a) clathrin-dependent; (b) caveolin-dependent; (c) clathrin- and caveolin-independent; (d) phagocytosis; and (e) macropinocytosis pathways. From(253).

Although the different endocytosis pathways are widely recognized as the major mechanisms NPs enter the cells, NPs can be internalized by the cells via other processes including passive diffusion,

hole formation, direct microinjection and electroporation. You can see the schematics of these mechanisms in **Fig 1.10**. After successful cellular entry, nanoparticles need to overcome intracellular barriers to reach cellular compartments and organelles, which is called intracellular trafficking of NPs.

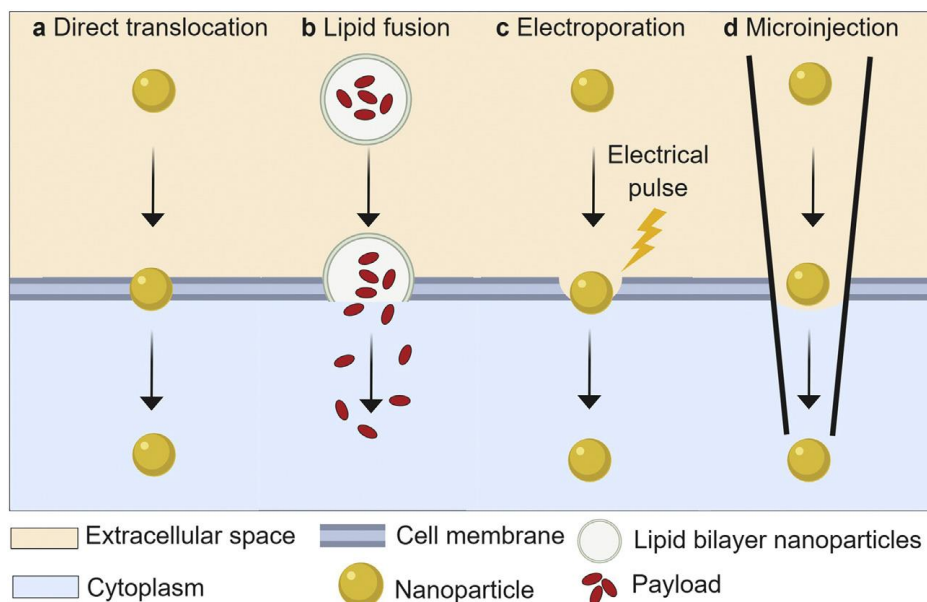


Figure 1.10. Schematic overview of nanoparticle cytoplasmic delivery pathways and strategies. Major pathways and strategies for nanoparticles to cross the cell plasma membrane for direct cytoplasmic entry include: (a) direct translocation; (b) lipid fusion; (c) electroporation; and (d) microinjection. Each of these pathways allows nanoparticles to enter the cell's cytoplasm, directly, from(253).

1.5.3. Intracellular trafficking of nanoparticles

After cellular internalization, nanoparticles undergo transport and trafficking to various intracellular destinations. Intracellular trafficking of NPs has a critical role in the cellular fate of NPs and their therapeutic/imaging efficacy. For example, If nanoparticle cellular uptake occurs via endocytic pathways, their ultimate fate is usually determined by the intracellular sorting/trafficking mechanisms mediated mainly by a network of cellular endosomes in conjunction with the Golgi apparatus, endoplasmic reticulum (ER), and lysosomes (258,259)(see **Fig. 1.11** for details).

Endosomes are relatively large (up to 1 μm and even larger) intracellular membrane-bound compartments initially produced by the plasma membrane, and later they convert to late endosomes followed by fusing with Golgi-derived vesicles (260). It is difficult to provide a complete picture of all intracellular events and processes that occur once nanoparticles enter cells due to the intricacy of nanoparticle intracellular trafficking patterns (253).

Currently used methods for probing the intracellular trafficking of nanoparticles include optical- and electron-based microscopy techniques, such as super resolution fluorescence microscopy, confocal laser scanning microscopy, transmission electron microscopy, scanning electron microscopy (261).

Colocalization of nanoparticles with labelled subcellular species could be used to assess their intracellular localization; colocalization is defined as the spatial coincidence or potential interactions between nanoparticles and cell organelles. Fluorescence microscopy is a powerful tool for tracking nanoparticle localization in biological samples; nevertheless, the constraints of this technology have limited such studies to qualitative observations utilizing the "dye-overlay" method. (262,263). The most common method for analyzing colocalization is superposition of fluorescence images and displaying the merged color images. This approach of evaluating colocalization is vulnerable to resolution limitations; a fluorescence overlap does not always indicate colocalization of two probes. The problem is that an intermediate color, showing colocalization, may only be obtained if the intensity of the two probes are similar, which can lead to misinterpretation. Image quantification appears to be necessary in order to achieve a reliable conclusion. (263,264). Such approaches can be broadly classified as threshold-based or intensity-based. Pixel values are taken into account in intensity-based methods. Pearson's correlation coefficient, for example, computes the correlation between pixel intensities in each channel, whereas Mander's coefficient computes the ratio of intensities in one channel relative to above-threshold regions in the other. (262). Pearson's correlation coefficient quantifies the linear relationship between gray values of fluorescence intensity pixels in image pairs (264). In my PhD, I tried both the Pearson's correlation coefficient (PCC) and the Manders overlap coefficient to assess colocalization and correlation between two channels of fluorophores in confocal fluorescence microscopy images. A comparison of a few pairs of images in 3D models revealed that the Pearson's correlation coefficient provides a more realistic and logical image analysis for my samples. Since Pearson's correlation coefficient considers mean intensity values in calculation, the analysis results are independent of the intensity of each fluorophore, so we can use it for fluorophores couple of images even if they do not have the same brightness.

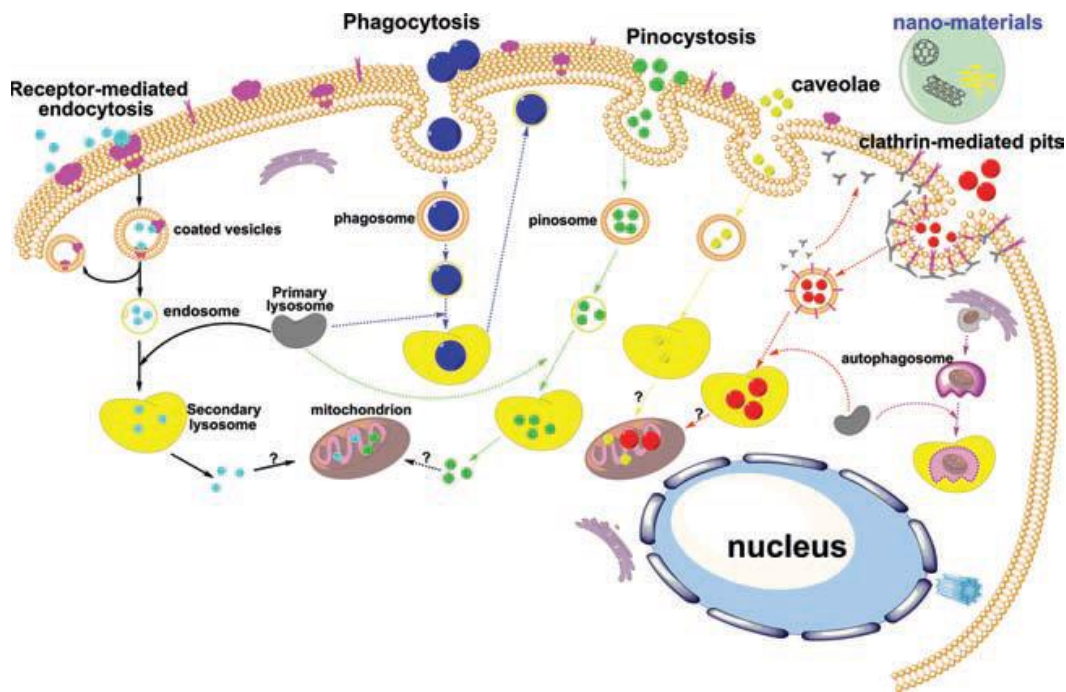


Figure 1.11. Schematic of known NPs internalization pathways and their following intracellular trafficking. From (258)

Similar to nanoparticle cellular uptake, nanoparticle intracellular trafficking is also dependent upon nanoparticle's physicochemical properties, including size, shape, and surface chemistry and also cell type and cell microenvironment (253,257). Hence, developing a 3D *in vitro* model capable of simulating various feature of natural TME with the possibility of high throughput screening and compatibility with microscopy techniques is crucial for study of cell-NPs interaction. As discussed earlier, MCTS are convenient *in vitro* models for recapitulating TME. The role and applications of MCTS models in screening of nanotherapeutics will be discussed in next section.

1.5.4. MCTS as a predictive model for nanodrug screening

For many NPs, safe entry into cells is a critical step toward high-yield prognostic and therapeutic efficacy. Furthermore, NPs' intracellular fate is critical to their success. However, efficient and controlled NPs entry/trafficking into cells remains a significant challenge (265).

Predictive *in vitro* assessment of tissue penetration capacity remains one of the most difficult aspects of preclinical testing for any new nanomedicine (266). Such information cannot be obtained from 2D cell cultures. Indeed, in conventional uptake studies, drugs and nanomedicines are added on top of cancer cells grown on flat monolayers, with the cell membrane serving as the only barrier to the intracellular compartment. Instead, useful data can be collected using 3D cell

culture models, which are more representative of the biological reality (267). The intracellular localization of AGuiX®-Cy5.5 in HCT-116 cells, and likely their entry pathways in spheroids and monolayer cells, will be presented in chapter 2, emphasizing the importance of using 3D cellular models, which, as previously discussed, are more biologically relevant.

NPs must interact with the milieu around cells before reaching the cell's exterior membrane. As stated earlier in this chapter, this microenvironment includes extracellular matrix, fibrosis, and other microenvironmental factors such as pH, nutrient gradient, and O₂; and these parameters can influence the interactions of NPs with cell membranes and, ultimately, the intracellular fate of NPs (257).

MCTS is now considered to be more reliable than 2D cell culture for high throughput drug screening prior to animal testing. In MCTS models similar to natural tumors hypoxia, cell-cell and cell-matrix interactions all play important role in anticancer drug resistance. On the other hand, poor drug and nanoparticle diffusion within spheroids, which resemble the condition in actual tumors, highlights that MCTS are powerful models for drug and nanoparticle evaluation (261,268,269).

Drug screening using MCTS involves several approaches like incubation of spheroids with nanoparticles for different periods of time, various concentrations of NPs, growth kinetics of spheroids, cell survival and cell proliferation assays (222). Using these approaches, penetration, distribution and efficacy of therapeutic strategies could be explored in MCTS (261).

When the MCTS model is coupled with microsystems, like those used in this project, it provides several benefits such as high throughput screening, compatibility with optical microscopy, and increased reproducibility of this model for screening NPs-cell interactions in a 3D cellular structure.

Chapter 2. Quantifying nanotherapeutics penetration using a hydrogel-based microsystem as a new 3D in vitro platform

Contents

Chapter 2. Quantifying nanotherapeutic penetration using a hydrogel-based microsystem as a new 3D in vitro platform	39
1. Introduction.....	41
1.1. Spheroids Preparation.....	42
1.2. Incubation with AGuIX®-Cy5.5 nanoparticles.....	44
1.3. Three dimensional fluorescence microscopy.....	45
1.4. Image analysis and quantification of fluorescence signals	48
1.5. Quantification of Gd content internalized by cells in spheroids using ICP-MS techniques	50
1.6. The compatibility with in situ immunostaining and quantification	51
1.6.1. Colocalization of nanoparticles with subcellular organelles	51
2. ABSTRACT	53
3. CORPUS.....	54
4. SUPPLEMENTARY MATERIALS	72
5. Study the penetration of fluorescence polymer probes	88
6. Study of the effect of nanoparticles on cell proliferation in multicellular tumor spheroids	92
7. CONCLUSION AND PERSPECTIVES	93

1. Introduction

In the first chapter, the essence and significance of using 3D *in vitro* models in preclinical cancer research and rapid screening of anti-cancer therapeutics candidates were discussed. In recent decades, many researchers have attempted to capture the complexity of the tumor microenvironment (TME) in a laboratory setting by developing various 3D cellular architectures. As described previously, one of the most promising 3D *in vitro* models is multicellular tumor spheroids model. In order to take a step forward in expansion and improvement of this three-dimensional *in vitro* cellular structure, a hydrogel-based microsystem with possibility of changing the design according to goal of studies has been developed in the Biophysics team at ILM(22) (**Fig.1** in article). These hydrogel-based microsystems could be prepared with classical photolithography and micro milling methods.

The microsystem being used in this study contains several micro wells; they are made of agarose gel allowing diffusion of molecules or nanoparticles smaller than 30 nm, which ensures transport of nutrients, and essential molecules to the cells. The softness of these systems can be controlled with type of agarose and its percentage in water. To make and maintain multicellular tumor spheroids in these microsystems, classical multi-well plate can be used, moreover, these microwells can be fabricated on glass coverslips compatible with high-resolution microscopy. Using these microwells several homogenous spheroids could be made by single-step cell seeding and could be imaged with *in situ* optical microscopy (**Figure 2.1**).

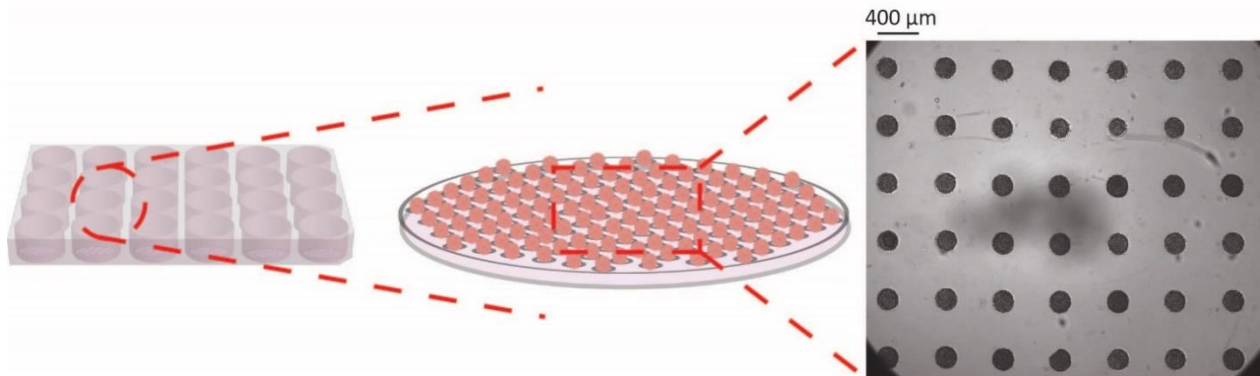


Figure 2.1. Placement of agarose microwells in a 24-well plate, schematic of spheroids in agarose microwells (cylindrical, $d=200\ \mu\text{m}$) and image of several homogenous spheroids via optical microscopy (130 spheroids in each well and more 3000 spheroids in each 24-well plate compared to 96 spheroids in each ultra-low adhesion (ULA) 96-well plate).

In order to assess cell response to anti-cancer therapy in multicellular tumor spheroids form, our team used different classical CRC cell lines (24). Since the HCT-116 cell line has demonstrated the

ability to form coherent spheroids (24), I started my thesis by generating HCT-116 cell spheroids in agarose microwells. The cylindrical microwells used in this part of my PhD had a diameter of 200 μm and a depth of 250 μm . These dimensions were chosen for spheroids generation to avoid necrotic core and to create simplest spheroid model for screening penetration, distribution and transport of NPs within spheroids, besides, this size for spheroids is compatible with optical microscopy. I worked on optimization of protocol for a variety of techniques, including cell seeding, AGuIX[®] nanoparticle incubation, confocal fluorescence microscopy, and the ICP-MS technique, as well as developing various Matlab routines to analyze data. In the following section, I will go through the preliminary experiments and trials that led to the key experiments and publication of my thesis's first articles.

1.1. Spheroids Preparation

Despite the benefits of MCTS outlined in chapter one, conventional methods for making MCTS have limitations in terms of homogeneity and reproducibility. Furthermore, in these approaches spheroids are often transferred to another platform for functional characterization and drug screening, which is laborious and may impair spheroids' quality (270). One the main goal of using agarose microwells was generating spheroids with an acceptable homogeneity in size distribution, moreover, the size of spheroids, which must be adjusted for different types of experiments with different time constraints. Making homogeneous spheroids is for example possible with the aid of hydrogel-based microwells developed by Biophysics team of ILM; however, depending on the cell type and experiment target, the subsequent procedure must be optimized. After preparing agarose microwells, sterilizing them and incubating them with medium, making spheroids starts with introducing a cell suspension with a particular concentration to the microwells followed by agitating them for a certain time and exchanging medium to remove suspend cells (**Figure 2.2 A-C**). Using this protocol, spheroids will form through self-assembly of cell aggregations (**Figure 2.2 D**).

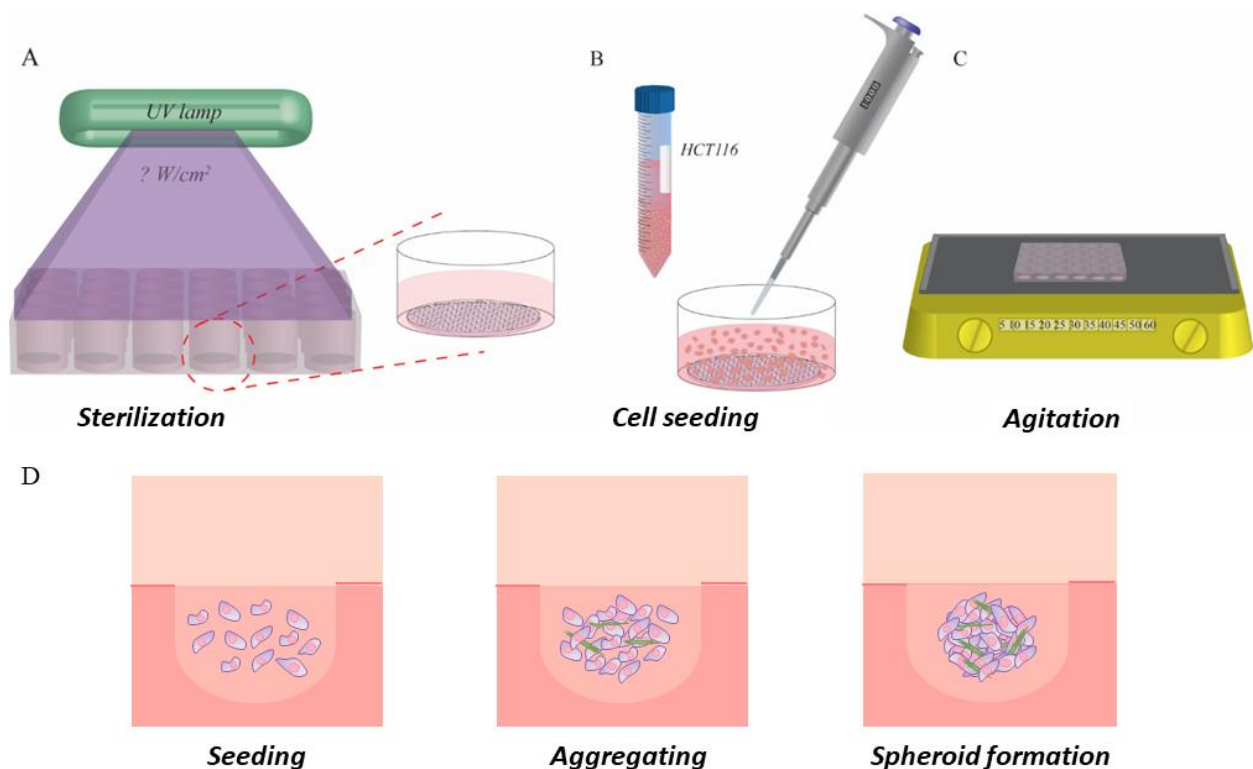


Figure 2.2. Procedure of spheroids preparation using agarose microwells, (A) sterilization with UV lamp, (B) cell seeding, (C) agitation, (D) steps of spheroids formation via self-assembly in microwells

In most of the experiments in this project, HCT-116 spheroids were made by seeding $1.2\text{E}+05$ cells per ml in each well of a 24-well plate. While this amount of cells was introduced to the microwells, only a few numbers of cells entered microwells and formed the cells aggregations. This assumption was supported by one experiment in which HCT-116 spheroids were generated using a ULA 96-well plate. HCT-116 cells were seeded at densities of 20, 40, 80, and 100 cells per well and imaged with phase contrast microscopy; spheroidal diameters were measured using ImageJ.

The analysis revealed the density of 20 cells/well produces spheroids that are nearly the same size as those created in microwells with $1.2\text{E}+05$ cells/ml seeding density. As a result, we can estimate that at $1.2\text{E}+05$ cells/microsystem, on average 20 cells enter micro wells and form cell aggregates; this cell density is much closer to 3D clonal assay than usual seeding densities for HCT-116 spheroids in ULA 96-well plates, which have been reported in several studies ranging from 300 to 20000 cells/well (24,271–273).

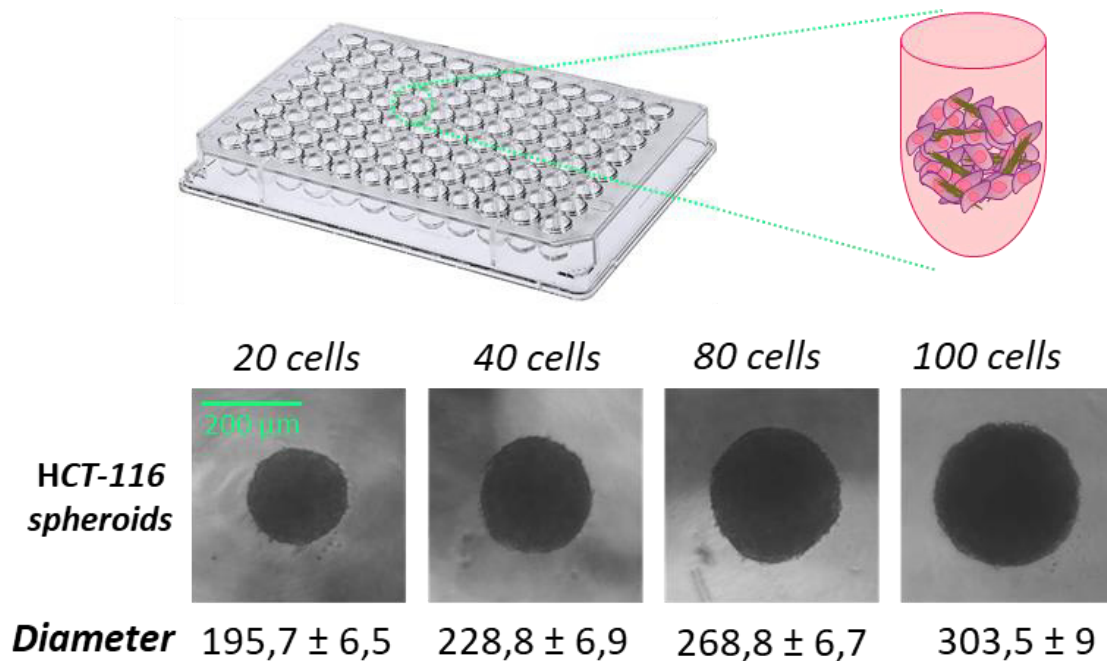


Figure 2.3. Schematics of spheroids in each well of a 96-well plate; phase contrast images of spheroids formed in ULA 96 well plate at day 3 for each cell seeding density and spheroids diameter at day 3.

1.2. Incubation with AGuIX®-Cy5.5 nanoparticles

In this study, AGuIX®-Cy5.5 nanoparticles were used as the nanoparticles model. AGuIX® nanoparticles were first described in 2011 (274). They are made of gadolinium cyclic chelates covalently grafted onto an inorganic polysiloxane matrix (**Fig. 2.4**) (23), DOTA-GA anhydride also were grafted to amine functions of the core-shell particles (275). AGuIX® NPs are multimodal nanoparticles with high radiosensitizing properties and MRI positive contrast properties due to gadolinium's paramagnetic properties. Thanks to their small hydrodynamic diameter (<5 nm), they are easily excreted via the renal system.(276). The AGuIX® NPs used in this study were conjugated to the NIR heptamethine cyanine dye (Cy5.5), allowing us to observe them using optical microscopy (277).

HCT-116 monolayer cells (2D) and HCT-116 spheroids were exposed to various concentrations of nanoparticles for various time intervals as part of my PhD; the results of these experiments were published in the chapter's published article.

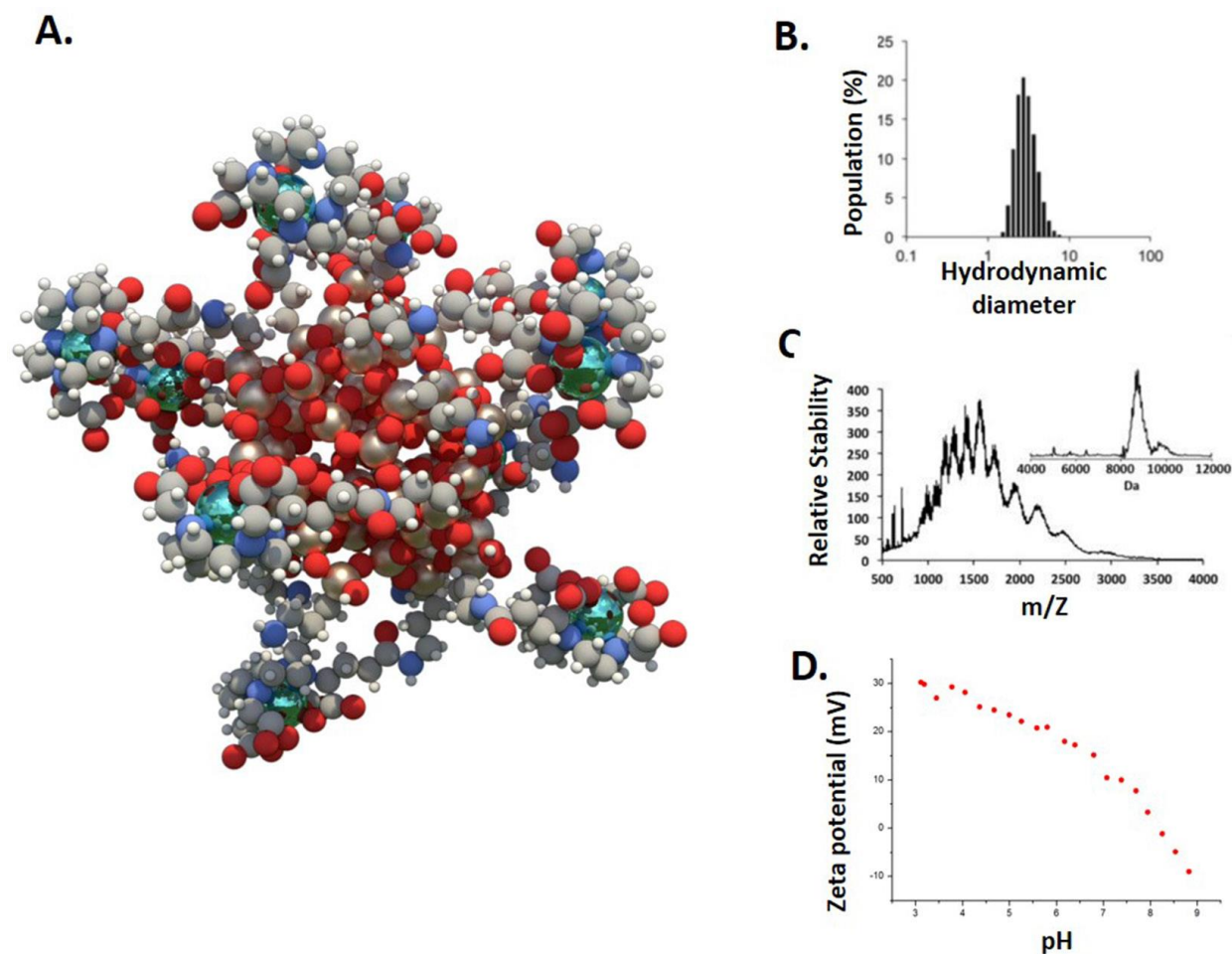


Figure 2.4. (A) Schematic of AGuIX[®] NPs (gadolinium atoms in green are chelated in DOTAGA ligands grafted to polysiloxane matrix) (B) Hydrodynamic diameter (~3 nm) distribution of AGuIX NPs as obtained by dynamic light scattering. (C) ESI-MS measurements on AGuIX[®] nanoparticles. A mass around 10 kDa is obtained for the particle. Inset is obtained after using deconvolution with a multiplicative correlation algorithm. (D) Zeta potential vs pH for AGuIX NPs(23).

1.3. Three dimensional fluorescence microscopy

As mentioned in chapter 1, one barrier in biological research and imaging of biological samples is development of high-resolution optical methods for labeling and imaging cell populations in three dimensions in intact tissue (278).

To shed more light on this complexity, the principles of confocal fluorescence microscopy, which was used in this study for characterization of cells in the developed 3D *in vitro* model, will be discussed. **Fig. 2.5 A** depicts the placement of spheroids in agarose microwells and during culture. Despite the fact that agarose gel does not act as a barrier for confocal fluorescence microscopy, reversing microwells containing spheroids was used to bring the spheroids closer to the objective

(Fig.2.5 B). The spheroids were imaged in Z direction, from the starting point in Fig.2.5 C on the outer side towards the center of the spheroid, taking images in each 1-micrometer thickness as an optical sectioning (Fig.2.5 C, D) which provides a sequence of images at different depths of spheroids (Fig.2.5 D).

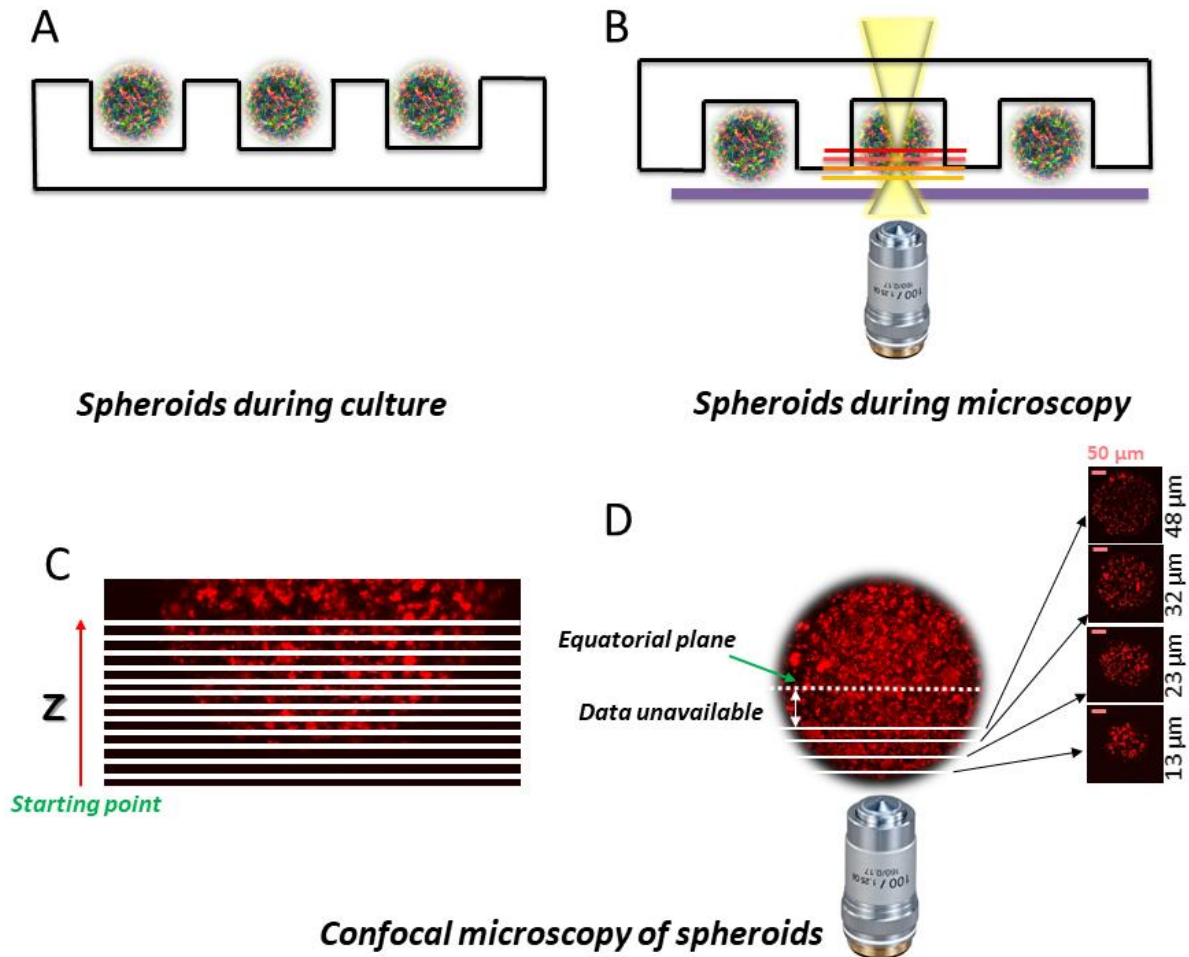


Figure 2.5. Principle of confocal microscopy of spheroids in microwells, (A) placement of spheroids in microwells during culture and other steps, (B) placement of spheroids in agarose microwells regarding the objective during confocal microscopy, (C) direction of image acquisition in confocal microscopy, (D) view of images taken by optical sectioning and limit of imaging deeper slices of spheroids

Optical sectioning offers a potentially fast, simple, and low-cost alternative for three-dimensional reconstruction of fluorescently labeled structures at subcellular resolution. Tissue opacity and light scattering, however, limit the utility of optical sectioning for deep imaging. As a result, while I had to image spheroids up to the equatorial plane, it was impossible to get a high-resolution image in deeper layers of spheroids ($>60 \mu\text{m}$) (Fig.2.3 D), so an optimal clarification technique is necessary for clearing the spheroids and optimizing confocal fluorescence microscopy.

During my PhD, I tried a variety of clarification protocols in order to find the one that best fits the 3D *in vitro* model in my experiments. Till now, various clarification techniques including seeDB (279), TDE(280), ClearT2(281), Scale A2 (278), CUBIC (282) and CLARITY (283) have been explored for optical clearing of 3D spheroids. In all these techniques biological samples are gradually cleared by immersing in solution with high RI, thus, due to the osmotic pressure, the water content in the sample (that has low RI= 1.33) will be replaced by clearing solution and RI of sample will be homogenized to 1.4-1.5, close to RI of lipids and proteins in biological samples. The first attempt used Nucgreen™ labeling to examine three different techniques, chosen according to their efficacy reported in literatures and also their compatibility with fluorophores being used for immunostaining of spheroids, *ClearT2* and *Scale A2* and TDE (summarized in **Table 2.1**) in HCT-116 cell spheroids; fluorescence signals of these samples were assessed using confocal fluorescence microscopy (**Fig 2.6**). Two other protocols using the commercial clarification reagent named *RapiClear*® and the solution of 80 percent *Glycerol* in PBS (**Table 2.1**) were used to optimize the clarification technique for HCT-116 cell spheroids in the agarose microwells. The fluorescence signal of Nucgreen™ in spheroids were assessed by confocal fluorescence microscopy and images were analyzed using a routine in Matlab; the results of this experiment were reported in the article's supplementary figures (**Figure SI 1**). According to these findings, *Glycerol* 80 percent/PBS was finally chosen for clearing HCT-116 spheroids in all experiments; the details of this protocol were described in the article's materials and methods in this chapter. Assessment of clarification quality was further analyzed in a collaborative work with D. Rousseau (Angers University, part of the PhD work of A. Ahmed) where deep convolutional neural network-based segmentation of nuclei was proposed to quantify the efficiency of clearing in such 200 µm-thick tissue (this work is under review (284), appendix II, bioRxiv version of this article).

Table 2.1. Overview of clarification techniques used in this study

Clarification method	Reagents	Incubation time	RI
Clear T2	Formamide;50% Polyethylene glycol (PEG) 20%	75 min	1.44(240)
Scale A2	Urea; 4 M Triton X-100; 0.2 wt/vol Glycerol; 10% wt/wt	24 -72 hours	1.38(240)
TDE	2,2'-thiodiethanol (TDE) (20% & 47%)	3 hours	1.42(240)
RapiClear®	Glycerol; Sodium Azide	overnight	1.52
Glycerol	Glycerol 80% vol/vol in PBS	overnight	1.52

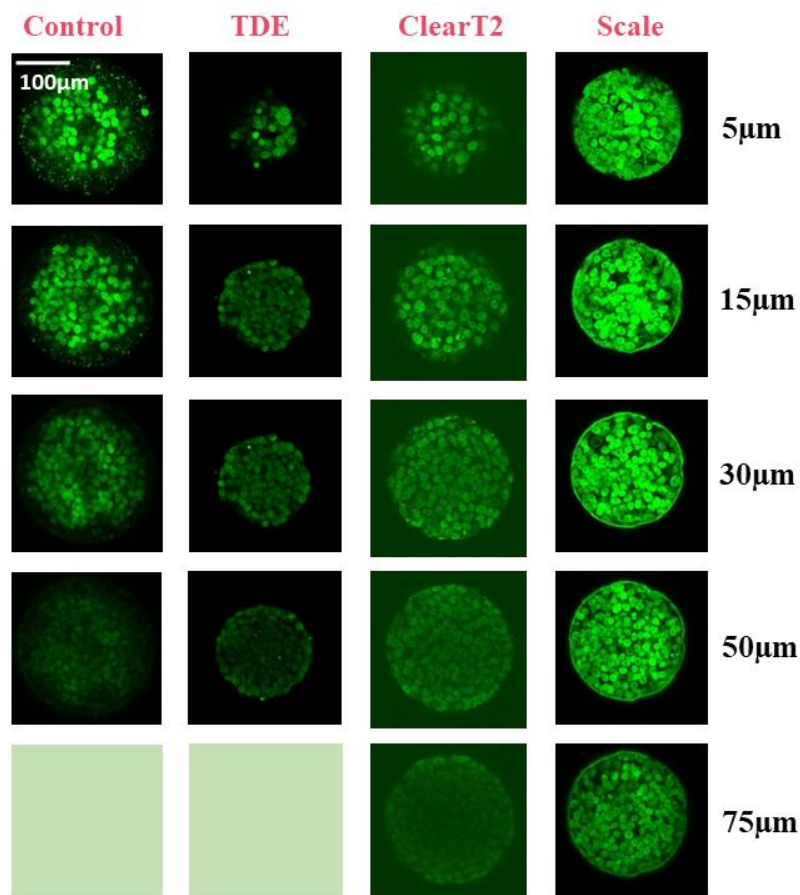


Figure 2.6. Confocal fluorescence microscopy images of HCT-116 spheroids labelled with nucgreen™-488 for nucleus in different depth Cleared with different clarification protocols

1.4. Image analysis and quantification of fluorescence signals

To maximize the benefits of using 3D optical microscopy characterization in this 3D *in vitro* model, fluorescence images were analyzed to quantify fluorescence signals of the nano-therapeutics and any other labeling.

Image acquisitions of 3D samples, HCT-116 spheroids with confocal microscopy were performed in the Z direction, as shown in **Fig.2.5**. According to this, the first image analysis approach was to quantify the area of nanoparticles in each slice of spheroids by segmentation based on image intensity (**Fig.2.7**) and normalizing total quantities in each slice by spheroidal area and plotting this normalized area as a function of depth in Z direction. Although the plots obtained by this analysis approach seemed logically correct for different incubation concentrations (**Fig. 2.6 B**), analysis in Z direction cannot be an optimal quantification of nanoparticle penetration and distribution in spheroids. To be more specific, **Fig. 2.7 C** depicts the image of AGuIX® nanoparticles in one slice of HCT-116 spheroids. Different points in this image have different radial position; in

other words, each slice contains a mix of cells with varying access to nanoparticles, nutrients, and so on. As a result, since it combines information from non-equal parts in spheroids, quantification in the Z direction lacks optimal accuracy for 3D spherical cellular structure.

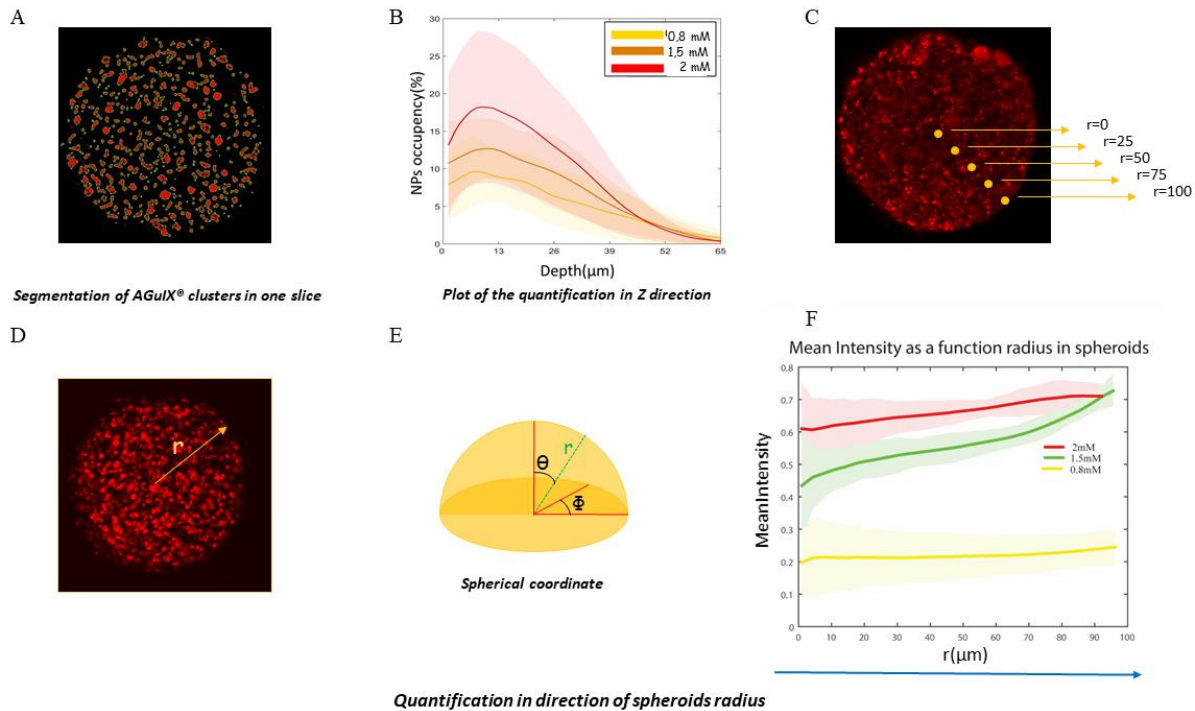


Figure 2.7. Quantification of confocal images, two different approaches; (A) NPs segmentation in one slice of HCT-116 spheroids with AGuIX[®] NPs – Cy5.5 imaged via confocal microscopy. (B) Graph resulted by image analysis in Z direction for HCT-116 spheroids incubated with different concentration of AGuIX[®] NPs – Cy5.5. (C) Difference in positions of nanoparticles in each imaged slice (D) Z-projection of an imaged spheroid incubated with AGuIX[®] NPs – Cy5 showing radius of spheroids. (E) Schematics of spherical coordinate in a spheroid. (F) Curved obtained via image analysis in spherical coordinate showing AGuIX[®] NPs – Cy5. Intensity in radial direction

Quantification of confocal fluorescence images in the direction of radius is a better approach since it does not combine different data as the cells in each radial position have the same situation and access in a spatial spherical structure (**Fig. 2.7 D**). This fact prompted the development of a new Matlab routine that measures the intensity of fluorescence signals in a radial direction, with the help of Dr. H. Delanoë-Ayari in the team. To begin, the nucgreen[™] channel was used to segment the area of spheroids in each slice, and these segmented regions were then fitted into a perfect circle, with all of these circles being used to estimate the spherical shape and radius of the spheroids. The results of this analysis were used to switch the direction of analysis from Cartesian coordinates (XYZ) to Spherical coordinate (r, θ, Φ) and the mean intensity was determined by averaging the intensity along angles θ and Φ giving the mean intensity in certain radius in each spheroid (**Fig. 2.7 E**). As a result, the mean fluorescence signal intensity could be calculated as a

function of spheroid radius, allowing for more precise quantification in 3D spherical architecture (Fig. 2.7 F).

1.5. Quantification of Gd content internalized by cells in spheroids using ICP-MS techniques

Inductively Coupled Plasma-Mass Spectrometry (ICP-MS) is a technology coupling ICP with MS for elemental analysis by generation of ions. The goal of this characterization technique was measuring the gadolinium content internalized by the cells during incubation with AGuIX[®] nanoparticles as a marker for cellular uptake of AGuIX[®].

The protocol for this characterization technique was originally intended to measure the average amount of Gd in HCT-116 spheroids incubated with a specific concentration of AGuIX[®] for a specific time. To accomplish this, I prepared samples for ICP-MS by dissolving microwells containing a known number of spheroids in nitric acid to begin the measurement, and then dividing the results of each sample by the number of spheroids. These measurements were repeated multiple times, but the results were illogical for different AGuIX[®] incubation concentrations and for different samples with the same incubation concentration, there was a clear discrepancy that increased with increase in incubation concentration.

This problem led us to assume that there is still some Gd in the agarose microwells, which is causing the discrepancy. To be sure about that, I prepared some microwells. I incubated half of them with AGuIX[®] for 24 hours and washed them with the usual protocol, I left the other microwells in culture medium without nanoparticles. These microwells then were prepared for ICP-MS measurement. The results confirmed the hypothesis, as there is still some Gd in the microwells after the usual washing procedure. In addition, even in microwells that were not incubated with nanoparticles some traces of Gd were found showing the pollution of some agarose batches used to make microwells. Because ICP-MS is highly sensitive technique, these very small amounts of Gd in agarose can create a discrepancy in results. This assumption was strengthened during a trial experiment with the laser-induced breakdown spectroscopy (LIBS) technique, which is a rapid analysis technology being used to detect elements in a variety of samples (285). Dr. Vincent Motto-Ros in SpectroBio team of ILM performed this experiment for spheroids in microwells incubated with AGuIX[®] that were fixed, mounted and prepared for this analysis. Gd was found in both spheroids and agarose microwells (in lower amount) in this experiment (appendix I, **Figure 1**).

To improve the sample preparation protocol for ICP-MS, spheroids were counted and extracted from agarose microwells to dissolve in nitric acid for measurement after incubation with AGuIX[®]. This time, the analysis results were more logical, but not as reproducible as what we had expected. As a result, we assumed that the discrepancy was caused by a difference in the size of the spheroids. As a result, we decided to dissociate spheroids, count cell numbers, and measure

the diameter of single cells with optical microscopy before dissolving these cells in nitric acid for ICP-MS calculation. The aim was to make results independent of spheroids size and to normalize measurement results by cell volume so that they could be compared to monolayer cells which were incubated with AGuIX[®]. Monolayer cells were removed from plates using trypsin; cells were counted and dissolved in nitric acid for ICP with a similar protocol for spheroids. Finally, this procedure worked for both spheroids and monolayer cells, and measurement results were reported in ppb/m³ in **figure 3** of this chapter's article.

1.6. The compatibility with *in situ* immunostaining and quantification

The developed 3D *in vitro* model in this study is compatible with *in situ* immunostaining, which is one of its main advantages. Indeed, this 3D *in vitro* model allows all steps of these types of experiments, from cell seeding to fixation and immunostaining, to be performed in the same plate without transferring spheroids. This makes it possible to have multiple labelling in several spheroids in one experiment, which is especially useful to find the localization of nanoparticles inside spheroids and within cells and subsequent quantification of these images.

Colocalization of nanoparticles with subcellular organelles

Because of using this 3D *in vitro* model, I was able to label several HCT-116 spheroids in each independent experiment of the incubation with AGuIX[®] nanoparticles. I labelled HCT-116 spheroids with nucgreen™ and one antibody specific to one subcellular organelle including labels for actins, mitochondria, lysosomes and early endosomes, images were shown in **figure 6** and **figure 7** of the articles in this chapter for 2D and 3D, respectively.

The study of potential nanoparticle co-localization with subcellular organelles using fluorescence microscopy begins with the acquisition of images of the nanoparticles and organelles with confocal fluorescence microscopy. After visualizing nanoparticles and organelles in various channels, overlay images display potential colocalization of nanoparticles with these organelles.

As described in the introduction chapter, the most common method for analyzing colocalization in biological images is superposition of fluorescence images. The results, however, can be misleading because the intermediate color, which indicates colocalization, is only achieved if the intensities of two probes in fluorescence images are similar (263). As a result, a quantitative analysis of these images based on the relative distribution of two probes appears to be required in order to draw a reliable and logical conclusion.

To determine the degree of AGuIX[®] colocalization with cellular organelles, images were analyzed using a routine developed in Matlab to calculate Pearson's Correlation Coefficient as a statistical and quantitative indicator for colocalization (introduced in chapter 1).

The image analysis began with using nucgreen™ channel to segment the region of spheroids in each slice. Using this mask to outline the region of interest, *Corr2* function in Matlab was used to calculate Pearson's Correlation Coefficient of two fluorophores belonging to AGuIX® and a cellular organelle. **Figures 2.6 E** and **2.7 E** in the article of this chapter show the results of these quantifications for both 2D and 3D cells.

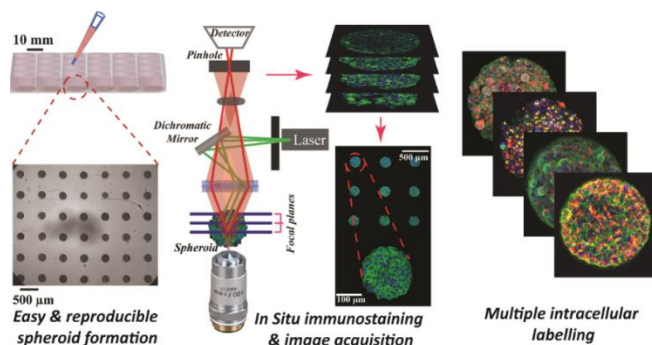
The following section of this chapter contains a copy of an article published in Lab on a Chip that represents the development of a 3D *in vitro* model and validation of this 3D model for characterization of different aspects of cell-nanoparticle interactions in a three-dimensional architecture primarily using optical microscopy.

2. ABSTRACT

The huge gap between 2D *in vitro* assays used for drug screening, and the *in vivo* 3D-physiological environment hampered reliable predictions for the route and accumulation of nanotherapeutics *in vivo*. For such nanotherapeutics, Multi-Cellular Tumour Spheroids (MCTS) is emerging as a good alternative *in vitro* model. However, the classical approaches to produce MCTS suffer from low yield, slow process, limited MCTS manipulation and compatibility with high-magnification fluorescent optical microscopy. On the other hand, spheroid-on-chip set-ups developed so far require a microfluidic practical knowledge difficult to transfer to a cell biology laboratory.

We present here a simple yet highly flexible 3D-model microsystem consisting of agarose-based micro-wells. Fully compatible with the multi-well plates format conventionally used in cell biology, our simple process enables the formation of hundreds of reproducible spheroids in a single pipetting. Immunostaining and fluorescent imaging including live high-resolution optical microscopy can be performed in-situ, with no manipulation of spheroids.

As a proof-of-principle of the relevance of such *in vitro* platform for nanotherapeutics evaluation, this study investigates the kinetic and localization of nanoparticles within colorectal cancer MCTS cells (HCT-116). The nanoparticles chosen are sub-5 nm ultrasmall nanoparticles made of polysiloxane and gadolinium chelates that can be visualized in MRI (AGuIX[®], currently implicated in clinical trials as effective radiosensitizers for radiotherapy) and confocal microscopy after addition of Cy 5.5. We show that the amount of AGuIX[®] nanoparticles within cells is largely different in 2D and 3D. Using our flexible agarose-based microsystems, we are able to resolve spatially and temporally the penetration and distribution of AGuIX[®] nanoparticles within MCTS. The nanoparticles are first found in both extracellular and intracellular space of MCTS. While the extracellular part is washed away after few days, we evidenced intracellular localisation of AGuIX[®], mainly within lysosomes compartment, but also occasionally within mitochondria. Our agarose-based microsystem appears hence as a promising 3D *in vitro* user-friendly platform for investigation of nanotherapeutics transport, ahead of *in vivo* studies.



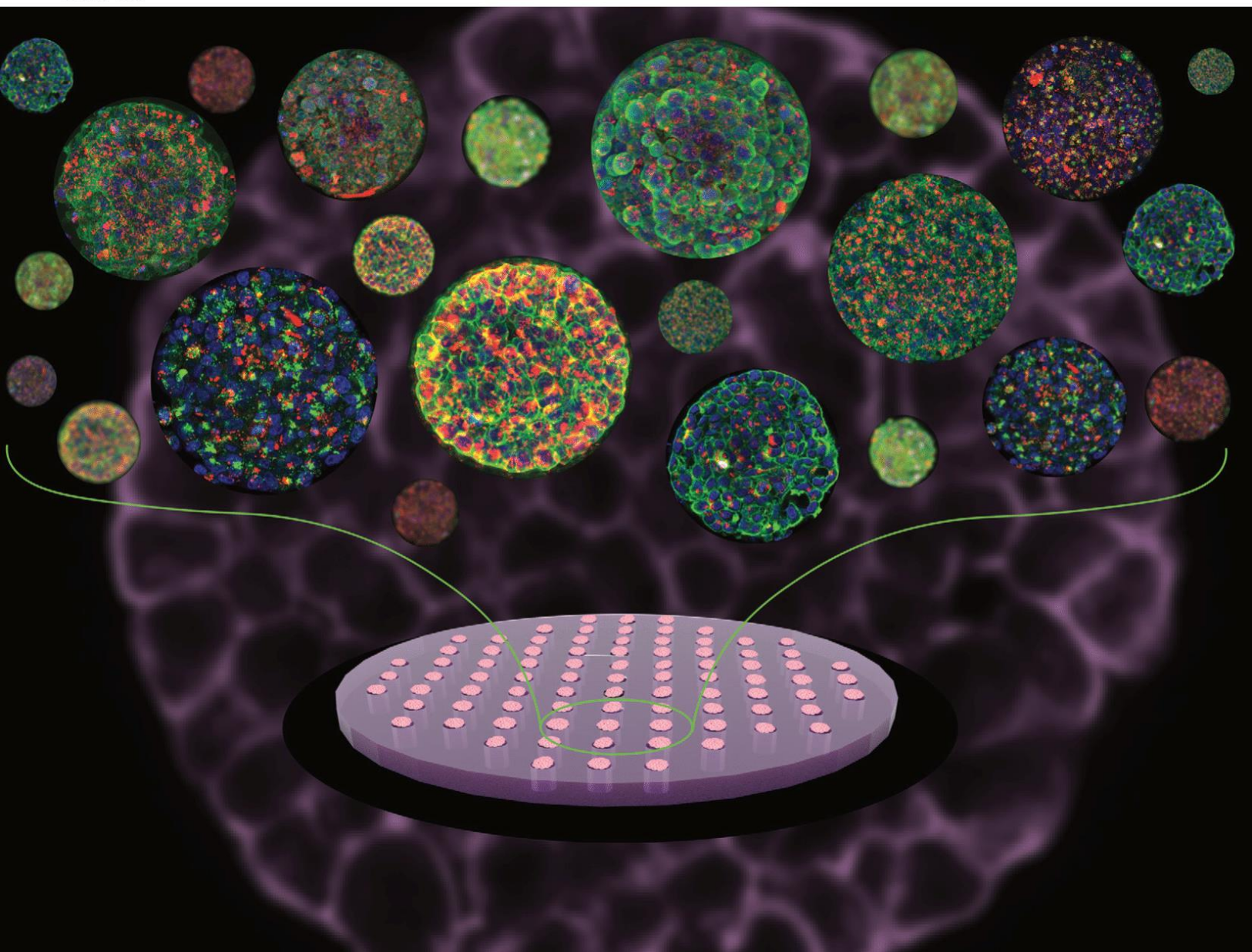
Graphical abstract: Easy and reproducible spheroids formation using agarose microwells, schematics of confocal microscopy and in situ image acquisition of spheroids with multiple intracellular labelling

3. CORPUS

Lab on a Chip

Devices and applications at the micro- and nanoscale

rsc.li/loc



ISSN 1473-0197

PAPER

Charlotte Rivière *et al.*
Quantifying nanotherapeutic penetration using a hydrogel-based microsystem as a new 3D *in vitro* platform


 Cite this: *Lab Chip*, 2021, 21, 2495

Quantifying nanotherapeutic penetration using a hydrogel-based microsystem as a new 3D *in vitro* platform†

 Saba Goodarzi, ^a Audrey Prunet,^a Fabien Rossetti, ^a Guillaume Bort, ^a Olivier Tillement, ^a Erika Porcel, ^b Sandrine Lacombe,^b Ting-Di Wu,^{cd} Jean-Luc Guerquin-Kern, ^{cd} H  l  ne Delano  -Ayari, ^a Fran  ois Lux ^{ae} and Charlotte Riviere ^{*ae}

The huge gap between 2D *in vitro* assays used for drug screening and the *in vivo* 3D physiological environment hampered reliable predictions for the route and accumulation of nanotherapeutics *in vivo*. For such nanotherapeutics, multi-cellular tumour spheroids (MCTS) are emerging as a good alternative *in vitro* model. However, the classical approaches to produce MCTS suffer from low yield, slow process, difficulties in MCTS manipulation and compatibility with high-magnification fluorescence optical microscopy. On the other hand, spheroid-on-chip set-ups developed so far require a practical knowledge of microfluidics difficult to transfer to a cell biology laboratory. We present here a simple yet highly flexible 3D model microsystem consisting of agarose-based microwells. Fully compatible with the multi-well plate format conventionally used in cell biology, our simple process enables the formation of hundreds of reproducible spheroids in a single pipetting. Immunostaining and fluorescence imaging including live high-resolution optical microscopy can be performed *in situ*, with no manipulation of spheroids. As a proof of principle of the relevance of such an *in vitro* platform for nanotherapeutic evaluation, this study investigates the kinetics and localisation of nanoparticles within colorectal cancer MCTS cells (HCT-116). The nanoparticles chosen are sub-5 nm ultrasmall nanoparticles made of polysiloxane and gadolinium chelates that can be visualized in MRI (AGuIX[®], currently implicated in clinical trials as effective radiosensitizers for radiotherapy) and confocal microscopy after addition of Cy5.5. We show that the amount of AGuIX[®] nanoparticles within cells is largely different in 2D and 3D. Using our flexible agarose-based microsystems, we are able to resolve spatially and temporally the penetration and distribution of AGuIX[®] nanoparticles within MCTS. The nanoparticles are first found in both extracellular and intracellular space of MCTS. While the extracellular part is washed away after a few days, we evidenced intracellular localisation of AGuIX[®], mainly within the lysosomal compartment, but also occasionally within mitochondria. Hence, our agarose-based microsystem appears as a promising 3D *in vitro* user-friendly platform for investigation of nanotherapeutic transport, ahead of *in vivo* studies.

 Received 10th March 2021,
Accepted 1st June 2021

DOI: 10.1039/d1lc00192b

rsc.li/loc

Introduction

There is an ongoing effort to develop efficient therapeutics for cancer treatment including nanodrugs and nanoparticles; nevertheless, the clinical translation of these therapeutics has to overcome numerous challenges from the early stages of development to a successful translation.^{1,2} Currently, the standard pipeline for drug development consists of the following: (1) efficacy tests on 2D *in vitro* assays and (2) on rodent *in vivo* models, (3) regulatory toxicity tests on two animal species and (4) clinical trials.

However, 2D *in vitro* assays do not replicate the 3D physiological environment encountered by the cells *in vivo*. This could be the underlying reason for the high rate of

^a University of Lyon, Universit   Claude Bernard Lyon 1, CNRS, Institut Lumiere Mati  re, F-69622, Villeurbanne, France. E-mail: charlotte.riviere@univ-lyon1.fr

^b Universit   Paris-Saclay, CNRS, Institut des Sciences Mol  culaires d'Orsay, 91405, Orsay, France

^c Institut Curie, Universit   PSL, Paris, France

^d Universit   Paris-Saclay, CNRS, Inserm, Centre d'Imagerie Multimodale, 91401, Orsay, France

^e Institut Universitaire de France (IUF), France

† Electronic supplementary information (ESI) available. See DOI: 10.1039/d1lc00192b

clinical failure in the development of new drugs. On the other hand, there is also a rising question as to the economical and ethical relevance of rodent animal models, in particular because such models are not fully representative of human specificity.³ Getting as close as possible to the *in vivo* situation in *in vitro* models is a key issue to truly understand and control cancer cell response, accompanied by reduction in animal usage. For the pharmaceutical industry, tackling this issue will enable better identification of relevant therapeutics by performing relevant screening on 3D models. For precision medicine, it will help physicians to adjust the therapeutic treatment to complement current clinical analysis.^{2,4} For fundamental research, it will allow deciphering cell response in a truly relevant context.

Many approaches have been developed during the past decade to set up various organ-on-a-chip or tumour-on-a-chip devices, integrating many different *in vivo* features in a miniaturized *in vitro* format.^{5,6} This is particularly important for emerging nanosized therapeutics.⁷ The presence of different physiological barriers, such as cell-cell compaction, tumour heterogeneity and dense extracellular matrix along with various cancer-associated cells, will decrease the amount of nanotherapeutics effectively reaching the targeted tumour cells.^{8,9} The lack of such a physiological context hampered reliable predictions for the route and accumulation of these nanoparticles *in vivo*¹⁰ and is a major limitation for the efficient development of novel therapeutic approaches.¹¹ To move beyond the classical 2D plastic dishes, different 3D *in vitro* models have been developed to try to better replicate *in vivo* the complexity of the tumour microenvironment.¹² Among them, multicellular tumour spheroids (MCTS) recapitulate many tumour features, including 3D cellular architecture, cellular heterogeneity, signalling pathways and physiochemical gradient, similar to real *in vivo* tumour micrometastasis (for spheroids >500 μm in diameter).^{13–17}

MCTS could be prepared with various techniques¹³ such as using non-adherent surfaces,¹⁸ spinner flasks¹⁹ or hanging drop methods.²⁰ Emerging attempts to integrate spheroids in microfluidic set-ups open up new possibilities to deal with the low yield and slow process of the classical approach.^{21,22} However, such spheroid-on-chip approaches require a practical knowledge of microfluidics that is difficult to transfer to a cell biology laboratory.

In addition, the polymeric materials commonly used for such devices (polydimethylsiloxane –PDMS) suffer from major limitations, precluding their usage for efficient drug screening under physiological conditions:²³ large absorption of therapeutics^{24,25} (resulting in the underestimation of cell response to drugs), non-permeability to small water-soluble molecules (leading to fast medium conditioning if continuous flow is not provided otherwise), rigidity several orders of magnitude larger than the physiological condition (MPa vs. kPa range *in vivo*²⁶).

To go beyond PDMS and its limitations, hydrogel-based microwell devices have been considered.^{27,28} Hydrogels are

networks of cross-linked polymers with tuneable physical properties, a high capacity for water retention and interconnected pores enabling free diffusion of O_2 , nutrient and metabolic wastes, which make them favourable alternatives in micro-system applications. Various techniques using natural or synthetic hydrogels for MCTS formation have been developed.^{28–33} However, none of these set-ups meets all the criteria required for long-term time-lapse analysis (*i.e.* compatibility with high-resolution video-microscopy, efficient medium and oxygen renewal, *in situ* immunostaining/drug application, no reduction of the available drug dose, easy cell retrieval for further standard molecular analyses) within a physiological stiffness range.

We present here a simple yet highly flexible 3D model microsystem consisting of agarose-based microwells. This hydrogel with tuneable rigidity and great integrity presents several advantages, making it a suitable biomaterial in cell studies.^{34,35} The tuneable mechanical properties of the agarose can reproduce the *in vivo* microenvironment stiffness. Its porous nature enables the free diffusion of salt and small chemical species (hydrodynamic diameter <30 nm in 2% agarose,³⁶ which is the case for most proteins). Our simple process enables the formation of hundreds of reproducible spheroids in a single pipetting, and its compatibility with multi-well plate formats conventionally used in cell biology can accelerate the screening of drugs in comparison with conventional 3D models. Of note, these microwells can also be manufactured on coverslips, opening the possibility for live high-resolution optical microscopy. In addition, hydrogel-based microwells provide a user-friendly platform for *in situ* immunostaining and can be used for in-depth analysis of cell phenotypic modifications after drug treatment.

As a proof of principle of the relevance of such an *in vitro* platform for the evaluation of nanoparticle screening, the aim of this study was to analyse the kinetics and localisation of these nanoparticles within colorectal cancer cell MCTS (HCT-116). The nanoparticles chosen for this proof-of-concept study are sub-5 nm ultrasmall nanoparticles made of polysiloxane and gadolinium (Gd) chelates that can be visualized in MRI and confocal microscopy (after functionalization by Cy5.5, a near-infrared fluorophore). These nanoparticles, called AGuIX®, are effective radiosensitizers for radiotherapy³⁷ and are now implicated in three clinical trials associating radiotherapy with AGuIX® for treatment of multiple brain metastases by whole brain radiation therapy (NanoRad 2, phase II, multicentric), stereotactic radiosurgery (NanoStereo, phase II, multicentric) and cervical cancer (phase Ib, Gustave Roussy). The nanoparticle–cell interactions and internalization pathways of these nanoparticles have been assessed *in vitro* in 2D,³⁸ but never in 3D, multicellular tumour spheroids.

We show in this study that the 3D cell arrangement highly impacts the amount of AGuIX® nanoparticles within cells.

Using our flexible agarose-based microsystem, we were able to resolve spatially and temporally the penetration and distribution of AGuIX® nanoparticles within tumour spheroids. The nanoparticles were first found in both the extracellular and the intracellular space of spheroids, mostly within the lysosomal compartment, but also occasionally

within mitochondria. Whereas the extracellular part was washed away after a few days, the colocalisation with lysosomes remained almost constant. Our agarose-based microsystem hence appears as a promising 3D *in vitro* platform for investigation of nanotherapeutic transport, ahead of *in vivo* studies.

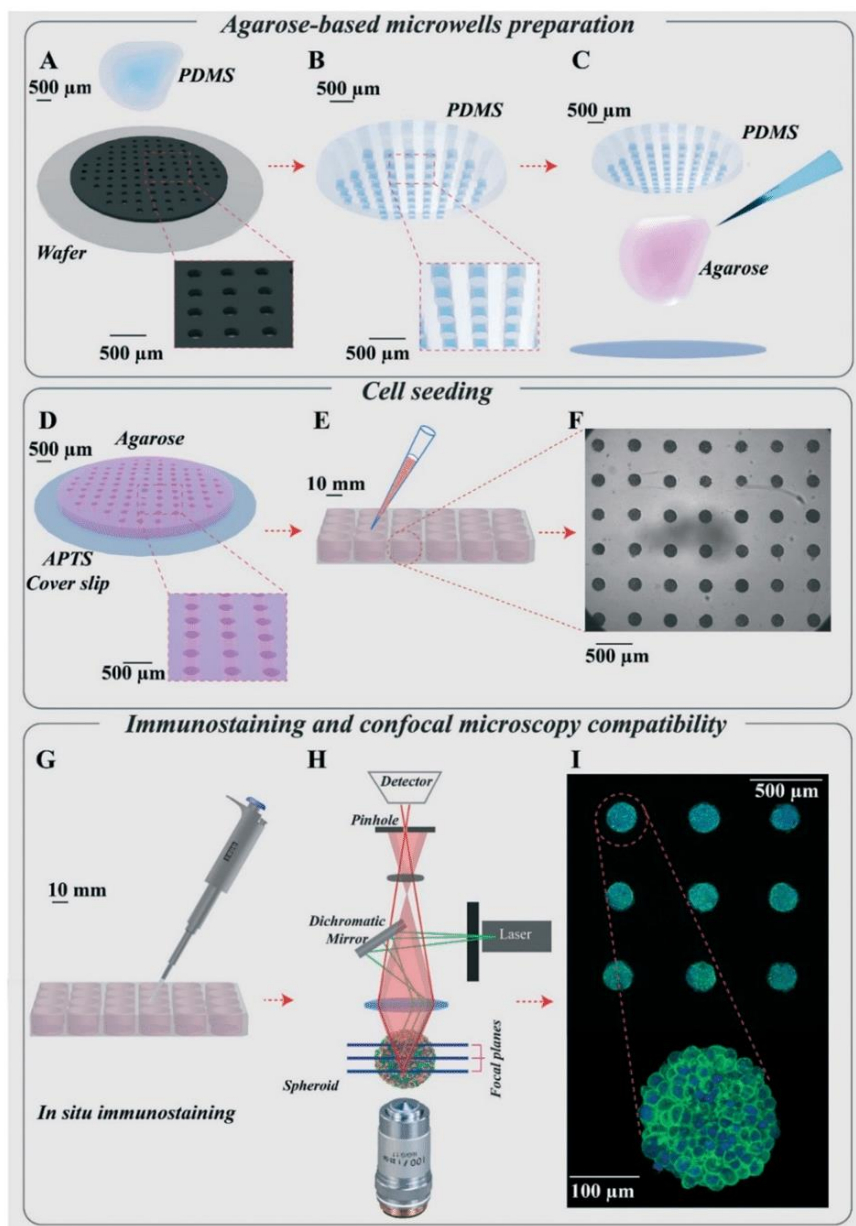


Fig. 1 Presentation of the hydrogel-based microsystems for spheroid growth and follow-up. (A) Silicon wafer mould made by photolithography. (B) PDMS replica mould made from the silicon wafer mould. (C) Moulding of agarose using PDMS replica moulds on a coverslip functionalized by APTS to make the agarose microsystem adhesive on the coverslip. (D) Cylindrical agarose microwells with diameter and height of 200 μm for each microwell. (E) Cell seeding using the agarose microsystem in a 24-well plate for the preparation of spheroids (leading to the formation of 130 spheroids per well). (F) Optical microscopy images of several homogenous HCT-116 cell spheroids made in the agarose microsystem (5 \times magnification) at day 6. (G) *In situ* immunostaining of spheroids in microwells in a 24-well plate. (H) Diagram of confocal fluorescence microscopy. (I) Maximal image projection (MIP) of confocal fluorescence images of spheroids in the agarose microsystem labelled for actin (green) and nuclei (blue) (10 \times magnification) and an enlarged MIP of one of the spheroids (20 \times magnification).

Materials and methods

Hydrogel based microsystem

Agarose-based microsystems were prepared using moulding procedures. First, a silicon wafer mould was made using a classical photolithography technique (Fig. 1A). The mould consists of an array of 130 cylindrical wells of 200 μm in diameter and 250 μm in height, created using the SU8-2100 photosensitive resin.

A polydimethylsiloxane (PDMS) replica mould was then casted on this master mould (Fig. 1B) and used for agarose moulding. The agarose moulding procedure differed depending on the aim of the experiments: (1) for imaging of fixed samples, the microwells were free-standing in each well of a multi-well plate, enabling easy retrieval and transfer (see detailed description below); (2) for time-lapse imaging, agarose moulding is performed on 3-aminopropyltriethoxysilane (APTS)-functionalised coverslips, enabling to directly bond the microwells to the coverslips and avoiding any drift during acquisition (Fig. 1D, patented process³⁹).

Agarose solution (2%, w/v) was prepared by dissolving ultra-pure agarose powder (InvitrogenTM) in water. An autoclave was used for the dissolution to avoid formation of bubbles (121 $^{\circ}\text{C}$, 15 min).

Moulding of free-standing microwells. The agarose solution (300 μL) was deposited on a warmed PDMS mould (at 78 $^{\circ}\text{C}$) and a coverslip was then placed on top of the drop of agarose to spread it with a constant thickness on the mould. After agarose gelation into the desired shape (10 min), the coverslip was removed and the moulded agarose microwells were cut to fit in the wells of a 24-well plate. The microwells were then placed in a 24-well plate and kept hydrated with PBS (1 mL per well). The plate was UV-sterilized (8 W, 254 nm) for 20 min in the opened and closed state and kept at 4 $^{\circ}\text{C}$ until used. The day before each experiment, PBS was replaced by culture medium and allowed to diffuse within each microwell by overnight incubation at 37 $^{\circ}\text{C}$ before cell seeding.

Moulding on APTS-functionalised coverslips. First, holes were drilled in each well of a 12-well plate (diameter 16 mm) to prepare the plate for the coverslips. Round coverslips (diameter 20 mm) were incubated in a 1% APTS–5 mM acetic acid solution (Acros ref 43094100 for APTS, vwr ref 20104298 for acetic acid) for 20 min under stirring condition. Coverslips were then extensively rinsed with water and dried on a hot plate (100 $^{\circ}\text{C}$, 15 min). Such APTS-functionalised coverslips are then used immediately for agarose moulding using the same procedure as the one described above for free-standing microwells. After agarose gelation, the PDMS mould was removed; the agarose microwells remained attached to the APTS-functionalised coverslip. These coverslips with microwells were glued to the 12-well plate using curing optical adhesive (Norland Products, NOA 81) activated by 30 seconds of exposure to a UV lamp (12 W, 365 nm). The plate was then UV-sterilized using the same procedure as the one described above for free-standing microwells.

Colorectal cancer cell line HCT-116 and culture conditions

HCT-116 colorectal carcinoma (CCL-247) cell line was purchased from the American Type Culture Collection (ATCC, Virginia, USA). All cells were cultured in Dulbecco's modified Eagle's medium (DMEM-Glutamax, GibcoTM) supplemented with 10% heat-inactivated fetal bovine serum (FBS; Sigma, St. Louis, Missouri, USA), 100 units/100 μg penicillin/streptomycin (GibcoTM).

Routinely, the HCT-116 cells were grown in T-25 cell culture flasks and were placed in an incubator at 37 $^{\circ}\text{C}$ with a 5% CO_2 atmosphere. The culture medium was changed regularly, and cell passage was carried out at 70% confluency every 3 days. The cell passage was performed using recombinant cell-dissociation enzyme (TrypLE, GibcoTM) to detach cells followed by neutralizing with culture medium. The cell suspension was centrifuged at 1000 rpm (equal to 106g) for 5 min, the supernatant was discarded, and the cell pellet was resuspended in 1 mL of complete culture medium. The number of cells was counted using a Neubauer chamber, and the final cell volume was adjusted to reach the desired cell concentration.

Multicellular tumour spheroids

MCTS of HCT-116 cells were formed in 24-well plates containing agarose in each well. After trypsinization and centrifugation, 120 000 cells in 1 mL complete medium was added in each well (each containing 1 microsystem). To encourage and accelerate cell aggregation, the 24-well plate was placed under orbital agitation (160 rpm) for 15 min in an incubator at 37 $^{\circ}\text{C}$ and 5% CO_2 . After 4 h, the plate was rinsed with fresh medium to remove cells that did not reach the microwells. After 2 days, spheroids were ready for incubation with nanoparticles.

Monolayer cell culture

After trypsinization and centrifugation of HCT-116 cells in culture, a cell suspension with 120 000 cells in 1 ml was prepared. The cell suspension was added to tissue-treated coverslip plates (either 300 μL in an 8-well Ibidi[®] or 2 mL in a 12-well plate). Cells were incubated with nanoparticles 48 h after cell seeding.

Preparation of Cy5.5-conjugated gadolinium-based nanoparticles (AGuIX[®]-Cy5.5)

The Gd-based nanoparticles (AGuIX[®]) synthesized by NH TherAguix (Lyon, France) are composed of a polysiloxane matrix surrounded by covalently bound DOTAGA-Gd ((1,4,7,10-tetraazacyclododecane-1-glutaric acid-4,7,10-triacetic acid)-Gd). The synthesis process is already described in the literature.⁴⁰ Briefly, AGuIX[®] nanoparticles are composed of a polysiloxane network surrounded by Gd chelates. The chemical composition of AGuIX[®] nanoparticles is $(\text{GdSi}_{6.5}\text{N}_6\text{C}_{25}\text{O}_{21}\text{H}_{42}\cdot 10\text{H}_2\text{O})_n$ with a molar mass of around 10 kDa. The hydrodynamic diameter of the AGuIX[®]

nanoparticles is close to 5 nm, and the AGuIX® nanoparticles are characterized by a zeta potential of 9.0 ± 5.5 mV at pH 7.2. These AGuIX® nanoparticles were further conjugated to cyanine-5.5 (Cy5.5) fluorophore to make them detectable by confocal fluorescence microscopy. They are referred to as AGuIX®-Cy5.5 nanoparticles in the rest of the article.

Incubation of cells with AGuIX®-Cy5.5 nanoparticles

To incubate MCTS and monolayer cells with AGuIX®-Cy5.5 nanoparticles, an intermediate solution of AGuIX®-Cy5.5 nanoparticles with 100 mM concentration of Gd was prepared in distilled-water. From this intermediate solution, just before the incubation with cells, AGuIX®-Cy5.5 solutions were prepared in fresh DMEM with Gd concentrations of 0.8, 1.5 and 2 mM, respectively. The MCTS in all microsystems of a 24-well plate were incubated with 1 mL of AGuIX®-Cy5.5 nanoparticle solution. For cell monolayers, an Ibidi® 8-well plate or a 12-well plate was used, and cells were incubated with 200 μ L or 2 mL AGuIX®-Cy5.5 solution, respectively.

Inductively coupled plasma-mass spectrometry (ICP-MS)

The concentration of Gd was analysed using a validated inductively coupled plasma-mass spectrometry (ICP-MS) analysis. To prepare samples for this analysis, spheroids and monolayer cultured cells were incubated with AGuIX®-Cy5.5 nanoparticles with 0.8, 1.5 and 2 mM concentration in Gd for 24 h. After incubation, spheroids were rinsed three times with PBS for 15 min each and dissociated using trypsin + EDTA (Gibco). The number of cells in each microwell was evaluated using a Neubauer chamber. The cell suspensions in trypsin + EDTA of each sample were then centrifuged (900g for 5 min), the supernatants were discarded, and the cells pellets were dissolved in 150 μ L 69% HNO₃ (ROTH) at 80 °C for 3 h. The volume of samples was adjusted to 10 mL by adding ultra-pure water and the Gd concentration in each sample was measured using an ICP-mass spectrometer (PerkinElmer, NexION® 2000). A similar procedure was used for the monolayer cell culture (the cells were rinsed with PBS (3 \times 5 min) and detached using trypsin (Gibco)).

The mean value of the cell volume was calculated by measuring the cell diameter after detachment or dissociation using bright-field microscopy followed by image processing using ImageJ software.⁴¹ Accordingly, Gd concentrations obtained by ICP-MS measurements were divided by the calculated average cell volume.

Localisation of nanoparticles: fixation, permeabilization and immunostaining

First, cell nuclei and actin filaments in the cytoskeleton were labelled. After incubation with AGuIX®-Cy5.5 nanoparticles, the spheroids were rinsed with PBS (3 \times 5 min), then fixed in paraformaldehyde (4%) for 20 min and permeabilized using 0.1% Triton X-100 (Acros) for 10 min. After blocking with 3% bovine serum albumin (BSA, Sigma-Aldrich) for 20 min, the samples were incubated with phalloidin-546 solution

(Invitrogen™, A22283, 1:50 in PBS) containing NucGreen™-Dead 488 (Invitrogen™, R37109, 1 drop per 5 ml in PBS) at 4 °C overnight. The procedure ended with rinsing spheroids with PBS (3 \times 5 min).

In a second series of experiments, to find out the precise intracellular localisation of AGuIX®-Cy5.5 nanoparticles, three antibodies were used to label the main cell compartments: EEA1 for early endosomes (Cell Signaling Technology, #3288), AIF for mitochondria (Cell Signaling Technology, #5318) and LAMP-1 for lysosomes (Cell Signaling Technology, #9091). After fixation in paraformaldehyde (4%) for 20 min and rinsing with PBS (3 \times 5 min) according to the protocol proposed by the manufacturer, cells were blocked in a buffer (PBS/5% BSA/0.3% Triton™ X-100) for 60 min and rinsed with PBS (3 \times 5 min). These samples, either spheroids in microwells or cell monolayers in Ibidi plates, were incubated with EEA1 (1:100), AIF (1:400) and LAMP1 (1:200) in a buffer (PBS/1% BSA/0.1% Triton™ X-100) overnight.

The incubation buffers were aspirated and cells were rinsed with PBS (3 \times 5 min). For the secondary antibody, goat-anti rabbit IgG-Alexa 555 (Invitrogen™, A21428, 1:500, in PBS/1% BSA/0.1% Triton™ X-100) was used. All samples were then incubated with NucGreen™ Dead 488 (Invitrogen™, 1 drop per 5 ml in PBS) overnight for spheroids and 4 h for cell monolayers. In the last step, they were rinsed with PBS (3 \times 5 min).

Spheroid clarification

Optical imaging of three-dimensional biological samples can be performed using confocal fluorescence microscopy which images these 3D samples *via* optical sectioning. However, this technique faces several limitations, including light scattering, attenuation of photons due to light absorption and local refractive index differences, limiting the light depth of penetration.⁴² Many different clarification techniques have been developed to overcome such issues.^{43,44} In the current study, the clearing efficiency of two methods was analysed using NucGreen™ signals in HCT-116 spheroids: RapiClear 1.52 (Sunjin Lab) and glycerol.⁴⁵ Based on the quantification of fluorescence intensities (Fig. S1†), clarification with glycerol/PBS (80%/20%) was chosen to clear spheroids in this study.

The solution for clarifying spheroids was prepared by mixing glycerol (99.5%, VWR Chemicals) with PBS in the ratio 80%/20%. A fresh solution was prepared for every experiment. To clarify spheroids, just after fixation, they were incubated in glycerol solution for 24 h. A detailed description of the mounting procedure used for imaging of live and fixed spheroids is described in Fig. S2.† For most experiments, the microsystems were incubated with a fresh glycerol solution and mounted between 2 coverslips separated by a 1 mm sticky spacer (2 \times 0.5 mm thick Ispacer, SunJin Lab).

Confocal fluorescence microscopy

Image acquisition of spheroids and cell monolayers was carried out with a confocal microscope (Leica SP5) using

either a 20× dry objective (NA = 0.7), a 25× water immersion objective (NA = 0.95), or a 40× oil immersion objective (NA = 1.25). Image acquisition in the Z direction was performed using a 1 μm z-step. Automatic image acquisitions for a large number of spheroids were performed (about 4 h for 30 spheroids using 30% power for AGuIX®-Cy5.5 nanoparticles ($\lambda_{\text{excitation}} = 633 \text{ nm}$)).

Image processing

Images obtained by confocal fluorescence microscopy were analysed using a dedicated MATLAB routine. While spheroids were imaged using optical sectioning in the Z direction, it was useful to quantify the average signal intensity along the radius of each spheroid.

To do this, the entire surface of each spheroid at each imaging depth was first segmented using the intensity signals coming from every nucleus (labelled with NucGreen™-488). From this segmentation, the segmented spheroid slices were first fitted into a perfect circle for each imaging depth, followed by fitting each spheroid z-stack into a perfect sphere. By changing the coordinates of analysis from Cartesian (x, y, z) to spherical (R, θ, ϕ) coordinates, the mean intensity of AGuIX®-Cy5.5 nanoparticles was averaged along θ and ϕ angles. The obtained averaged intensity was normalised with the maximum grey value of images obtained and plotted as a function of the distance from the periphery.

For cell monolayers, the maximum Z-projection of each field of view imaged by confocal microscopy (obtained by ImageJ) was used and analysed with a MATLAB script to quantify the mean intensity in these images. For each sample, the average of the mean intensity computed in the different fields of view was calculated.

Colocalisation quantification

To quantify the colocalisation of AGuIX®-Cy5.5 nanoparticles with cell organelles from confocal fluorescence images, a dedicated routine was developed to calculate the Pearson correlation coefficient, indicating the degree of colocalisation between fluorophores. Briefly, for each image of the acquired stack, a mask of the spheroid was automatically defined using nucleus staining. The correlation between the far-red and red channels (corresponding to AGuIX®-Cy5.5 and organelle-immunostaining, respectively) was then computed using the `corr2` MATLAB function. Using this routine, the Pearson correlation coefficient was calculated in the spheroid area for each image along the Z-direction (same as acquisition).

NanoSIMS cellular imaging

To prepare samples for NanoSIMS cellular imaging, HCT-116 cell spheroids were incubated with 2 mM AGuIX® nanoparticles for 72 h and then fixed with 2% glutaraldehyde in cacodylate buffer (0.1 M, pH 7.8) for 60 min followed by rinsing with PBS (3 × 5 min). Samples were then postfixed with 1% osmium tetroxide followed by uranyl acetate staining

and gradually dehydrated in ethanol (30% to 100%) and embedded in Epon.

A 0.2 μm relatively thick section was deposited onto a clean Si chip and dried in air before being introduced into a NanoSIMS-50 Ion microprobe (CAMECA, Gennevilliers, France) operating in scanning mode.^{46,47} For the present study, a tightly focused Cs⁺ primary ion beam at an impact energy of 16 keV was used to monitor up to five secondary ion species in parallel from the same sputtered volume: ¹²C⁻, ¹²C¹⁴N⁻, ²⁸Si⁻, ³¹P⁻, as well as ³⁵Cl⁻. The primary beam steps over the surface of the sample to create images for these selected ion species. The primary beam intensity was 3 pA with a typical probe size of ≈200 nm. The raster size was 60 μm with an image definition of 512 × 512 pixels. The acquisition was carried out in multiframe mode with a dwell time of 0.5 ms per pixel and 220 frames were recorded. The image processing was performed using ImageJ software.⁴¹ Successive image frames were properly aligned using the TOMOJ plugin⁴⁸ with ¹²C¹⁴N⁻ images as reference to correct the slight image field shift during the 8 h signal accumulation before a summed image was obtained for each ion species.

Results and discussion

A hydrogel-based microsystem was developed to generate uniform-sized multicellular tumour spheroids (Fig. 1). The design of these microwells was meant to meet the following goals: (1) to make homogenous and uniform cell spheroids, (2) to increase the throughput in drug screening and (3) to be compatible with *in situ* treatment, immunostaining and image acquisition as well as *ex situ* characterization techniques. First, a silicon wafer mould was designed and made using a classical photolithography technique (Fig. 1A). From this silicon wafer mould, counter moulds in polydimethylsiloxane (PDMS) were prepared (Fig. 1B), which could be used several times to replicate microwells with agarose hydrogel. To prepare agarose microwells, 2% ultra-pure agarose solution was poured on the PDMS moulds (Fig. 1C) and after gelation, they were placed on APTS-functionalized coverslips (Fig. 1D) or directly transferred to any classical multi-well plate (Fig. 1E).

This method enabled us to generate hundreds of homogenous spheroids per microsystem in each well of a multi-well plate (Fig. 1E and F). Thanks to the hydrogel nature of the microwells, many experimental steps including rinsing, changing the medium, spheroid fixation and immunostaining could be implemented in the same multi-well plate with no manipulation of spheroids, which resulted in the treatment and labelling of several spheroids simultaneously (Fig. 1G). The advantage of the agarose microwells was the efficient transfer of medium and solutions through it. The exchange rate has been quantified by following up the removal of the FITC dye and AGuIX®-Cy5.5 nanoparticles from the agarose microwells *via* time-lapse image acquisition using confocal

microscopy (Fig. S3†). All curves were exponentially decreasing with a characteristic time of 25 min for FITC (23–27 min depending on the depth) and of 1 to 2 hours for AGuIX@-Cy5.5 nanoparticles depending on the depth of the focal plane.

A plateau is reached after two hours for FITC (at $25 \pm 5\%$) and after 10 hours for AGuIX@-Cy5.5 nanoparticles (at $5 \pm 3\%$).

Of note, the compatibility of the hydrogel-based microsystem with coverslips enabled *in situ* quantification of nanoparticle penetration and their 3D distribution within

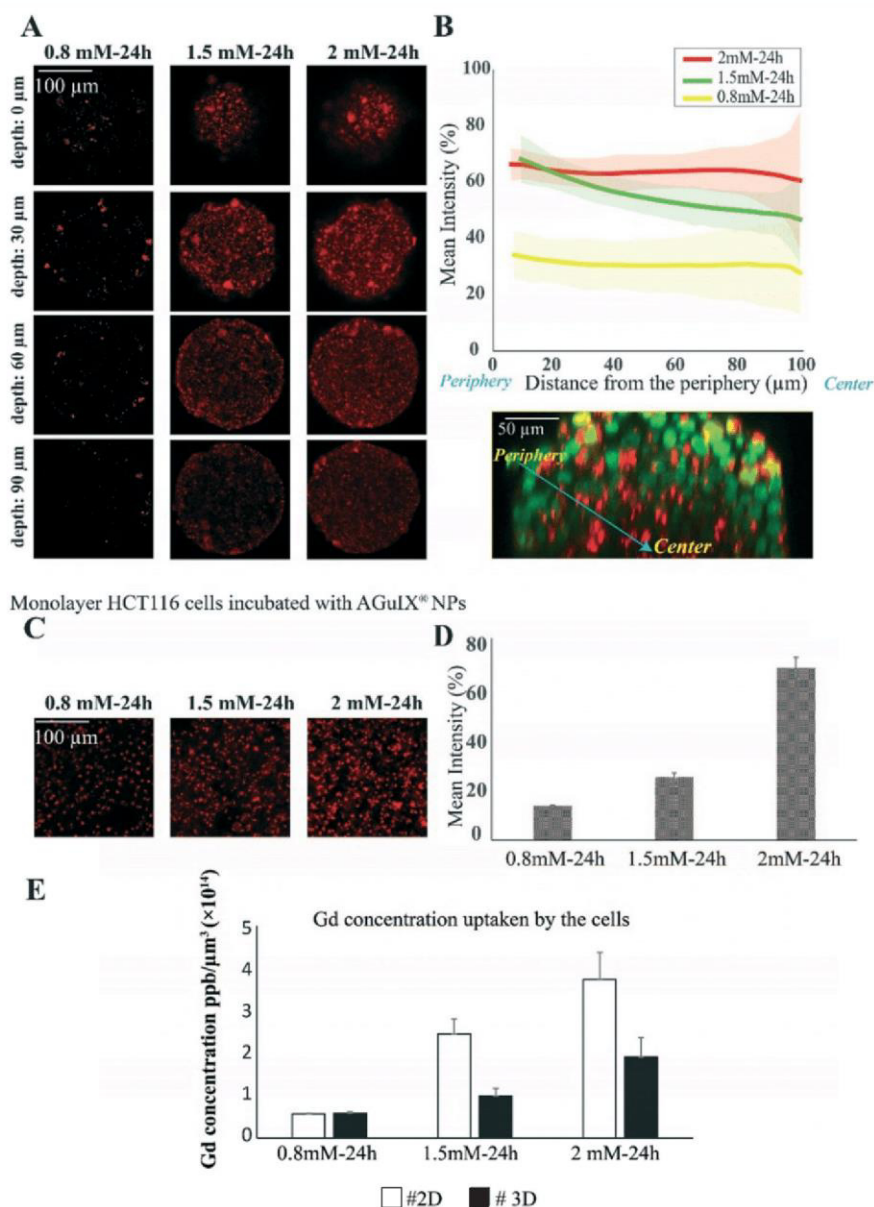


Fig. 2 Quantification of penetration and cellular uptake of AGuIX@-Cy5.5 nanoparticles in HCT-116 tumour spheroids and monolayer cell culture. (A) Representative confocal fluorescence images of HCT-116 spheroids incubated with 0.8, 1.5 and 2 mM concentration of AGuIX@-Cy5.5 for 24 h for four different depths (0, 30, 60 and 90 μm). (B) Mean intensity along with standard deviation (light colors) of AGuIX@-Cy5.5 as a function of the distance from the spheroid periphery (see the orthogonal view in the inset, green = nuclei, red = AGuIX@-Cy5.5) for 0.8 mM (yellow, $N = 73$), 1.5 mM (green, $N = 68$) and 2 mM (red, $N = 121$); three independent experiments. (C) Representative confocal fluorescence images of monolayer HCT-116 cells exposed to AGuIX@-Cy5.5 nanoparticles with 0.8, 1.5 and 2 mM concentration. (D) Quantification of the mean intensity of AGuIX@-Cy5.5 nanoparticles in maximal projection of confocal fluorescence images of monolayer cells after 24 h of incubation with different AGuIX@-Cy5.5 concentrations: 0.8 mM (yellow, $N = 40$), 1.5 mM (green, $N = 40$) and 2 mM (red, $N = 40$); three independent experiments. Error bars represent the standard deviations. (E) Mean and standard deviation of the concentration of Gd (ppb μm^{-2}) uptaken by the cells after incubation with 0.8, 1.5 and 2 mM concentration of AGuIX@ for 24 h in HCT-116 cell spheroids and monolayer cell culture measured with ICP-MS ($N = 6$, two independent experiments).

spheroids with high-resolution optical microscopy such as confocal fluorescence microscopy (Fig. 1H). All spheroids were within the same focal plane, giving access to easy parallelization of 3D spheroid imaging (Fig. 1I). This is an important aspect compared to already proposed hydrogel microwells, where spheroids need to be transferred to a dedicated microscopy plate for high-resolution 3D imaging.^{27,49–51} Such a transfer first increases the complexity in terms of handling and imaging, and second may induce fusion between spheroids or deformation of spheroids, which in turn may introduce biases in the analysis. Our original and simple process (Biocompatible hydrogel microwell plate, under patent³⁹) bridges an important gap for in-depth optical spheroid analysis.

Moreover, these microwells are compatible with time-lapse optical microscopy, facilitating follow-up of spheroid growth for several days (Fig. S4 and Movie S1†). The system enables us to produce very homogenous spheroids (Fig. S5†), which gives access to the heterogeneity of cell response, with no bias induced by size heterogeneity. In our study, nanoparticle penetration was mainly evaluated using fluorescence intensity obtained from 3D confocal image acquisition. Taking advantage of the large statistics provided by our microsystems, we assessed the minimum number of spheroids required to get reliable results (Fig. S6†). A minimum of $N = 30$ spheroids is recommended to obtain reliable results at an imaging depth corresponding to the first quarter of the spheroids (0–50 μm from the periphery). This number rises to $N = 70$ spheroids for an accurate analysis close to the equatorial plane.

Cellular uptake of AGuIX®-Cy5.5 nanoparticles in 2D and 3D

As a proof of concept of the relevance of this new hydrogel-based microsystem, the penetration and distribution of AGuIX®-Cy5.5 nanoparticles ($D_{\text{H}} = 5$ nm) within spheroids was investigated using the colorectal cancer cell line HCT-116. In a previous study, it has been proven that the localisation of Gd-based nanoparticles tagged with Cy5.5 is the same as that of label-free nanoparticles in U87 cells.⁵² After 48 h of growth within 200 μm agarose microwells, spheroids were incubated with three different concentrations of AGuIX®-Cy5.5, 0.8, 1.5 and 2 mM in Gd, selected according to previous studies performed in 2D cell culture.⁵³ In Fig. 2A, fluorescence images show the distribution of AGuIX®-Cy5.5 nanoparticles in spheroids after 24 h of incubation with the three different concentrations at different depths. These images showed qualitatively that the number of nanoparticle clusters in spheroids directly increases with the increase in initial concentration of AGuIX®-Cy5.5 nanoparticles. For 0.8 mM, very few nanoparticle clusters could be observed, while the number of clusters increased in 1.5 and 2 mM concentrations. For 2 mM concentration, nanoparticles were detected within the deeper layers of spheroids. Taking the spherical geometry of the sample into account to quantify the fluorescence in each image of spheroids, the mean intensity was calculated by

averaging the intensity along theta and phi angles in the direction of the radius. The *in situ* fluorescence analysis of Fig. 2B enabled us to decipher the relative differences in nanoparticle penetration in the range of concentrations analysed. Consistent with the fluorescence images in Fig. 2A, the mean intensity increased as the incubation concentration increased. From the outermost layer to the centre of the spheroids, the mean intensity decreased differently depending on the concentration (from $34 \pm 8\%$ to $28 \pm 14\%$ for 0.8 mM, from $68 \pm 8\%$ to $46 \pm 15\%$ for 1.5 mM and from $66 \pm 5\%$ to $60 \pm 24\%$ for 2 mM). For the largest concentration (2 mM), deep penetration was possible, while the penetration decreased exponentially with the depth for 1.5 mM, with a characteristic length of 44 ± 2 μm . Such a difference could be attributed to the higher number of nanoparticles reaching the centre of the spheroids for an incubation with 2 mM Gd. The relative independence of fluorescence intensity with depth for the lowest concentration (0.8 mM) could be attributed to a level close to noise, with no real penetration of nanoparticles in the periphery or in the centre of the spheroids.

To be sure that the presence of agarose in our microsystem does not affect the distribution and cellular uptake of AGuIX®-Cy5.5 nanoparticles within spheroids, a control experiment was made using an ultralow adhesion 96-well plate and 2 mM AGuIX®-Cy5.5 nanoparticle concentration (Fig. S7†). Similar results concerning the penetration of the nanoparticles were obtained: the same normalised intensity range and similar evolution as a function of distance from the periphery.

Deep penetration of small nanoparticles (<12 nm) within deep interstitial space has already been reported *in vivo*.⁵⁴ The *in vitro* platform described in the current study enables assessing more quantitatively such penetration. Hence, it will be a valuable tool to relate such penetration with therapeutic efficacy in future studies.

To make a direct comparison with cellular uptake in 2D cell culture, monolayers of HCT-116 cells were incubated with the same concentrations of AGuIX®-Cy5.5 nanoparticles (Fig. 2C). As expected, the number of AGuIX®-Cy5.5 clusters increased as the initial concentration increased and the quantification of fluorescence images of cell monolayers (based on the mean intensity of AGuIX®-Cy5.5) confirmed that the uptake of nanoparticles increased with the concentration of AGuIX®-Cy5.5 in the incubation medium (Fig. 2D, from $14.0 \pm 0.3\%$ for 0.8 mM, $25.8 \pm 1.8\%$ for 1.5 mM to $70.8 \pm 4.4\%$ for 2 mM). This mean intensity evolution was hence different from the one obtained in 3D in the periphery. However, as a true quantitative comparison is not possible using fluorescence analysis, elemental analysis by ICP-MS was performed concurrently to obtain a quantitative analysis of Gd content within cells for both 2D and 3D models (Fig. 2E). While the average nanoparticle uptake per cell in 2D and 3D was similar for 0.8 mM ($(0.580 \pm 0.006) \times 10^{-14}$ ppb μm^{-3} in 2D *vs.* $(0.59 \pm 0.05) \times 10^{-14}$ in 3D), the uptake was two-fold higher in 2D compared to 3D for both 1.5 mM ($(2.5 \pm 0.5) \times 10^{-14}$ ppb μm^{-3} in 2D *vs.* $(1.0 \pm 0.2) \times$

10^{-14} in 3D) and 2 mM $((3.8 \pm 0.9) \times 10^{-14}$ ppb μm^{-3} in 2D vs. $(1.9 \pm 0.6) \times 10^{-14}$ ppb μm^{-3} in 3D).

One of the reasons for the reduction in effectiveness of therapeutics *in vivo* compared to monolayer cell cultures is the lack of efficient penetration and distribution of therapeutics throughout the tumour tissue.⁵⁵ This is what we also observed here, with a large reduction of nanoparticle uptake in 3D compared to 2D cell culture.

Another approach was used to compare the cellular uptake of AGuIX@-Cy5.5 nanoparticles in 2D and 3D: 2D cells were treated with 2 mM AGuIX@-Cy5.5 nanoparticles for 24 h, then spheroids were made from these AGuIX@-Cy5.5 labelled cells using the usual protocol (Fig. S8†). Interestingly, the distribution of nanoparticles differs when spheroids are made with already labelled cells compared to direct incubation with already formed spheroids, further highlighting the difference in nanoparticle availability between 2D and 3D models.

Kinetics of AGuIX@-Cy5.5 nanoparticle transport into spheroids

One of the crucial parameters in nanoscale design is the pharmacokinetics of nanoparticles and understanding this aspect of cell–nanoparticle interactions has a great importance.^{56,57} The kinetics of penetration of AGuIX@-Cy5.5 nanoparticles within HCT-116 cell spheroids grown for 48 h were assessed by analysing confocal images obtained for different incubation times (1, 24 and 72 h) for the highest concentration investigated (2 mM) (Fig. 3A). After 1 h of incubation, the AGuIX@-Cy5.5 nanoparticles were mostly residing in the peripheral layer of the spheroids, especially in the extracellular space. After 24 h, clusters of nanoparticles were found throughout the spheroids. At 72 h, the number of

clusters was increasing for all depths up to the equatorial plane (100 μm).

The average intensity exhibited a different evolution with the distance from the periphery, depending on the incubation time (Fig. 3B). At the periphery, the average intensity was lower for 1 h incubation ($52.2 \pm 1.3\%$) than for 24 h and 72 h that exhibited similar values ($68 \pm 1\%$ and $65.8 \pm 0.7\%$, respectively). When we moved to the centre of the spheroids, the mean intensity was slightly lowered for 1 h and 24 h incubation (from $52.2 \pm 1.3\%$ down to $38.7 \pm 2.7\%$ for 1 h, from $68 \pm 1\%$ down to $59.5 \pm 1.9\%$ for 24 h). Accordingly, in 1 h incubation the mean intensity was less than that of 24 h and 72 h samples in all regions of the spheroids. Surprisingly, for 72 h, the average intensity exhibited a non-monotonous evolution with the distance from the periphery, with an intensity larger for the middle layers than at the periphery ($66 \pm 5\%$ vs. $73.8 \pm 8.5\%$ at a depth of 60 μm). This may be the result of the increased number of clusters found for intermediate layers after 72 h of incubation time.

To follow the distribution and the transport of nanoparticles within spheroids, an experiment was designed to assess changes in AGuIX@-Cy5.5 nanoparticle distribution before and after rinsing steps (Fig. 4). In this experiment, 2 days after cell seeding (Fig. 4, step I), the formed HCT-116 spheroids were incubated with 2 mM AGuIX@-Cy5.5 solution for 72 h (Fig. 4, step II). Spheroids were then imaged in incubation medium (Fig. 4, step III) and after three washing steps of 15 min each (Fig. 4, step IV). Spheroids were kept in the incubator for an additional 24 h and then imaged before (Fig. 4, step V) and after (Fig. 4, step VI) another washing procedure. Confocal fluorescence microscopy of living spheroids showed that AGuIX@-Cy5.5 nanoparticle fluorescence signals of the surrounding background (fluorescence signal outside spheroids) was decreasing

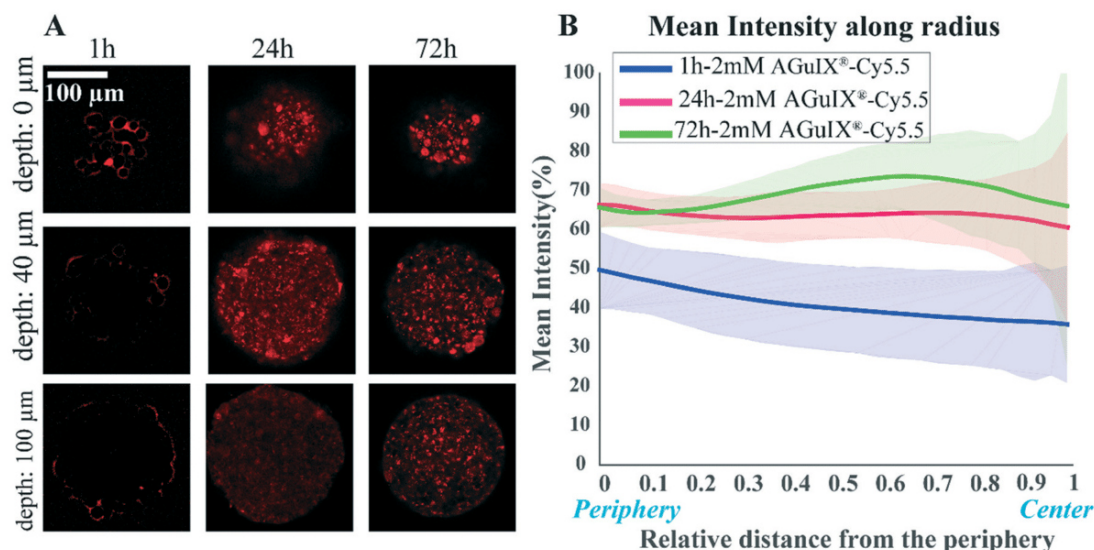


Fig. 3 Kinetics of penetration of AGuIX@-Cy5.5 nanoparticles in HCT-116 cell spheroids. (A) Representative confocal fluorescence images of HCT-116 grown for 48 h and exposed to 2 mM concentration of AGuIX@-Cy5.5 nanoparticles for 1, 24 and 72 h. (B) Mean intensity along with standard deviation (light colours) as a function of relative distance from the periphery for 1 h (blue, $N = 50$), 24 h (magenta, $N = 121$) and 72 h (green, $N = 63$; three independent experiments).

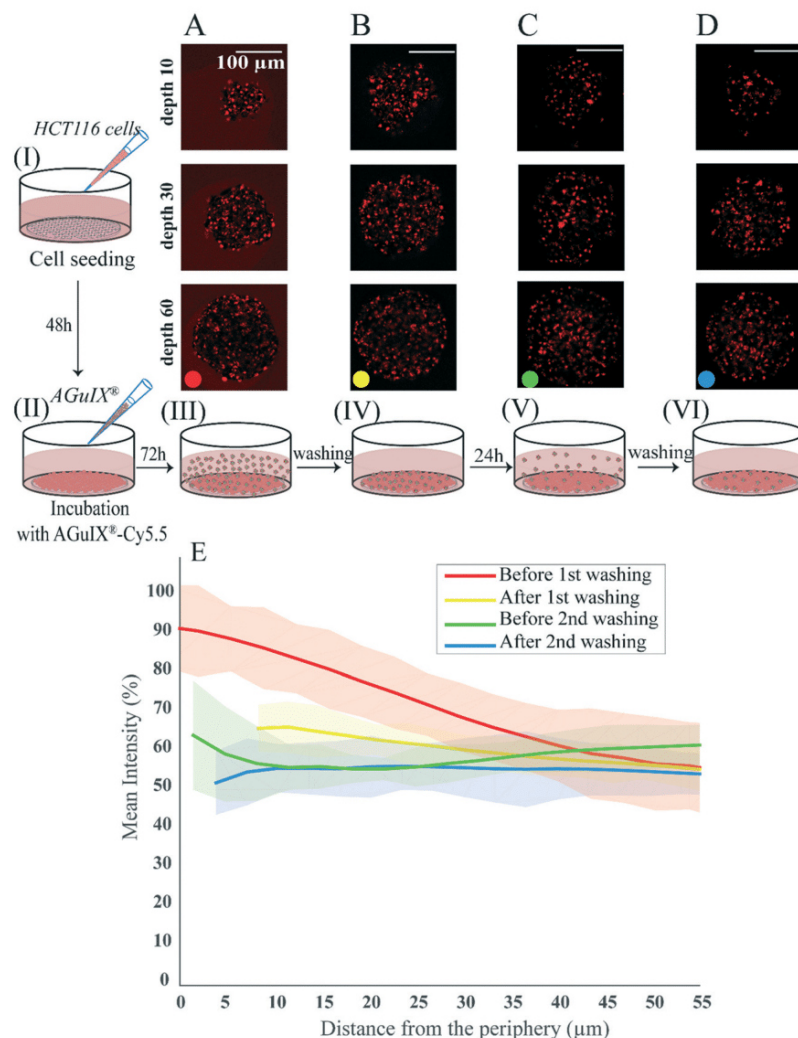


Fig. 4 Dynamic analysis of AGuIX@-Cy5.5 nanoparticle transport and localisation within spheroids. HCT-116 cell spheroids were prepared using the agarose microsystem (step I). After 48 h of growth, they were exposed to 2 mM AGuIX@-Cy5.5 solution for 72 h (step II). (A) Spheroids were imaged in the incubation medium (step III). (B) Spheroids were then rinsed with fresh medium three times for 15 min each and were imaged again (step IV). (C) Spheroids were allowed to grow for an additional 24 h (in an incubator at 37 °C and 5% CO₂) before imaging (step V). (D) Spheroids were rinsed again with fresh medium (3 × 15 min) before imaging (step VI). (E) Quantification of AGuIX@-Cy5.5 nanoparticle mean intensity along the distance from the periphery ($N = 25$). Bold lines represent the mean intensities, averaged for all spheroids. Light colours represent the standard deviations.

gradually with the different washing steps for all depths (Fig. 4A–D). This is confirmed by the quantification of the mean intensity along the spheroid radius (Fig. 4E): while the mean intensity before washing (red curve) at the periphery was around $92 \pm 10\%$, it was decreasing to $59 \pm 10\%$ at 55 μm distance from the periphery. After the first washing step (yellow curve), the mean intensity at the periphery reduced to $66 \pm 6\%$ and reached a similar intensity level to the one before washing at 55 μm distance from the periphery ($58 \pm 4\%$). Additional washing steps further reduced the mean intensity at the periphery ($64 \pm 14\%$ and $54 \pm 14\%$ before and after the second washing step), while the mean intensity obtained for deeper layers exhibited similar levels. The second washing (blue curve) led to a steady value of mean intensity ($\sim 54\%$) close to the mean intensity obtained at 55

μm distance from the periphery of spheroids for all washing steps. This mean intensity should correspond to the signal coming from nanoparticles that are internalized by the cells, as all nanoparticles residing in the extracellular space have been washed away.

Localisation of AGuIX@-Cy5.5 nanoparticles in spheroids using their chemical signature

Due to the limit of resolution using standard confocal optical microscopy (200 nm in the best imaging conditions), only clusters of nanoparticles can be detected. In addition, we cannot rule out that the distribution of the fluorophores does not truly represent the distribution of the nanoparticles themselves. To confirm the presence of nanoparticles,

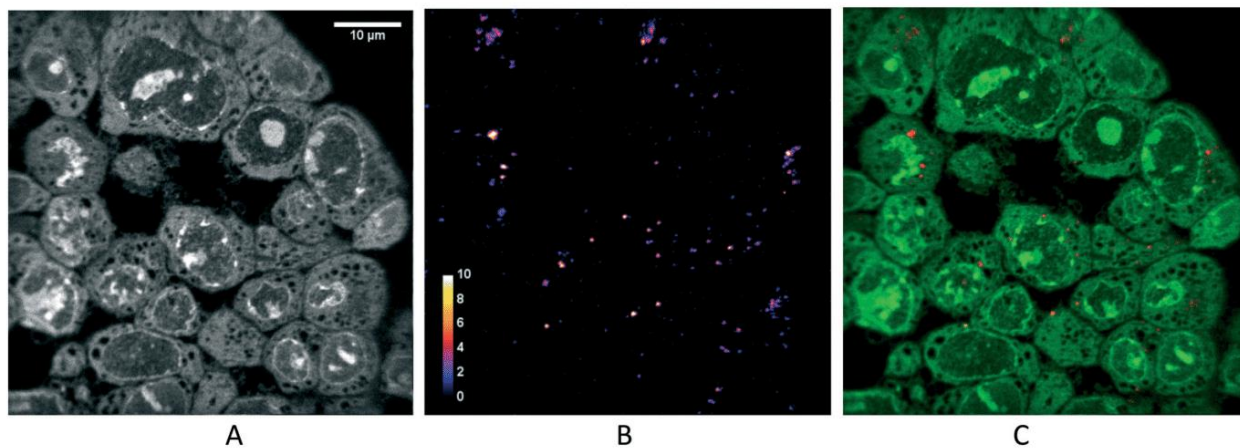


Fig. 5 Localisation of the AGuIX@-Cy5.5 nanoparticles in spheroids using NanoSIMS. NanoSIMS images of HCT-116 spheroids loaded with AGuIX@-Cy5.5 nanoparticles. (A) Corresponds to the signal of $^{31}\text{P}^-$ showing the cell structure. (B) Highlights the signal of $^{28}\text{Si}^-$ representing the intracellular location of AGuIX@-Cy5.5 nanoparticles. (C) Merged image of $^{28}\text{Si}^-$ and $^{31}\text{P}^-$. Scale bar: 10 μm .

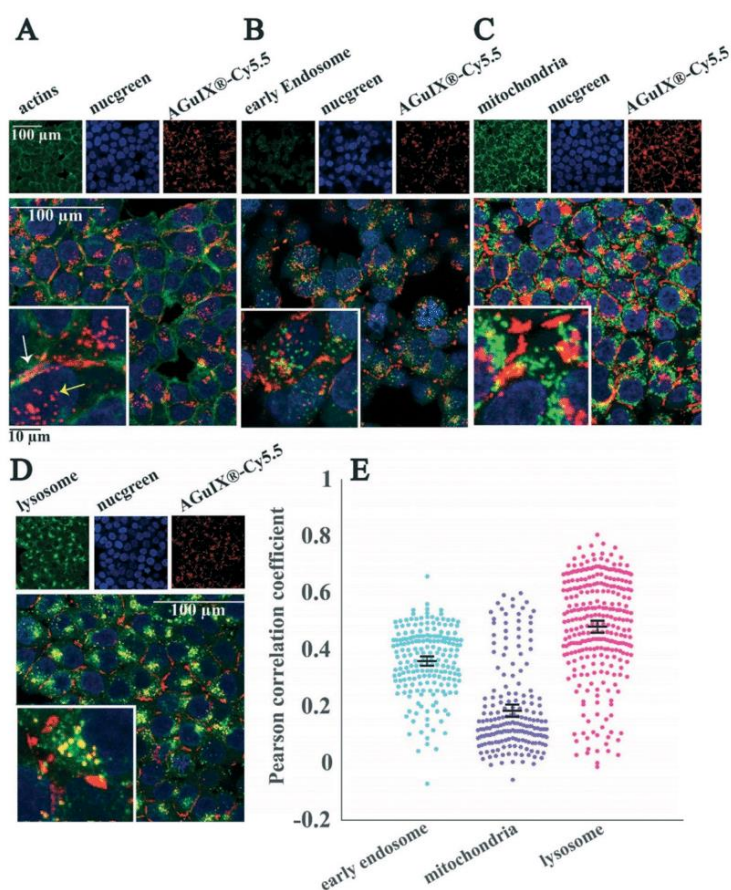


Fig. 6 Localisation of the AGuIX@-Cy5.5 nanoparticles in 2D monolayers. Fluorescence images of HCT-116 cells incubated with AGuIX@-Cy5.5 nanoparticles (2 mM, 24 h) and immunostained with antibodies to find the colocalization of nanoparticles inside cells. In all images, the red channel and blue channel represent AGuIX@-Cy5.5 nanoparticles and cell nuclei, respectively. (A) The green channel depicts phalloidin, a marker of actin in cells, which demonstrates nanoparticles localising both inside cells (yellow arrow) and in the space between cells (white arrow). (B) The green channel shows early endosome in the cells, with no colocalisation with AGuIX@-Cy5.5 nanoparticles. (C) The green channel shows mitochondria and reveal very low colocalisation with AGuIX@-Cy5.5 nanoparticles (yellow colour). (D) The green channel shows the lysosomes, and colocalisation is demonstrated by the yellow colour. White scale bar, 100 μm ; black scale bar, 10 μm . (E) Distribution of Pearson correlation coefficients in the different fields of view to quantify the colocalisation of AGuIX@-Cy5.5 nanoparticles with the three different cell organelles investigated. Error bars represent the standard errors of the mean (SEM) of Pearson correlation coefficient values obtained for all fields of view and all available depths for three independent experiments. It was plotted as scatter plots using the MATLAB UnivarScatter function (©Manuel Lera Ramirez, 2015, available in MATLAB exchange files).

nanoscale secondary ion mass spectrometry (nanoSIMS) was performed on spheroid sections (Fig. 5). This analytical technique allows the acquisition of elemental composition maps with a spatial resolution down to 50 nm. The images of $^{12}\text{C}^-$ (see Fig. S7†) and $^{35}\text{Cl}^-$ (data not shown) indicate the absence of defect in the sample section. Any damage, even tiny holes, would appear with high contrast in the signal, and such a signal was not observed. This validated that the signal measured originated from the sample and not from the subjacent pure silicon substrate. The image of $^{12}\text{C}^{14}\text{N}^-$ showed the histological aspect of the cell (data not shown), while the one of $^{31}\text{P}^-$ (Fig. 5A) highlights the cell nucleus. Since AGuIX@-Cy5.5 nanoparticles are mainly made of Si, the

images of $^{28}\text{Si}^-$ allowed the observation of the chemical signature of the nanoparticles (Fig. 5B). Thereby, the nanoparticles were found unequivocally inside the spheroid, exclusively in the cytoplasm of the cells. Of note, again our microsystems enabled an easy sample preparation, as all spheroids were within the same sectioning plane.

Localisation of AGuIX@-Cy5.5 within cells in 2D and 3D using immunostaining

Thanks to the full compatibility of the microsystems with *in situ* immunostaining, it was possible to assess the localisation of nanoparticles in 2D cells (Fig. 6) and

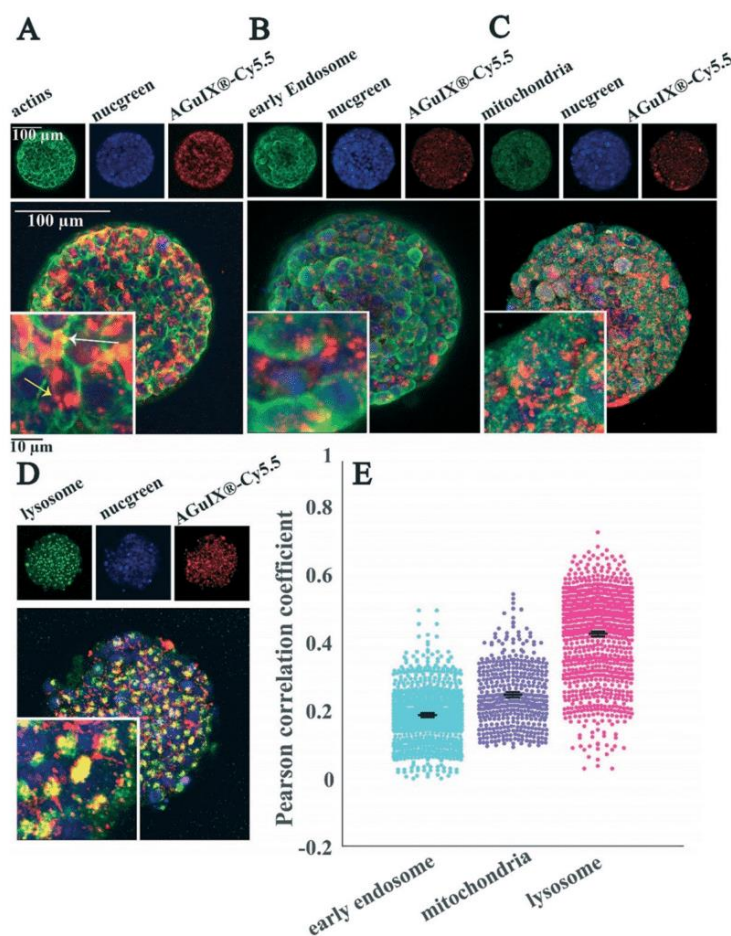


Fig. 7 Localisation of AGuIX@-Cy5.5 nanoparticles within spheroids. Fluorescence images of HCT-116 cell spheroids incubated with AGuIX@-Cy5.5 nanoparticles (2 mM, 24 h) and immunostained with antibodies to find the colocalisation of nanoparticles inside cells. In all images, red and blue channels represent AGuIX@-Cy5.5 nanoparticles and cell nuclei, respectively. (A) The green channel depicts phalloidin, a marker of actin in cells, which demonstrates that nanoparticles localise both inside cells (yellow arrow) and in the extracellular space of spheroids (white arrow). (B) EEA1 antibody in the green channel shows early endosome; with very low colocalisation with nanoparticles (yellow colour). (C) AIF antibody labelled mitochondria are shown in green, with very low colocalisation with AGuIX@-Cy5.5 nanoparticles (yellow colour). (D) LAMP1 antibody in green channel stains lysosomes. Yellow colour represents the colocalisation of nanoparticles in red and lysosomes in green. White scale bar, 100 μm ; black scale bar, 10 μm . (E) Quantification of the colocalisation of AGuIX@-Cy5.5 nanoparticles with the three different cell organelles investigated using Pearson correlation coefficient. Distribution obtained for all imaged spheroids and all imaging depths for the three different cell organelles. Error bars represent standard errors of the mean (SEM) of Pearson correlation coefficient values obtained for all fields of view and all available depths for three independent experiments. It was plotted as scatter plots using the MATLAB UnivarScatter function (©Manuel Lera Ramirez, 2015, available in MATLAB exchange files).

multicellular tumour spheroids (Fig. 7) using confocal fluorescence microscopy.

Labelling of cell organelles confirmed that nanoparticles were present in both extracellular and intracellular space in 2D cells (Fig. 6A) and in 3D spheroids (Fig. 7A). Very low

colocalisation of AGuIX®-Cy5.5 with early endosomes (Fig. 6B and E in 2D and Fig. 7B and E in 3D) or mitochondria (Fig. 6C and E in 2D and Fig. 7C and E in 3D) was evidenced by immunostaining, while a large colocalisation with lysosomes was observed in both 2D (Fig. 6D and E) and 3D environments

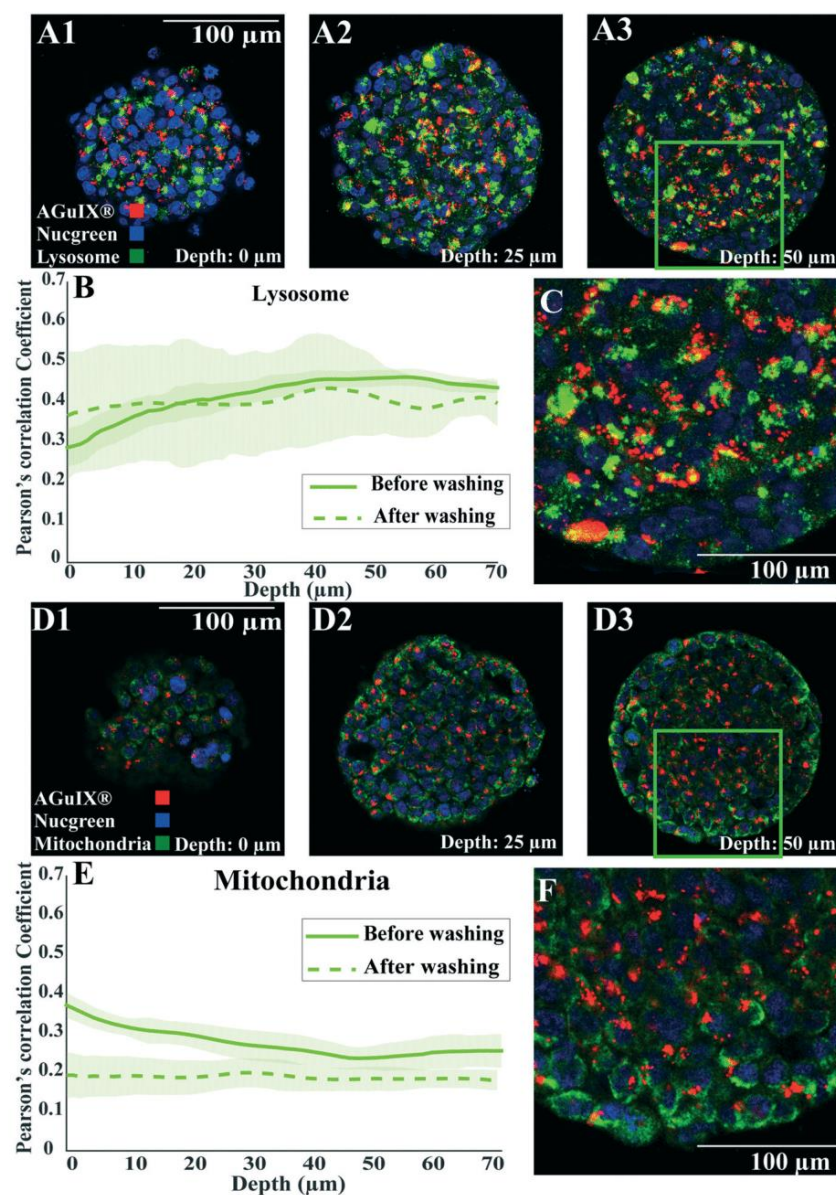


Fig. 8 Localisation of AguilX®-Cy5.5-nanoparticles after an extensive washing procedure. Confocal fluorescence images of HCT-116 spheroids incubated with AGuIX®-Cy5.5 nanoparticles for 72 h with 2 mM AGuIX® solution and washed according to the procedure mentioned in Fig. 4, then fixed and immunostained with antibodies to find the colocalisation of nanoparticles in spheroids. For all images, red and blue channels are stained AGuIX®-Cy5.5 and nuclei, respectively. (A1–A3) Representative images of lysosome immunostaining obtained at various depths (A1, 0 μm ; A2, 25 μm ; A3, 50 μm). Green channel = lysosome [LAMP1 antibody], yellow colour = possible colocalisation of AGuIX®-Cy5.5 nanoparticles with lysosomes). (B) Pearson correlation coefficient for AGuIX®-Cy5.5 nanoparticles with lysosomes along with standard error of the mean (light colour) as a function of depth ($n = 27$ spheroids, 3 independent experiments before washing, $n = 5$ spheroids after washing). (C) Zoomed-in portion of merged image at a depth of 50 μm (square in A3). (D1–D3) Representative images of mitochondria immunostaining obtained at various depths (D1, 0 μm ; D2, 25 μm ; D3, 50 μm). Green channel = mitochondria [AIF antibody], yellow colour = possible colocalisation of AGuIX®-Cy5.5 nanoparticles with mitochondria). (E) Pearson correlation coefficient for AGuIX®-Cy5.5 nanoparticles and mitochondria along with standard error of the mean (light colour) as a function of depth ($n = 22$ spheroids, 3 independent experiments before washing, $n = 5$ spheroids after washing). (F) Zoomed-in portion of merged image at a depth of 50 μm (square in D3).

(Fig. 7D and E). The Pearson correlation coefficient in both 2D cells and 3D spheroids (Fig. 6E in 2D and Fig. 7E in 3D) showed a higher value for lysosomes (0.48 ± 0.18 and 0.42 ± 0.12 for 2D and 3D, respectively), compared to 0.36 ± 0.12 and 0.18 ± 0.09 for early endosomes in 2D and 3D and 0.19 ± 0.15 and 0.24 ± 0.09 for mitochondria in 2D and 3D), showing the main intracellular localisation of AGuIX@-Cy5.5 nanoparticles. It is noteworthy that this colocalisation was not total and some nanoparticles were still residing in between cells. These outcomes are in accordance with previous studies showing localisation of nanoparticles in the endocytic pathway and in lysosomes.^{38,52}

The internalization mechanisms of AGuIX@ have been thoroughly investigated in 2D.³⁸ It has been shown that the entry of such sub-5 nm nanoparticles is different depending on nanoparticle concentration: passive diffusion and eventually macropinocytosis, in case of formation of nanoparticle clusters at the surface of the cell. It is known that the internalization pathway for a specific nanoparticle can differ between cell lines.⁵⁸ For the HCT-116 cell line used in this study, localisation of AGuIX@-Cy5.5 nanoparticles in lysosomes and in smaller amounts in early endosomes confirms that they were likely internalized by an endocytic mechanism.⁵⁹ Despite dominant colocalisation for both 2D and 3D with lysosomes, in 2D images the Pearson correlation coefficient average value for early endosomes is higher than that for mitochondria (Fig. 6B and E), which contrasts with these values in 3D (Fig. 7B and E). One explanation for this difference is that for spheroids, cells have varying access to the nanoparticles depending on their spatial position within spheroids, which could lead to different internalization processes. In 3D spheroids, AGuIX@-Cy5.5 nanoparticles were confronted by barriers to reach the cells in deeper layers; therefore they reach deeper layers in a lower amount (Fig. 2B) and with a delay (Fig. 3B), which can change their intracellular fate. This is another argument in favour of the 3D system for nanoparticle transport analysis. In 2D, all cells are submitted to the same homogeneous concentration of nanoparticles, while in 3D, there is a large difference in nanoparticle availability between cells that are at the periphery and cells in the centre of the spheroids. In addition, in spheroids, similar to natural tumours, there is a gradient of pH, oxygen and metabolites,⁶⁰ which might affect internalization and intracellular trafficking of nanoparticles in deeper layers.⁶¹

As highlighted by the overall mean intensity decrease with the washing procedure for the peripheral layers of the spheroids (Fig. 4), the extracellular nanoparticles were efficiently washed away after a long washing procedure (Fig. S10,† no extracellular nanoparticles were detected with immunostaining). Similar to results obtained after 72 h of incubation, colocalisation with lysosomes was still the major localisation of nanoparticles after this extensive washing procedure (Fig. 8A–C for lysosomes compared to Fig. 8D–F for mitochondria). The comparison of the Pearson correlation coefficient of AGuIX@-Cy5.5 with both lysosomes and mitochondria before and after washing suggests minor intracellular trafficking and/or exocytosis of nanoparticles

over time (Fig. 8B for lysosomes and 8E for mitochondria). The Pearson correlation coefficient of AGuIX@-Cy5.5 with lysosomes remained within a similar range before and after washing (mean values of 0.41 ± 0.03 vs. 0.40 ± 0.11 , respectively), while a decrease in the Pearson correlation coefficient of AGuIX@-Cy5.5 with mitochondria is observed after washing, particularly in outer layers (0.26 ± 0.02 vs. 0.18 ± 0.04 at 10 μm depth before and after washing, respectively), reaching very low values for inner layers (0.20 ± 0.04 vs. 0.18 ± 0.02 at 60 μm depth before and after washing, respectively). Such a decrease could be attributed to the removal of a few AGuIX@-Cy5.5 clusters residing in mitochondria or possible intracellular trafficking during the washing procedure. Hence, we could say that the washing procedure had lesser effect on AGuIX@-Cy5.5 nanoparticles residing in lysosomes.

Conclusion and outlook

We show in this study a simple agarose-based microsystem to quantitatively track nanoparticle penetration and subcellular localisation within a 3D cell culture model. The reproducibility of the spheroid size obtained with such a procedure dispenses the use of sophisticated automatic procedures to choose and pick the appropriate spheroids. Of note, our microsystems can be manufactured on conventional multi-well plates. It is hence fully compatible with available multi-well automated strategies.⁶² In the present study, the proof of concept was validated using spheroids made with the classical colorectal cell line HCT-116. Nevertheless, our approach is fully compatible with primary cells from patients that could be grown as organoids⁶³ in our microsystems, combining full optical microscopy compatibility, size and shape reproducibility, and large statistics. Combined with optical and digital clearing,⁶⁴ our approach opens up the possibility to resolve tumour heterogeneity, at the single cell-level, in a physiological context.

In the present study, the standard agarose used for the preparation of the microsystems provides a cell-repellent surface, with a stiffness in the 150 kPa range.^{65,66} In future studies, the mechanical properties of the agarose gels will be adjusted using different concentrations and types of agarose. Elastic hydrogels as soft as 1 kPa can be obtained using low concentrations of ultra-low agarose,⁶⁵ matching the physiological range of stiffness. It now calls for dedicated studies to assess how nanoparticle penetration and therapeutic efficacy is affected by the size of the 3D cell assembly, the presence of an extracellular matrix of different stiffness and composition, and the presence of associated tumour cells.⁶⁷

Author contributions

Saba Goodarzi: methodology, investigation, validation, formal analysis, visualization, writing – original draft; Audrey Prunet: methodology, investigation, visualization, writing – review and editing; Fabien Rossetti: methodology, investigation; Guillaume Bort: writing – review and editing; Olivier

Tillement: conceptualization; Erika Porcel: methodology, investigation, validation, visualization, writing – review and editing; Sandrine Lacombe: methodology, writing – review and editing; Ting-Di Wu: methodology: writing – review and editing; Jean-Luc Guerquin-Kern: methodology, investigation, writing – review and editing; H el ene Delano -Ayari: methodology, formal analysis; Fran ois Lux: conceptualization, supervision, writing – review and editing; Charlotte Riv iere: conceptualization, supervision, writing – original draft, writing – review and editing.

Conflicts of interest

CR, AP and HDA have to disclose the patent FR3079524A1. This patent protects the process to produce agarose-based microsystems on coverslips described in this publication. FL and OT have to disclose the patent WO2011/135101. This patent protects the AGuIX® NPs described in this publication. FL and OT possess shares of this company.

Acknowledgements

This work was supported by the ‘‘Institut Universitaire de France’’ (IUF). We thank L. Fuoco for her help in the early development of this project, R. Fulcrand for his support in photolithography, M. G. Blanchin for her help in spheroid preparation protocols for electron microscopy as well as the CTµ platform (Centre Technologique des Microstructures) for resin embedding of spheroids.

References

- S. Hua, M. B. C. de Matos, J. M. Metselaar and G. Storm, *Front. Pharmacol.*, 2018, **9**, 1–14.
- L. J. Bray, D. W. Hutmacher and N. Bock, *Front. Bioeng. Biotechnol.*, 2019, **7**, 1–36.
- S. E. Gould, M. R. Junttila and F. J. De Sauvage, *Nat. Med.*, 2015, **21**, 431–439.
- G. Lazzari, P. Couvreur and S. Mura, *Polym. Chem.*, 2017, **8**, 4947–4969.
- A. Sontheimer-Phelps, B. A. Hassell and D. E. Ingber, *Nat. Rev. Cancer*, 2019, **19**, 65–81.
- S. Peel, A. M. Corrigan, B. Ehrhardt, K. J. Jang, P. Caetano-Pinto, M. Boeckeler, J. E. Rubins, K. Kodella, D. B. Petropolis, J. Ronxhi, G. Kulkarni, A. J. Foster, D. Williams, G. A. Hamilton and L. Ewart, *Lab Chip*, 2019, **19**, 410–421.
- D. Peer, J. M. Karp, S. Hong, O. C. Farokhzad, R. Margalit and R. Langer, *Nat. Nanotechnol.*, 2007, **2**, 751–760.
- D. Rosenblum, N. Joshi, W. Tao, J. M. Karp and D. Peer, *Nat. Commun.*, 2018, **9**, 1410.
- M. Zanoni, F. Piccinini, C. Arienti, A. Zamagni, S. Santi, R. Polico, A. Bevilacqua and A. Tesei, *Sci. Rep.*, 2016, **6**, 1–11.
- S. Wilhelm, A. J. Tavares, Q. Dai, S. Ohta, J. Audet, H. F. Dvorak and W. C. W. Chan, *Nat. Rev. Mater.*, 2016, **1**, 16014.
- E. J. Guggenheim, S. Milani, P. J. F. R ottgermann, M. Dusinska, C. Saout, A. Salvati, J. O. R adler and I. Lynch, *NanoImpact*, 2018, **10**, 121–142.
- W. Asghar, R. El Assal, H. Shafiee, S. Pitteri, R. Paulmurugan and U. Demirci, *Mater. Today*, 2015, **18**, 539–553.
- S. Nath and G. R. Devi, *Pharmacol. Ther.*, 2016, **163**, 94–108.
- M. Millard, I. Yakavets, V. Zorin, A. Kulmukhamedova, S. Marchal and L. Bezdetnaya, *Int. J. Nanomed.*, 2017, **12**, 7993–8007.
- F. Hirschhaeuser, H. Menne, C. Dittfeld, J. West, W. Mueller-Klieser and L. A. Kunz-schughart, *J. Biotechnol.*, 2010, **148**, 3–15.
- H. L. Ma, Q. Jiang, S. Han, Y. Wu, J. C. Tomshine, D. Wang, Y. Gan, G. Zou and X. J. Liang, *Mol. Imaging*, 2012, **11**, 487–498.
- S. Huo, H. Ma, K. Huang, J. Liu, T. Wei, S. Jin, J. Zhang, S. He and X. J. Liang, *Cancer Res.*, 2013, **73**, 319–330.
- A. Virgone-Carlotta, M. Lemasson, H. C. Mertani, J. J. Diaz, S. Monnier, T. Dehoux, H. Delano -Ayari, C. Riv iere and J. P. Rieu, *PLoS One*, 2017, **12**(11), e0188100.
- B. Rodday, F. Hirschhaeuser, S. Walenta and W. Mueller-Klieser, *J. Biomol. Screening*, 2011, **16**, 1119–1124.
- J. M. Kelm, N. E. Timmins, C. J. Brown, M. Fussenegger and L. K. Nielsen, *Biotechnol. Bioeng.*, 2003, **83**, 173–180.
- Y.-C. Chen, P. N. Ingram, S. Fouladdel, S. P. McDermott, E. Azizi, M. S. Wicha and E. Yoon, *Sci. Rep.*, 2016, **6**, 27301.
- M. Akay, J. Hite, N. G. Avci, Y. Fan, Y. Akay, G. Lu and J. J. Zhu, *Sci. Rep.*, 2018, **8**, 1–9.
- R. Mukhopadhyay, *Anal. Chem.*, 2007, **79**, 3249–3253.
- B. J. van Meer, H. de Vries, K. S. A. Firth, J. van Weerd, L. G. J. Tertoolen, H. B. J. Karperien, P. Jonkheijm, C. Denning, A. P. IJzerman and C. L. Mummery, *Biochem. Biophys. Res. Commun.*, 2017, **482**, 323–328.
- M. W. Toepke and D. J. Beebe, *Lab Chip*, 2006, **6**, 1484–1486.
- D. T. Butcher, T. Alliston and V. M. Weaver, *Nat. Rev. Cancer*, 2009, **9**, 108–122.
- J. M. Lee, D. Y. Park, L. Yang, E. J. Kim, C. D. Ahrberg, K. B. Lee and B. G. Chung, *Sci. Rep.*, 2018, **8**, 1–10.
- Y. Li and E. Kumacheva, *Sci. Adv.*, 2018, **4**, 1–11.
- X. Gong, C. Lin, J. Cheng, J. Su, H. Zhao, T. Liu, X. Wen and P. Zhao, *PLoS One*, 2015, **10**, e0130348.
- J. Dahlmann, G. Kensah, H. Kempf, D. Skvorc, A. Gawol, D. A. Elliott, G. Dr ager, R. Zweigerdt, U. Martin and I. Gruh, *Biomaterials*, 2013, **34**, 2463–2471.
- D. L. Priwitaningrum, J. B. G. Blond e, A. Sridhar, J. van Baarlen, W. E. Hennink, G. Storm, S. Le Gac and J. Prakash, *J. Controlled Release*, 2016, **244**, 257–268.
- G. Fang, H. Lu, A. Law, D. Gallego-Ortega, D. Jin and G. Lin, *Lab Chip*, 2019, **19**, 4093–4103.
- X. Hu, X. Hu, S. Zhao, S. Zhao, Z. Luo, Y. Zuo, Y. Zuo, F. Wang, F. Wang, J. Zhu, J. Zhu, L. Chen, L. Chen, D. Yang, Y. Zheng, Y. Zheng, Y. Cheng, F. Zhou, Y. Yang and Y. Yang, *Lab Chip*, 2020, **20**, 2228–2236.
- V. Normand, D. L. Lootens, E. Amici, K. P. Plucknett and P. Aymard, *Biomacromolecules*, 2000, **1**, 730–738.
- T. H. Jovic, G. Kungwengwe, A. C. Mills and I. S. Whitaker, *Front. Mech. Eng.*, 2019, **5**, 19.
- A. Pluen, P. A. Netti, R. K. Jain and D. A. Berk, *Biophys. J.*, 1999, **77**, 542–552.

- 37 F. Lux, V. L. Tran, E. Thomas, S. Dufort, F. Rossetti, M. Martini, C. Truillet, T. Doussineau, G. Bort, F. Denat, F. Boschetti, G. Angelovski, A. Detappe, Y. Crémillieux, N. Mignet, B. T. Doan, B. Larrat, S. Meriaux, E. Barbier, S. Roux, P. Fries, A. Müller, M. C. Abadjian, C. Anderson, E. Canet-Soulas, P. Bouziotis, M. Barberi-Heyob, C. Frochot, C. Verry, J. Balosso, M. Evans, J. Sidi-Boumedine, M. Janier, K. Butterworth, S. McMahon, K. Prise, M. T. Aloy, D. Ardail, C. Rodriguez-Lafrasse, E. Porcel, S. Lacombe, R. Berbeco, A. Allouch, J. L. Perfettini, C. Chargari, E. Deutsch, G. Le Duc and O. Tillement, *Br. J. Radiol.*, 2019, **92**, 109320180365.
- 38 W. Rima, L. Sancey, M. T. Aloy, E. Armandy, G. B. Alcantara, T. Epicier, A. Malchère, L. Joly-Pottuz, P. Mowat, F. Lux, O. Tillement, B. Burdin, A. Rivoire, C. Boulé, I. Anselme-Bertrand, J. Pourchez, M. Cottier, S. Roux, C. Rodriguez-Lafrasse and P. Perriat, *Biomaterials*, 2013, **34**, 181–195.
- 39 C. Riviere, A. Prunet, L. Fuoco and H. Delanoë-Ayari, *Patent*, FR3079524A1, 2018, <https://patents.google.com/patent/FR3079524B1/en>.
- 40 G. Le Duc, S. Roux, A. Paruta-Tuarez, S. Dufort, E. Brauer, A. Marais, C. Truillet, L. Sancey, P. Perriat, F. Lux and O. Tillement, *Cancer Nanotechnol.*, 2014, **5**, 1–14.
- 41 C. A. Schneider, W. S. Rasband and K. W. Eliceiri, *Nat. Methods*, 2012, **9**, 671–675.
- 42 L. Le Roux, A. Volgin, D. Maxwell, K. Ishihara, J. Gelovani and D. Schellingerhout, *Mol. Imaging*, 2008, **7**, 214–221.
- 43 J. F. Dekkers, M. Alieva, L. M. Wellens, H. C. R. Ariese, P. R. Jamieson, A. M. Vonk, G. D. Amatngalim, H. Hu, K. C. Oost, H. J. G. Snippert, J. M. Beekman, E. J. Wehrens, J. E. Visvader, H. Clevers and A. C. Rios, *Nat. Protoc.*, 2019, **14**, 1756–1771.
- 44 T. Silva Santisteban, O. Rabajania, I. Kalinina, S. Robinson and M. Meier, *Lab Chip*, 2018, **18**, 153–161.
- 45 E. Nürnberg, M. Vitacolonna, J. Klicks, E. von Molitor, T. Cesetti, F. Keller, R. Bruch, T. Ertongur-Fauth, K. Riedel, P. Scholz, T. Lau, R. Schneider, J. Meier, M. Hafner and R. Rudolf, *Front. Mol. Biosci.*, 2020, **7**, 1–19.
- 46 J. L. Guerquin-Kern, T. D. Wu, C. Quintana and A. Croisy, *Biochim. Biophys. Acta*, 2005, **1724**, 228–238.
- 47 G. Slodzian, B. Daigne, F. Girard, F. Boust and F. Hillion, *Biol. Cell*, 1992, **74**, 43–50.
- 48 C. Messaoudil, T. Boudier, C. O. S. Sorzano and S. Marco, *BMC Bioinf.*, 2007, **8**, 1–9.
- 49 M. Singh, D. A. Close, S. Mukundan, P. A. Johnston and S. Sant, *Assay Drug Dev. Technol.*, 2015, **13**, 570–583.
- 50 L. B. Sims, L. T. Curtis, H. B. Frieboes and J. M. Steinbach-Rankins, *J. Nanobiotechnol.*, 2016, **14**, 1–12.
- 51 A. R. Kang, H. I. Seo, B. G. Chung and S. H. Lee, *Nanomedicine*, 2015, **11**, 1153–1161.
- 52 L. Štefančíková, E. Porcel, P. Eustache, S. Li, D. Salado, S. Marco, J. L. Guerquin-Kern, M. Réfrégiers, O. Tillement, F. Lux and S. Lacombe, *Cancer Nanotechnol.*, 2014, **5**, 1–15.
- 53 L. Sancey, F. Lux, S. Koth, S. Roux, S. Dufort, A. Bianchi, Y. Crémillieux, P. Fries, J.-L. Coll, C. Rodriguez-Lafrasse, M. Janier, M. Dutreix, M. Barberi-Heyob, F. Boschetti, F. Denat, C. Louis, E. Porcel, S. Lacombe, G. Le Duc, E. Deutsch, J.-L. Perfettini, A. Detappe, C. Verry, R. Berbeco, K. T. Butterworth, S. J. McMahon, K. M. Prise, P. Perriat and O. Tillement, *Br. J. Radiol.*, 2014, **87**, 20140134.
- 54 T. Stylianopoulos, L. L. Munn and R. K. Jain, *Trends Cancer*, 2018, **4**, 292–319.
- 55 K. Carver, X. Ming and R. L. Juliano, *Mol. Ther. – Nucleic Acids*, 2014, **3**, e153.
- 56 H. Kang, S. Mintri, A. V. Menon, H. Y. Lee, H. S. Choi and J. Kim, *Nanoscale*, 2015, **7**, 18848–18862.
- 57 K. Raza, P. Kumar, N. Kumar and R. Malik, *Pharmacokinetics and biodistribution of the nanoparticles*, Elsevier Ltd, 2017.
- 58 V. Ivošev, G. J. Sánchez, L. Stefancikova, D. A. Haidar, C. R. González Vargas, X. Yang, R. Bazzi, E. Porcel, S. Roux and S. Lacombe, *Nanotechnology*, 2020, **31**, 13.
- 59 N. D. Donahue, H. Acar and S. Wilhelm, *Adv. Drug Delivery Rev.*, 2019, **143**, 68–96.
- 60 C. A. Lyssiatis and A. C. Kimmelman, *Trends Cell Biol.*, 2017, **27**, 863–875.
- 61 S. Behzadi, V. Serpooshan, W. Tao, M. A. Hamaly, M. Y. Alkawareek, E. C. Dreaden, D. Brown, A. M. Alkilany, O. C. Farokhzad and M. Mahmoudi, *Chem. Soc. Rev.*, 2017, **46**, 4218–4244.
- 62 J. Kondo, T. Ekawa, H. Endo, K. Yamazaki, N. Tanaka, Y. Kukita, H. Okuyama, J. Okami, F. Imamura, M. Ohue, K. Kato, T. Nomura, A. Kohara, S. Mori, S. Dan and M. Inoue, *Cancer Sci.*, 2019, **110**, 345–355.
- 63 S. E. Park, A. Georgescu and D. Huh, *Science*, 2019, **364**, 960–965.
- 64 A. Ahmed, S. Goodarzi, C. Frindel, G. Recher, C. Riviere and D. Rousseau, *bioRxiv*, 2021, DOI: 10.1101/2021.01.31.428996.
- 65 A. Prunet, S. Lefort, H. Delanoë-Ayari, B. Laperrousaz, G. Simon, C. Barentin, S. Saci, F. Argoul, B. Guyot, J.-P. Rieu, S. Gobert, V. Maguer-Satta and C. Rivière, *Lab Chip*, 2020, **20**, 4016–4030.
- 66 I. F. Rizzuti, P. Mascheroni, S. Arcucci, Z. Ben-Mériem, A. Prunet, C. Barentin, C. Rivière, H. Delanoë-Ayari, H. Hatzikirou, J. Guillermet-Guibert and M. Delarue, *Phys. Rev. Lett.*, 2020, **125**, 128103.
- 67 A. Albanese, A. K. Lam, E. A. Sykes, J. V. Rocheleau and W. C. W. Chan, *Nat. Commun.*, 2013, **4**, 1–8.

4. SUPPLEMENTARY MATERIALS

Figure SI 1: Quantification of photon penetration within spheroids

In optical imaging of thick three-dimensional biological samples, light scattering due to mismatch of refractive index between cellular components limits imaging of deep layers in these samples (Yu et al., 2018). To deal with this issue and to evaluate clarification techniques on enhancement of confocal microscopy of multicellular tumour spheroids, HCT-116 spheroids were prepared via agarose microwells and fixed 72 h after cell seeding. Nuclei were then stained using Nucgreen™ -Dead 488. Two of the samples were incubated in RapiClear or 80%/20% glycerol/PBS solution overnight and the third sample was kept in PBS. All samples were then mounted in iSpacers (2x0.5 mm) with fresh clarification solutions or fresh PBS for control sample. Ten spheroids from each sample were imaged. A qualitative analysis of the images (**Fig. SI 1A**) shows that nuclei fluorescence signal is detected much deeper for clarified spheroids compared to unclarified ones. The orthogonal views of spheroids confirm this (**Fig. SI 1B**). These images were analysed using a routine prepared in Matlab to measure the average fluorescence intensity along the spheroids radius (**Fig. SI 1C**). The mean Intensity of spheroids clarified with glycerol (Green curve) shows the highest mean intensity for all regions in spheroids compared to the two other samples. While the mean intensity of RapiClear-clarified spheroids (Red curve) is lower than glycerol-clarified spheroids in all regions of the spheroids, the intensity decay is similar for both clarified solutions. The 80% glycerol solution was hence selected as the standard clarification technique for all this study.

Yu, T., Zhu, J., Li, Y., Ma, Y., Wang, J., Cheng, X., ... Zhu, D. (2018). RTF: A rapid and versatile tissue optical clearing method. *Scientific Reports*, 8(1), 1–9. <https://doi.org/10.1038/s41598-018-20306-3>

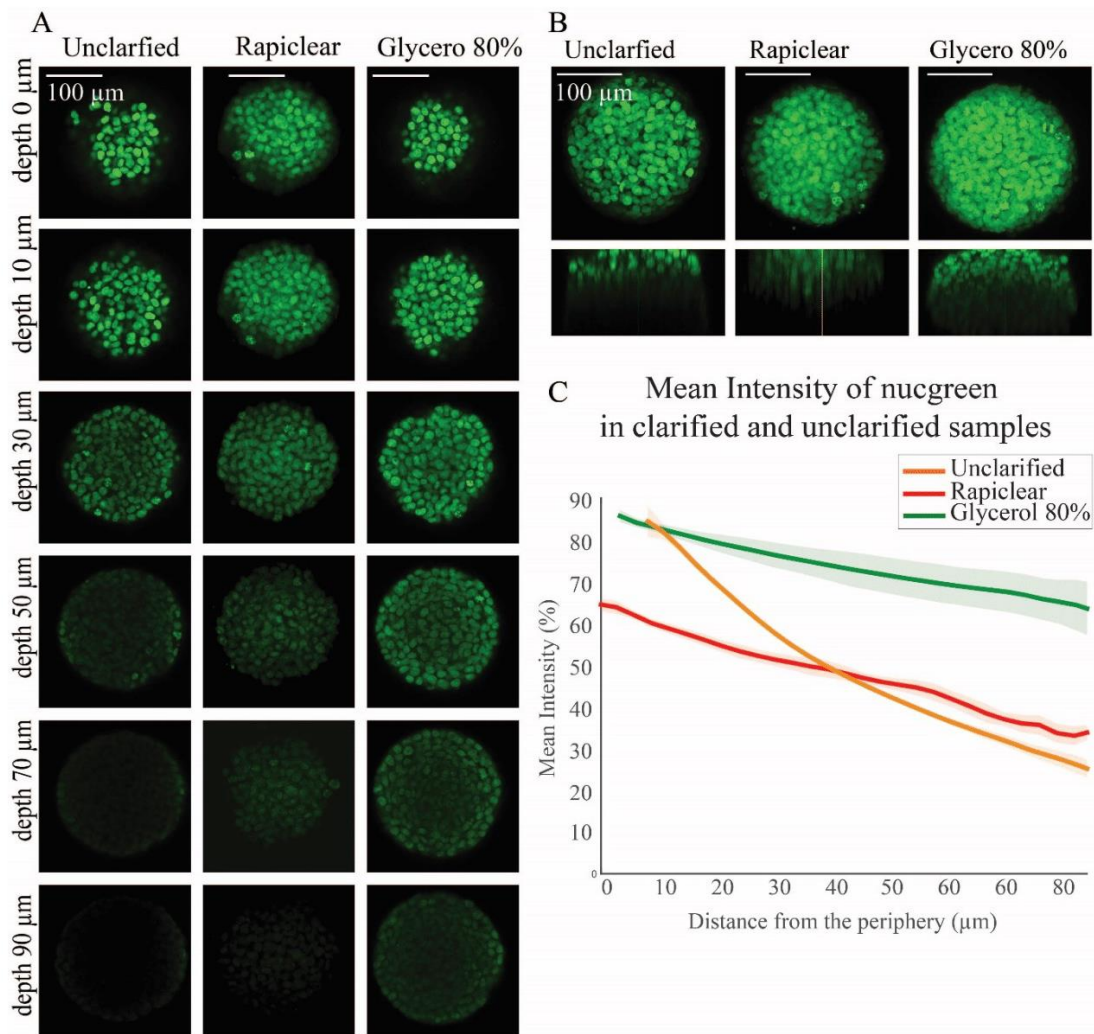


Figure SI 1. Influence of clarification technique on image acquisition and fluorescence signals

(A) Confocal fluorescence images of HCT-116 cell spheroids labelled with Nucgreen in different depth for unclarified, clarified with Rapiclear and clarified with 80%/20% glycerol/PBS respectively. **(B)** Maximal Image Projection (MIP) and xz images of clarified and unclarified spheroids. **(C)** Mean intensity of clarified (green, glycerol-clarification, red, rapiclear-clarification) and unclarified (orange curve) spheroids as a function of the distance from the periphery. Error bars represent standard errors of the Mean (N=10 spheroids for each condition).

Figure SI 2: Detailed mounting procedure for imaging

There are different possibilities to mount the microwells for optical imaging, depending if one wants to acquire fixed, live spheroids, or to follow spheroids over time using time-lapse.

1-For fixed spheroids, the easiest and quickest way is to mount the microwells between 2 coverslips, separated by a 1 mm sticky spacer (two 0.5 mm-thick iSpacer provided by SunJin Lab were used for their convenience, but other spacers could also be used, **Fig. SI2 B**).

2-For live spheroids, it is possible to transfer the microwells in optical imaging chamber (such as Ibidi® 8-well plate, **Fig. SI2 C**). We used such possibility in preliminary experiments to check that distribution of nanoparticles were not modified by fixation procedure (data not shown), as well as for the assessment of nanoparticles transport and localization after extensive washing procedure (**Fig. 4**).

3-For time-lapse follow-up, to avoid any drift during acquisition, it is necessary to directly bond the microwells to the coverslips. This is possible using APTS-functionalized coverslips (representation in **Fig. 1D**, patented process³⁹). We used such procedure for growth monitoring using time lapse microscopy (**Fig. SI 4**).

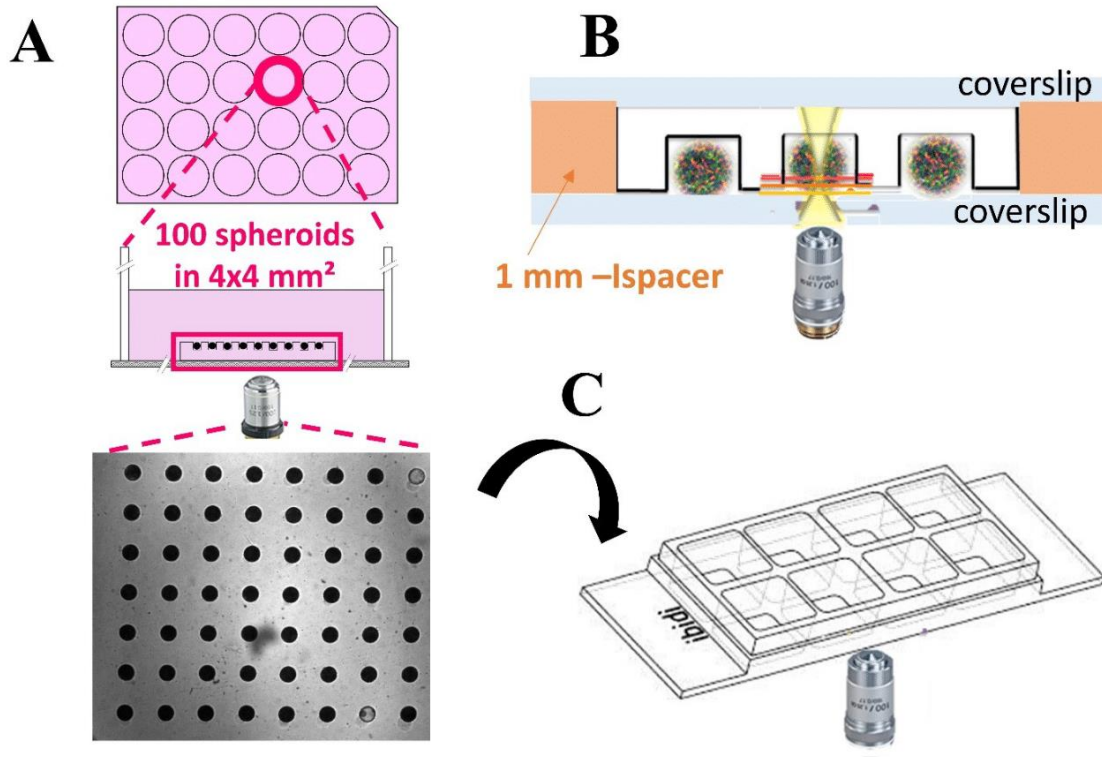


Figure SI 2. Schematic representation of the mounting procedures used for optical imaging

(A) Schematic representation of free-standing microwells, placed on each well of a multi-well plate. **(B)** Schematic representation of the mounting used for optical imaging of fixed samples. The agarose microsystems containing the fixed, immunostained and clarified spheroids are mounted between 2 coverslips using a 1 mm sticky spacer (orange-part, Ispacer from SunjinLab). **(C)** For live imaging of spheroids, it is also possible to transfer the microwells in optical imaging chamber (such as Ibidi® 8-well plates).

Figure SI 3: Quantification of the removal of FITC and AGuiX[®]-Cy5.5 nanoparticles in agarose-based microwells

To understand the ability of agarose gel in transporting molecules, the agarose-based microsystems were incubated with either FITC solution (0.05 mM in PBS), either AGuiX[®]-Cy5.5 nanoparticles (2 mM in complete culture medium). The fluorescent solution was then replaced with PBS (for FITC) or culture medium (for AGuiX[®]-Cy5.5) and the decrease in fluorescence intensity was followed by time-lapse confocal microscopy. The images of different depths of agarose-based microwells were analysed using a Matlab routine quantifying the mean intensity changes over time (**Fig. SI 3**). For FITC (**Fig.SI3 A**), after the first two hours, there is a 75±5% reduction in the initial mean intensity in the microsystem, reaching a plateau at 25±5 % depending on the depth of the focal plane. All curves were exponentially decreasing with a characteristic time of 25 min (23-27 min depending on the depth of the focal plane).

As expected, as AGuiX[®]-Cy5.5 nanoparticles ($D_H=5$ nm) are much larger than FITC ($M_w=376$ g/mol, $D_H\sim 0,25$ nm), the diffusion is one order of magnitude slower than with FITC, but still efficient in the agarose, both when culture medium is replaced by AGuiX[®]-Cy5.5 (**Fig.SI3 B**), or when AGuiX[®]-Cy5.5 is replaced by culture medium (**Fig.SI3 C**). When culture medium is replaced by AGuiX[®]-Cy5.5, the characteristic time obtained for the deepest part of the gel is of the order of 22-24 min (23,9 ±0.4 min for Z=0, 23,6 ±0.6 min for Z=80 μm and 22,4 ±1,7 min for Z=160 μm), while it already reached the maximum intensity upon imaging for the upper part (z=240 μm). When AGuiX[®]-Cy5.5 is replaced by culture medium (after 3x15 min washing, following the procedure done for all experiments), the fluorescent is decreasing with a characteristic time of the order of 1-2h, depending of the depth (69 ±5 min for Z=0, 82±6 min for Z=80 μm, 104 ±5 min for Z=160 μm and 129 ±5 min for Z=240 μm).

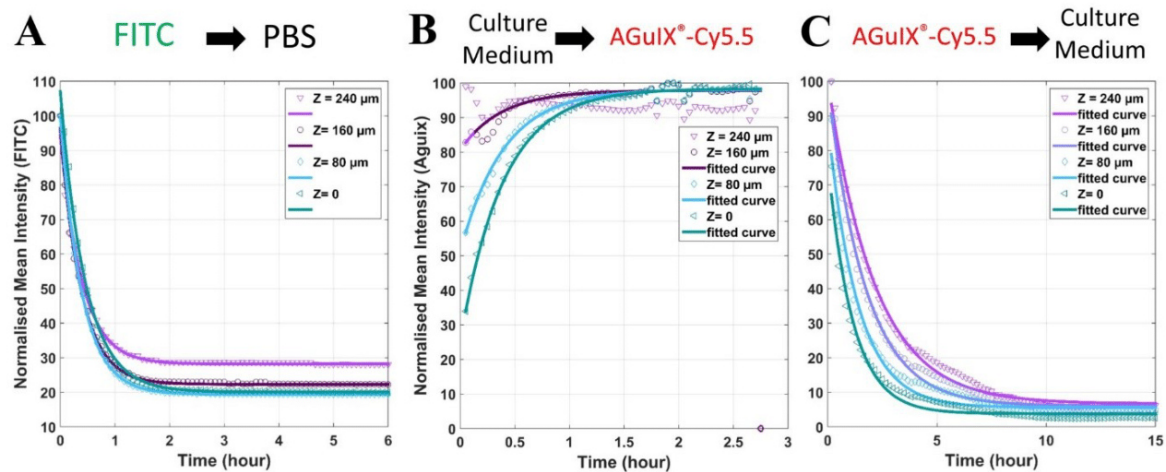


Figure SI 3.

(A) Reduction in fluorescence intensity of FITC dye in an agarose microsystem over time for different depth (from $Z=0$, corresponding to the depth closest to the objective and farthest from the solution reservoir to $Z=240\ \mu\text{m}$, farthest from the objective and closest to solution reservoir). Experimental points are plotted with different markers ($Z=0$, (pink triangles pointing down), $Z=80\ \mu\text{m}$ (blue diamonds), $Z=160\ \mu\text{m}$ (purple circles), $Z=240\ \mu\text{m}$ (green triangles pointing left)) and the corresponding exponential fit are plotted in bold lines [fitting model $a \cdot \exp(-\text{time}/T) + b$].

(B) Increase in fluorescence intensity of AGuIX[®]-Cy5.5 nanoparticles in an agarose microsystem over time for different depth (same legend than in (A)). [fitting model $a \cdot (1 - \exp(-\text{time}/T)) + c$].

(C) Reduction in fluorescence intensity of AGuIX[®]-Cy5.5 nanoparticles in an agarose microsystem over time for different depth (same legend than in (A)). [fitting model $a \cdot \exp(-\text{time}/T) + b$].

Figure SI 4. Time-lapse follow-up of spheroid growth

To understand the influence of AGuIX[®]-Cy5.5 nanoparticles on the cell proliferation and growth rate of HCT-116 cell spheroids, cells were seeded in agarose-based microwells using APTS-functionalised coverslips. This procedure enables live imaging with no drift of the microwells over-time. After 48 h, the HCT-116 spheroids were exposed to AGuIX[®]-Cy5.5 nanoparticles with three different concentrations (0.8, 1.5 and 2 mM). Control samples with no AGuIX[®]-Cy5.5 nanoparticles were also monitored in parallel. The growth of spheroids was followed by time-lapse optical microscopy during three days of incubation with AGuIX[®]-Cy5.5 nanoparticles (time interval between each image acquisition = 4 h). These images were manually segmented using a dedicated routine in Matlab. Then, from the projected area, an equivalent diameter was computed, and making the assumption of spherical shape, the equivalent volume of each spheroids was calculated. Spheroids growth is followed by representing the relative evolution of the volume over time (Volume normalised by the initial volume [at day 2]).

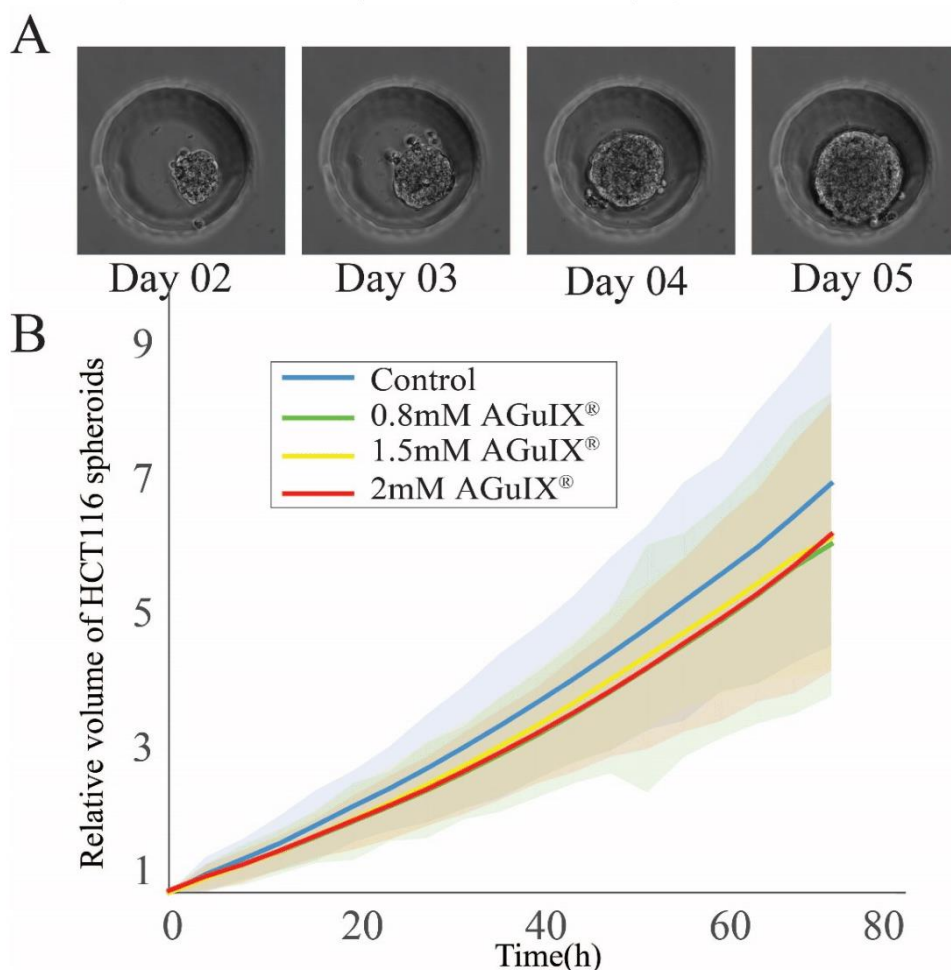


Figure SI 4. Follow-up of spheroids growth via optical time-lapse microscopy.

(A) Representative images of daily growth of control HCT-116 spheroids from day 2 to day 5. The well is 200 μm in diameter. **(B)** Evolution of the relative volume of spheroids as a function of time for control sample and in the presence of three different concentrations of AGuIX[®]-Cy5.5 nanoparticles. Bold lines represent the mean values, and light area represents the standard

deviation for each condition (control –blue- [N=102 spheroids], 0.8mM –green-[N=89 spheroids], 1.5mM –yellow-[N=88 spheroids], 2mM –red-[N=102 spheroids]). Three independent experiments for each condition.

Figure SI 5. Characterization of spheroids size distribution from Day 2 to Day 4 after cell seeding

One advantage of using agarose-based microwells to prepare multicellular tumour spheroids is the homogeneity of spheroids size. To show the homogeneity of spheroids, the equivalent diameter for each spheroid was calculated during the growth follow-up (**Fig. SI 4**). From this, the distribution of spheroids diameter in day 2, day 3 and day 4 for control conditions were plotted using the UnivarScatter matlab function developed by Manuel Lera Ramírez (Copyright (c) 2015).

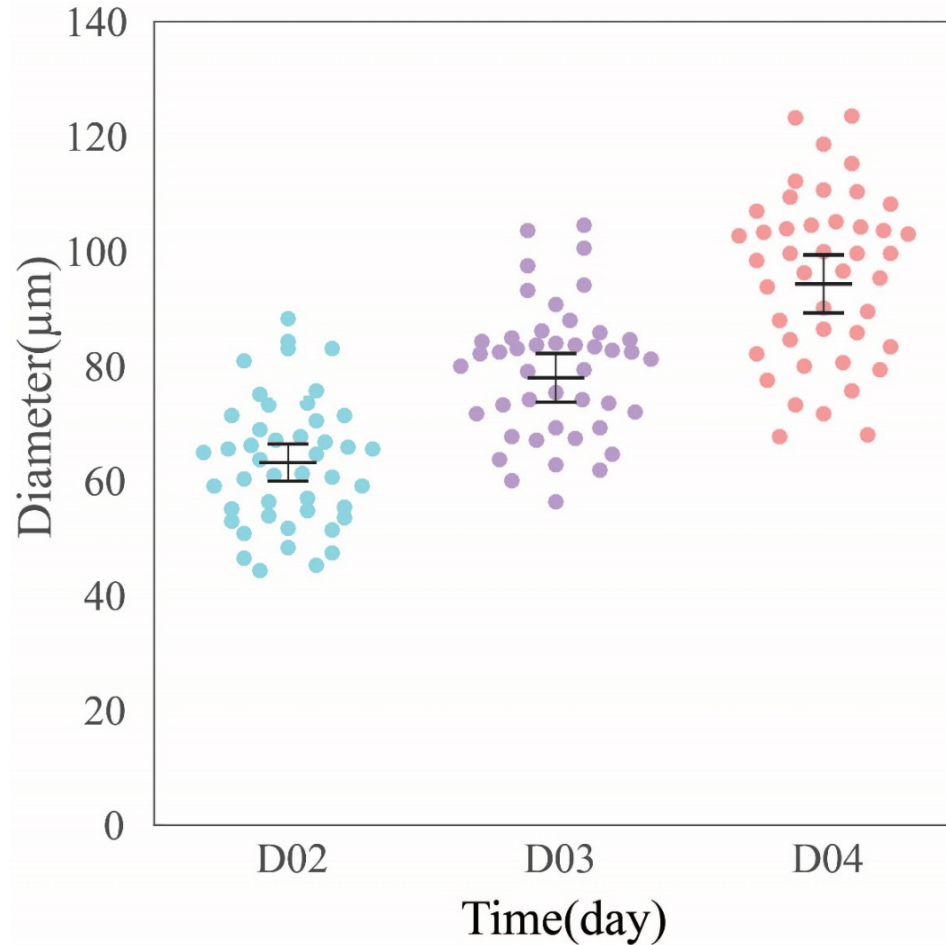


Figure SI 5.

Distribution of HCT-116 multicellular tumour spheroids at day two (blue circles), day three (purple circle) and day four (orange circles) after cell seeding in the agarose-based microwells. Mean values and 95 % Standard Error of the Mean are represented.

Figure SI 6. Importance of statistics

Due to cell heterogeneity, large statistical variances are expected, even if our process enables to generate very reproducible spheroids in terms of size. The variance on the Mean Intensity of the fluorescence signal of AGuIX[®]-Cy5.5 nanoparticles is analysed in **Fig.SI 6**, for different distance from the periphery.

The standard deviation of the normalized Intensity of AGuIX[®]-Cy5.5 obtained, is calculated as a function of the number (N) of spheroids, with a random sampling of N spheroids over the 121 spheroids acquired for this experimental condition (24h incubation with 2mM AGuIX[®]-Cy5.5). The random sampling is repeated 10 times to simulate 10 different experiments, and the mean of the obtained SD computed. The obtained SD first increases, until reaching a plateau around N=20-40 spheroids (**Fig. SI6, Inset**). The initial rising may be attributed to the heterogeneity among spheroids.

The plateau of the SD is increasing with the distance from the periphery (with a plateau at ~5% for 30 and 50 μm from the periphery, and up to ~10% for 80 μm from the periphery).

Once the plateau is reached, the standard error of the mean (SEM) and the relative standard errors ($RSE=SEM/mean$) on the normalized Intensity are therefore decreasing with N as $N^{-1/2}$ (**Fig. SI 6**). To get a RSE below 2%, N=20-25 spheroids are necessary for an analysis up to 60 μm from the periphery. For deep layers, a larger number of spheroids are needed to reach such RSE (N=70 spheroids for 80 μm from the periphery). Hence a minimum of N=30 spheroids is recommended to get reliable results at an imaging depth corresponding to the first quarter of the spheroids. This number rises up to N=70 spheroids for an accurate analysis close to the equatorial plane.

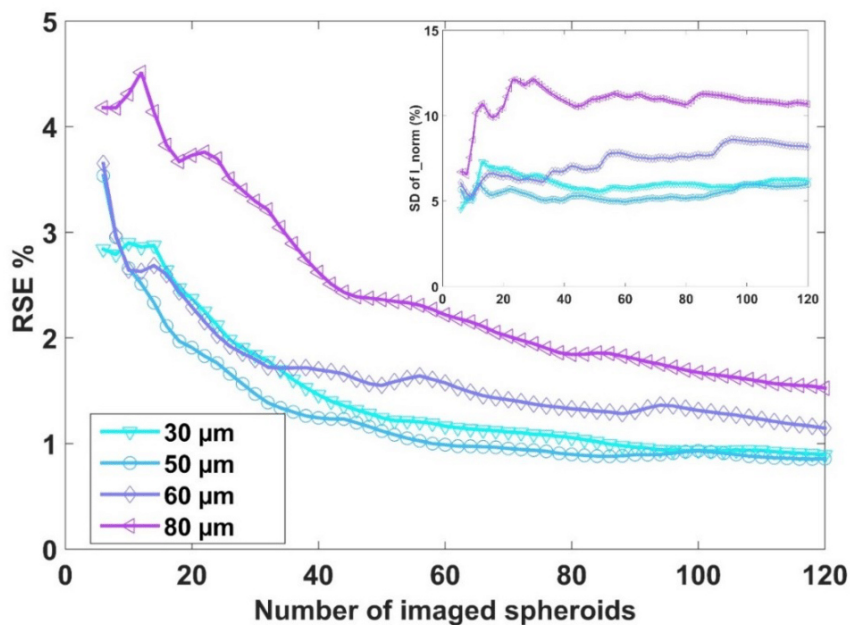


Figure SI 6. Error analysis due to the number of spheroids analysed.

Relative Standard Error ($RSE=SEM/mean$) as a function of the number of spheroids for different distance from the periphery (30 μm (cyan, triangles pointing down), 50 μm (light blue, circles), 60 μm (intense blue, diamonds) and 80 μm (purple, triangles pointing left)). **Inset:** Standard Deviation (SD) of the normalised Intensity I_{norm} as a function of the number of spheroids, for the same distance from the periphery.

Figure SI 7. Control experiments using Ultra-Low Adhesion multi-well plate

The goal of this experiment was to compare the distribution of AGuIX[®]-Cy5.5 nanoparticles in HCT-116 spheroids prepared in a traditional ultra-low adhesion 96-well plate with spheroids made in agarose microwells. HCT-116 cells were seeded at a density of 10 cells/well in a 96-well plate (200 µl culture medium per well), and spheroids were formed through self-assembly aggregation. During culture, the plate was on the agitator. Spheroids were exposed to 2 mM AGuIX[®]-Cy5.5 nanoparticles at day 3. To avoid losing spheroids, half of the medium was withdrawn and 100 µl of AGuIX[®]-Cy5.5 nanoparticles at a concentration of 4mM were added in each well to have a final concentration of 2mM. After 24 h, spheroids were rinsed with fresh medium (3X, 15 min), fixed with PFA 4%, permeabilized with PBS/0.1% Triton-X, and blocked with PBS/2% BSA/0.1% Triton-X. The spheroids were then labelled with nucgreen™ at a dilution of 1 drop/ 2 ml for overnight at room temperature before being rinsed with PBS (3X, 5 min).

Spheroids could not be imaged in a standard 96-well plate using confocal microscopy; thus they were transferred to an ibidi 96-well plate and imaged.

The same Matlab routine that was used to analyse images of spheroids in microwells was used to analyse these images. Despite the fact that the number of imaged spheroids in this experiment is considerably lower than spheroids in microwells which is due to the limitations of different steps of experiments using a standard 96-well plate, the analysed results show that the distribution and amount of uptaken nanoparticles are similar to spheroids in microwells. This finding supports the permeability of agarose gels for AGuIX[®]-Cy5.5 nanoparticles and validates the usage of such microsystems for spheroids generation and high-throughput drug screening in a more practicable and reproducible manner.

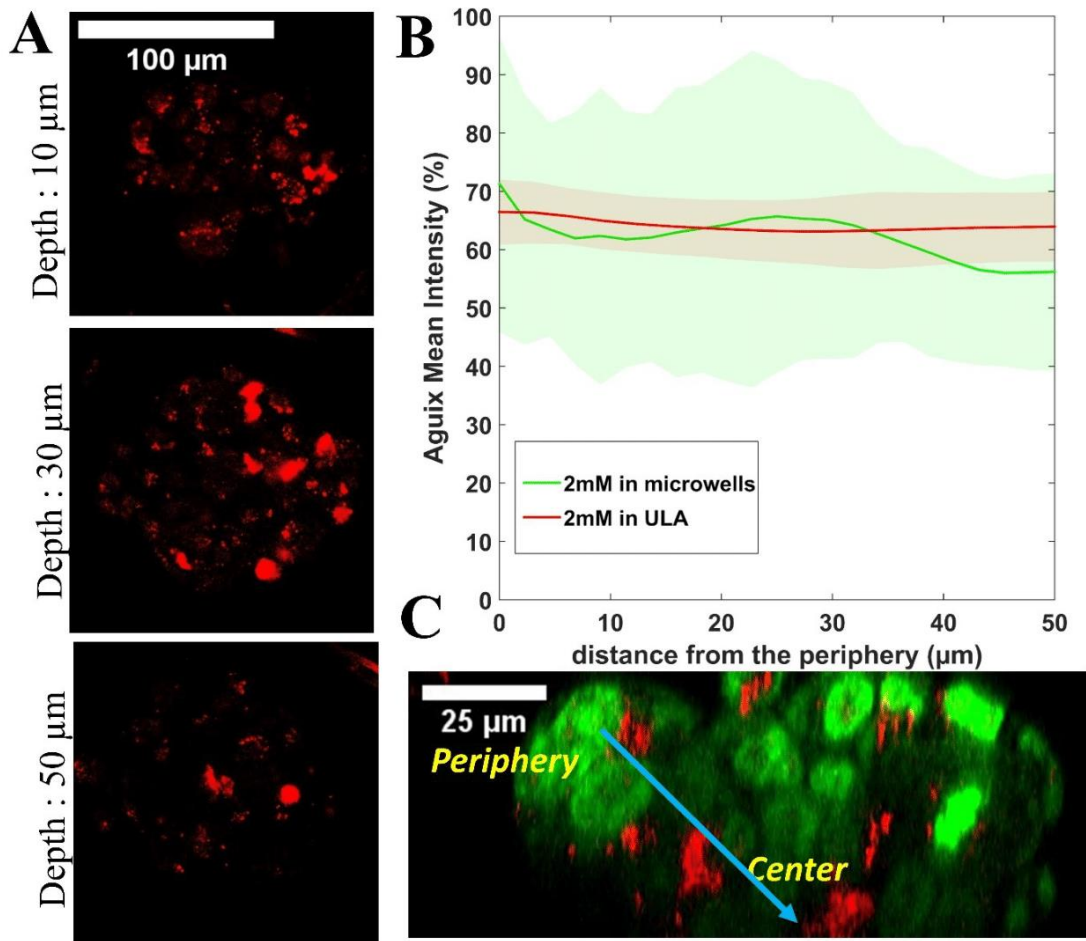


Figure SI 7. Control experiments using Ultra-Low Adhesion (ULA) multi-well plate

(A) Representative confocal fluorescence images of HCT-116 spheroids grown in Ultra-Low-Adhesion multi-well plates for 4 days, then incubated with 2 mM concentration of AGuIX[®]-Cy5.5 for 24 h for three different depths (10, 30 and 50 μm). (B) Mean intensity of AGuIX[®]-Cy 5.5 after 24h incubation with 2 mM AGuIX[®]-Cy5.5 as a function of the distance from the periphery in our microsystems (red, N=121, three independent experiment), and in ULA multi-well plates (green, N=10, one experiment). Standard deviations are shown in light colors. (C) Orthogonal view of the spheroid in (A) (green=nuclei, red = AGuIX[®]-Cy5.5).

Figure SI 8. HCT-116 cell incubated in 2D with nanoparticles and spheroid formation afterwards

To make a comparison between cellular uptake of AGuIX[®]-Cy5.5 nanoparticles in monolayer cells and multicellular tumour spheroids, two parallel experiments have been done.

In the first experiment, HCT-116 cells were seeded in agarose-based microwells (**Fig. SI 8A A, Step I**) and after 48 h were exposed to AGuIX[®]-Cy5.5 nanoparticles for 24h (**Fig. SI 8A, Step II**) followed by fixation (**Fig. SI 8A, Step III**).

In the other experiment HCT-116 monolayer cells that were first exposed to AGuIX[®]-Cy5.5 nanoparticles for 24 h (**Fig. SI 8B, Step I**), and then seeded in agarose-based microwells to allow spheroid formation (**Fig. SI 8B, Step II**). After 72h, these spheroids were fixed (**Fig. SI 8B, Step III**).

Spheroids from both experiments were clarified with glycerol 80% (**Fig. SI 8, Step III**) and imaged via confocal microscopy. The confocal images of these two experiments and orthogonal view of spheroids demonstrate that when spheroids are incubated with nanoparticles, clusters could be observed evenly in extracellular and intracellular regions of spheroids and nanoparticles clusters are more in peripheral region than in the centre (**Fig. SI 8A**). When spheroids are made from already AGuIX[®]-Cy5.5 labelled cells, only sparse clusters, with a scattered distribution are observed in spheroids (**Fig. SI 8B**).

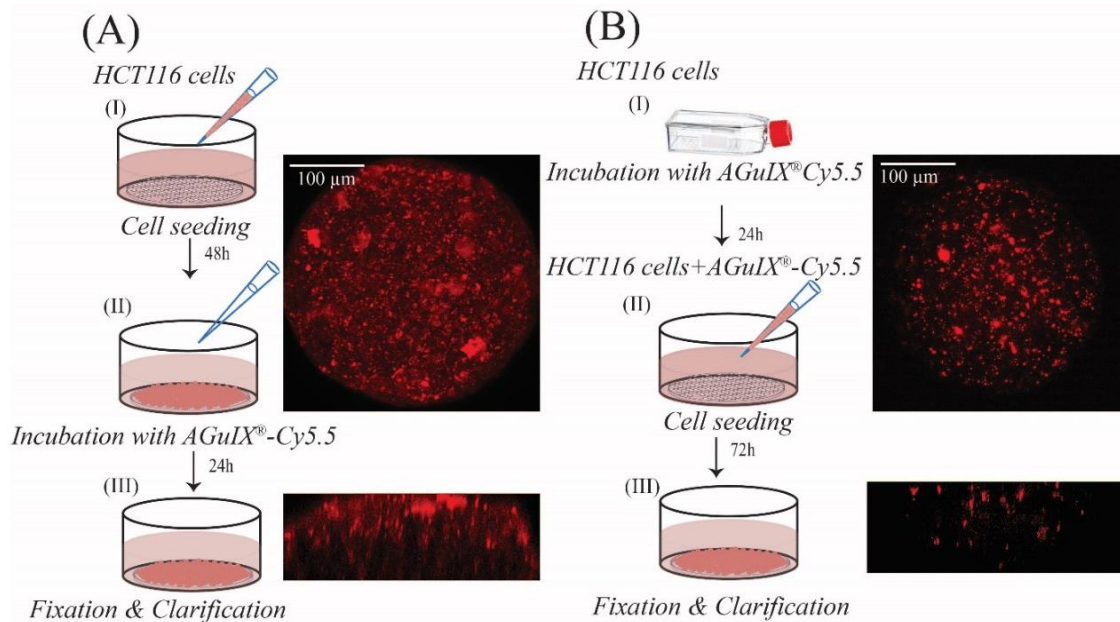


Figure SI. 8. Difference in distribution of AGuIX[®]-Cy 5.5 nanoparticles in HCT116 multicellular tumour spheroids incubated in 2D and 3D cell culture.

(A) Spheroids were prepared with agarose-based microwells (**Step I**). After 48 h, they were exposed to 2mM AGuIX[®]-Cy5.5 nanoparticles for 24h (**step II**) and were fixed, clarified (**Step III**) and imaged with confocal microscopy. (B) Monolayer HCT116 cells were first incubated with 2mM AGuIX[®] nanoparticles for 24h (**Step I**) and then HCT116 spheroids were prepared with these cells (**step II**). Spheroids were fixed, clarified (**Step III**) and imaged with confocal microscopy.

Figure SI 9. Nanoscale Secondary Ion Mass Spectrometry control analysis

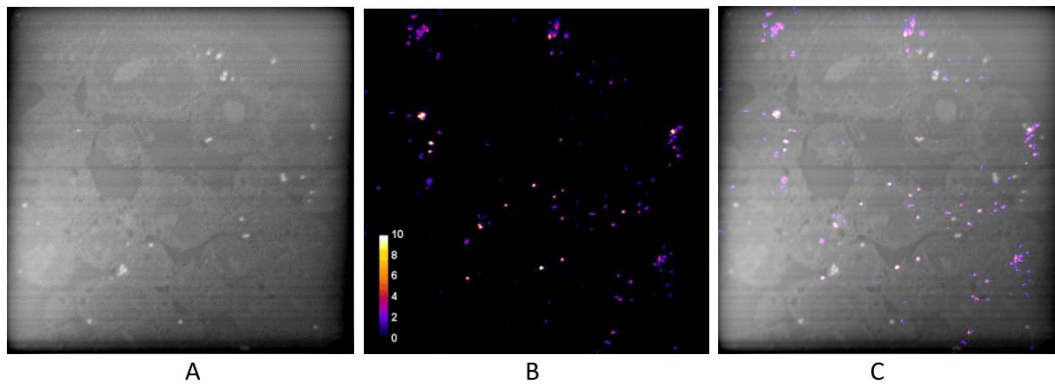


Figure SI. 9.

(A) NanoSIMS image of $^{12}\text{C}^-$ of the same area as in **Figure 5** provides the proof of the entirety of the section. The slight contrast is due to the compositional variation of different cells compartments and the surrounding resin (the actual contrast is much lower). A few spots with unusually high $^{12}\text{C}^-$ emission are probably location of vacuoles. **(B)** Recalled of the distribution of AGuIX®-Cy5.5 nanoparticles. **(C)** Merged image of $^{28}\text{Si}^-$ and $^{12}\text{C}^-$. Image field: 60 μm .

Figure SI 10. Localization of AGuIX-Cy5.5-nanoparticles after an extensive washing procedure

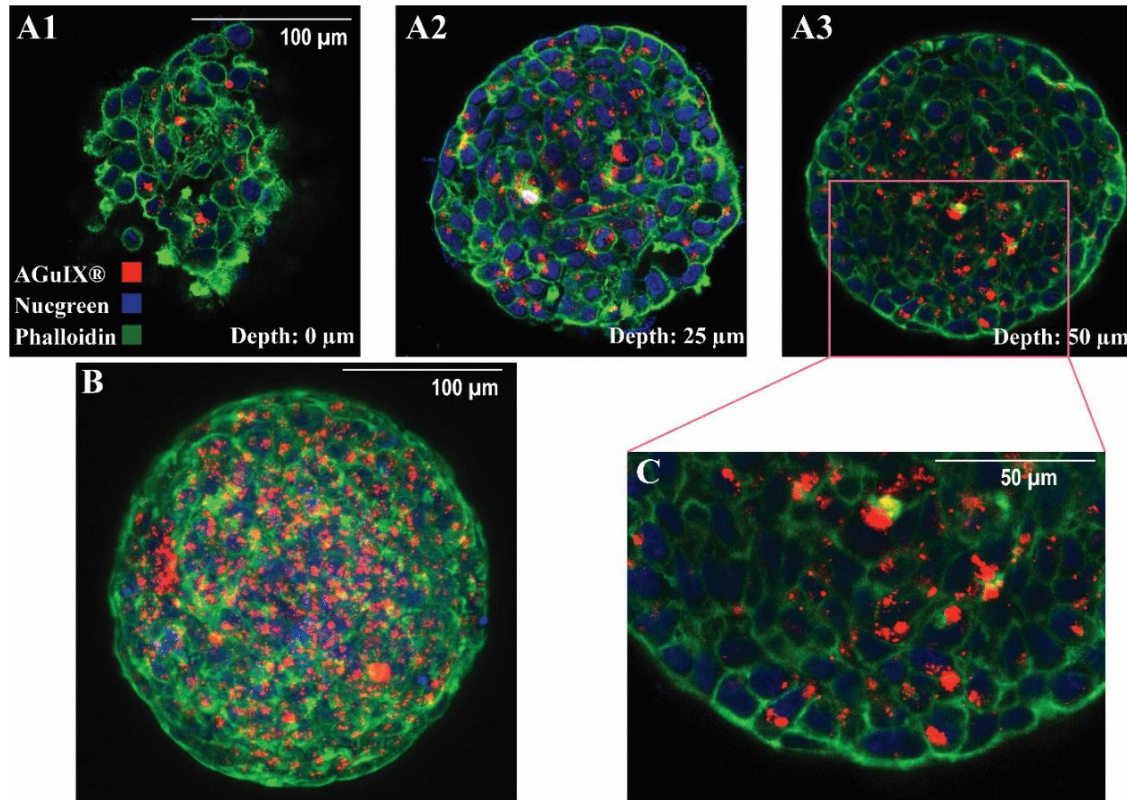


Figure SI. 10. Localization of Aguix-Cy5.5-nanoparticles after an extensive washing procedure within HCT-116 spheroids

Confocal fluorescence images of HCT-116 spheroids incubated with AGuIX®-Cy5.5 nanoparticles for 72 h with 2 mM AGuIX®-Cy5.5 solution, and washed according to the procedure mentioned in Figure 4, then fixed and immunostained with antibodies to find colocalization of nanoparticles in spheroids. For all images, red, blue and green channels are staining AGuIX®-Cy5.5, nuclei and phalloidin (Actins) respectively.

(A1-A3) Representative images of phalloidin immunostaining merged with AGuIX®-Cy5.5 and Nucgreen layers obtained at various depths (**A1-0 μm**, **A2-25 μm**, **A3-50 μm**). **(B)** Maximal Image Projection (MIP) of confocal fluorescence image of spheroid in (A1-A3). **(C)** Zoomed-in portion of merged image at a depth of 50 μm (square in A3).

5. Study the penetration of fluorescence polymer probes

In the published article, we demonstrated how the developed 3D *in vitro* model can be used to screen nanoparticles and study the penetration of NPs into spheroids, as well as their transport and localization within spheroids. However, as discussed in Chapter 1, the physio-chemical properties of nanoparticles can alter their fate in biological environments. We used this 3D *in vitro* model to test the behavior of fluorescent polymer probes that are very different from AGuIX® nanoparticles in HCT-116 spheroids. This part of the research was done in the framework of the M2 internship project of Daiva Vozgirdaite, which I co-supervised with Dr. Charlotte Rivière and Dr. Arnaud Favier in the Laboratory of Polymer Materials Engineering at IMP.

The goal of the internship was to evaluate fluorescent polymer probes behaviour in 3D *in vitro* spheroid models (MCTS) created using the same protocol described earlier in this chapter.

These biocompatible conjugates can be used for the vectorization of diagnostic and therapeutic entities (286). Controlled radical polymerisation, more specifically reversible addition-fragmentation chain transfer (RAFT) polymerisation, provide direct control over the chemical composition of polymers and their functionality, as well as the high control over molecular weight and narrow distribution (286,287). Two different types of systems prepared thanks to RAFT controlled radical polymerization: chains and NPs were used in this study (**Fig.2.8**).

- a) Polymer chains, (PCs);
- b) Polymer nanoparticles (PNPs).

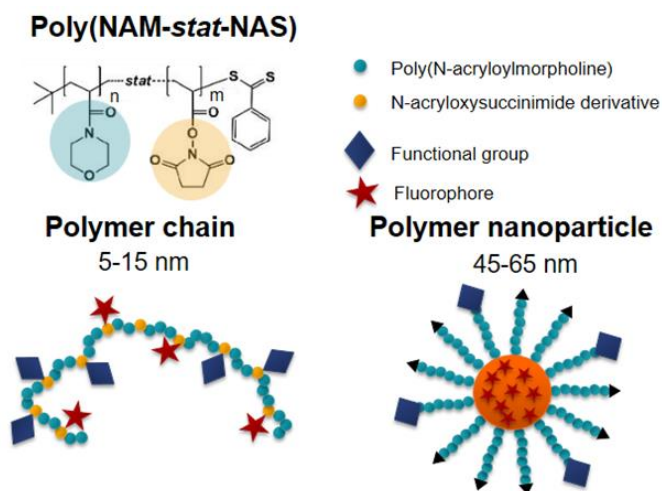


Figure 2.8. Schematic representation of poly(NAM-*stat*-NAS) and its corresponding structure in polymer chain and nanoparticle form.

These polymers exhibit fluorescent properties in the near infrared range, Cyanine 5.5 fluorophores to have low signal caused by autofluorescence from biological components, same fluorophores used for AGuiX® nanoparticles.

Polymer nanoparticles (PNPs) are 50-60 nm spherical nanoprobes, while polymer chains (PCs) are polymer chains with the same 50-60 kDa backbone that forms dynamic coils with 5-15 nm in size in aqueous solutions (By DLS analysis), more or less expanded depending on their chemical structure and on their environment (**Fig. 2.8**).

Some of the results associated with polymer chains (PCs) achieved in this project will be presented below.

HCT-116 spheroids were incubated with polymer chains (PCs) with three different overall charge, neutrally charged (PC_(0)), negatively charged (PC_(-)) and positively charged (PC_(+)) and were imaged via confocal fluorescence microscopy. The clarification solutions used for clearing spheroids incubated with PCs seemed to cause loss of polymer fluorescence signal as well as altering their overall distribution, thus clarification was not included in the final experimental setup of this project. Qualitatively, neutrally charged PC_(0) exhibited higher MCTS penetration at various depths than negatively ones (**Fig2.9 A**). Using the same Matlab routine used for AGuiX®-Cy5.5 penetration, it was possible to quantify the distribution of these probes in the first 40 µm : negatively charged PCs displayed relatively low fluorescence intensity in confocal images, and fluorescence signals was distributed homogeneously across MCTS. Positively charged PCs demonstrated different results; the fluorescence signals were significantly higher than the other PCs, suggesting strong cell internalisation of PCs with positive charge in outer layer cells in spheroids, however, positively charged PCs exhibited drastic decrease in normalised mean fluorescence intensity (**Fig.2.9 B**).

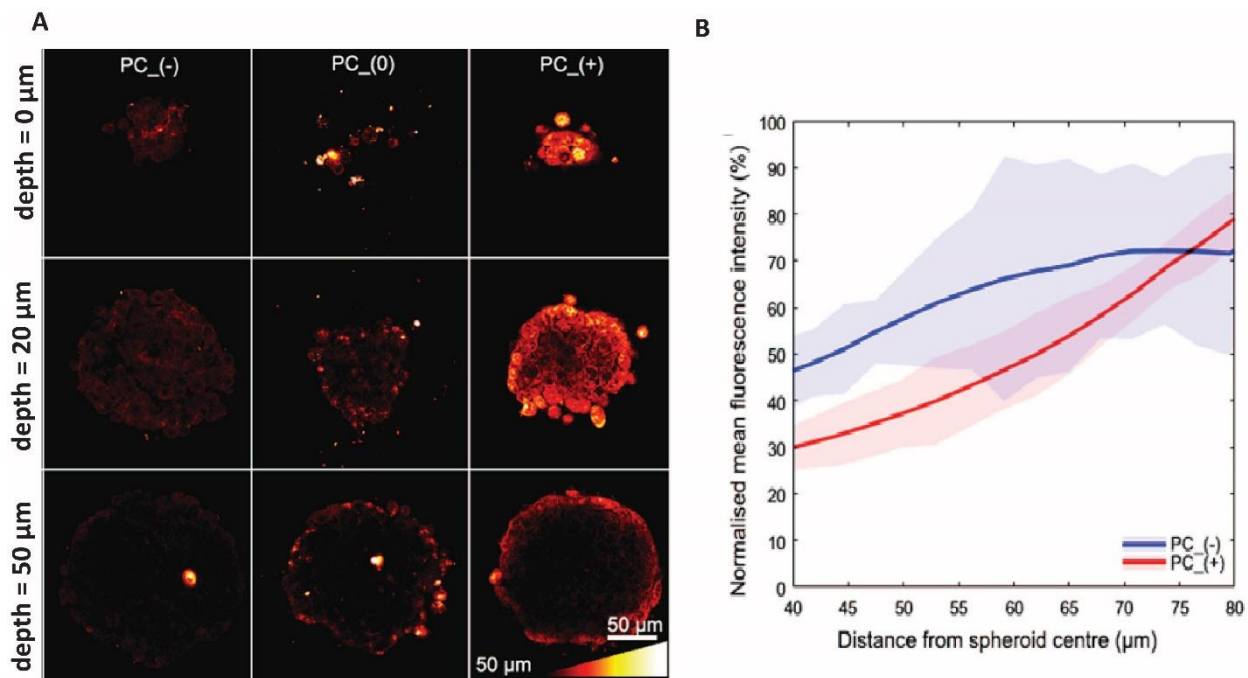


Figure 2.9. Confocal images of PCs diffusion into HCT-116 MCTS exposed to PCs for 24 hours, at various depths, for PC_(-), PC_(0), PC_(+) (A). Normalized mean fluorescence signal plotted as a function of distance from the **spheroid centre** for various PCs.

To study the localization of PCs within spheroids, actin filaments, lysosomes, and mitochondria were labeled with appropriate antibodies (using the same protocol used in the article for AGuIX®-Cy5.5), and cell nuclei were labeled with nucgreen™-488. To visualize these subcellular compartments and PCs, samples were imaged with confocal fluorescence microscopy, and localizations of PCs were observed in overlay images. Localization of neutral and positively charged PCs were mainly observed within cells (**Fig. 2.10**), which was consistent with previous experiments that cellular uptake of neutral and positively charged PCs was higher than negatively charged ones.

Colocalization with lysosomes and mitochondria (**Fig. 2.10 B,C**) demonstrated that neutral polymer chain probes were found in both lysosomes and mitochondria with a similar fluorescence intensity. Slight PC_(-) presence was observed in lysosomes, but no polymer was found to be in mitochondria. This suggests that small parts of these probes were internalized by endocytosis.

Some positively charged PC_(+) were found to be in mitochondria, however the majority of the fluorescent signal corresponded to other intracellular areas. The route of cellular internalization of positively charged polymer chains PC_(+) is most likely caused by the previously mentioned electrostatic attraction between the cell membrane and the polymer probe, which leads to their distribution in the cytosol, as no probes were found in lysosomes, thus limiting the possibility of

endocytosis as the main internalization route. **Table 2.2** summarized and compared the behavior of polymer chains with different charges.

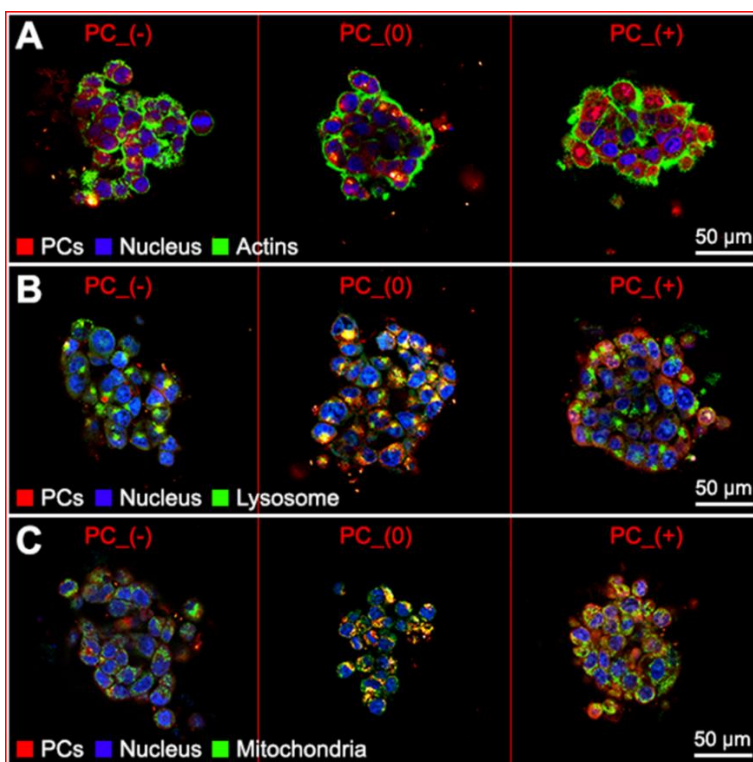


Figure 2.10. Confocal images of PCs localization inside HCT-116 spheroids at 10 μm depth, Blue channels are cell nuclei stained with nucgreen™-488 and red channels shows PCs. (A) green channel is actin filaments stained with phalloidin-546. (B) Green channel shows lysosomes, where yellow color represents colocalization of PCs with lysosomes. (C) Green channel displays mitochondria inside HCT 116, where yellow color represents colocalization with mitochondria.

Table 2.2. Comparison of polymer probe behaviour inside HCT 116 MCTS

	PC_P(0)	PC_P(-)	PC_P(+)
Accumulation in MCTS	++	+	+++
Diffusion across MCTS	+	++	-
In ECM	+	+	+
Inside cell	+++	+	++++
Inside lysosome	++	+	-
Inside mitochondria	++	-	+

This developed *in vitro* model has been shown to be applicable for other types of nanoparticles, such as the polymer chains described above, to study the effect of their physicochemical

properties on their behavior in biological environments in a relatively simple and rapid assay that is more biologically relevant than classical monolayer assays.

6. Study of the effect of nanoparticles on cell proliferation in multicellular tumor spheroids

As discussed in chapter 1, a gradient of nutrients, oxygen, and essential molecules produces a gradient in cell proliferation in both natural tumors and cell spheroids as a laboratory model. As a result, in spheroids with a diameter 200 μm only cells in the peripheral region of these 3D biological structures are proliferative.

The study of the impact of AGuIX[®]-Cy5.5 nanoparticles on cell proliferation has already been discussed in this chapter (**Fig. SI 4** in supplementary materials of the article), using time-lapse microscopy to track the growth of spheroids. Using Click-iT[®] EdU is a more precise method for studying proliferation and finding proliferative cells in spheroids of various sizes, as well as exploring the effect of various treatments such as nanoparticles, chemotherapeutic drugs, and irradiation on cell proliferation in this 3D *in vitro* model.

The Click-iT[®] EdU Imaging Kits (Invitrogen/Molecular Probes) will detect cells in the active DNA synthesis process. To incorporate DNA during replication in cells entering S-phase of replication, spheroids must be incubated with EdU (5-ethynyl-2-deoxyuridine) incorporation for 24 hours, the labelling spheroids with Click-iT[®] reaction cocktail were performed according to the protocol suggested by the manufacturer.

Here, HCT-116 spheroids were incubated with different concentrations of AGuIX[®]- Cy5.5 nanoparticles and at the same time with EDU for 24 hours, followed by fixation and labelling with Click-iT[®] cocktail for detection of EDU in proliferative cells. The spheroids then were labelled nucgreen[™]-488 to stain all cell nucleus.

To quantify the acquired images, in the radial direction, in addition to previous routine used for segmentation of spheroids labelled with nucgreen[™], I developed a routine in Matlab to calculate Pearson's Correlation Coefficient in radial direction.

The overlay images of nucgreen and EDU channels in different acquisition depths are shown in **Fig. 2.11 A**. The graph of Pearson's Correlation Coefficient as a function of distance from the periphery (**Fig. 2.11 B**) shows that the proliferative cell rings are comparable with and without AGuIX[®], which is consistent with previous findings with time-lapse growth follow up (**Fig. SI 4**).

In addition, in a live and dead assay using Calcein and propidium iodide (PI), AGuIX[®]- Cy5.5 nanoparticles did not show any toxicity in HCT-116 spheroids in 72 hours incubation as, qualitatively, the fluorescence images do not show any change in the number of dead cells for samples exposed to nanoparticles compared control samples (**Fig. 2.11 C**)

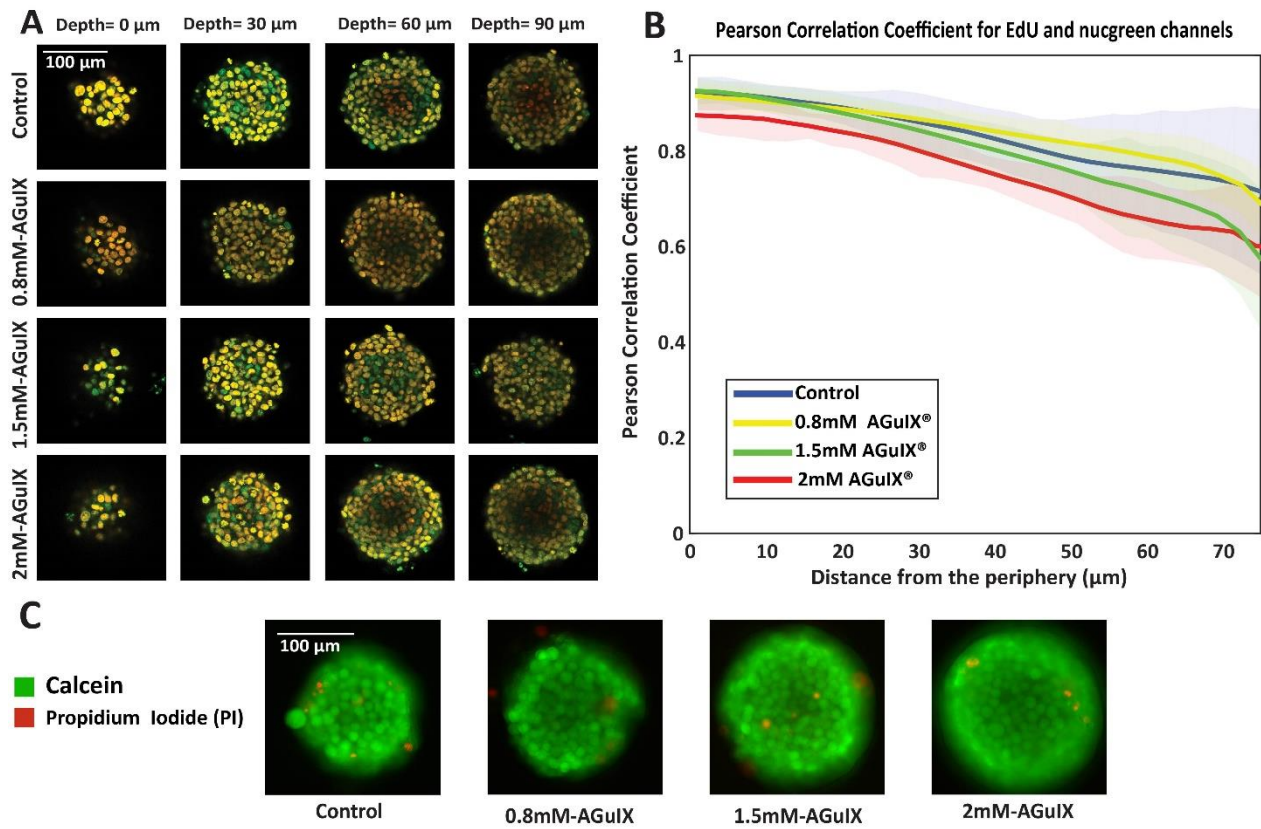


Figure 2.11. (A) Overlaid images acquired Confocal fluorescence microscopy of cell nucleus in HCT-116 spheroids incubated with different concentrations of AGuIX[®]- Cy5.5 nanoparticles for 24 hours, where green channel shows nucleus stained with nucgreen[™] dead 488 and red channel show nucleus of proliferative cells labelled with Click-iT[®]-EDU 555, Yellow color displays superposition of these channels indicating proliferative cells in spheroids. (B) Pearson's correlation coefficient for EDU and nucgreen channel in radial direction as a function of distance from the periphery. (C) Epifluorescence images of HCT-116 spheroids after 72 hours exposure to different concentrations of AGuIX[®]- Cy5.5 nanoparticles, where green is Calcein labelled live cells and red is PI labelled dead cells.

7. Conclusion and perspectives

The 3D *in vitro* models based on multicellular tumor spheroids must be capable of producing spheroids and maintaining them in culture for several days, they must be compatible with the various characterization techniques for nanotherapeutics screening, such as classical biological assays, optical microscopy techniques, and the other techniques.

In the first part of my PhD, microsystem with a specific design containing 130 microwells with a diameter of 200 μm have been prepared with agarose gel for spheroids generation. The colorectal

cancer cell line, HCT-116 cells, which are capable of forming coherent spheroids, were used as a cellular model, and radiosensitizing AGuIX[®]- Cy5.5 nanoparticles used as a model of nanoparticles. These nanoparticles were introduced to HCT-116 spheroids to explore their penetration, distribution, kinetics of penetration, and localization in multicellular tumor spheroids. For characterization of cell-nanoparticle interactions, optical microscopy techniques, primarily confocal fluorescence microscopy and, to a lesser extent, time-lapse phase contrast microscopy, were used and images were then analyzed in Matlab using dedicated routines. The ICP-MS technique was also used to quantify cellular uptake of these nanoparticles based on gadolinium concentration. NanoSIMS as well was used for the sub-200nm localization of nanoparticles, in complement to confocal microscopy.

The experimental setups and results validated this 3D *in vitro* model for nanotherapeutics screening, emphasizing the utility and importance of using this 3D *in vitro* model over conventional 2D assays. The next step was to investigate the therapeutic efficacy of AGuIX[®]- Cy5.5 nanoparticles as well as the cellular response to radiotherapy in HCT-116 spheroids made in agarose based microwells.

The potentials of the 3D *in vitro* model containing Spheroids in microwells for screening the behavior of polymer chains and nanoparticles in 3D cellular structures using optical microscopy were shown.

The experiments that investigated the effect of nanoparticles on cell proliferation (**Fig. SI 4** in supplementary materials of the article and **Fig. 2.11**) demonstrated the possibility of studying cellular response to treatment using optical microscopy; thus, the following chapter focuses on the cellular response to radiotherapy in the presence and absence of AGuIX[®]- Cy5.5 nanoparticles using classical clonogenic survival assays and optical microscopy techniques.

Chapter 3. Evaluation of radiosensitization effect of AGuIX[®] nanoparticles using multicellular tumor spheroids

Contents

Chapter 3. Evaluation of radiosensitization effect of AGuIX® nanoparticles using multicellular tumor spheroids	95
1. INTRODUCTION	97
1.1. Effect of spheroid size on cell proliferation.....	97
1.2. The workflow of assessment of therapeutic efficacy of AGuIX® nanoparticles in radiotherapy using 3D in vitro model	99
2. ABSTRACT	101
3. CORPUS.....	102
Introduction.....	102
Materials and Methods	104
Results & Discussion.....	109
Conclusion	125
4. Supplementary Materials	126
5. Outlooks of this work	128

1. INTRODUCTION

Experiments aimed at validating the developed 3D in vitro model for nanotherapeutics screening were described in the previous chapter. The results demonstrated that this 3D in vitro model containing spheroids in agarose microwells could indeed investigate various aspects of cell-nanoparticle interactions with high throughput in a more relevant in vitro model than monolayer cell culture.

Following these experiments, which yielded promising results, it was time to use this 3D in vitro model for investigating the therapeutic efficacy of nanotherapeutics. HCT-116 spheroids were generated in agarose microsystems as a 3D in vitro model, this agarose microsystem was slightly different from the one used in the previous part of my PhD. The new agarose microsystem had microwells with a spherical shape rather than the cylindrical shape of previous microwells, and the diameter of these microwells was 300 μm , allowing extended culture time of the spheroids in relatively long experiments (up to 10 days) and allowing the generation of larger spheroids and increasing heterogeneity in cell layers. The effect of spheroids' size on cell proliferation throughout spheroids has been investigated, and the findings will be discussed further below.

1.1. Effect of spheroid size on cell proliferation

The influence of spheroids features on the response of cells to therapy will be discussed further in this chapter. One of these characteristics is the difference in cell proliferation between different cell layers in spheroids. At day 3 and day 10, several spheroids were grown, fixed, and labeled. To analyse cell proliferation within spheroids, spheroids stained with EdU (labeling nuclei of proliferating cells) and nucgreen™ (labeling all nuclei) were imaged with fluorescence confocal microscopy and their correlation was quantified by computing the Pearson's Correlation Coefficient (PCC) as a function of the distance from the periphery using a dedicated Matlab routine. At day 3, the average diameter of the spheroids was (153 \pm 10 μm), and at day 10, it was (284 \pm 8 μm) (measured using ImageJ). The concept and details of this quantification is explained in Materials and Methods of the article in this chapter. In spheroids fixed at day 3, PCC values in whole spheroids were greater than 0.6, indicating the presence of EdU in most cells in the center of all spheroids and implying that they were proliferative. The mean PCC value in cells residing in deeper layers (> 65 μm) of spheroids fixed at day 10 was less than 0.5, demonstrating the absence of EdU and implying that most cells were not proliferative. As a result, in spheroids with diameters around 283 μm (at day 10), there were two distinct cell layers: a proliferative and a quiescent zone.

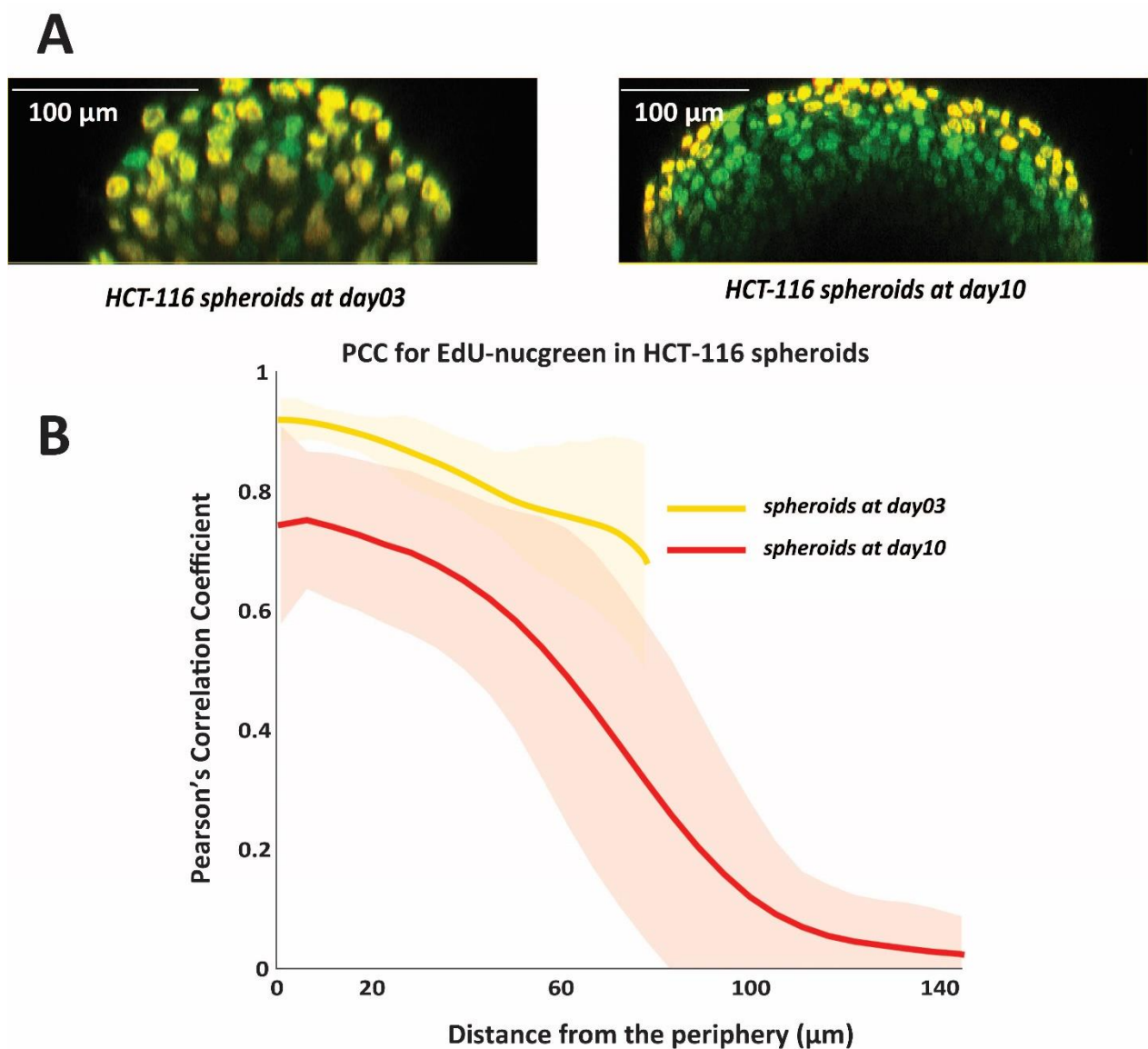


Figure 3.1. Quantification of cell proliferation in HCT-116 spheroids labelled with EdU and nucgreen™ imaged by confocal fluorescence microscopy; (A) Orthogonal view of HCT-116 spheroids fixed at day3 and day10 after cells seeding, in merged image the green channel represents cell nuclei (nucgreen™) and yellow color show cell nuclei in proliferative cells (EdU-555) resulted by overlay of these two channels. (B) Mean PCC values (bold lines) and standard deviations (shaded area) for HCT-116 spheroids fixed at day3 (yellow curve) and day10 (red curve).

1.2. The workflow of assessment of therapeutic efficacy of AGuiX® nanoparticles in radiotherapy using 3D in vitro model

Therapeutic and diagnostic applications of AGuiX® nanoparticles serving as radiosensitizers in tumor radiotherapy (RT) and contrast agents in tumor MRI diagnosis had previously been thoroughly investigated in several in vitro, *in vivo* studies and in clinical trials (288,289).

The goal of this section of my PhD was to use this 3D in vitro model for the evaluation of the therapeutic efficacy of AGuiX® nanoparticles in radiotherapy of HCT-116 spheroids.

Delphine Vernos-Brichart, PhD student of Dr. Claire Rodriguez-Lafrasse and Dr. Olivier Tillement, collaborated on this part of the project. Delphine Vernos-Brichart conducted the irradiations and clonogenic survival assays at the Laboratoire de Radiobiologie Cellulaire et Moléculaire and I performed HCT-116 spheroids generation, post-irradiation optical microscopy follow-ups and subsequent image analysis at ILM.

In another collaboration, Alexis Chambost, PhD student of Dr. Sylvain Monnier at ILM's Biophysics team and Dr. Mathieu Gabut at the Centre de recherche en cancérologie de Lyon (CRCL), used his developed 3D in vitro model for single cell seeding to develop a protocol similar to the clonogenic survival assay, but in a 3D environment, with no possibility of cell-substrate adhesion.

The growth and in-situ proliferation of irradiated spheroids were monitored using optical microscopy in parallel to classical clonogenic survival assays(290) which is a standard assay in in vitro irradiation experiments. These spheroids were fixed and labeled in order to study proliferation at the single cell level. EdU and nucgreen™ fluorescence probes were imaged, and cell proliferation was assessed by quantifying the correlation between EdU and nucgreen™ channels in fluorescence microscopy to study the variation of proliferation within spheroids. The framework of this part of my thesis is presented in **Fig. 3.2**.

The experiments and results will be described in the following section in the format of a scientific article including *Introduction, Materials and Methods, Results and Discussion and conclusion*.

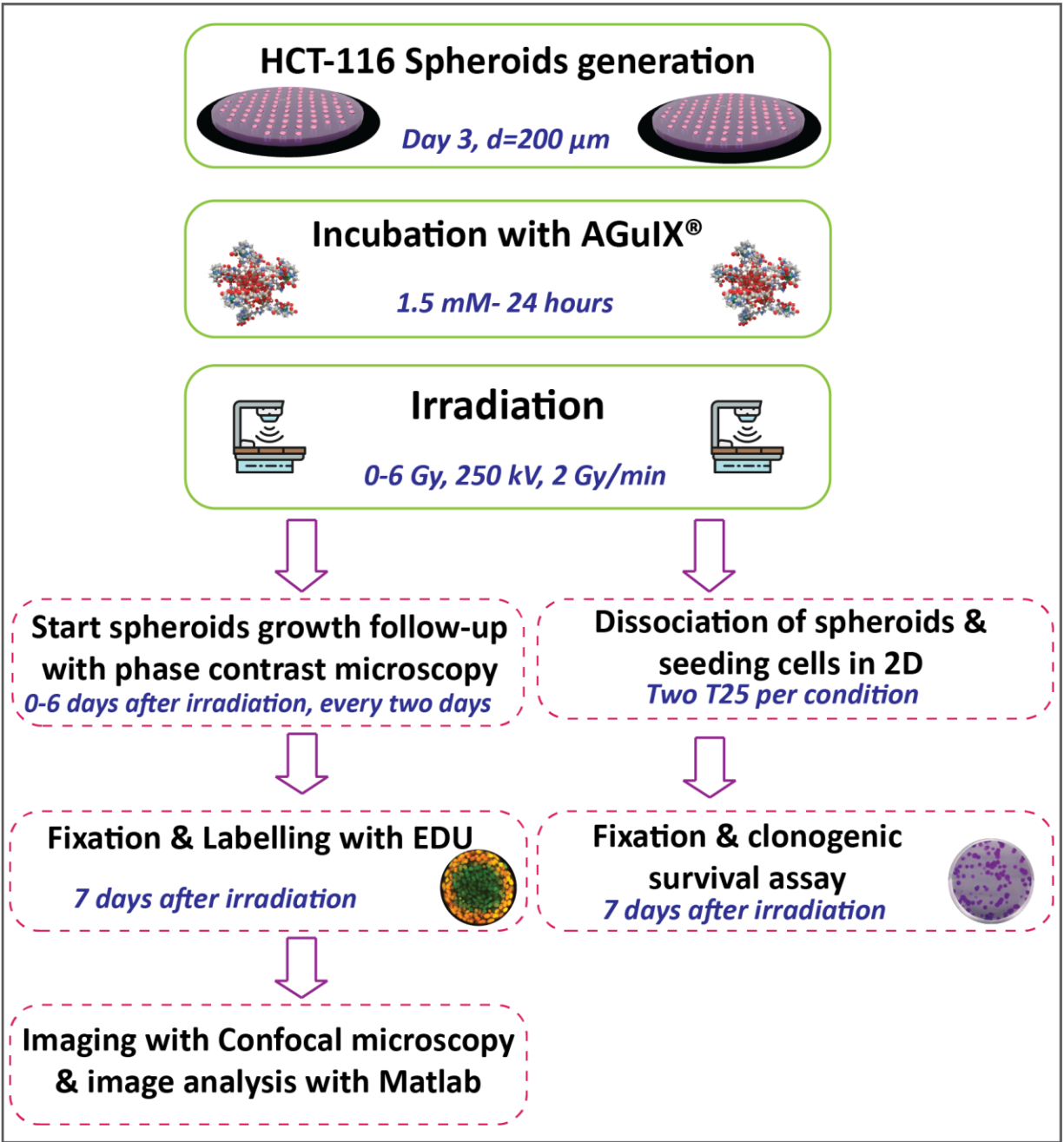


Figure 3.2. Framework of irradiation of spheroids in microwells and subsequent follow-ups

2. ABSTRACT

While monolayer cell culture assays have been used in cancer research for decades, they have been criticized for their inability to predict treatment response in *in vivo* and clinical trials. Multicellular tumor spheroids, which can replicate many key features of the tumor microenvironment, are one of the most popular alternatives. However, limitations in compatibility with standard biological assays, low throughput, and complexity in translating results into clinical settings have limited their use. To address current challenges associated with multicellular tumor spheroids models, agarose-based microsystems were developed for spheroids culture. In this study, the capacity of this model was investigated to assess therapeutic efficacy of AGuIX[®] (ultrasmall gadolinium based nanoparticles), which are currently implicated in clinical trials as effective radiosensitizers. The response of HCT-116 spheroids to radiotherapy was assessed using a classical clonogenic survival assay and *in situ* optical imaging. The radiosensitivity of HCT-116 cells in spheroid form has been shown to be lower than in 2D monolayer, highlighting the advantage of using 3D cellular structures for therapy assessments. A radiosensitization effect of AGuIX[®] was found in the 2-3 Gy range. The unique *in situ* proliferation analysis revealed a different repartition of the remaining proliferative cells, with a reduced proliferating ring when AGuIX[®] nanoparticles were combined with radiotherapy. This effect was more pronounced for the intermediate dose of 2-3 Gy. The growth of spheroids after irradiation highlights the importance of monitoring effect of irradiation in intact spheroids along with single cell level analysis to extent our knowledge on response to therapeutic strategies.

3. CORPUS

Introduction

Cancer is still one of the deadliest diseases impacting the world's population, and it is a major impediment to increase life expectancy (291). Colorectal cancer is one of the most common malignant tumors, accounting for the third highest incidence and the second highest cancer-related death rate worldwide (292).

While the use of radiotherapy for colon cancer is limited, rectal cancer requires multimodal treatment, which includes a combination of surgery, chemotherapy, and radiotherapy to achieve the best possible outcome (293,294). In particular, radiotherapy combined with surgical resection improves local control of rectal cancer significantly (295,296). Despite low local relapse rates, a combination of factors results in radio-resistance and poor prognosis in rectal cancer (294,297). Furthermore, in colorectal cancer, radiotherapy treatment side effects and distant metastasis are major concerns, resulting in a poor quality of life and a high mortality rate for patients (298).

Positioning and precision of radiation fields to target tumor have improved to reduce the toxicity caused by irradiation of vulnerable and surrounding organs (299). High atomic number (Z) nanoparticles such as gadolinium (Z = 64) (300), hafnium (Z = 72) (301), platinum (Z = 78) (302), gold (Z = 79) (303), or bismuth (Z = 82) (304) have recently been investigated as an approach to improve the therapeutic index of radiotherapy.

High-Z metallic nanoparticles can accumulate in cancer cells either by Enhanced Permeability and Retention (EPR) effect and/or by the use of active targeting (305), increasing the absorption coefficient of radiation in tumor tissues and causing fewer side effects than conventional radiosensitizers. High-Z nanoparticles can also be used as theranostic agents, which combine anticancer therapeutic activity with diagnostic capability in medical imaging modalities (306,307). Two-dimensional (2D) *in vitro* cancer models may be too simplistic and insufficient to accurately assess the value of various RT/molecular or nanoparticle agent combinations. Spheroids, which are three-dimensional (3D) *in vitro* models, have characteristics such as close cell-cell interactions, lactic acidosis, and hypoxia that could better mimic *in vivo* conditions and improve screening accuracy for novel anti-cancer strategies (308,309). As spheroids grow in size, deeper lying cells may be exposed to increasing levels of lactic acid and hypoxia, reducing the efficacy of RT. Similarly, because certain drugs have difficulty diffusing and penetrating to the center of spheroids, the measured efficacy of RT in 3D models is lower than in 2D models (71,310). Cell signaling also contributes to tumor radioresistance by assisting cells in exchanging materials and agents for cellular repair in order to overcome radiation damage (311). Nutrient gradients control the proliferating and metabolic states of tumor cells, resulting in metabolically active and proliferating cells in the outer cell layers, necrotic and apoptotic cells in the center of the spheroids, and quiescent cells in between (18,167). Because of differences in proliferation and

oxygenation, cells in the proliferating and quiescent layers respond differently to radiation (312). While ionizing radiation causes a variety of cellular responses, cell cycle arrest in G2, as well as apoptosis and senescence, are of particular interest in terms of radiotherapy efficacy. Spheroid models, provide an intermediate situation, between 2D cell culture and *in vivo* models, for assessing the effects of radiotherapy on cancers (16,312).

Thus, when 3D spheroid models are used instead of or in addition to monolayer models in the screening of combinatorial therapeutic agents for use with radiotherapy, candidates with higher subsequent developmental success rates may be identified (313). Nevertheless, using these models for standard biological assays and extracting the cells for post-treatment studies is still challenging (314).

In radiobiology, cell death has traditionally been determined by the cell's loss of reproductive integrity. Therefore, a cell is thought to be killed by radiation rather than by its own ability to physically survive in the population, but through its reproductive ability integrity (314). As a result, the clonogenic assay is regarded as a valuable and reliable method for determining cell death following radiation treatment. This assay assesses a cell's ability to form colonies (290). This simple and inexpensive method is well-known as a gold standard approach for evaluating radiotherapy for several decades (315). Nevertheless, while clonogenic survival and 2D growth data provide a valid indication of a cell line's intrinsic treatment sensitivity, it has been demonstrated that clonogenic survival alone may be insufficient to calculate biologically equivalent doses (272). As a results, it is important to develop protocols enabling post-treatment monitoring in a 3D manner which better estimate cellular response to clinical irradiation doses.

The therapeutic efficacy of AGuIX[®] nanoparticles as a radiosensitization agent in radiotherapy was investigated on HCT-116 spheroids prepared using the previously described 3D *in vitro* model. HCT-116 spheroids were screened for radiation response using the classical clonogenic survival assay, optical microscopy techniques for growth monitoring, cell viability, and the spatial distribution of proliferative cells within spheroids after irradiation. We show that HCT-116 spheroids demonstrated higher radioresistance compared to monolayer cells in clonogenic survival assay which was consistent with previous finding on higher radioresistance of spheroids compared to monolayer cells in pancreatic cancer cells (316,317). Interestingly, spheroids after irradiation even at the highest dose (6 Gy) displayed the ability to grow during 6 days of monitoring, while in the clonogenic assay they were unable to make colonies at higher doses. The *in-situ* single cell optical imaging and analysis of spheroids revealed that 7 days after irradiation, the depth of proliferative layers decreased as irradiation dose increased. The reduction of this proliferative layer was detected for lower irradiation dose in the presence of AGuIX[®] nanoparticles. The methodology presented in this study appears hence as a promising *in vitro* assay for the evaluation of irradiation therapy efficacy.

Materials and Methods

Molding of free-standing microwells

The agarose solution (150 μ L) was deposited on a warmed PDMS mold (at 78°C) and a coverslip was then placed on top of the drop of agarose to spread it with a constant thickness on the mold. After agarose gelation into the desired shape (10 min), the coverslip was removed and the molded agarose microwells were cut to fit in the wells of a 24 multi-well plate. The microwells were then placed in a 24-multi well plate and kept hydrated with PBS (1 mL/well). The plate was UV-sterilized (8 W, 254 nm) for 20 min on opened and closed state and kept at 4°C until used. The day before each experiment, PBS was replaced by culture medium and let to diffuse within each microwell by overnight incubation at 37°C before cell seeding.

Colorectal cancer cell line, HCT-116 and culture condition

HCT-116 colorectal carcinoma (CCL-247) cell line was purchased from the American Type Culture Collection (ATCC, Virginia, USA). All cells were cultured in Dulbecco's Modified Eagle's medium (DMEM-Glutamax, Gibco™), supplemented with 10% of heat-inactivated Fetal Bovine Serum (FBS; Sigma, St. Louis, Missouri, US), 100 units/100 μ g of penicillin/streptomycin (Gibco™).

Routinely, the HCT-116 cells were grown in T-25 cell culture flasks and were placed in the incubator at 37°C with a 5% CO₂ atmosphere. The culture medium was changed regularly, and the cell passage was carried out at 70% confluency every 3 days. The cell passage was performed using recombinant cell-dissociation enzyme (TrypLE, Gibco™) to detach cells followed by neutralizing with culture medium. The cell suspension was centrifuged at 1000 rpm (equal to 106 g) for 5 min, the supernatant was discarded, and the cell pellet was resuspended in 1 mL. The number of cells was counted with a Neubauer chamber, and final cell volume was adjusted to reach the desired cell concentration.

Multicellular tumour spheroids (MCTS) formation

MCTS of HCT-116 cells were formed in 24-well plates containing agarose microwells in each well. After trypsinization and centrifugation, 120,000 cells in 1 mL complete medium was added in each well (containing each 1 microsystem). To encourage and accelerate cell aggregation, the 24-well plate was agitated for 15 min in the incubator at 37°C and 5% CO₂. After 4 h, the plate was rinsed with fresh medium to remove cells that did not reach the microwells. After 2 days, spheroids were ready for incubation with nanoparticles.

Preparation of Cy5.5 conjugated Gadolinium based nanoparticles (AGuIX®-Cy5.5)

The Gd-based nanoparticles (AGuIX®) synthesized by NH TherAguix (Lyon, France) are composed of a polysiloxane matrix surrounded by covalently bound DOTAGA-Gd ((1,4,7,10-

tetraazacyclododecane-1-glutaric acid-4,7,10-triacetic acid)-Gd). The synthesis process is already described in the literature (318). Briefly, AGuIX[®] nanoparticles are composed of a polysiloxane network surrounded by Gd chelates. The chemical composition of AGuIX[®] nanoparticles is (GdSi_{6.5}N₆C₂₅O₂₁H₄₂, 10 H₂O)_n with a molar mass around 10 kDa. The hydrodynamic diameter of the AGuIX[®] nanoparticles is close to 5 nm; and the AGuIX[®] nanoparticles are characterized by a zeta potential of 9.0 ± 5.5 mV at pH 7.2. These AGuIX[®] nanoparticles were further conjugated to Cyanine-5.5(Cy5.5) fluorophore to make them detectable by confocal fluorescence microscopy. They are referred as AGuIX[®]-Cy5.5 nanoparticles in the rest of the article.

Incubation of cells with AGuIX[®]-Cy5.5 nanoparticles

To incubate MCTS and monolayer cells with AGuIX[®]-Cy5.5 nanoparticles, an intermediate solution of AGuIX[®]-Cy5.5 nanoparticles with 100 mM concentration of Gd was prepared in distilled-water. From this intermediate solution, just before the incubation with cells, AGuIX[®]-Cy5.5 solutions were prepared in fresh DMEM with Gd concentration of 1.5 mM respectively. The MCTS in half of the microsystems of the 24-well plates were incubated with 1 mL of AGuIX[®]-Cy5.5 nanoparticles solution. Prior to the irradiation, spheroids were rinsed with fresh medium, three times, each 15 min.

Irradiation of Spheroids

Cells were irradiated with X-rays at Lyon-Sud Medical School (France) using an X-RAD320 irradiator (250 kV). 24-well plates containing spheroids in agarose microwells were horizontally irradiated with 2 Gy at a dose rate of 2 Gy min⁻¹.

Clonogenic survival assay

Immediately after irradiation at doses varying from 2 to 8 Gy, spheroids were trypsinized to dissociate and the single cells plated at two different concentrations in three replicate 25 cm² flasks (densities of 150–1600 cells, to yield 10–120 colonies after six cell divisions). Then they were allowed to grow at 37°C for about 7-8 days (corresponding to six cell divisions, medium was renewed every two days). At this time, cells were washed with PBS, fixed with 95% ethanol, and stained with Giemsa. Colonies containing more than 64 cells were scored and the percentage of surviving cells was calculated. The surviving fraction (SF) after each treatment were determined as the number of counted colonies divided by the number of seeded cells and normalized to the plating efficiency (PE) of non-irradiated cells. (PE = number of colonies formed/number of seeded cells).

SER Calculation

The amplification efficiency of AGuIX[®]-Cy5.5 nanoparticles in irradiation of HCT-116 spheroids was quantified using radiation Sensitizer Enhancement Ratio (SER). This parameter was defined at a

dose point, specifically 2 Gy, which is the reference dose/fraction in conventional radiotherapy treatments.

$$SER_D(\%) = 100 \times \frac{SF_D^C - SF_D^{NPs}}{SF_D^C}$$

Where SF_D^C and SF_D^{NPs} refer to survival fractions at the dose D for control spheroids and spheroids exposed to AGuIX[®], respectively.

The radiosensitivity of HCT-116 cells in 2D culture and spheroid form has been compared and quantified using following equation.

$$SER_D(\%) = 100 \times \frac{SF_D^{2D} - SF_D^{Sph}}{SF_D^{2D}}$$

Where SF_D^{2D} and SF_D^{Sph} refer to survival fractions at the dose D for 2D cells and spheroids, respectively.

Spheroids growth follow-up

Just after irradiation, monitoring of spheroids growth started with phase contrast microscopy. The images were taken at day 0,2,4 and 6 after irradiation with a 20X objective. For each condition, spheroids in two replicates were imaged in three independent experiments. The medium over the spheroids was changed every three days.

Quantification of phase contrast microscopy images

Images of growth follow up were analyzed using a dedicated routine in Matlab for manual segmentation of spheroids area. From this segmented area, equivalent diameter and volume of spheroids were calculated. The spheroids volume was plotted as scatter plots using the MATLAB UnivarScatter function (©Manuel Lera Ramírez, 2015, available in MATLAB exchange files).

Live and dead assay

At the end of the growth follow up, Calcein (Thermofisher) and propidium iodide (PI, Sigma) labeling were used to assess cell viability. Calcein is used to label the cytoplasm of viable cells in green, whereas PI is used to label the nuclei of dead cells in red. After removing the culture medium, the spheroids were washed in pre-warmed PBS (3X, 5min). Calcein (1 µM) and PI (20 µg mL⁻¹) diluted in pre-warmed sterile PBS were then incubated for 20 minutes at 37 °C before epifluorescence microscopy.

Immunostaining of proliferative cells using EdU.

For EdU incorporation and detection, the Click-IT 555 kit was used (Invitrogen C10338), following the manufacturer's instructions, with spheroids model adaptations. After removing half of the

medium from the spheroids, a 20 μM EdU solution was prepared and added to the HCT-116 spheroids to keep them in 10 μM EdU for 24 hours.

To detect EdU, spheroids were fixed in paraformaldehyde (4%) for 20 minutes, washed with PBS/5% BSA (3X,15 min), permeabilized with 0.5% Triton X-100 (Acros) for 20 minutes, and the washing procedure was repeated. The Click-iT[®] reaction cocktail was prepared according to the manufacturer's protocol, the 500 μL was added to each microwell for 30 minutes before washing.

Then samples were incubated with nucgreen[™]-Dead 488 (Invitrogen[™], R37109, 1 drop/2mL in PBS) at room temperature overnight. The procedure ended with rinsing spheroids with PBS (3x 5 min).

Spheroids Clarification

To overcome the limitations of optical microscopy of 3D biological samples, Spheroids were clarified using glycerol/PBS solution (80%/20%) (319).

The solution for clarifying spheroids was prepared by mixing glycerol (99.5%, VWR Chemicals) with PBS by the ratio of (80%/20%). A fresh solution was prepared for every experiment. To clarify spheroids, just after fixation, they were incubated in glycerol solution for 24 h. A detailed description of the mounting procedure used for imaging of spheroids was described in Supplementary **Fig. SI 1** of the article in chapter two. For most experiments, the microsystems were incubated with a fresh glycerol solution and mounted between 2 coverslips, separated by a 1 mm sticky spacer (2x0.5mm thick Ispacer, SunJin Lab).

Confocal fluorescence microscopy

Image acquisitions of spheroids and cell monolayers were carried out with a confocal microscope (Leica SP5) using a 25X water immersion objective (NA=0.95). Image acquisitions in Z direction was performed using a 1 μm z-step. Automatic image acquisitions for a large number of spheroids were performed.

Image processing

Images obtained by confocal fluorescence microscopy were analyzed using a dedicated Matlab routine. While spheroids were imaged using optical sectioning in Z direction, it was useful to quantify the average signal intensity along the radius of each spheroid.

To do this, the entire surface of each spheroid, at each imaging depth were first segmented using the intensity signals coming from every nuclei (labelled with nucgreen[™]-488). From this segmentation, the segmented spheroids slices were first fitted into a perfect circle for each imaging depth, followed by fitting each spheroid z-stack into a perfect sphere. By changing the

coordinates of analysis from Cartesian (x, y, z) to the spherical (R, theta, phi) coordinates, analysis was performed in radial direction.

Quantifying EdU+ cells using Pearson's correlation coefficient

Pearson's correlation coefficient (PCC) values in analysis of fluorescence microscopy images indicate the degree of association between fluorophores; this coefficient was considered as a criterion for quantifying proliferative cells in each spheroid. As a result, the intensities for nucgreen™ and EdU channels in segmented images fitted into a perfect sphere, were measured in radial direction, using these intensities for each radius slice (dr). In Matlab, the PCC was calculated using the following equation.

$$PCC = \frac{\sum_i (R_i - \bar{R}) \times (G_i - \bar{G})}{\sqrt{\sum_i (R_i - \bar{R})^2 \times \sum_i (G_i - \bar{G})^2}}$$

Where R_i and G_i refer to intensity values of the two probe channels and \bar{R} and \bar{G} refer to the mean intensities of two probes in each radius slice. Finally, the mean values of this calculation were plotted as a function of distance from the periphery in the radial direction for several spheroids in each condition. The higher PCC values correspond to higher correlation of EdU with nucGreen™ probes and hence more proliferative cells, whereas lower PCC values correspond to the low intensity of EdU compared to nucgreen™ channel showing lower proliferating cells ratio. In this study, a PCC value larger than 0.5 were considered as a proliferative cell layer and a value lower than 0.5 were considered as a non-proliferative cell layer.

Using proliferative depth values, Sensitizer Enhancement Ratio (SER) of AGuIX® was calculated via the following equation.

$$SER_{2Gy} = 100 \times \frac{d_{2Gy}^C - d_{2Gy}^{Nps}}{d_{2Gy}^C}$$

Where d_{2Gy}^C and d_{2Gy}^{Nps} are the proliferative depth of control spheroids and spheroids exposed to AGuIX®, respectively.

Results & Discussion

The simple monolayer cell culture, cannot replicate the important features of the natural tumor microenvironment, which becomes even more important when the response to therapy strategies needs to be investigated (96). Multicellular tumor spheroids, as discussed earlier, have properties that make them a good choice for simulating the natural tumor microenvironment in in vitro assays. The gradient of oxygen, metabolites, and pH in multicellular tumor spheroids, enable this model to exhibit a degree of therapy resistance, increasing the liability of in vitro assays for novel drugs and nanoparticles (18,72,76). The lack of oxygen within the spheroids has been linked to a reduction in radiation-induced cell damage. Indeed, the availability of local molecular oxygen improves radiotherapy efficacy because DNA lesions caused by ROS generated during water radiolysis react with oxygen to form stable DNA peroxides. Oxygen is responsible for approximately 65% of DNA damage caused by irradiation(312). With this in mind, cancer cells that receive less oxygen, such as those from the core of spheroids, are typically more radioresistant (72,312,320). It has been demonstrated that the 0–10 Gy radiation had a greater effect on the glioblastoma cell model BMG1 on cell monolayers than on spheroids, because ROS production in the cells after the radiation was higher in the monolayers than in the spheroids (215).

Cell signaling also assists cells in exchanging materials and agents for cellular repair in order to overcome radiation damage, which contributes to tumor radioresistance. Furthermore, nutrient gradients create three distinct zones in tumors: proliferative, quiescent, and necrotic cells, each of which responds differently to radiotherapy due to differences in proliferation and oxygenation (312).

Conventional methods for producing spheroids limit the use of this cellular structure in nanotherapeutics screening, particularly when it comes to assessing therapeutic efficacy of these novel drugs and translating it to standard biological assays and clinical expectations. HCT-116 spheroids were prepared using a newly developed agarose microsystems (319). This 3D in vitro model provides us with thousands of spheroids for irradiation and enabled us to have enough cells for performing clonogenic survival assay and optical microscopy monitoring in a high throughput manner, which was impossible with classical spheroids generation techniques.

First, the radiosensitivity of HCT-116 monolayer cells and spheroids was tested using a clonogenic survival assay after being irradiated with different doses (0, 2, 4, 6, and 8 Gy).

The primary experiment, which assessed HCT-116 cell radiosensitivity using clonogenic survival assay revealed that HCT-116 cells in spheroids are more resistant to irradiation than monolayer

cells (**Fig. 3.3**). At 6 Gy irradiation, no colony for irradiated 2D cells was observed in contrast to spheroids, although these spheroids were dissociated immediately after irradiation and seeded in T25 culture flasks in a 2D manner. In addition, when we compared the radiosensitivity of cells in 2D and spheroids using the radiation Sensitizer Enhancement Ratio (SER), the radiosensitivity of spheroids at 2Gy irradiation is 133.3 % lower than 2D cells (**Table 3.1**), remarking considerable difference of cell response to radiotherapy in monolayer culture and spheroid form.

The developed 3D in vitro model was used to evaluate radiosensitizer agents (AGuIX[®]-Cy5.5 nanoparticles) using parallel follow-up strategies; one is the classical clonogenic assay, and the other is using optical microscopy, which includes spheroids growth follow-up with phase contrast microscopy, cell viability assay with epifluorescence microscopy, spatial distribution of proliferative cell nuclei using confocal fluorescence microscopy.

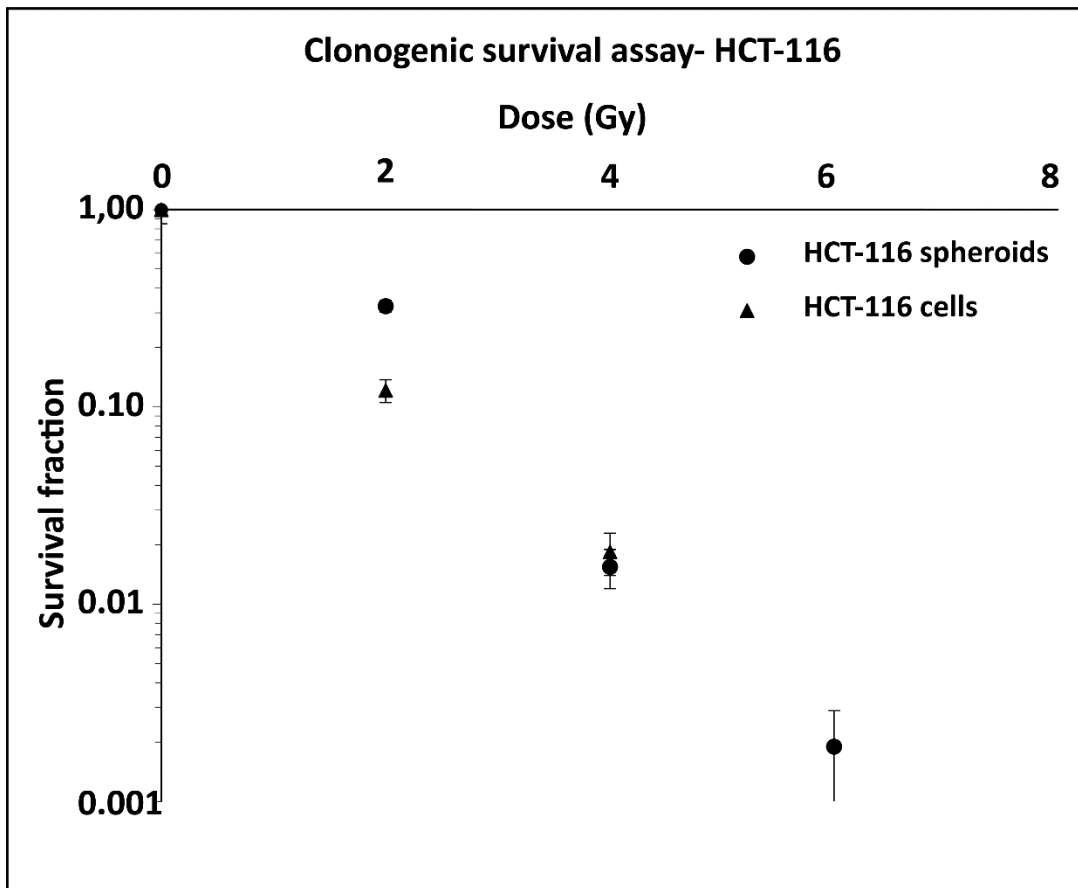


Figure 3.3. Clonogenic Survival curves; Monolayer HCT-116 cells (2D) and HCT-116 cells in spheroid form (3D) treated with 0, 2, 4, 6 and 8 Gy of irradiation. Markers correspond to the mean value and standard deviation of two replicates in a single experiment.

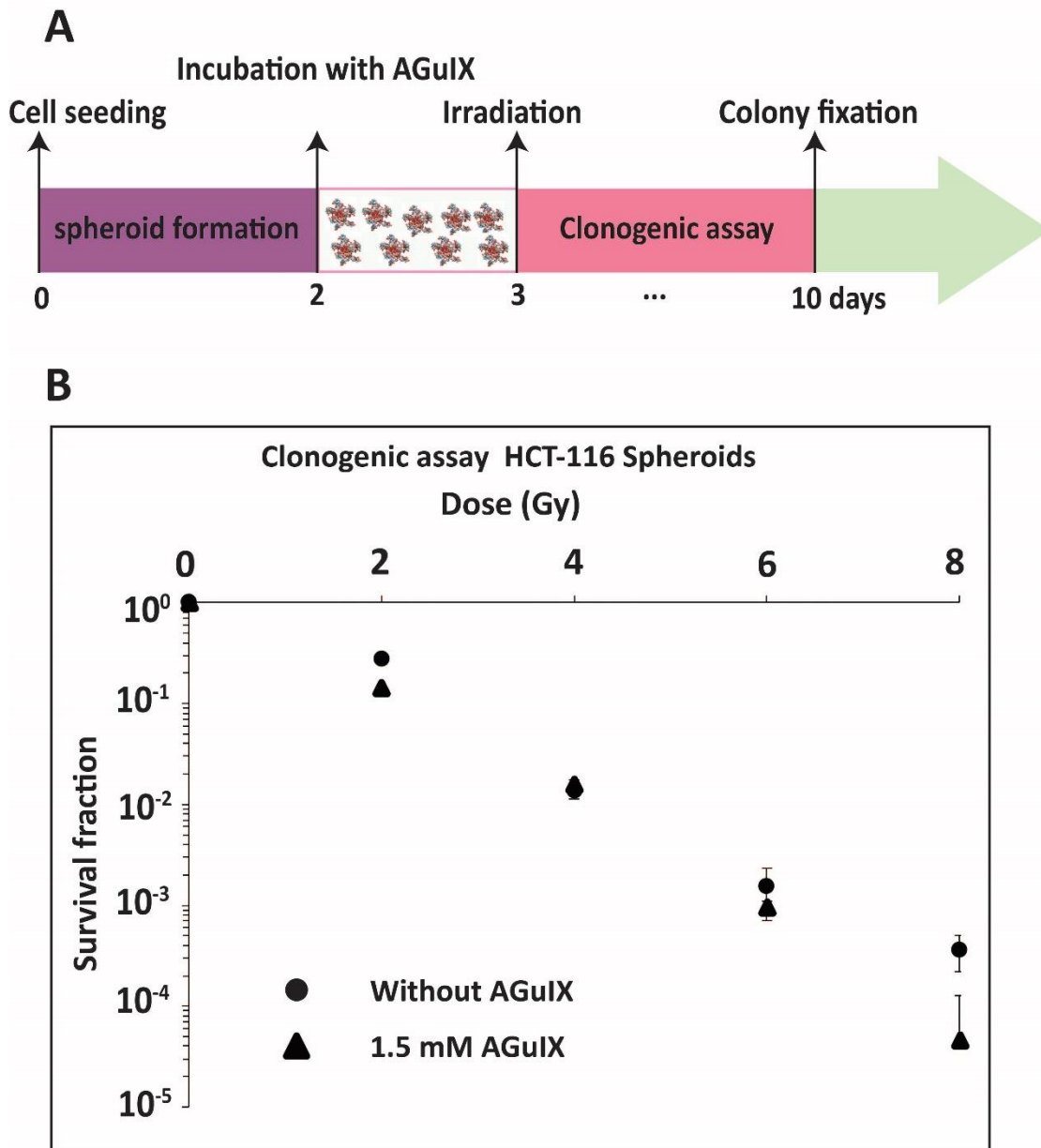


Figure 3.4. Analysis of radiosensitizing effect of AGuIX[®]-Cy5.5 nanoparticles in HCT-116 spheroids ($d=100\ \mu\text{m}$); (A) The experimental timeline for irradiation of HCT-116 spheroids. (B) Clonogenic Survival curves for HCT-116 spheroids that were treated or not with 1.5 mM AGuIX[®]-Cy5.5 nanoparticles for 24 hours prior to irradiation at 0, 2, 4 and 6 Gy (250 kV, 2 Gy/min). Irradiated cells were cultured for 8 days. Colonies of more than 64 daughter cells in a culture were counted. The markers are mean values and standard deviations extracted from three independent experiments.

To evaluate the therapeutic efficacy of AGuIX[®]-Cy5.5 nanoparticles in radiotherapy of HCT-116 cell spheroids, all spheroids in plates (exposed or not to AGuIX[®]-Cy5.5 nanoparticles) were

irradiated to specific irradiation doses. Following irradiation, a portion of spheroids from each condition in each plate were dissociated to single cells, which were then counted and seeded in accordance with the clonogenic survival assay protocol. The timeline of these experiments is shown in **Fig.3.4 A**.

Table.3.1. Sensitizer Enhancement Ratio (SER) for comparison of HCT-116 cells radiosensitivity in 2D/spheroids and in spheroids/spheroids + AGuIX®.

	SF_{2Gy}	$SER_{2Gy}^{2D/Spheroids}$ (%)	$SER_{2Gy}^{Spheroids/Spheroids+AGuIX}$ (%)
Control – 2D	0.12±0.01	-133.3	-----
Control – Spheroids	0.28± 0.01		50
Spheroids + AGuIX®	0.14± 0.01		

The clonogenic survival curves in **Fig. 3.4 B** revealed a moderate radiosensitizing effect of AGuIX®-Cy5.5 nanoparticles in combination with radiotherapy for HCT-116 cell spheroids, with a decrease in cell survival fraction in the presence of AGuIX®-Cy5.5. However, at high irradiation doses (> 4 Gy), survival fractions are smaller than 0.01 even without AGuIX® which are not conclusive: the irradiation doses chosen were too high for the HCT- 116 cell line, to clearly demonstrate a radiosensitizing effect at these doses using the classical 2D clonogenic assay. The Sensitizer Enhancement Ratio (SER) calculation at 2 Gy, showed 50% increase in irradiation effect when spheroids were exposed to 1.5 mM AGuIX®-Cy5.5 for 24 hours prior to irradiation, which is significant compared to the other study on AGuIX® radiosensitizing effect on other cell lines and another kind of 3D model (321).

Nevertheless, a set of complementary optical microscopy follow-up revealed interesting results. The remaining spheroids in the other microwells in each plate were kept intact for growth monitoring via phase contrast microscopy, live and dead assays with epifluorescence microscopy and analysis of cell proliferation with confocal fluorescence microscopy **Figure 3.5** presents the timeline of the characterization of cell response to radiotherapy with and without AGuIX®-Cy5.5 nanoparticles using various methods mentioned above.

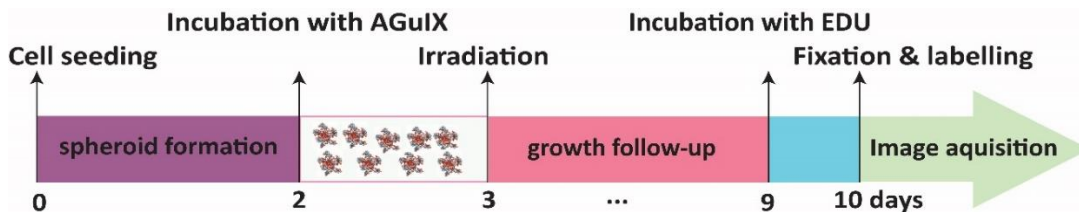


Figure 3.5. Experimental timeline of the irradiation experiment characterized with optical microscopy, Spheroids were treated with AGuIX®-Cy5.5 nanoparticles at day 2 after cell seeding for 24 hours, at day 3 spheroids were irradiated. At day 0,2,4 and 6 after irradiation spheroids were imaged with optical microscopy, 7 days after irradiation spheroids were stained for live/dead assay using Calcein and PI for live

and dead cells, respectively, followed by fixation for detecting EdU in proliferative cells and labelling with nucgreen™.

To achieve a better understanding of the effect of AGuIX®-Cy5.5 nanoparticles on the growth of HCT-116 spheroids after irradiation, the results were presented for each dose, separately and spheroids growth with and without AGuIX®-Cy5.5 nanoparticles were compared (**Fig. 3.6, Fig. SI.1, Fig. SI.2**).

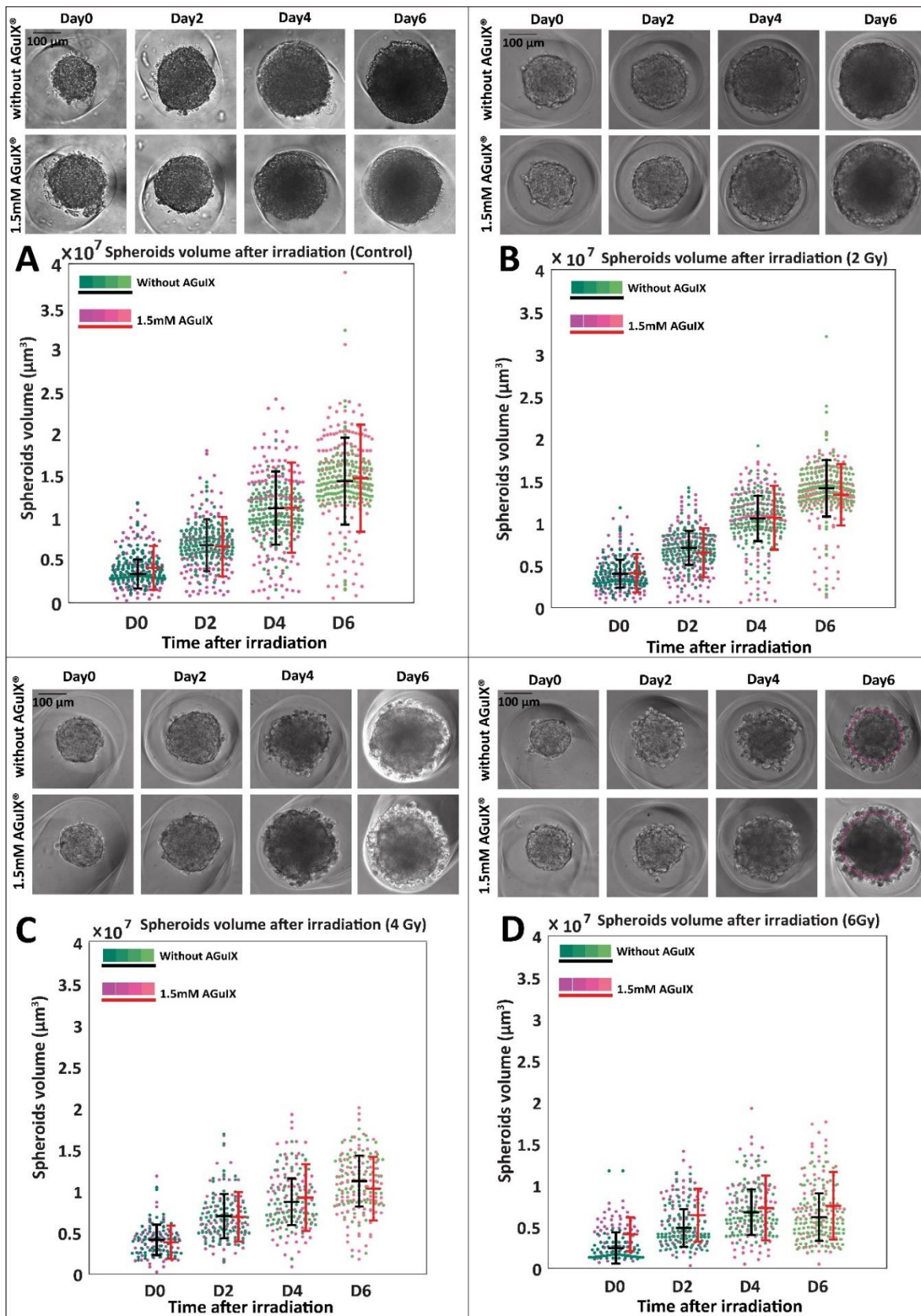


Figure 3.6. Spheroids growth follow-up using phase contrast microscopy for **(A)** control, **(B)** 2Gy, **(C)** 4Gy and **(D)** 6 Gy.

For each irradiation dose, (top rows): representative spheroids images at day 0,2,4 and 6 after irradiation with phase contrast microscopy. (bottom graph) Scatter plot of the volume of spheroids with and without AGuIX[®]-Cy5.5 nanoparticles were calculated by manual segmentation of spheroids area in images in Matlab and scatter plots were plotted using the MATLAB UnivarScatter function (©Manuel Lera Ramírez, 2015, available in MATLAB exchange files). Pink dots are the volume of single spheroids treated with AGuIX[®]-Cy5.5, with grey error bar showing mean and standard deviation of three independent experiments. Green dots show the volume of single spheroids not exposed to AGuIX[®]-Cy5.5 with black error bar showing mean and standard deviation of independent experiments. Number of total spheroids analysed : (Control) three independent experiments (without AGuIX[®], N=172, with AGuIX[®], N=143); (2Gy) three independent experiments (without AGuIX[®], N=179, with AGuIX[®], N=167) ;(4Gy) two independent experiments (without AGuIX[®], N=97, with AGuIX[®], N=93) (6Gy) two independent experiments (without AGuIX[®], N=116, with AGuIX[®], N=82).

While in the clonogenic survival assay, single cells seeded in T25 flask at doses higher than 4 Gy were not able to make any colony, the growth monitoring of spheroids after irradiation showed the ability of overall spheroids growth during 6 days follow-up for all conditions. Nevertheless, it should be mentioned that the growth rate decreased with increase in irradiation dose. Moreover, the microscopy images of various doses show that as the irradiation dose increases, so does the disorganization of spheroids. Some cells were observed surrounding the spheroids, implying possible dead cells detached from the main spheroids. This behavior of HCT-116 spheroids in response to irradiation has been already observed in another study (272), in which HCT-116 spheroids, after irradiation at doses between 2 -10 Gy, continued to grow; however the growth rate showed a reduction depending on the irradiation dose. They have also reported the detachment of dead cells from outer layer in higher doses, while spheroids retained their dense structure (272). These findings highlight the importance of using 3D cell models in radiotherapy experiments, particularly monitoring intact spheroids after irradiation to improve prediction of *in vivo* and clinical outcomes in which cells response to treatment in the form of solid tumor.

The scatter plots of spheroids volume were plotted at each irradiation dose for spheroids incubated and not with AGuIX[®]-Cy5.5 nanoparticles. The mean values of HCT-116 spheroids volume with and without AGuIX[®]-Cy5.5 nanoparticles in all days were almost overlapped for non-irradiated spheroids, but the larger standard deviations of spheroids volumes exposed to nanoparticles showed higher discrepancy in overall spheroids growth.

At the end of the growth follow up microscopy, these spheroids were labelled with Calcein and PI and were imaged with epifluorescence microscopy for live and dead assay. Even if such optical imaging is not resolved in the depth of the spheroids, the images confirmed the death of majority

of cells surrounding the spheroids and an increase in dead cells with increasing irradiation dose (**Fig.3.7**). Interestingly, the majority of dead cells, especially in spheroids without AGuIX[®] were cells in the periphery of spheroids or proliferative zone, showing the difference in response to irradiation in different cell layers. Qualitatively, it appeared that the presence of AGuIX[®] in spheroids increased cell death in the central part of the spheroids. Such dead cell repartition needs to be explored quantitatively, and for a reliable quantification, they need to be imaged in fixed/clarified state via confocal fluorescence microscopy.

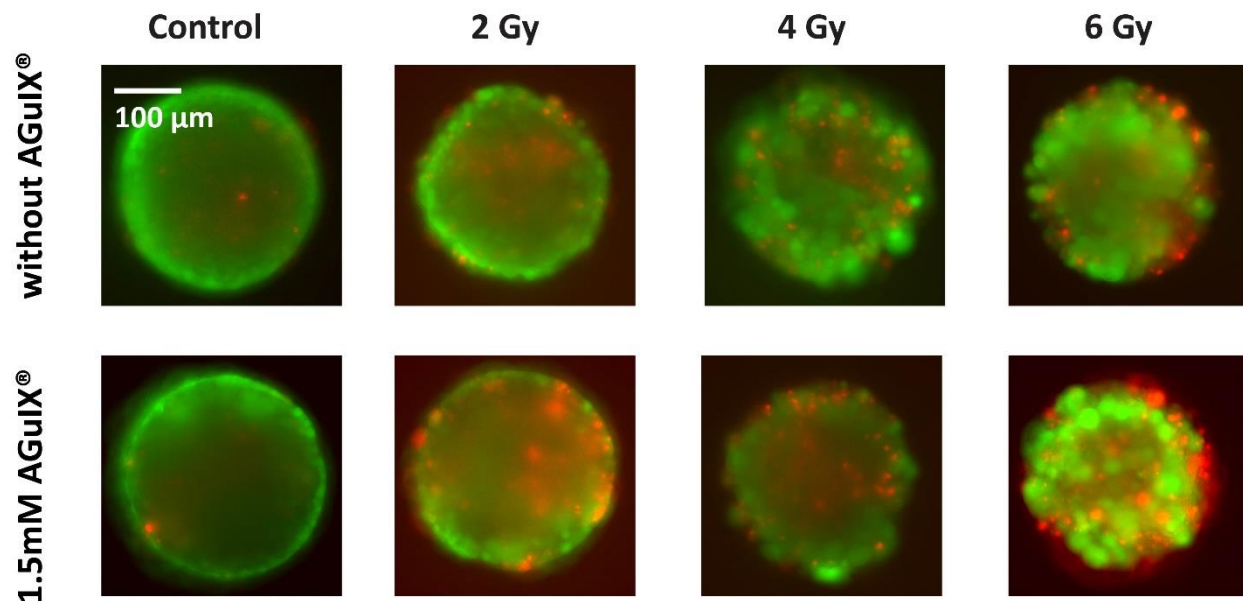


Figure 3.7. Epifluorescence microscopy images of HCT-116 spheroids in live and dead assays, 7 days after irradiation. Green color show live cells labeled with Calcein and red color shows dead cells labelled with propidium iodide (PI).

We chose to analyse proliferating cells instead of dead cells. Indeed, monitoring of spheroids growth after irradiation seems to be a valuable approach for evaluation of overall response of these tumor models to radiotherapy, nonetheless, a screening approach at single cell level is highly crucial to extent the knowledge regarding the cellular response to treatment in such heterogeneous environment.

To analyze the proliferation state *in situ*, at the single cell level, EdU immunostaining was performed (**Fig. 3.8 to 3.13**). The approach used to analyze the confocal z-stack obtained intended to calculate the coincidence of nucgreen[™] and EdU for quantification of proliferative cells in spheroids using the Pearson's correlation coefficient (PCC) for EdU and nucgreen[™]. For all irradiation doses, the analysis was performed in the radial direction, and the PCC values were plotted as a function of distance from the periphery in the radial direction to compare proliferation in irradiated spheroids incubated or not with AGuIX[®]-Cy5.5 nanoparticles. In PCC curves, the value higher than 0.5 were considered as a proliferative cell layer and values lower

than 0.5 as a non-proliferative cell layer. The point that PCC goes under 0.5 considered as the proliferative depth. **Figure 3.14** showed the proliferative depth for all condition in one plot.

As previously discussed, one intrinsic feature of tumor spheroids that is shared with natural tumors is cellular heterogeneity, in spheroids with a diameter smaller than 500 μm and larger than 200 μm , there are two distinct zones, proliferative and quiescent zones (18). The diameter of spheroids used in this study was between 200 μm and 300 μm . As shown in **Fig. 3.1**, in these spheroids there are two different zones, a proliferative layer and a quiescent core.

As shown in **Fig. 3.8 A**, the yellow region appears as a ring in spheroids exposed or not to AGuIX[®]-Cy5.5 nanoparticles, becoming less visible in deeper layers. The plot of the Pearson's correlation coefficient of nucgreen[™] and EdU as a function of distance from the periphery for non-irradiated spheroids was shown in **Fig. 3.8 B**. As expected for these non-irradiated spheroids, the proliferative depth was similar for both samples ($57.0 \pm 4.2 \mu\text{m}$ versus $58.5 \pm 3.5 \mu\text{m}$ for spheroids without and with AGuIX[®] respectively).

The Pearson's correlation coefficient was plotted for spheroids irradiated at 1Gy dose (**Fig.3.9 B**), even though at the periphery PCC has same value, the proliferative depth for spheroids not exposed to AGuIX[®]-Cy5.5 was $67 \pm 11 \mu\text{m}$ and for spheroids exposed to AGuIX[®]-Cy5.5 was $83 \pm 4 \mu\text{m}$. The higher proliferation in spheroids exposed to nanoparticles might result from low statistics of this experiment (one independent experiment) and low dose of irradiation, which has not been enough to see an effect of radiosensitization of AGuIX[®].

On the other hand, at 2 Gy (**Fig. 3.10 B**), two curves were clearly distinguishable, and the radiosensitizing effect of AGuIX[®]-Cy5.5 nanoparticles could have been observed, which was consistent with clonogenic assay results at 2 Gy showing the greatest effect of AGuIX[®]-Cy5.5 nanoparticles on HCT-116 response to irradiation. The proliferative depths for spheroids not exposed and exposed to AGuIX[®]-Cy5.5 nanoparticles were $55.5 \pm 3.5 \mu\text{m}$ and $27.0 \pm 7.0 \mu\text{m}$, respectively. Similar to this, at 3 Gy (**Fig. 3.11 B**), spheroids with AGuIX[®]-Cy5.5 nanoparticles were less proliferative ($32.5 \pm 3.5 \mu\text{m}$) than spheroids not exposed to AGuIX[®]-Cy5.5 nanoparticles ($61.0 \pm 4.2 \mu\text{m}$). At 4 Gy (**Fig. 3.12 B**), the two curves overlap ($43.5 \pm 3.5 \mu\text{m}$ $38.5 \pm 3.5 \mu\text{m}$, without and with AGuIX[®]-Cy5.5 respectively).

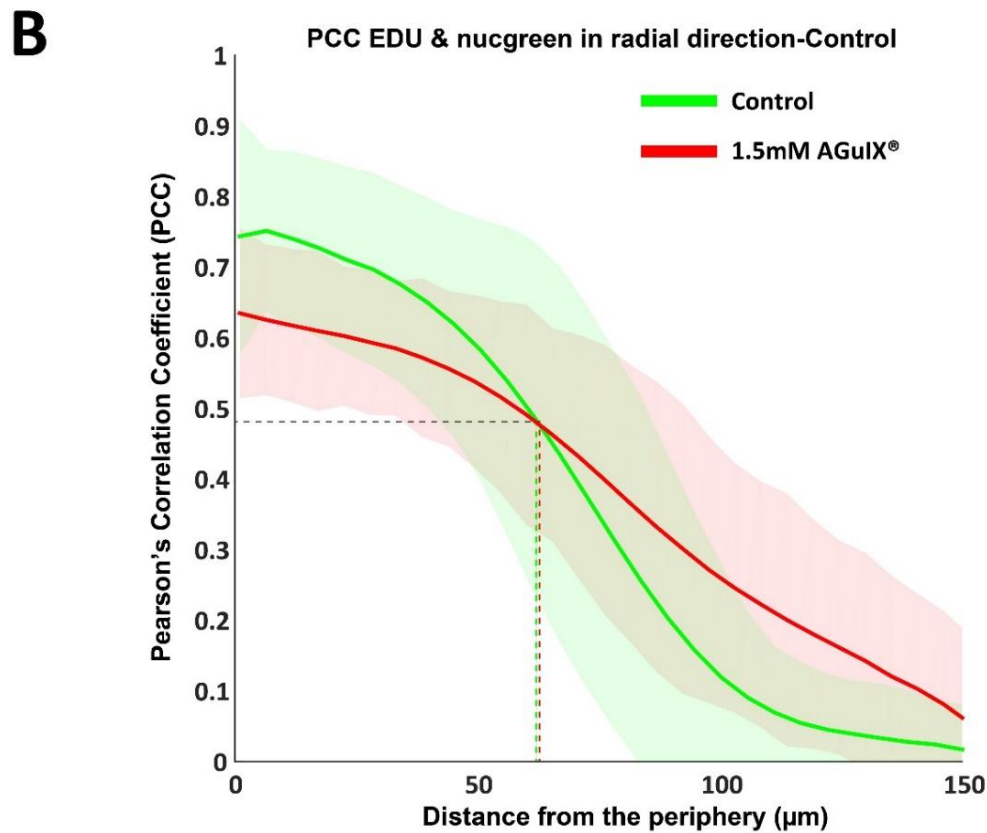
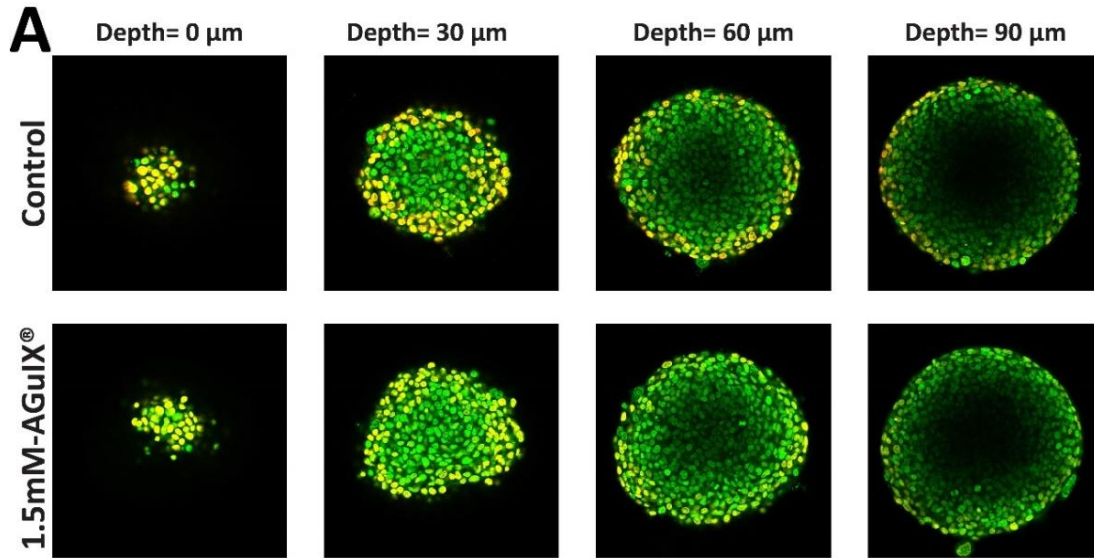


Figure 3.8 (A) Overlaid images acquired using confocal fluorescence microscopy of cell nuclei in HCT-116 spheroids of control sample (**0 Gy-not irradiated**), where green channel shows nuclei stained with nucgreen™ dead 488 and red channel show nuclei of proliferative cells labelled with Click-iT®-EdU 555, Yellow color displays superposition of these channels indicating proliferative cells in spheroids. (B) Mean of Pearson's correlation coefficient for EdU and nucgreen™ channel in radial direction as a function of distance from the periphery and light colors are standard deviation of three independent experiments (without AGuIX®, N=152, with AGuIX®, N=118). Dotted lines correspond to proliferative depth in spheroids.

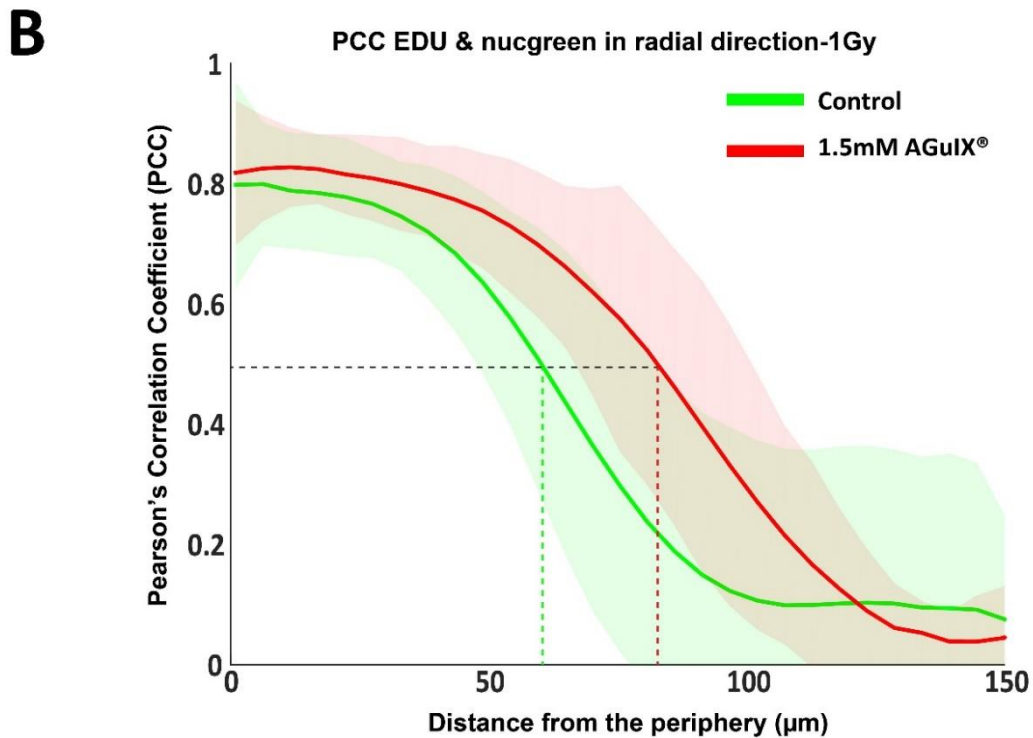
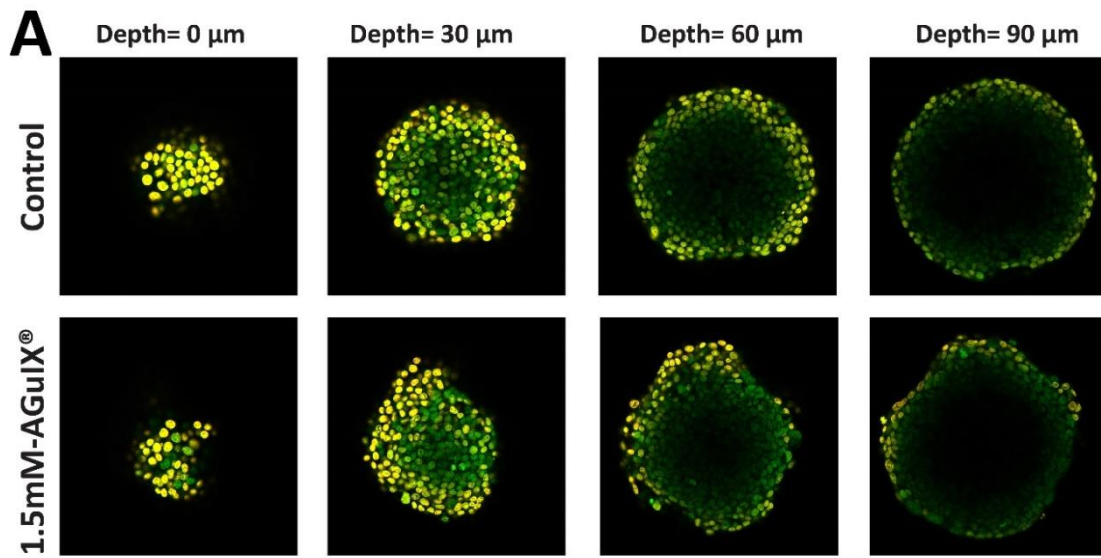


Figure 3.9 (A) Overlaid images acquired using confocal fluorescence microscopy of cell nucleus in HCT-116 spheroids irradiated at 1 Gy dose, where green channel shows nucleus stained with nucgreen™ dead 488 and red channel show nucleus of proliferative cells labelled with Click-iT®-EdU 555, Yellow color displays superposition of these channels indicating proliferative cells in spheroids. (B) Mean of Pearson's correlation coefficient for EdU and nucgreen™ channel in radial direction as a function of distance from the periphery and light colors are standard deviation of a single experiment (without AGuIX®, N=55, with AGuIX®, N=21). Dotted lines correspond to proliferative depth in spheroids.

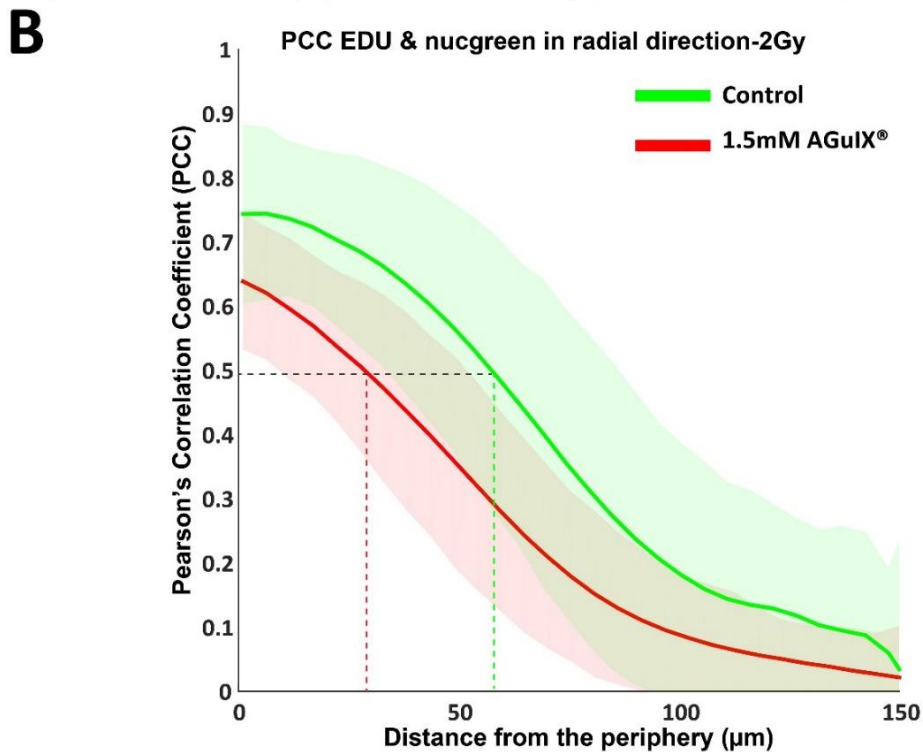
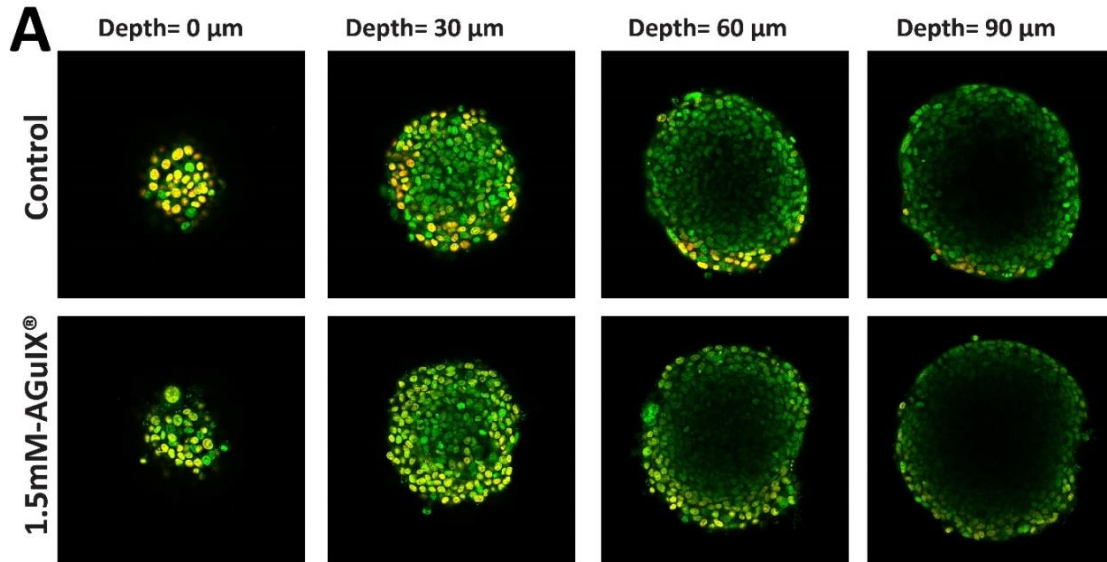


Figure 3.10 (A) Overlaid images acquired using confocal fluorescence microscopy of cell nucleus in HCT-116 spheroids irradiated at 2 Gy dose, where green channel shows nucleus stained with nucgreen™ dead 488 and red channel show nucleus of proliferative cells labelled with Click-iT®-EdU 555, Yellow color displays superposition of these channels indicating proliferative cells in spheroids. (B) Mean of Pearson's correlation coefficient for EdU and nucgreen™ channel in radial direction as a function of distance from the periphery and light colors are standard deviation of three independent experiments (without AGuIX®, N=110, with AGuIX®, N=114). Dotted lines correspond to proliferative depth in spheroids.

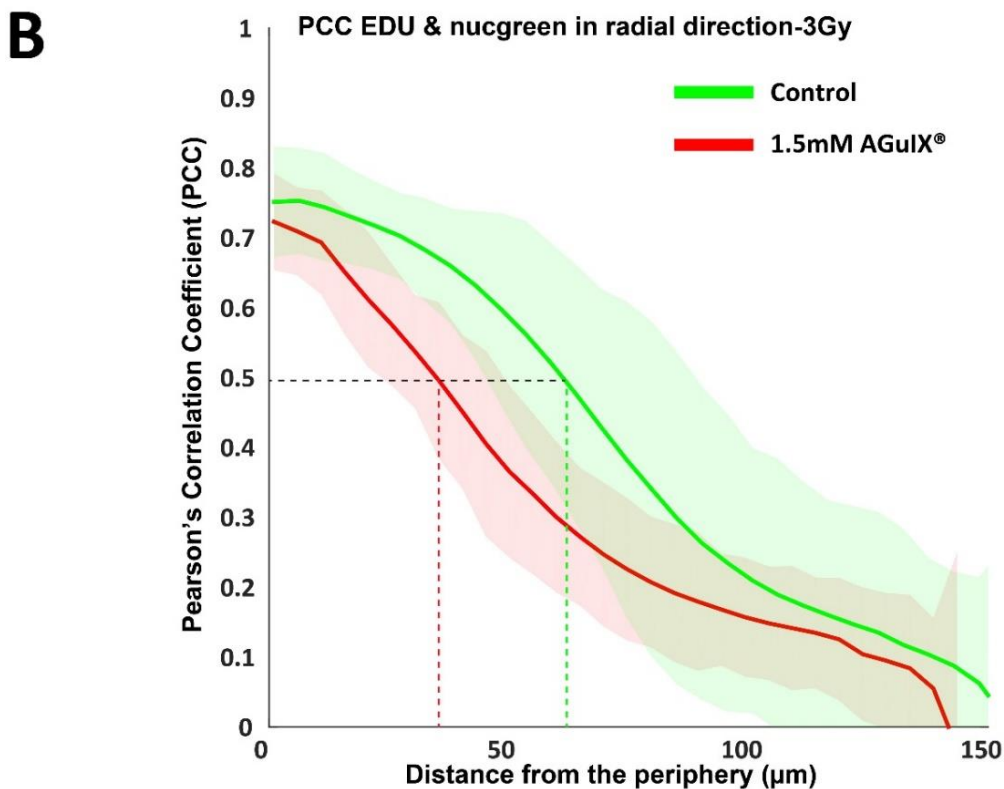
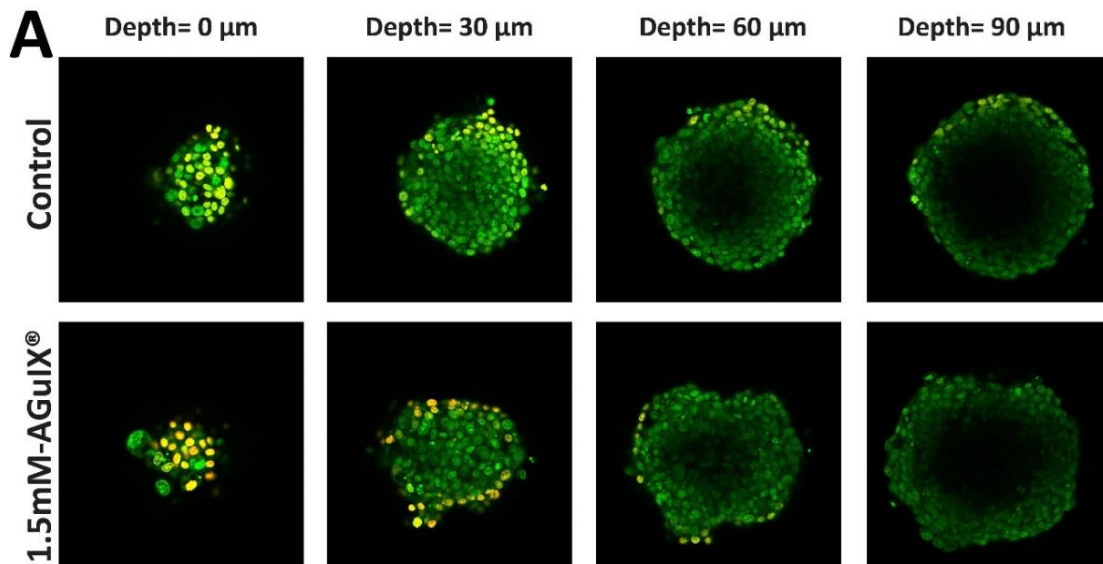


Figure 3.11 (A) Overlaid images acquired using confocal fluorescence microscopy of cell nucleus in HCT-116 spheroids irradiated at 3 Gy dose, where green channel shows nucleus stained with nucgreen™ dead 488 and red channel show nucleus of proliferative cells labelled with Click-iT®-EdU 555, Yellow color displays superposition of these channels indicating proliferative cells in spheroids. (B) Mean of Pearson's correlation coefficient for EdU and nucgreen™ channel in radial direction as a function of distance from the periphery and light colors are standard deviation of a single experiment (without AGuIX®, N=20, with AGuIX®, N=38). Dotted lines correspond to proliferative depth in spheroids.

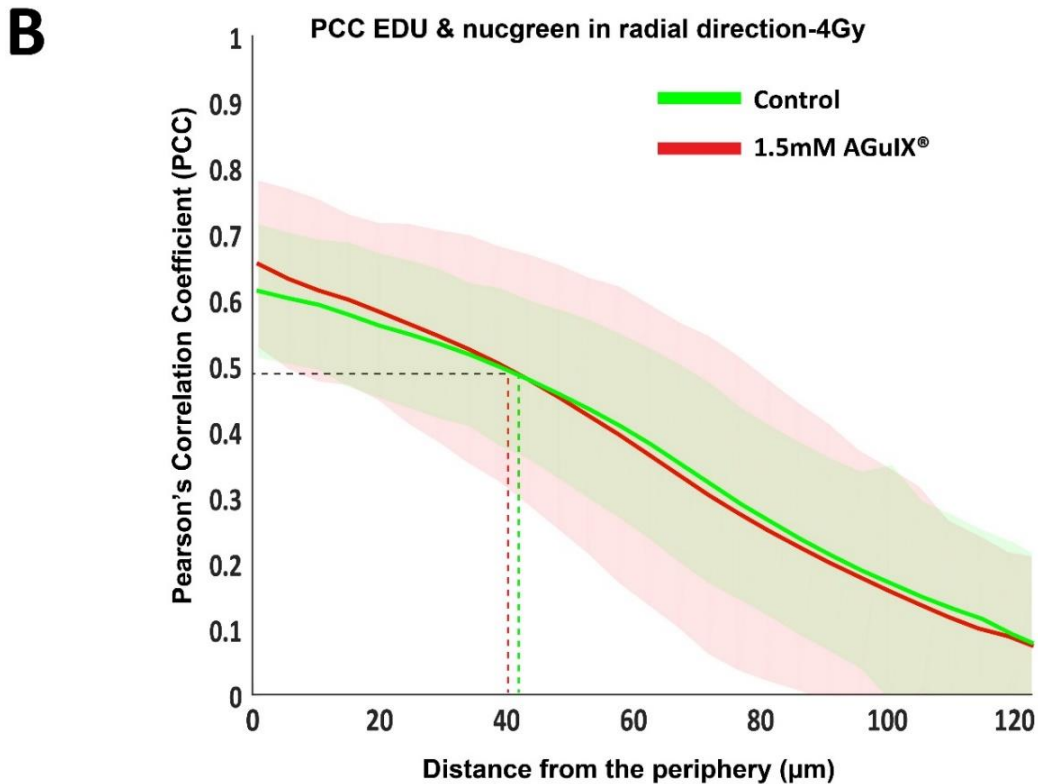
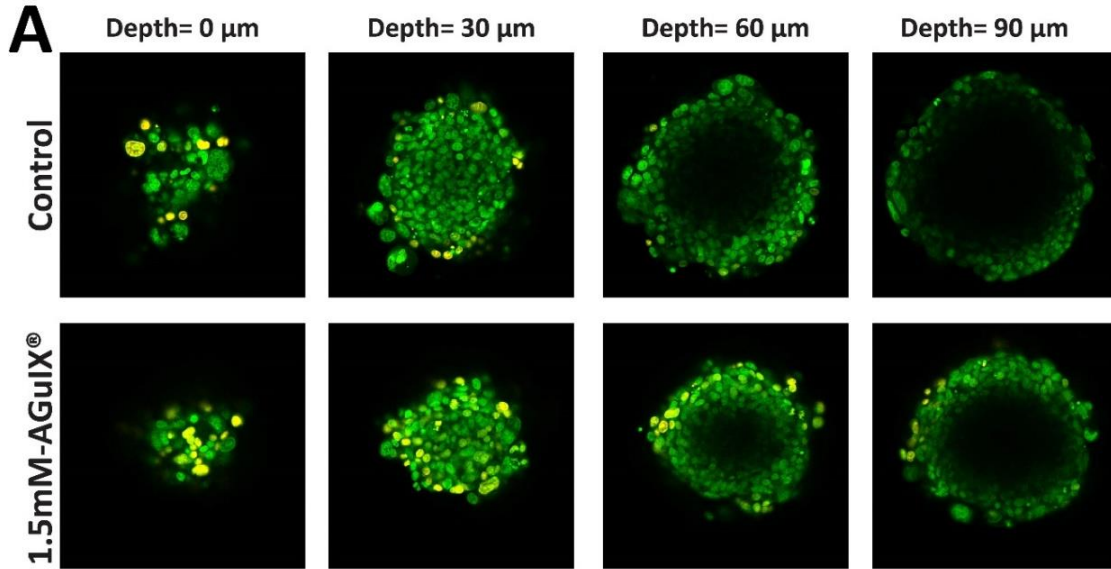


Figure 3.12 (A) Overlaid images acquired using confocal fluorescence microscopy of cell nucleus in HCT-116 spheroids irradiated at 4 Gy dose, where green channel shows nucleus stained with nucgreen™ dead 488 and red channel show nucleus of proliferative cells labelled with Click-iT[®]-EdU 555, Yellow color displays superposition of these channels indicating proliferative cells in spheroids. (B) Mean of Pearson's correlation coefficient for EdU and nucgreen™ channel in radial direction as a function of distance from the periphery and light colors are standard deviation of three independent experiments (without AGuIX[®], N=102, with AGuIX[®], N=89). Dotted lines correspond to proliferative depth in spheroids.

The images of spheroids irradiated at 6 Gy were shown in **Fig.3.13** displayed very few proliferative cells could be observed even at peripheral zone, consequently, the quantification approach did not seem valid for 6 Gy dose, since PCC calculation is valid when the intensity of fluorescence channels are higher than background (263). While in 6 Gy, due to the lack of proliferation in cells, EdU intensity is almost at the level of the background.

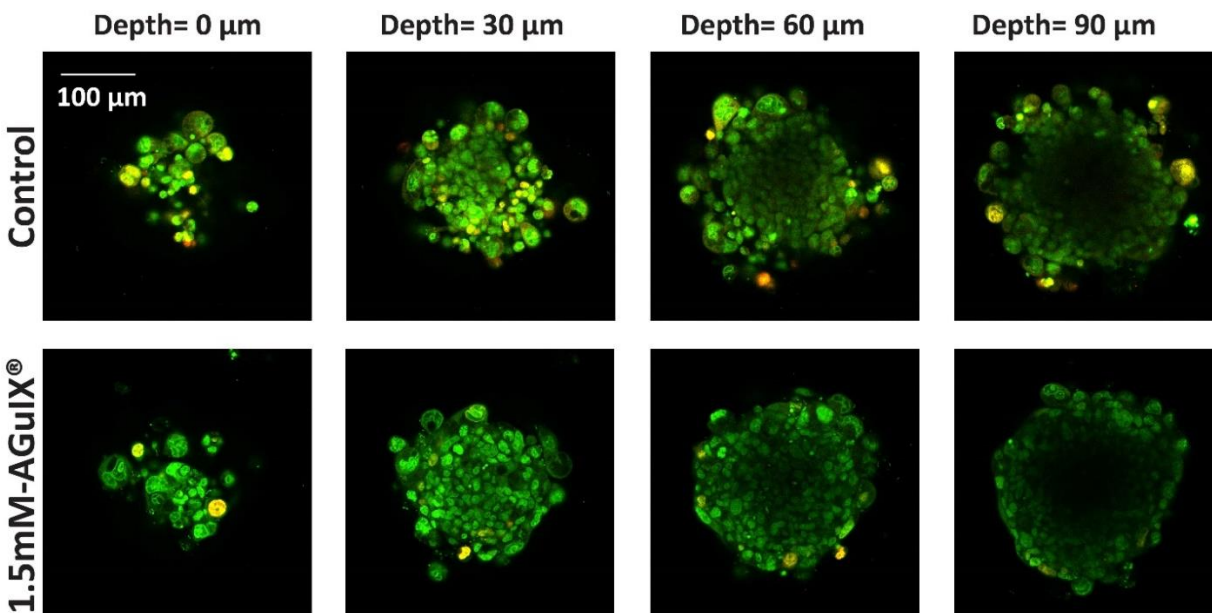


Figure 3.13 (A) Overlaid images acquired using confocal fluorescence microscopy of cell nuclei in HCT-116 spheroids irradiated at **6 Gy** dose, where green channel shows nuclei stained with nucgreen™ dead 488 and red channel show nuclei of proliferative cells labelled with Click-iT®-EdU 555, Yellow color displays superposition of these channels indicating proliferative cells in spheroids.

Generally, overlaid images of EdU and nucgreen™ showed that the depth of the proliferative layer decreases with increase in irradiation dose, insofar that in 6 Gy there were only few proliferative cells at the periphery of spheroids. The analysis of PCC for EdU and nucgreen™ in all radiation doses (except 1 Gy) showed a higher value for spheroids that were not incubated with AGuIX®-Cy5.5 nanoparticles, implying that AGuIX®-Cy5.5 nanoparticles boosted the efficacy of irradiation in HCT-116 spheroids, as further quantified below

From these analyses, we chose to synthetically represent the results using the measure of the proliferative depth as a proxy for the radiotherapy efficacy (**Fig. 3.14**, the lower the proliferative layer, the better the efficacy of the treatment). While for control spheroids, a decrease in the proliferative depth is only visible at 4Gy (from $57.0 \pm 4.2 \mu\text{m}$ to $43.5 \pm 3.5 \mu\text{m}$ for control vs 4Gy

respectively), the decrease is already important at 2 Gy in the presence of AGuIX[®] (reduction of the proliferative layer from 58.5±3.5 μm to 27.0±7.0 μm for control vs 2Gy).

In a similar calculation of Sensitizing enhancement ratio (SER) for clonogenic assay at 2 Gy, this ratio was calculated using proliferative depths of spheroids not exposed and exposed to AGuIX[®], the SER_{2Gy} of AGuIX[®] was calculated 51.3 % which is very close to SER_{2Gy} value of 50%, calculated by survival fractions in clonogenic assay.

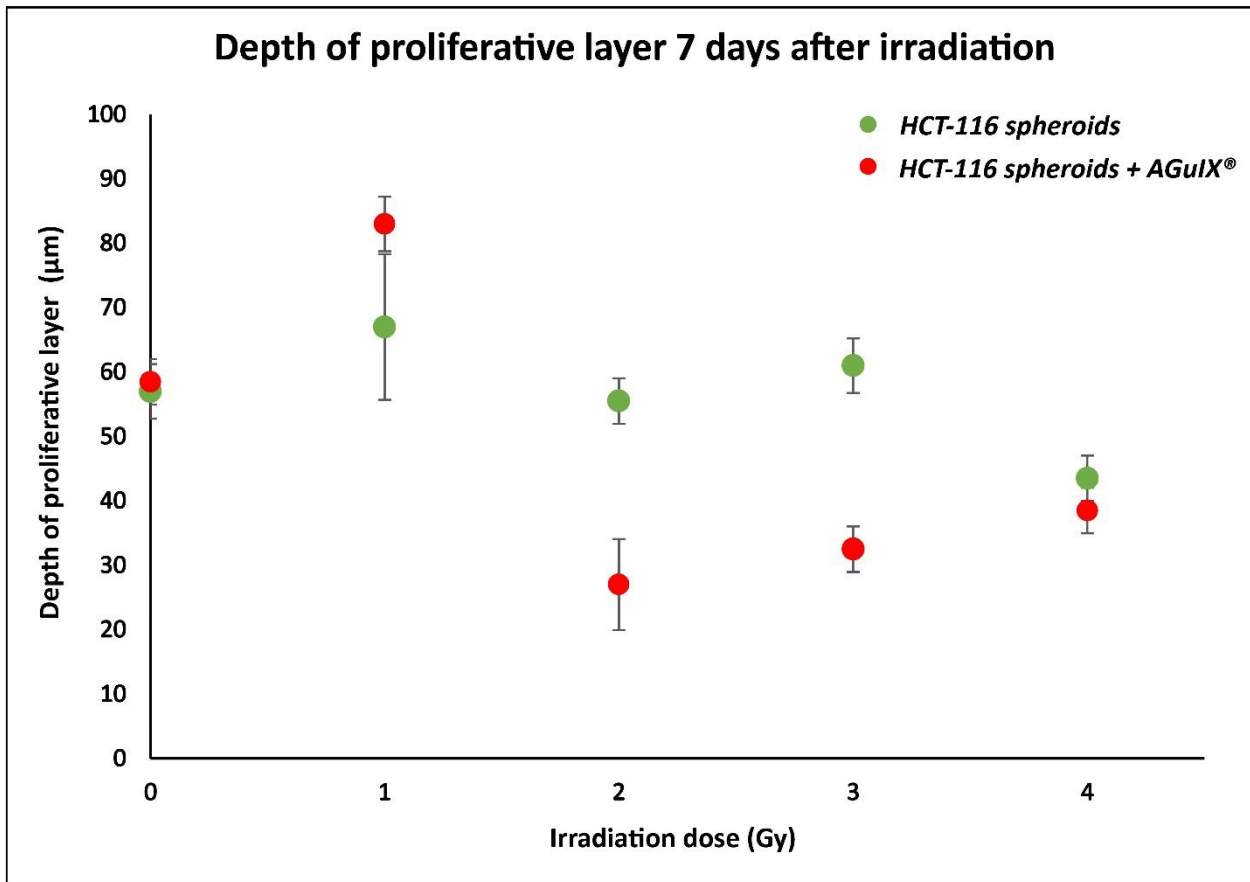


Figure 3.14. Depth of proliferative zone in HCT-116 spheroids exposed 7 days after irradiation. Using the calculation of Pearson's Correlation Coefficient for EdU and nucgreen[™] channels in all conditions, the values higher than 0.5 considered a proliferative cell. Green dots correspond to HCT-116 spheroids not exposed to AGuIX[®]-Cy5.5 nanoparticles, red dots correspond to HCT-116 spheroids exposed to 1,5 mM AGuIX[®]-Cy5.5 nanoparticles. Error bars are standard deviation of three independent experiments.

Conclusion

The agarose-based microsystem, which has previously been validated for tracking nanoparticle penetration and subcellular localization in a 3D cellular model, was used to assess the therapeutic efficacy of AGuIX[®]-Cy5.5 nanoparticles in combination with radiotherapy. This 3D in vitro model has been shown to be compatible with the classic clonogenic assay, the in vitro gold standard for assessing cell radiosensitivity. In this study, optical microscopy-based assays were used to enable post-treatment monitoring of multicellular tumor spheroids without dissociating them. HCT-116 spheroids outperformed monolayer HCT-116 cells in terms of radioresistance, highlighting the benefit of using such 3D in vitro models for assessing cell response to radiotherapy in preclinical studies. Interestingly, growth follow-up of HCT-116 spheroids revealed their ability to grow after irradiation in all doses, while the growth rate decreased at higher doses, emphasizing the need for the follow-up of intact spheroids after irradiation. The highest radiosensitizing effect of AGuIX[®] was found at 2 Gy in a study of cell proliferation 7 days after irradiation and the unique image analysis approach intending to quantify proliferative depth at each dose was consistent with clonogenic survival assay resulting in very close SER value for sensitizing effect of AGuIX[®] at 2 Gy irradiation.

4. Supplementary Materials

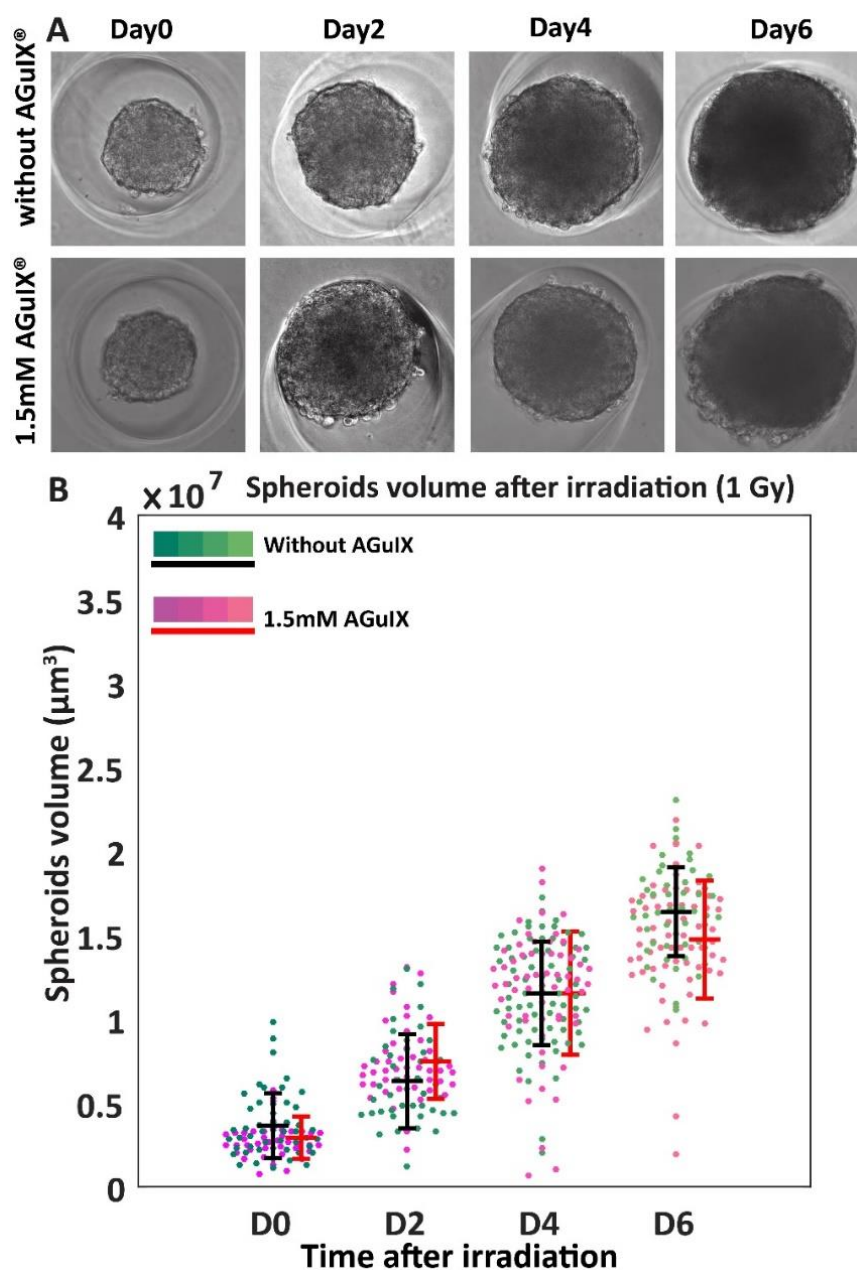


Figure SI.1. Spheroids growth follow-up using phase contrast microscopy. (A) spheroids images at day 0,2,4 and 6 after irradiation with phase contrast microscopy (1 Gy) (B) Scatter plot of the volume of spheroids with and without AGuIX[®]-Cy5.5 nanoparticles were calculated by manual segmentation of spheroids area in images in Matlab and scatter plots were plotted using the MATLAB UnivarScatter function (©Manuel Lera Ramírez, 2015, available in MATLAB exchange files), pink dots are the volume of single spheroids treated with AGuIX[®]-Cy5.5, with grey error bar showing mean and standard deviation of three independent experiments. Green dots show the volume of single spheroids were not exposed to AGuIX[®]-Cy5.5 with black.

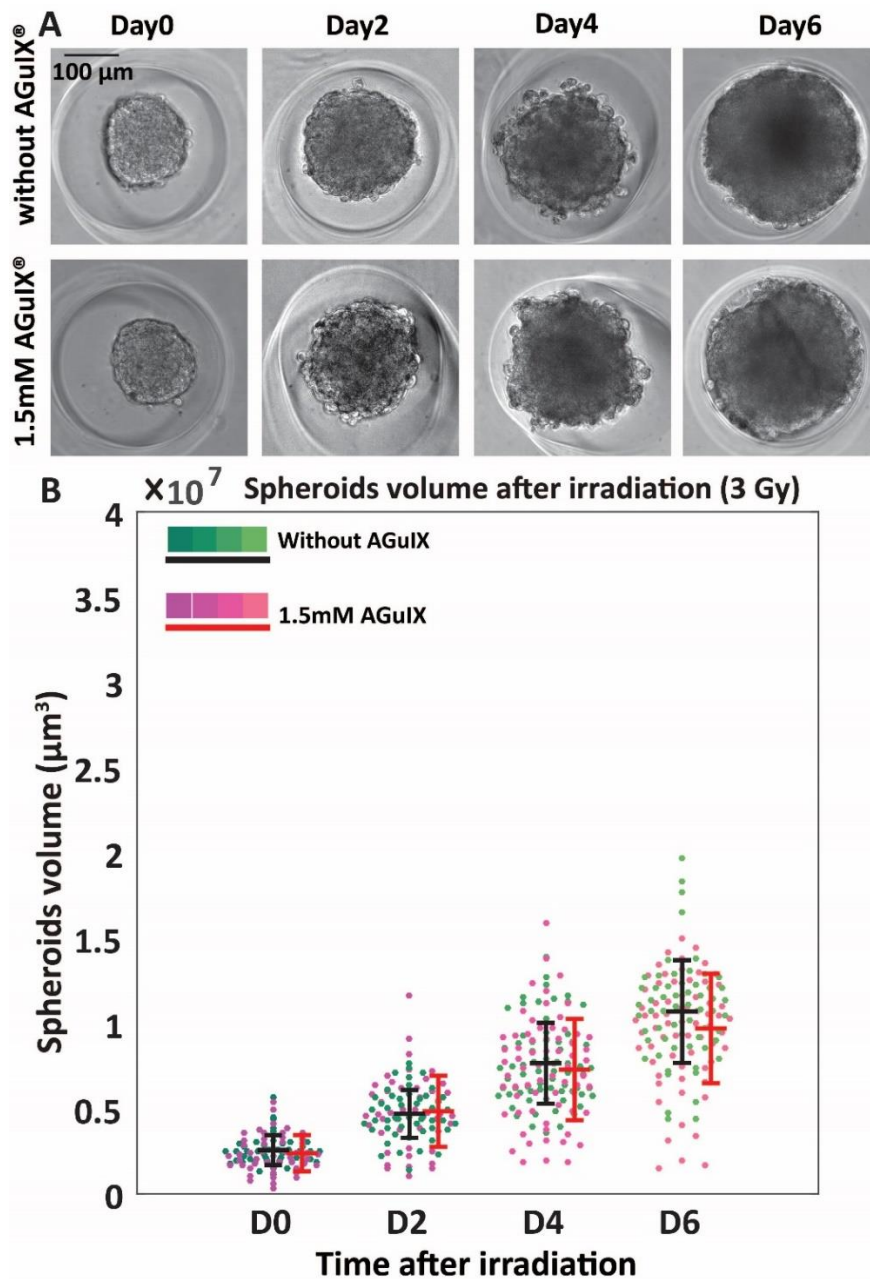


Figure SI.2. Spheroids growth follow-up using phase contrast microscopy. (A) spheroids images at day 0, 2, 4 and 6 after irradiation with phase contrast microscopy (3 Gy) (B) Scatter plot of the volume of spheroids with and without AGuIX[®]-Cy5.5 nanoparticles were calculated by manual segmentation of spheroids area in images in Matlab and scatter plots were plotted using the MATLAB UnivarScatter function (©Manuel Lera Ramirez, 2015, available in MATLAB exchange files), pink dots are the volume of single spheroids treated with AGuIX[®]-Cy5.5, with grey error bar showing mean and standard deviation of three independent experiments. Green dots show the volume of single spheroids were not exposed to AGuIX[®]-Cy5.5 with black error bar showing mean and standard deviation of spheroids volume in single experiment (without AGuIX[®], N=70, with AGuIX[®], N=69).

5. Outlooks of this work

Although HCT-116 cells were more resistant in spheroids than in 2D culture, detecting the radiosensitization effect of AGuiX[®]-Cy5.5 nanoparticles at higher doses was challenging due to intrinsic radiosensitivity of the HCT116 cell line. As a result, the irradiation dose in subsequent studies must be reduced to an optimal window for this cell line. The effect of nanoparticles was best revealed at 2 Gy. Spheroids' growth was monitored for up to six days after irradiation, though in future studies, spheroids' growth will be monitored for a longer period using microsystems with larger microwells to increase our knowledge regarding the effect of radiation on spheroids' growth. In addition, live and dead assay that has been done with epifluorescence microscopy could be performed via confocal fluorescence microscopy enabling observing inside of spheroids to quantitatively analyze dead cells distribution.

In a preliminary experiment, an assay was designed to evaluate the ability of HCT-116 single cells derived from irradiated spheroids to form spheres. The single cell seeding protocol developed by Alexis Chambost was used to seed cells obtained by dissociating HCT-116 spheroids after irradiation (similar to clonogenic assay). The single cells were then imaged with bright field microscopy using 10X objective on day 0 to find single cells in microwells, day 3 and day 7 to find spheres. Images were analyzed using a convolutional neural network developed by Alexis Chambost. For each condition, the percentage of single cells that formed spheres was calculated and plotted. A similar sensitivity was found using a 3D single cell assay (**Fig. 3.15**). The ability to form sphere start to decrease with irradiation larger than 2Gy with or without the presence of AGuiX[®]. But interestingly, the percentage of cells able to form sphere decrease much more in the presence of AGuiX[®] (60 % for spheroids not exposed to AGuiX[®] and 43% for spheroids exposed to AGuiX[®] at 2 Gy). The 3D in vitro system used for single cell seeding in agarose microwells after irradiation revealed that not only cells in spheroid form after irradiation, but also when seeded as single cells in a 3D manner, show more resistance to irradiation.

Despite the fact that this experiment was only conducted once, the results were promising and Alexis's 3D in vitro model for single cell seeding has the potential for developing a reproducible and standard 3D clonal assay for such studies to go beyond classical clonogenic assay.

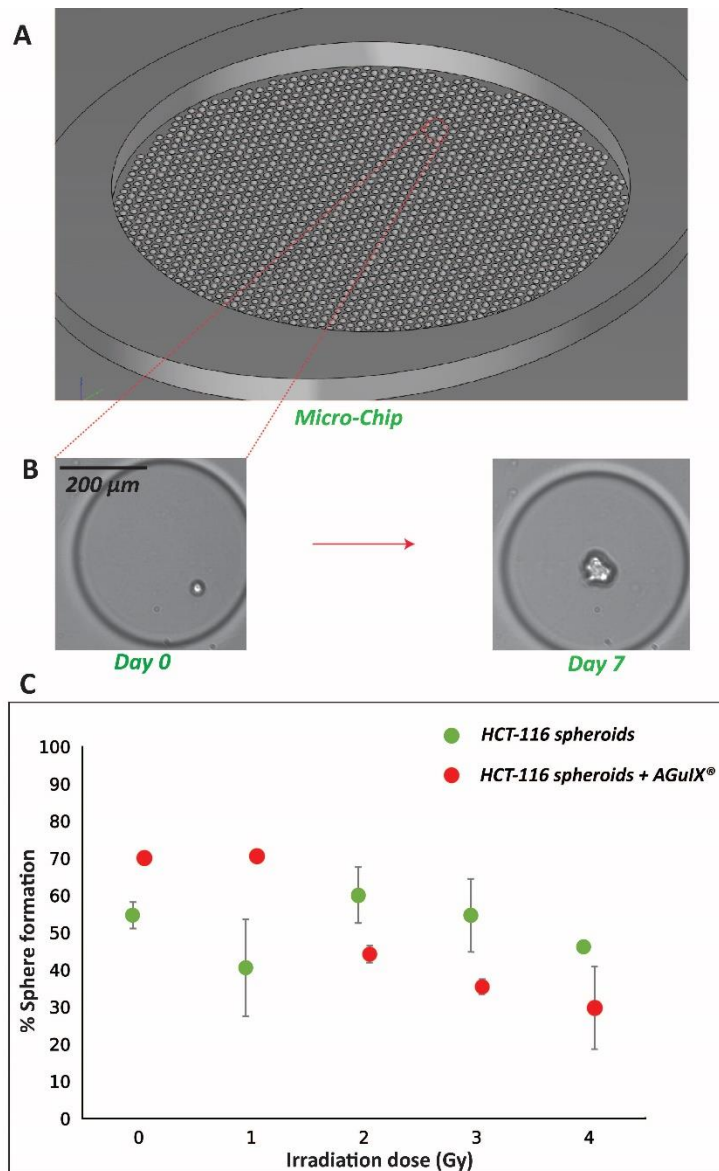


Figure 3.20. Screening the ability of irradiated single cells to form spheres after irradiation. (A) Agarose based microchip designed for single cell seeding; $d = 200 \mu\text{m}$. (B) Bright field microscopy images of a single cells at day 0 and formed sphere at day 7 after irradiation (10X). (C) The percentage of single cells formed spheres during 7 days after irradiation in a single experiment (accuracy=89.3 %, $N = 892$ cells). The error bars are standard deviation of two replicates for each condition.

Chapter 4. Conclusion and Perspectives

General Conclusion

The 3D *in vitro* models based on multicellular tumor spheroids must not only be capable of producing spheroids and maintaining them in culture for several days, but they must also be compatible with the various characterization techniques currently used for nanotherapeutics screening, such as classical biological assays, optical microscopy techniques, and other techniques. To achieve these goals, hydrogel based microsystems were designed and developed in the Biophysics Team of the Institute of Light and Matter (ILM).

In my PhD which was a proof of concept study, microsystem with a specific design containing 130 cylindrical microwells with a diameter of 200 μm have been prepared using agarose hydrogel for spheroids generation. The colorectal cancer cell lines, HCT-116, which are capable of forming coherent spheroids, were used as a cellular model, and radiosensitizing AGuIX[®]- Cy5.5 nanoparticles developed by the FENNEC team of the ILM were used as a model of nanoparticles. These nanoparticles were introduced to HCT-116 spheroids to explore their penetration, distribution, kinetics of penetration, and localization in multicellular tumor spheroids. Cellular uptake of AGuIX[®]- Cy5.5 nanoparticles in HCT-116 monolayer cells (2D) and HCT-116 spheroids (3D) were compared. For characterization of cell-nanoparticle interactions, optical microscopy techniques, primarily confocal fluorescence microscopy and, to a lesser extent, time-lapse phase contrast microscopy, were used. The acquired images were then analyzed in Matlab using dedicated routines. Because AGuIX[®]- Cy5.5 nanoparticles are composed of polysiloxane and gadolinium chelates, the ICP-MS technique could be used to measure quantitatively cellular uptake of these nanoparticles based on gadolinium concentration; thus, a protocol compatible with this measurement was developed in order to achieve reliable and reproducible results.

The findings of this section of the study first demonstrated the feasibility and advantages of using this 3D *in vitro* model to investigate various aspects of cell-nanoparticle interactions in a 3D cellular architecture. The results also revealed that the penetration of AGuIX[®]- Cy5.5 nanoparticles is highly dependent on the incubation concentration and duration. Localizations of AGuIX[®]- Cy5.5 nanoparticles in HCT-116 spheroids and monolayer cells were studied using confocal fluorescence microscopy. While nanoparticles are residing in both extracellular and intracellular space in spheroids, their main intracellular localization in both 2D and 3D are within lysosomes. Nevertheless, they were also observed in other compartments, such as early endosomes and mitochondria. Interestingly, further quantifications of images using Matlab based on the calculation of Pearson's Correlation Coefficient revealed that nanoparticle localizations in 2D and 3D were different; indicating that intracellular fate in monolayer cells and cell spheroids is different. Variable access to nanoparticles when cells are organized in a 3D structure like spheroids, as well as gradients in pH, oxygen, and nutrients, are all factors that influence

nanoparticle internalization, highlighting the advantages of using such 3D *in vitro* models in cell-nanoparticle interactions research while enabling screening of all these parameters with highly remarkable statistics.

While another interesting element of cell-nanoparticle interactions is understanding how nanoparticles or any therapeutic agent can affect cell viability and cell proliferation, 3D *in vitro* spheroids models appear promising for such studies, as the growth rate of spheroids could be tracked using time-lapse microscopy, live and dead assays could be implemented and assessed using fluorescence microscopy and proliferative cells could be labeled with Click-iT® EdU incorporating newly synthesized DNA and imaged via confocal fluorescence microscopy. These experiments were carried out with high throughput thanks to the agarose-based microwells used in this project, resulted in statistically reliable results. The findings showed that the presence of AGuIX®-Cy5.5 nanoparticles alone do not affect the growth rate of HCT-116 spheroids. This 3D *in vitro* model has also been used to investigate the distribution and localization of another type of nanoparticle, polymer nanoparticles and polymer chains, emphasizing the utility of using this *in vitro* model in nanotherapeutics screening.

These experiments served as the foundation for another part of my PhD, which aimed to assess the therapeutic efficacy of AGuIX®-Cy5.5 in the radiotherapy of HCT-116 cells in spheroids. The primary experiment, which aimed to assess HCT-116 cells' radiosensitivity using a classical clonogenic assay, revealed that HCT-116 cells in spheroid form had higher radioresistance than HCT-116 monolayer cells, indicating that this 3D model could replicate response to therapy in an *in vitro* platform. Further experiments were carried out to determine the therapeutic efficacy of AGuIX®-Cy5.5 on HCT-116 spheroids, which were analyzed using a classical clonogenic survival assay as well as optical microscopy techniques for spheroids growth, cell proliferation, and live/dead assays after irradiation with various doses. The findings confirmed AGuIX®-Cy5.5's radiosensitizing effects, which were previously reported in other AGuIX® preclinical studies. However, in higher doses radiosensitizing effect of AGuIX® was not detectable due to intrinsic radiosensitivity of HCT-116 cell line implying the importance of choosing the right irradiation range for each cell line. The highest radiosensitization effect of AGuIX®-Cy5.5 was observed at 2 Gy, where a SER of 50 % for AGuIX®-Cy5.5 was found, meaning that these NPs amplified the efficacy of irradiation by 50 %. Furthermore, clonogenic assays revealed that HCT-116 cells were incapable of forming colonies when seeded very diluted in a 2D manner; while in a 6-day growth follow-up of spheroids after irradiation, spheroids continued to grow and the growth rate decreased as the radiation dose increased. The cell proliferation assay that I used for my PhD allowed us to see the effect of irradiation at the single cell level in spheroids and quantify the cell proliferation in a unique approach using Pearson's Correlation Coefficient. In study of cell proliferation 7 days after treatment at single cell level, again, the highest radiosensitivity of AGuIX®-Cy5.5 was observed at 2 Gy, where depth of proliferative layer in control spheroids decreased by 50% in spheroids exposed to AGuIX®-Cy5.5.

Perspectives

During my PhD, I validated agarose-based microwells for the production of hundreds to thousands of homogeneous spheroids and their characterization using various nanotherapeutics assessment techniques.

Basically, these agarose-based microwells can be changed and their mechanical properties, such as stiffness, which was in the range of 150 kPa, can be adjusted and prepared with very low stiffness around 1 kPa using a low concentration of ultra-low agarose. The design of these microwells could also be changed depending on the experiment's goal. Microwells with larger wells, for example, enable exploring the impact of spheroids' size on microenvironment parameters like hypoxia and acidity, as well as cellular response to treatments.

Parameters such as cell cohesion, the presence of extracellular matrix, and a heterogeneous cell population, on the other hand, could be provided in this 3D *in vitro* model, making the microenvironment more complex and changing cell-nanoparticle interaction and therapy response. For instance, a colorectal cancer cell model can be created using cell lines with varying metastatic stages and invasive properties (low to high invasiveness; HT-29, HCT-116, SW-620), or stromal cells such as cancer associated fibroblast can be added to cancerous cells to increase extracellular matrix in spheroids, which influences cell responses to treatments. As shown, response to treatment can be investigated using a variety of optical based microscopy techniques. The longer growth follow-up could extend our knowledge in tumor growth after irradiation, which of course needs microsystems with larger microwells enabling extended culture of spheroids. Other assays, such as the invasion assay, which has already been applied to spheroids in a preliminary experiment, could be used to promote nanotherapeutics screening in simple to complex spheroids models, while reinforcing the classical clonogenic assay, which is a gold standard in radiosensitization studies but is not adapted for 3D models. In general, the model I developed for my PhD has promising potential for simulating natural tumor microenvironments of varying complexity as well as high-throughput drug and nanoparticle screening. Because of its ability to generate a large number of uniform spheroids and change various parameters, this novel model is a powerful tool for studying tumor physiological and biological properties, as well as *in vitro* studies of novel nanotherapeutics.

REFERENCES

1. Brancato V, Oliveira JM, Correlo VM, Reis RL, Kundu SC. Could 3D models of cancer enhance drug screening? *Biomaterials*. 2020;232.
2. Cekanova M, Rathore K. Animal models and therapeutic molecular targets of cancer: utility and limitations. *Drug Des Devel Ther* [Internet]. 2014 Oct;1911. Available from: <http://www.dovepress.com/animal-models-and-therapeutic-molecular-targets-of-cancer-utility-and-peer-reviewed-article-DDDT>
3. Ellem SJ, De-Juan-Pardo EM, Risbridger GP. In vitro modeling of the prostate cancer microenvironment. *Adv Drug Deliv Rev* [Internet]. 2014 Dec;79–80:214–21. Available from: <https://linkinghub.elsevier.com/retrieve/pii/S0169409X14000933>
4. Choi SYC, Lin D, Gout PW, Collins CC, Xu Y, Wang Y. Lessons from patient-derived xenografts for better in vitro modeling of human cancer. *Adv Drug Deliv Rev* [Internet]. 2014 Dec;79–80:222–37. Available from: <https://linkinghub.elsevier.com/retrieve/pii/S0169409X14002075>
5. Sung KE, Beebe DJ. Microfluidic 3D models of cancer. *Adv Drug Deliv Rev* [Internet]. 2014 Dec;79–80:68–78. Available from: <https://linkinghub.elsevier.com/retrieve/pii/S0169409X14001434>
6. Kimlin L, Kassis J, Virador V. 3D in vitro tissue models and their potential for drug screening. *Expert Opin Drug Discov*. 2013;8(12):1455–66.
7. Lipponen P, Aaltomaa S, Tammi R, Tammi M, Ågren U, Kosma V-M. High stromal hyaluronan level is associated with poor differentiation and metastasis in prostate cancer. *Eur J Cancer* [Internet]. 2001 May;37(7):849–56. Available from: <https://linkinghub.elsevier.com/retrieve/pii/S0959804900004482>
8. Thoma CR, Zimmermann M, Agarkova I, Kelm JM, Krek W. 3D cell culture systems modeling tumor growth determinants in cancer target discovery. *Adv Drug Deliv Rev* [Internet]. 2014 Apr;69–70:29–41. Available from: <https://linkinghub.elsevier.com/retrieve/pii/S0169409X14000350>
9. Luca AC, Mersch S, Deenen R, Schmidt S, Messner I, Schäfer K-L, et al. Impact of the 3D Microenvironment on Phenotype, Gene Expression, and EGFR Inhibition of Colorectal Cancer Cell Lines. Cordes N, editor. *PLoS One* [Internet]. 2013 Mar 26;8(3):e59689. Available from: <https://dx.plos.org/10.1371/journal.pone.0059689>
10. Asghar W, El Assal R, Shafiee H, Pitteri S, Paulmurugan R, Demirci U. Engineering cancer microenvironments for in vitro 3-D tumor models. *Materials Today*. 2015.
11. Li L, Sun J, He Z. Deep Penetration of Nanoparticulate Drug Delivery Systems into Tumors: Challenges and Solutions. *Curr Med Chem* [Internet]. 2013 Jun 1;20(23):2881–91. Available from: <http://www.eurekaselect.com/openurl/content.php?genre=article&issn=0929-8673&volume=20&issue=23&page=2881>
12. Carver K, Ming X, Juliano RL. Multicellular Tumor Spheroids as a Model for Assessing Delivery of Oligonucleotides in Three Dimensions. *Mol Ther - Nucleic Acids* [Internet]. 2014 Jan;3(January):e153. Available from: <http://dx.doi.org/10.1038/mtna.2014.5>
13. Huang BW, Gao JQ. Application of 3D cultured multicellular spheroid tumor models in tumor-

- targeted drug delivery system research. *J Control Release*. 2018;270(December 2017):246–59.
14. Meng F, Meyer CM, Joung D, Vallera DA, McAlpine MC, Panoskaltsis-Mortari A. 3D Bioprinted In Vitro Metastatic Models via Reconstruction of Tumor Microenvironments. *Adv Mater* [Internet]. 2019 Mar;31(10):1806899. Available from: <http://doi.wiley.com/10.1002/adma.201806899>
 15. Kunz-Schughart L. Multicellular tumor spheroids: intermediates between monolayer culture and in vivo tumor. *Cell Biol Int* [Internet]. 1999 Mar;23(3):157–61. Available from: <http://doi.wiley.com/10.1006/cbir.1999.0384>
 16. Hirschhaeuser F, Menne H, Dittfeld C, West J, Mueller-Klieser W, Kunz-Schughart LA. Multicellular tumor spheroids: An underestimated tool is catching up again. *J Biotechnol* [Internet]. 2010;148(1):3–15. Available from: <http://dx.doi.org/10.1016/j.jbiotec.2010.01.012>
 17. Friedrich J, Ebner R, Kunz-Schughart LA. Experimental anti-tumor therapy in 3-D: Spheroids – old hat or new challenge? *Int J Radiat Biol* [Internet]. 2007 Jan 3;83(11–12):849–71. Available from: <https://www.tandfonline.com/doi/full/10.1080/09553000701727531>
 18. Friedrich J, Seidel C, Ebner R, Kunz-Schughart LA. Spheroid-based drug screen: considerations and practical approach. *Nat Protoc* [Internet]. 2009 Mar 12;4(3):309–24. Available from: <http://www.nature.com/articles/nprot.2008.226>
 19. Gong X, Lin C, Cheng J, Su J, Zhao H, Liu T, et al. Generation of multicellular tumor spheroids with microwell-based agarose scaffolds for drug testing. *PLoS One*. 2015;10(6):1–18.
 20. Rodrigues J, Heinrich MA, Teixeira LM, Prakash J. 3D In Vitro Model (R)evolution: Unveiling Tumor–Stroma Interactions. *Trends in Cancer* [Internet]. 2021 Mar;7(3):249–64. Available from: <https://linkinghub.elsevier.com/retrieve/pii/S2405803320302831>
 21. Mukhopadhyay R. When PDMS isn't the best. *Anal Chem*. 2007;79(9):3249–53.
 22. Riviere Charlotte , Prunet Audrey , Fuoco Layla AH. BIOCOMPATIBLE HYDROGEL MICROWELL PLATES [Internet]. FR3079524A1, 2018. Available from: <https://patents.google.com/patent/FR3079524A1/en#patentCitations>
 23. Lux F, Tran VL, Thomas E, Dufort S, Rossetti F, Martini M, et al. AGuiX[®] from bench to bedside-transfer of an ultrasmall theranostic gadolinium-based nanoparticle to clinical medicine. *British Journal of Radiology*. 2019.
 24. Virgone-Carlotta A, Lemasson M, Mertani HC, Diaz J-J, Monnier S, Dehoux T, et al. In-depth phenotypic characterization of multicellular tumor spheroids: Effects of 5-Fluorouracil. Castresana JS, editor. *PLoS One* [Internet]. 2017 Nov 15;12(11):e0188100. Available from: <https://dx.plos.org/10.1371/journal.pone.0188100>
 25. Balkwill FR, Capasso M, Hagemann T. The tumor microenvironment at a glance. *J Cell Sci*. 2012;125(23):5591–6.
 26. Wang M, Zhao J, Zhang L, Wei F, Lian Y, Wu Y, et al. Role of tumor microenvironment in tumorigenesis. *J Cancer*. 2017;8(5):761–73.
 27. Labani-Motlagh A, Ashja-Mahdavi M, Loskog A. The Tumor Microenvironment: A Milieu Hindering and Obstructing Antitumor Immune Responses. *Front Immunol*. 2020;11(May):1–22.

28. Brassart-Pasco S, Brézillon S, Brassart B, Ramont L, Oudart JB, Monboisse JC. Tumor Microenvironment: Extracellular Matrix Alterations Influence Tumor Progression. *Front Oncol*. 2020;10(April):1–13.
29. Siemann DW. Tumor Microenvironment [Internet]. Siemann DW, editor. Tumor Microenvironment. Chichester, UK: John Wiley & Sons, Ltd; 2010. Available from: <http://doi.wiley.com/10.1002/9780470669891>
30. Cheng YQ, Wang SB, Liu JH, Jin L, Liu Y, Li CY, et al. Modifying the tumour microenvironment and reverting tumour cells: New strategies for treating malignant tumours. *Cell Prolif*. 2020;53(8):1–17.
31. Farhood B, Najafi M, Mortezaee K. CD8+ cytotoxic T lymphocytes in cancer immunotherapy: A review. *J Cell Physiol*. 2019;234(6):8509–21.
32. Vitale I, Manic G, Coussens LM, Kroemer G, Galluzzi L. Macrophages and Metabolism in the Tumor Microenvironment. *Cell Metab [Internet]*. 2019;30(1):36–50. Available from: <https://doi.org/10.1016/j.cmet.2019.06.001>
33. Whiteside TL. The tumor microenvironment and its role in promoting tumor growth. *Oncogene*. 2008;27(45):5904–12.
34. De Palma M, Biziato D, Petrova T V. Microenvironmental regulation of tumour angiogenesis. *Nat Rev Cancer [Internet]*. 2017;17(8):457–74. Available from: <http://dx.doi.org/10.1038/nrc.2017.51>
35. Shi R, Tang Y, Miao H. Metabolism in tumor microenvironment: Implications for cancer immunotherapy. *MedComm [Internet]*. 2020 Jun 3;1(1):47–68. Available from: <https://onlinelibrary.wiley.com/doi/abs/10.1002/mco2.6>
36. Ribeiro Franco PI, Rodrigues AP, de Menezes LB, Pacheco Miguel M. Tumor microenvironment components: Allies of cancer progression. *Pathol Res Pract [Internet]*. 2020;216(1):152729. Available from: <https://doi.org/10.1016/j.prp.2019.152729>
37. Henke E, Nandigama R, Ergün S. Extracellular Matrix in the Tumor Microenvironment and Its Impact on Cancer Therapy. *Front Mol Biosci*. 2020;6(January):1–24.
38. Egeblad M, Rasch MG, Weaver VM. Dynamic interplay between the collagen scaffold and tumor evolution. *Curr Opin Cell Biol [Internet]*. 2010;22(5):697–706. Available from: <http://dx.doi.org/10.1016/j.ceb.2010.08.015>
39. Wyckoff JB, Wang Y, Lin EY, Li JF, Goswami S, Stanley ER, et al. Direct visualization of macrophage-assisted tumor cell intravasation in mammary tumors. *Cancer Res*. 2007;67(6):2649–56.
40. Loo CH. Tumor microenvironment. *Mass Transport of Nanocarriers*. 2012. 185–219 p.
41. Theocharis AD, Tsara ME, Papageorgacopoulou N, Karavias DD, Theocharis DA. Pancreatic carcinoma is characterized by elevated content of hyaluronan and chondroitin sulfate with altered disaccharide composition. *Biochim Biophys Acta - Mol Basis Dis [Internet]*. 2000 Oct;1502(2):201–6. Available from: <https://linkinghub.elsevier.com/retrieve/pii/S092544390000051X>
42. Cheng XB, Sato N, Kohi S, Yamaguchi K. Prognostic impact of hyaluronan and its regulators in pancreatic ductal adenocarcinoma. *PLoS One*. 2013;8(11):1–7.

43. Bertrand P, Girard N, Delpech B, Duval C, D'Anjou J, Dauce JP. Hyaluronan (hyaluronic acid) and hyaluronectin in the extracellular matrix of human breast carcinomas: Comparison between invasive and non-invasive areas. *Int J Cancer* [Internet]. 1992 Aug 19;52(1):1–6. Available from: <http://doi.wiley.com/10.1002/ijc.2910520102>
44. Auvinen PK, Parkkinen JJ, Johansson RT, Ågren UM, Tammi RH, Eskelinen MJ, et al. Expression of hyaluronan in benign and malignant breast lesions. *Int J Cancer* [Internet]. 1997 Oct 21;74(5):477–81. Available from: [https://onlinelibrary.wiley.com/doi/10.1002/\(SICI\)1097-0215\(19971021\)74:5%3C477::AID-IJC1%3E3.0.CO;2-0](https://onlinelibrary.wiley.com/doi/10.1002/(SICI)1097-0215(19971021)74:5%3C477::AID-IJC1%3E3.0.CO;2-0)
45. Wang C, Tammi M, Guo H, Tammi R. Hyaluronan distribution in the normal epithelium of esophagus, stomach, and colon and their cancers. *Am J Pathol*. 1996;148(6):1861–9.
46. Jadin L, Pastorino S, Symons R, Nomura N, Jiang P, Juarez T, et al. Hyaluronan expression in primary and secondary brain tumors. *Ann Transl Med*. 2015;3(6).
47. Knudson W, Biswas C, Toole BP. Interactions between human tumor cells and fibroblasts stimulate hyaluronate synthesis. *Proc Natl Acad Sci* [Internet]. 1984 Nov 1;81(21):6767–71. Available from: <http://www.pnas.org/cgi/doi/10.1073/pnas.81.21.6767>
48. Zhang H, Tsang JYS, Ni Y-B, Chan S-K, Chan K-F, Cheung S-Y, et al. Hyaluronan synthase 2 is an adverse prognostic marker in androgen receptor-negative breast cancer. *J Clin Pathol* [Internet]. 2016 Dec;69(12):1055–62. Available from: <http://jcp.bmj.com/lookup/doi/10.1136/jclinpath-2016-203617>
49. Engvall E, Wewer UM. Domains of laminin. *J Cell Biochem* [Internet]. 1996 Jun 16;61(4):493–501. Available from: [https://onlinelibrary.wiley.com/doi/10.1002/\(SICI\)1097-4644\(19960616\)61:4%3C493::AID-JCB2%3E3.0.CO;2-J](https://onlinelibrary.wiley.com/doi/10.1002/(SICI)1097-4644(19960616)61:4%3C493::AID-JCB2%3E3.0.CO;2-J)
50. Gudjonsson T. Isolation, immortalization, and characterization of a human breast epithelial cell line with stem cell properties. *Genes Dev* [Internet]. 2002 Mar 15;16(6):693–706. Available from: <http://www.genesdev.org/cgi/doi/10.1101/gad.952602>
51. Malinda KM, Kleinman HK. The laminins. *Int J Biochem Cell Biol* [Internet]. 1996 Sep;28(9):957–9. Available from: <https://linkinghub.elsevier.com/retrieve/pii/1357272596000428>
52. Alon Y, Horowitz AT, Biran S, Weiss DW, Doljanski F. Immunofluorescent characterization of fibronectin, laminin, and keratin in normal and neoplastic human mammary epithelial cells in culture and in breast tissue sections. *Int J Tissue React* [Internet]. 1986;8(5):401–10. Available from: <http://www.ncbi.nlm.nih.gov/pubmed/2430910>
53. Lyssiotis CA, Kimmelman AC. Metabolic Interactions in the Tumor Microenvironment. *Trends Cell Biol* [Internet]. 2017;27(11):863–75. Available from: <http://dx.doi.org/10.1016/j.tcb.2017.06.003>
54. Wiedmann RM, von Schwarzenberg K, Palamidessi A, Schreiner L, Kubisch R, Liebl J, et al. The V-ATPase-Inhibitor Archazolid Abrogates Tumor Metastasis via Inhibition of Endocytic Activation of the Rho-GTPase Rac1. *Cancer Res* [Internet]. 2012 Nov 15;72(22):5976–87. Available from: <http://cancerres.aacrjournals.org/lookup/doi/10.1158/0008-5472.CAN-12-1772>
55. Estrella V, Chen T, Lloyd M, Wojtkowiak J, Cornell HH, Ibrahim-Hashim A, et al. Acidity generated by the tumor microenvironment drives local invasion. *Cancer Res*. 2013;73(5):1524–35.

56. Luo W, Wang Y. Hypoxia mediates tumor malignancy and therapy resistance. *Adv Exp Med Biol*. 2019;1136:1–18.
57. Kaemmerer E, Loessner D, Avery VM. Addressing the tumour microenvironment in early drug discovery: a strategy to overcome drug resistance and identify novel targets for cancer therapy. *Drug Discov Today* [Internet]. 2021;26(3):663–76. Available from: <https://doi.org/10.1016/j.drudis.2020.11.030>
58. Trédan O, Galmarini CM, Patel K, Tannock IF. Drug resistance and the solid tumor microenvironment. *J Natl Cancer Inst*. 2007;99(19):1441–54.
59. Carmona-Fontaine C, Deforet M, Akkari L, Thompson CB, Joyce JA, Xavier JB. Metabolic origins of spatial organization in the tumor microenvironment. *Proc Natl Acad Sci* [Internet]. 2017 Mar 14;114(11):2934–9. Available from: <http://www.pnas.org/lookup/doi/10.1073/pnas.1700600114>
60. Libutti SK, Tamarkin L, Nilubol N. Targeting the invincible barrier for drug delivery in solid cancers: interstitial fluid pressure. *Oncotarget* [Internet]. 2018 Nov 6;9(87):35723–5. Available from: <https://www.oncotarget.com/lookup/doi/10.18632/oncotarget.26267>
61. Yu T, Wang Z, Liu K, Wu Y, Fan J, Chen J, et al. High interstitial fluid pressure promotes tumor progression through inducing lymphatic metastasis-related protein expressions in oral squamous cell carcinoma. *Clin Transl Oncol* [Internet]. 2014 Jun 2;16(6):539–47. Available from: <http://link.springer.com/10.1007/s12094-013-1115-0>
62. Wei R, Liu S, Zhang S, Min L, Zhu S. Cellular and Extracellular Components in Tumor Microenvironment and Their Application in Early Diagnosis of Cancers. *Anal Cell Pathol* [Internet]. 2020 Jan 8;2020:1–13. Available from: <https://www.hindawi.com/journals/acp/2020/6283796/>
63. Yamauchi M, Barker TH, Gibbons DL, Kurie JM. The fibrotic tumor stroma. *J Clin Invest* [Internet]. 2018 Jan 2;128(1):16–25. Available from: <https://www.jci.org/articles/view/93554>
64. Muz B, de la Puente P, Azab F, Azab AK. The role of hypoxia in cancer progression, angiogenesis, metastasis, and resistance to therapy. *Hypoxia (Auckland, NZ)* [Internet]. 2015;3:83–92. Available from: <http://www.ncbi.nlm.nih.gov/pubmed/27774485>
65. Wojtkowiak JW, Verduzco D, Schramm KJ, Gillies RJ. Drug resistance and cellular adaptation to tumor acidic pH microenvironment. *Mol Pharm* [Internet]. 2011 Dec 5;8(6):2032–8. Available from: <http://www.ncbi.nlm.nih.gov/pubmed/21981633>
66. Williams AC, Collard TJ, Paraskeva C. An acidic environment leads to p53 dependent induction of apoptosis in human adenoma and carcinoma cell lines: implications for clonal selection during colorectal carcinogenesis. *Oncogene* [Internet]. 1999 May 25;18(21):3199–204. Available from: <http://www.nature.com/articles/1202660>
67. Nath S, Devi GR. Three-dimensional culture systems in cancer research: Focus on tumor spheroid model. *Pharmacol Ther* [Internet]. 2016;163:94–108. Available from: <http://dx.doi.org/10.1016/j.pharmthera.2016.03.013>
68. Unger C, Kramer N, Walzl A, Scherzer M, Hengstschläger M, Dolznig H. Modeling human carcinomas: Physiologically relevant 3D models to improve anti-cancer drug development. *Adv Drug Deliv Rev* [Internet]. 2014 Dec;79–80:50–67. Available from: <https://linkinghub.elsevier.com/retrieve/pii/S0169409X14002233>

69. Santo VE, Rebelo SP, Estrada MF, Alves PM, Boghaert E, Brito C. Drug screening in 3D in vitro tumor models: overcoming current pitfalls of efficacy read-outs. *Biotechnol J* [Internet]. 2017 Jan;12(1):1600505. Available from: <http://doi.wiley.com/10.1002/biot.201600505>
70. Zaroni M, Piccinini F, Arienti C, Zamagni A, Santi S, Polico R, et al. 3D tumor spheroid models for in vitro therapeutic screening: A systematic approach to enhance the biological relevance of data obtained. *Sci Rep*. 2016;6(August 2015):1–11.
71. Mehta G, Hsiao AY, Ingram M, Luker GD, Takayama S. Opportunities and challenges for use of tumor spheroids as models to test drug delivery and efficacy. *J Control Release*. 2012;164(2):192–204.
72. Nunes AS, Barros AS, Costa EC, Moreira AF, Correia IJ. 3D tumor spheroids as in vitro models to mimic in vivo human solid tumors resistance to therapeutic drugs. *Biotechnol Bioeng*. 2019;116(1):206–26.
73. Mahmood TA, De Jong R, Riesle J, Langer R, Van Blitterswijk CA. Adhesion-mediated signal transduction in human articular chondrocytes: The influence of biomaterial chemistry and tenascin-C. *Exp Cell Res*. 2004;301(2):179–88.
74. Cui X, Hartanto Y, Zhang H. Advances in multicellular spheroids formation. *J R Soc Interface*. 2017;14(127).
75. Ivanov DP, Parker TL, Walker DA, Alexander C, Ashford MB, Gellert PR, et al. Multiplexing Spheroid Volume, Resazurin and Acid Phosphatase Viability Assays for High-Throughput Screening of Tumour Spheroids and Stem Cell Neurospheres. Mancini MA, editor. *PLoS One* [Internet]. 2014 Aug 13;9(8):e103817. Available from: <https://dx.plos.org/10.1371/journal.pone.0103817>
76. Edmondson R, Broglie JJ, Adcock AF, Yang L. Three-dimensional cell culture systems and their applications in drug discovery and cell-based biosensors. *Assay Drug Dev Technol*. 2014;12(4):207–18.
77. Zietarska M, Maugard CM, Filali-Mouhim A, Alam-Fahmy M, Tonin PN, Provencher DM, et al. Molecular description of a 3D in vitro model for the study of epithelial ovarian cancer (EOC). *Mol Carcinog*. 2007;46(10):872–85.
78. Fontoura JC, Viezzer C, Dos Santos FG, Ligabue RA, Weinlich R, Puga RD, et al. Comparison of 2D and 3D cell culture models for cell growth, gene expression and drug resistance. *Mater Sci Eng C Mater Biol Appl* [Internet]. 2020 Feb;107:110264. Available from: <http://www.ncbi.nlm.nih.gov/pubmed/31761183>
79. IMAMURA Y, MUKOHARA T, SHIMONO Y, FUNAKOSHI Y, CHAYAHARA N, TOYODA M, et al. Comparison of 2D- and 3D-culture models as drug-testing platforms in breast cancer. *Oncol Rep* [Internet]. 2015 Apr;33(4):1837–43. Available from: <https://www.spandidos-publications.com/10.3892/or.2015.3767>
80. Breslin S, O’Driscoll L. The relevance of using 3D cell cultures, in addition to 2D monolayer cultures, when evaluating breast cancer drug sensitivity and resistance. *Oncotarget* [Internet]. 2016 Jul 19;7(29):45745–56. Available from: <https://www.oncotarget.com/lookup/doi/10.18632/oncotarget.9935>
81. Fernandes S, Cassani M, Pagliari S, Filipensky P, Cavalieri F, Forte G. Tumor in 3D: In Vitro Complex

Cellular Models to Improve Nanodrugs Cancer Therapy. *Curr Med Chem*. 2020;27(42):7234–55.

82. Stevens JL, Baker TK. The future of drug safety testing: expanding the view and narrowing the focus. *Drug Discov Today* [Internet]. 2009 Feb;14(3–4):162–7. Available from: <https://linkinghub.elsevier.com/retrieve/pii/S1359644608004066>
83. Huh D, Matthews BD, Mammoto A, Montoya-Zavala M, Hsin HY, Ingber DE. Reconstituting Organ-Level Lung Functions on a Chip. *Science* (80-) [Internet]. 2010 Jun 25;328(5986):1662–8. Available from: <https://www.sciencemag.org/lookup/doi/10.1126/science.1188302>
84. Lv D, Hu Z, Lu L, Lu H, Xu X. Three-dimensional cell culture: A powerful tool in tumor research and drug discovery. *Oncol Lett*. 2017;14(6):6999–7010.
85. Achilli T-M, Meyer J, Morgan JR. Advances in the formation, use and understanding of multi-cellular spheroids. *Expert Opin Biol Ther* [Internet]. 2012 Oct 12;12(10):1347–60. Available from: <http://www.tandfonline.com/doi/full/10.1517/14712598.2012.707181>
86. Kenny PA, Lee GY, Myers CA, Neve RM, Semeiks JR, Spellman PT, et al. The morphologies of breast cancer cell lines in three-dimensional assays correlate with their profiles of gene expression. *Mol Oncol* [Internet]. 2007 Jun;1(1):84–96. Available from: <http://doi.wiley.com/10.1016/j.molonc.2007.02.004>
87. Weaver VM, Bissell MJ, Fischer AH, Peterson OW. The importance of the microenvironment in breast cancer progression: recapitulation of mammary tumorigenesis using a unique human mammary epithelial cell model and a three-dimensional culture assay. *Biochem Cell Biol* [Internet]. 1996 Dec 1;74(6):833–51. Available from: <http://www.nrcresearchpress.com/doi/10.1139/o96-089>
88. Debnath J, Brugge JS. Modelling glandular epithelial cancers in three-dimensional cultures. *Nat Rev Cancer* [Internet]. 2005 Sep;5(9):675–88. Available from: <http://www.nature.com/articles/nrc1695>
89. Debnath J, Muthuswamy SK, Brugge JS. Morphogenesis and oncogenesis of MCF-10A mammary epithelial acini grown in three-dimensional basement membrane cultures. *Methods* [Internet]. 2003 Jul;30(3):256–68. Available from: <https://linkinghub.elsevier.com/retrieve/pii/S104620230300032X>
90. Shaw KRM, Wrobel CN, Brugge JS. Use of Three-Dimensional Basement Membrane Cultures to Model Oncogene-Induced Changes in Mammary Epithelial Morphogenesis. *J Mammary Gland Biol Neoplasia* [Internet]. 2004 Oct;9(4):297–310. Available from: <http://link.springer.com/10.1007/s10911-004-1402-z>
91. Mabry KM, Payne SZ, Anseth KS. Microarray analyses to quantify advantages of 2D and 3D hydrogel culture systems in maintaining the native valvular interstitial cell phenotype. *Biomaterials* [Internet]. 2016 Jan;74:31–41. Available from: <https://linkinghub.elsevier.com/retrieve/pii/S0142961215007863>
92. Caballero D, Kaushik S, Correlo VM, Oliveira JM, Reis RL, Kundu SC. Organ-on-chip models of cancer metastasis for future personalized medicine: From chip to the patient. *Biomaterials* [Internet]. 2017 Dec;149:98–115. Available from: <https://linkinghub.elsevier.com/retrieve/pii/S014296121730635X>
93. Melissaridou S, Wiechec E, Magan M, Jain MV, Chung MK, Farnebo L, et al. The effect of 2D and

- 3D cell cultures on treatment response, EMT profile and stem cell features in head and neck cancer. *Cancer Cell Int* [Internet]. 2019 Dec 14;19(1):16. Available from: <https://cancer-ci.biomedcentral.com/articles/10.1186/s12935-019-0733-1>
94. Duval K, Grover H, Han L-H, Mou Y, Pegoraro AF, Fredberg J, et al. Modeling Physiological Events in 2D vs. 3D Cell Culture. *Physiology* [Internet]. 2017 Jul;32(4):266–77. Available from: <https://www.physiology.org/doi/10.1152/physiol.00036.2016>
 95. Langhans SA. Three-Dimensional in Vitro Cell Culture Models in Drug Discovery and Drug Repositioning. *Front Pharmacol* [Internet]. 2018 Jan 23;9. Available from: <http://journal.frontiersin.org/article/10.3389/fphar.2018.00006/full>
 96. Costa EC, Moreira AF, de Melo-Diogo D, Gaspar VM, Carvalho MP, Correia IJ. 3D tumor spheroids: an overview on the tools and techniques used for their analysis. *Biotechnol Adv* [Internet]. 2016 Dec;34(8):1427–41. Available from: <https://linkinghub.elsevier.com/retrieve/pii/S0734975016301379>
 97. Zanoni M, Piccinini F, Arienti C, Zamagni A, Santi S, Polico R, et al. 3D tumor spheroid models for in vitro therapeutic screening: a systematic approach to enhance the biological relevance of data obtained. *Sci Rep* [Internet]. 2016 Jan 11;6:19103. Available from: <http://www.ncbi.nlm.nih.gov/pubmed/26752500>
 98. Carvalho MP, Costa EC, Miguel SP, Correia IJ. Tumor spheroid assembly on hyaluronic acid-based structures: A review. *Carbohydr Polym* [Internet]. 2016 Oct;150:139–48. Available from: <https://linkinghub.elsevier.com/retrieve/pii/S0144861716305185>
 99. Fang Y, Eglen RM. Three-Dimensional Cell Cultures in Drug Discovery and Development. *SLAS Discov Adv Sci Drug Discov* [Internet]. 2017 Jun 18;22(5):456–72. Available from: <http://journals.sagepub.com/doi/10.1177/1087057117696795>
 100. Knight E, Przyborski S. Advances in 3D cell culture technologies enabling tissue-like structures to be created in vitro. *J Anat*. 2015;227(6):746–56.
 101. Carletti E, Motta A, Migliaresi C. Scaffolds for Tissue Engineering and 3D Cell Culture. In 2011. p. 17–39. Available from: http://link.springer.com/10.1007/978-1-60761-984-0_2
 102. Sultana N, Hassan MI, Lim MM. Composite Synthetic Scaffolds for Tissue Engineering and Regenerative Medicine [Internet]. Cham: Springer International Publishing; 2015. (SpringerBriefs in Materials). Available from: <http://link.springer.com/10.1007/978-3-319-09755-8>
 103. Lu T, Li Y, Chen T. Techniques for fabrication and construction of three-dimensional scaffolds for tissue engineering. *Int J Nanomedicine* [Internet]. 2013 Jan;337. Available from: <http://www.dovepress.com/techniques-for-fabrication-and-construction-of-three-dimensional-scaff-peer-reviewed-article-IJN>
 104. Gupta N, Liu JR, Patel B, Solomon DE, Vaidya B, Gupta V. Microfluidics-based 3D cell culture models: Utility in novel drug discovery and delivery research. *Bioeng Transl Med* [Internet]. 2016 Mar 5;1(1):63–81. Available from: <https://onlinelibrary.wiley.com/doi/10.1002/btm2.10013>
 105. Datta P, Dey M, Ataie Z, Unutmaz D, Ozbolat IT. 3D bioprinting for reconstituting the cancer microenvironment. *npj Precis Oncol*. 2020;4(1).

106. Oztan YC, Nawafleh N, Zhou Y, Liyanage PY, Hettiarachchi SD, Seven ES, et al. Recent advances on utilization of bioprinting for tumor modeling. *Bioprinting*. 2020;18(November 2019).
107. Langer EM, Allen-Petersen BL, King SM, Kendersky ND, Turnidge MA, Kuziel GM, et al. Modeling Tumor Phenotypes In Vitro with Three-Dimensional Bioprinting. *Cell Rep [Internet]*. 2019;26(3):608-623.e6. Available from: <https://doi.org/10.1016/j.celrep.2018.12.090>
108. Daly AC, Prendergast ME, Hughes AJ, Burdick JA. Bioprinting for the Biologist. *Cell*. 2021;184(1):18–32.
109. Vanaei S, Parizi MS, Vanaei S, Salemizadehparizi F, Vanaei HR. An Overview on Materials and Techniques in 3D Bioprinting Toward Biomedical Application. *Eng Regen*. 2021;2(December 2020):1–18.
110. Li J, Chen M, Fan X, Zhou H. Recent advances in bioprinting techniques: Approaches, applications and future prospects. *J Transl Med*. 2016;14(1):1–15.
111. Dai X, Liu L, Ouyang J, Li X, Zhang X, Lan Q, et al. Coaxial 3D bioprinting of self-assembled multicellular heterogeneous tumor fibers. *Sci Rep [Internet]*. 2017 Dec 3;7(1):1457. Available from: <http://www.nature.com/articles/s41598-017-01581-y>
112. Wang X, Li X, Dai X, Zhang X, Zhang J, Xu T, et al. Coaxial extrusion bioprinted shell-core hydrogel microfibers mimic glioma microenvironment and enhance the drug resistance of cancer cells. *Colloids Surfaces B Biointerfaces [Internet]*. 2018 Nov;171:291–9. Available from: <https://linkinghub.elsevier.com/retrieve/pii/S0927776518304909>
113. Kingsley DM, Roberge CL, Rudkouskaya A, Faulkner DE, Barroso M, Intes X, et al. Laser-based 3D bioprinting for spatial and size control of tumor spheroids and embryoid bodies. *Acta Biomater [Internet]*. 2019 Sep;95:357–70. Available from: <https://linkinghub.elsevier.com/retrieve/pii/S1742706119301187>
114. Wang Y, Shi W, Kuss M, Mirza S, Qi D, Krasnoslobodtsev A, et al. 3D Bioprinting of Breast Cancer Models for Drug Resistance Study. *ACS Biomater Sci Eng [Internet]*. 2018 Dec 10;4(12):4401–11. Available from: <https://pubs.acs.org/doi/10.1021/acsbomaterials.8b01277>
115. Almela T, Al-Sahaf S, Brook IM, Khoshroo K, Rasoulianboroujeni M, Fahimipour F, et al. 3D printed tissue engineered model for bone invasion of oral cancer. *Tissue Cell [Internet]*. 2018 Jun;52:71–7. Available from: <https://linkinghub.elsevier.com/retrieve/pii/S0040816618300089>
116. Wang X, Shan T, Pang S. Phytoremediation Potential of *Saccharina japonica* and *Sargassum horneri* (Phaeophyceae): Biosorption Study of Strontium. *Bull Environ Contam Toxicol [Internet]*. 2018 Oct 3;101(4):501–5. Available from: <http://link.springer.com/10.1007/s00128-018-2435-0>
117. Pang Y, Mao SS, Yao R, He JY, Zhou ZZ, Feng L, et al. TGF- β induced epithelial–mesenchymal transition in an advanced cervical tumor model by 3D printing. *Biofabrication [Internet]*. 2018 Sep 10;10(4):044102. Available from: <https://iopscience.iop.org/article/10.1088/1758-5090/aadbde>
118. Lee VK, Guohao Dai, Hongyan Zou, Seung-Schik Yoo. Generation of 3-D glioblastoma-vascular niche using 3-D bioprinting. In: 2015 41st Annual Northeast Biomedical Engineering Conference (NEBEC) [Internet]. IEEE; 2015. p. 1–2. Available from: <http://ieeexplore.ieee.org/document/7117111/>
119. Heinrich MA, Bansal R, Lammers T, Zhang YS, Michel Schiffelers R, Prakash J. 3D-Bioprinted Mini-

- Brain: A Glioblastoma Model to Study Cellular Interactions and Therapeutics. *Adv Mater* [Internet]. 2019 Apr;31(14):1806590. Available from: <https://onlinelibrary.wiley.com/doi/abs/10.1002/adma.201806590>
120. Duarte Campos DF, Bonnin Marquez A, O'Seanain C, Fischer H, Blaeser A, Vogt M, et al. Exploring Cancer Cell Behavior In Vitro in Three-Dimensional Multicellular Bioprintable Collagen-Based Hydrogels. *Cancers (Basel)* [Internet]. 2019 Feb 5;11(2):180. Available from: <http://www.mdpi.com/2072-6694/11/2/180>
 121. Skardal A, Devarasetty M, Forsythe S, Atala A, Soker S. A reductionist metastasis-on-a-chip platform for in vitro tumor progression modeling and drug screening. *Biotechnol Bioeng* [Internet]. 2016 Sep;113(9):2020–32. Available from: <http://doi.wiley.com/10.1002/bit.25950>
 122. Zhou X, Zhu W, Nowicki M, Miao S, Cui H, Holmes B, et al. 3D Bioprinting a Cell-Laden Bone Matrix for Breast Cancer Metastasis Study. *ACS Appl Mater Interfaces* [Internet]. 2016 Nov 9;8(44):30017–26. Available from: <https://pubs.acs.org/doi/10.1021/acsami.6b10673>
 123. Zhu W, Holmes B, Glazer RI, Zhang LG. 3D printed nanocomposite matrix for the study of breast cancer bone metastasis. *Nanomedicine Nanotechnology, Biol Med* [Internet]. 2016 Jan;12(1):69–79. Available from: <https://linkinghub.elsevier.com/retrieve/pii/S1549963415001884>
 124. Zervantonakis IK, Hughes-Alford SK, Charest JL, Condeelis JS, Gertler FB, Kamm RD. Three-dimensional microfluidic model for tumor cell intravasation and endothelial barrier function. *Proc Natl Acad Sci* [Internet]. 2012 Aug 21;109(34):13515–20. Available from: <http://www.pnas.org/cgi/doi/10.1073/pnas.1210182109>
 125. Dai X, Ma C, Lan Q, Xu T. 3D bioprinted glioma stem cells for brain tumor model and applications of drug susceptibility. *Biofabrication* [Internet]. 2016 Oct 11;8(4):045005. Available from: <https://iopscience.iop.org/article/10.1088/1758-5090/8/4/045005>
 126. Katt ME, Placone AL, Wong AD, Xu ZS, Searson PC. In vitro tumor models: Advantages, disadvantages, variables, and selecting the right platform. *Front Bioeng Biotechnol*. 2016;4(FEB).
 127. Soman P, Kelber JA, Lee JW, Wright TN, Vecchio KS, Klemke RL, et al. Cancer cell migration within 3D layer-by-layer microfabricated photocrosslinked PEG scaffolds with tunable stiffness. *Biomaterials* [Internet]. 2012 Oct;33(29):7064–70. Available from: <https://linkinghub.elsevier.com/retrieve/pii/S0142961212006485>
 128. Swaminathan S, Hamid Q, Sun W, Clyne AM. Bioprinting of 3D breast epithelial spheroids for human cancer models. *Biofabrication* [Internet]. 2019 Jan 24;11(2):025003. Available from: <https://iopscience.iop.org/article/10.1088/1758-5090/aafc49>
 129. Wang X, Zhang X, Dai X, Wang X, Li X, Diao J, et al. Tumor-like lung cancer model based on 3D bioprinting. *3 Biotech* [Internet]. 2018 Dec 27;8(12):501. Available from: <http://link.springer.com/10.1007/s13205-018-1519-1>
 130. Sánchez-Salazar MG, Álvarez MM, Trujillo-de Santiago G. Advances in 3D bioprinting for the biofabrication of tumor models. *Bioprinting*. 2021;21(December 2020).
 131. Nie J, Gao Q, Fu J, He Y. Grafting of 3D Bioprinting to In Vitro Drug Screening: A Review. *Adv Healthc Mater*. 2020;9(7):1–18.

132. Bengtsson A, Andersson R, Rahm J, Ganganna K, Andersson B, Ansari D. Organoid technology for personalized pancreatic cancer therapy. *Cell Oncol*. 2021;44(2):251–60.
133. Zachos NC, Kovbasnjuk O, Foulke-Abel J, In J, Blutt SE, de Jonge HR, et al. Human Enteroids/Colonoids and Intestinal Organoids Functionally Recapitulate Normal Intestinal Physiology and Pathophysiology. *J Biol Chem* [Internet]. 2016 Feb;291(8):3759–66. Available from: <https://linkinghub.elsevier.com/retrieve/pii/S0021925820436877>
134. Hofer M, Lutolf MP. Engineering organoids. *Nat Rev Mater* [Internet]. 2021;6(5):402–20. Available from: <http://dx.doi.org/10.1038/s41578-021-00279-y>
135. Sato T, Stange DE, Ferrante M, Vries RGJ, van Es JH, van den Brink S, et al. Long-term Expansion of Epithelial Organoids From Human Colon, Adenoma, Adenocarcinoma, and Barrett’s Epithelium. *Gastroenterology* [Internet]. 2011 Nov;141(5):1762–72. Available from: <https://linkinghub.elsevier.com/retrieve/pii/S0016508511011085>
136. Bartfeld S, Bayram T, van de Wetering M, Huch M, Begthel H, Kujala P, et al. In Vitro Expansion of Human Gastric Epithelial Stem Cells and Their Responses to Bacterial Infection. *Gastroenterology* [Internet]. 2015 Jan;148(1):126-136.e6. Available from: <https://linkinghub.elsevier.com/retrieve/pii/S0016508514012037>
137. Fujii M, Shimokawa M, Date S, Takano A, Matano M, Nanki K, et al. A Colorectal Tumor Organoid Library Demonstrates Progressive Loss of Niche Factor Requirements during Tumorigenesis. *Cell Stem Cell* [Internet]. 2016 Jun;18(6):827–38. Available from: <https://linkinghub.elsevier.com/retrieve/pii/S1934590916300467>
138. Sachs N, de Ligt J, Kopper O, Gogola E, Bounova G, Weeber F, et al. A Living Biobank of Breast Cancer Organoids Captures Disease Heterogeneity. *Cell* [Internet]. 2018 Jan;172(1–2):373-386.e10. Available from: <https://linkinghub.elsevier.com/retrieve/pii/S0092867417313193>
139. Gao D, Vela I, Sboner A, Iaquina PJ, Karthaus WR, Gopalan A, et al. Organoid Cultures Derived from Patients with Advanced Prostate Cancer. *Cell* [Internet]. 2014 Sep;159(1):176–87. Available from: <https://linkinghub.elsevier.com/retrieve/pii/S0092867414010472>
140. Drost J, Karthaus WR, Gao D, Driehuis E, Sawyers CL, Chen Y, et al. Organoid culture systems for prostate epithelial and cancer tissue. *Nat Protoc* [Internet]. 2016 Feb 21;11(2):347–58. Available from: <http://www.nature.com/articles/nprot.2016.006>
141. Broutier L, Mastrogiovanni G, Verstegen MM, Francies HE, Gavarró LM, Bradshaw CR, et al. Human primary liver cancer–derived organoid cultures for disease modeling and drug screening. *Nat Med* [Internet]. 2017 Dec 13;23(12):1424–35. Available from: <http://www.nature.com/articles/nm.4438>
142. Cao W, Liu J, Wang L, Li M, Verstegen MMA, Yin Y, et al. Modeling liver cancer and therapy responsiveness using organoids derived from primary mouse liver tumors. *Carcinogenesis* [Internet]. 2019 Mar 12;40(1):145–54. Available from: <https://academic.oup.com/carcin/article/40/1/145/5115755>
143. Kim M, Mun H, Sung CO, Cho EJ, Jeon H-J, Chun S-M, et al. Patient-derived lung cancer organoids as in vitro cancer models for therapeutic screening. *Nat Commun* [Internet]. 2019 Dec 5;10(1):3991. Available from: <http://www.nature.com/articles/s41467-019-11867-6>
144. Sachs N, Papaspyropoulos A, Zomer-van Ommen DD, Heo I, Böttinger L, Klay D, et al. Long-term

- expanding human airway organoids for disease modeling. *EMBO J* [Internet]. 2019 Feb 15;38(4). Available from: <https://onlinelibrary.wiley.com/doi/10.15252/embj.2018100300>
145. Reynolds DS, Tevis KM, Blessing WA, Colson YL, Zaman MH, Grinstaff MW. Breast Cancer Spheroids Reveal a Differential Cancer Stem Cell Response to Chemotherapeutic Treatment. *Sci Rep* [Internet]. 2017 Dec 4;7(1):10382. Available from: <http://www.nature.com/articles/s41598-017-10863-4>
 146. Chambers KF, Mosaad EMO, Russell PJ, Clements JA, Doran MR. 3D Cultures of Prostate Cancer Cells Cultured in a Novel High-Throughput Culture Platform Are More Resistant to Chemotherapeutics Compared to Cells Cultured in Monolayer. Huss WJ, editor. *PLoS One* [Internet]. 2014 Nov 7;9(11):e111029. Available from: <https://dx.plos.org/10.1371/journal.pone.0111029>
 147. Ward JP, King JR. Mathematical modelling of avascular-tumour growth. *IMA J Math Appl Med Biol* [Internet]. 1997 Mar;14(1):39–69. Available from: <http://www.ncbi.nlm.nih.gov/pubmed/9080687>
 148. Zanoni M, Pignatta S, Arienti C, Bonafè M, Tesei A. Anticancer drug discovery using multicellular tumor spheroid models. *Expert Opin Drug Discov* [Internet]. 2019;14(3):289–301. Available from: <https://doi.org/10.1080/17460441.2019.1570129>
 149. Fennema E, Rivron N, Rouwkema J, van Blitterswijk C, De Boer J. Spheroid culture as a tool for creating 3D complex tissues. *Trends Biotechnol*. 2013;31(2):108–15.
 150. De Witt Hamer PC, Leenstra S, Van Noorden CJF, Zwinderman AH. Organotypic glioma spheroids for screening of experimental therapies: How many spheroids and sections are required? *Cytom Part A* [Internet]. 2009 Jun;75A(6):528–34. Available from: <http://doi.wiley.com/10.1002/cyto.a.20716>
 151. Rodrigues T, Kundu B, Silva-Correia J, Kundu SC, Oliveira JM, Reis RL, et al. Emerging tumor spheroids technologies for 3D in vitro cancer modeling. *Pharmacol Ther*. 2018;184(October 2017):201–11.
 152. Vinci M, Gowan S, Boxall F, Patterson L, Zimmermann M, Court W, et al. Advances in establishment and analysis of three-dimensional tumor spheroid-based functional assays for target validation and drug evaluation. *BMC Biol* [Internet]. 2012;10(1):29. Available from: <http://bmcbiol.biomedcentral.com/articles/10.1186/1741-7007-10-29>
 153. Mueller-Klieser W. Multicellular spheroids. *J Cancer Res Clin Oncol* [Internet]. 1987 Apr;113(2):101–22. Available from: <http://link.springer.com/10.1007/BF00391431>
 154. Gottfried E, Kunz-Schughart LA, Andreesen R, Kreutz M. Brave Little World: Spheroids as an in vitro Model to Study Tumor-Immune-Cell Interactions. *Cell Cycle* [Internet]. 2006 Apr 24;5(7):691–5. Available from: <https://www.tandfonline.com/doi/full/10.4161/cc.5.7.2624>
 155. Lin R-Z, Chang H-Y. Recent advances in three-dimensional multicellular spheroid culture for biomedical research. *Biotechnol J* [Internet]. 2008 Oct;3(9–10):1172–84. Available from: <http://doi.wiley.com/10.1002/biot.200700228>
 156. Li Y, Kumacheva E. Hydrogel microenvironments for cancer spheroid growth and drug screening. 2018;(April):1–11.

157. Weiswald L-B, Bellet D, Dangles-Marie V. Spherical Cancer Models in Tumor Biology. *Neoplasia* [Internet]. 2015 Jan;17(1):1–15. Available from: <https://linkinghub.elsevier.com/retrieve/pii/S1476558614001948>
158. Lazzari G, Couvreur P, Mura S. Multicellular tumor spheroids: A relevant 3D model for the: In vitro preclinical investigation of polymer nanomedicines. *Polym Chem*. 2017;8(34):4947–69.
159. Yang Q, Yang Y, Li L, Sun W, Zhu X, Huang Y. Polymeric Nanomedicine for Tumor-Targeted Combination Therapy to Elicit Synergistic Genotoxicity against Prostate Cancer. *ACS Appl Mater Interfaces* [Internet]. 2015 Apr 23;7(12):6661–73. Available from: <https://pubs.acs.org/doi/10.1021/am509204u>
160. Wei X, Senanayake TH, Warren G, Vinogradov S V. Hyaluronic Acid-Based Nanogel–Drug Conjugates with Enhanced Anticancer Activity Designed for the Targeting of CD44-Positive and Drug-Resistant Tumors. *Bioconjug Chem* [Internet]. 2013 Apr 17;24(4):658–68. Available from: <https://pubs.acs.org/doi/10.1021/bc300632w>
161. Lei H, Hofferberth SC, Liu R, Colby A, Tevis KM, Catalano P, et al. Paclitaxel-loaded expansile nanoparticles enhance chemotherapeutic drug delivery in mesothelioma 3-dimensional multicellular spheroids. *J Thorac Cardiovasc Surg* [Internet]. 2015 May;149(5):1417-1425.e1. Available from: <https://linkinghub.elsevier.com/retrieve/pii/S0022522315001531>
162. Cheng X, Wang X, Cao Z, Yao W, Wang J, Tang R. Folic acid-modified soy protein nanoparticles for enhanced targeting and inhibitory. *Mater Sci Eng C* [Internet]. 2017 Feb;71:298–307. Available from: <https://linkinghub.elsevier.com/retrieve/pii/S0928493116311079>
163. Agarwal R, Journey P, Raythatha M, Singh V, Sreenivasan S V., Shi L, et al. Effect of Shape, Size, and Aspect Ratio on Nanoparticle Penetration and Distribution inside Solid Tissues Using 3D Spheroid Models. *Adv Healthc Mater*. 2015;4(15):2269–80.
164. Ma S, Zhou J, Zhang Y, He Y, Jiang Q, Yue D, et al. Highly Stable Fluorinated Nanocarriers with iRGD for Overcoming the Stability Dilemma and Enhancing Tumor Penetration in an Orthotopic Breast Cancer. *ACS Appl Mater Interfaces* [Internet]. 2016 Oct 26;8(42):28468–79. Available from: <https://pubs.acs.org/doi/10.1021/acsami.6b09633>
165. Liu K, Holz JA, Ding Y, Liu X, Zhang Y, Tu L, et al. Targeted labeling of an early-stage tumor spheroid in a chorioallantoic membrane model with upconversion nanoparticles. *Nanoscale* [Internet]. 2015;7(5):1596–600. Available from: <http://xlink.rsc.org/?DOI=C4NR05638H>
166. Sharma S, Singh J, Verma A, Teja BV, Shukla RP, Singh SK, et al. Hyaluronic acid anchored paclitaxel nanocrystals improves chemotherapeutic efficacy and inhibits lung metastasis in tumor-bearing rat model. *RSC Adv* [Internet]. 2016;6(77):73083–95. Available from: <http://xlink.rsc.org/?DOI=C6RA11260A>
167. Ivascu A, Kubbies M. Rapid Generation of Single-Tumor Spheroids for High-Throughput Cell Function and Toxicity Analysis. *J Biomol Screen* [Internet]. 2006 Dec 2;11(8):922–32. Available from: <http://journals.sagepub.com/doi/10.1177/1087057106292763>
168. Priwitaningrum DL, Blondé JBG, Sridhar A, van Baarlen J, Hennink WE, Storm G, et al. Tumor stroma-containing 3D spheroid arrays: A tool to study nanoparticle penetration. *J Control Release* [Internet]. 2016;244:257–68. Available from: <http://dx.doi.org/10.1016/j.jconrel.2016.09.004>
169. Benien P, Swami A. 3D tumor models: History, advances and future perspectives. *Futur Oncol*.

2014;10(7):1311–27.

170. Patel NR, Aryasomayajula B, Abouzeid AH, Torchilin VP. Cancer cell spheroids for screening of chemotherapeutics and drug-delivery systems. *Ther Deliv* [Internet]. 2015 Apr;6(4):509–20. Available from: <http://www.future-science.com/doi/10.4155/tde.15.1>
171. Breslin S, O'Driscoll L. Three-dimensional cell culture: the missing link in drug discovery. *Drug Discov Today* [Internet]. 2013 Mar;18(5–6):240–9. Available from: <https://linkinghub.elsevier.com/retrieve/pii/S1359644612003376>
172. Gunay G, Kirit HA, Kamatar A, Baghdasaryan O, Hamsici S, Acar H. The effects of size and shape of the ovarian cancer spheroids on the drug resistance and migration. *Gynecol Oncol* [Internet]. 2020 Nov;159(2):563–72. Available from: <https://linkinghub.elsevier.com/retrieve/pii/S0090825820338579>
173. Sarisozen C, Dhokai S, Tsikudo EG, Luther E, Rachman IM, Torchilin VP. Nanomedicine based curcumin and doxorubicin combination treatment of glioblastoma with scFv-targeted micelles: In vitro evaluation on 2D and 3D tumor models. *Eur J Pharm Biopharm* [Internet]. 2016 Nov;108:54–67. Available from: <https://linkinghub.elsevier.com/retrieve/pii/S0939641116304647>
174. Neto AI, Correia CR, Oliveira MB, Rial-Hermida MI, Alvarez-Lorenzo C, Reis RL, et al. A novel hanging spherical drop system for the generation of cellular spheroids and high throughput combinatorial drug screening. *Biomater Sci* [Internet]. 2015;3(4):581–5. Available from: <http://xlink.rsc.org/?DOI=C4BM00411F>
175. Upreti M, Jamshidi-Parsian A, Koonce NA, Webber JS, Sharma SK, Asea AAA, et al. Tumor-Endothelial Cell Three-dimensional Spheroids: New Aspects to Enhance Radiation and Drug Therapeutics. *Transl Oncol* [Internet]. 2011 Dec;4(6):365-IN3. Available from: <https://linkinghub.elsevier.com/retrieve/pii/S1936523311800422>
176. Ingram M, Techy GB, Saroufeem R, Yazan O, Narayan KS, Goodwin TJ, et al. Three-dimensional growth patterns of various human tumor cell lines in simulated microgravity of a NASA bioreactor. *Vitr Cell Dev Biol - Anim* [Internet]. 1997 Jun;33(6):459–66. Available from: <http://link.springer.com/10.1007/s11626-997-0064-8>
177. Chen Y, Gao D, Wang Y, Lin S, Jiang Y. A novel 3D breast-cancer-on-chip platform for therapeutic evaluation of drug delivery systems. *Anal Chim Acta* [Internet]. 2018 Dec;1036:97–106. Available from: <https://linkinghub.elsevier.com/retrieve/pii/S0003267018308031>
178. Chen Y, Gao D, Liu H, Lin S, Jiang Y. Drug cytotoxicity and signaling pathway analysis with three-dimensional tumor spheroids in a microwell-based microfluidic chip for drug screening. *Anal Chim Acta* [Internet]. 2015 Oct;898:85–92. Available from: <https://linkinghub.elsevier.com/retrieve/pii/S0003267015012404>
179. Zuchowska A, Marciniak K, Bazylińska U, Jastrzebska E, Wilk KA, Brzozka Z. Different action of nanoencapsulated meso-tetraphenylporphyrin in breast spheroid co-culture and mono-culture under microfluidic conditions. *Sensors Actuators B Chem* [Internet]. 2018 Dec;275:69–77. Available from: <https://linkinghub.elsevier.com/retrieve/pii/S0925400518314679>
180. Patra B, Peng C-C, Liao W-H, Lee C-H, Tung Y-C. Drug testing and flow cytometry analysis on a large number of uniform sized tumor spheroids using a microfluidic device. *Sci Rep* [Internet].

2016 Aug 15;6(1):21061. Available from: <http://www.nature.com/articles/srep21061>

181. Ruppen J, Wildhaber FD, Strub C, Hall SRR, Schmid RA, Geiser T, et al. Towards personalized medicine: chemosensitivity assays of patient lung cancer cell spheroids in a perfused microfluidic platform. *Lab Chip* [Internet]. 2015;15(14):3076–85. Available from: <http://xlink.rsc.org/?DOI=C5LC00454C>
182. Kim C, Bang JH, Kim YE, Lee SH, Kang JY. On-chip anticancer drug test of regular tumor spheroids formed in microwells by a distributive microchannel network. *Lab Chip* [Internet]. 2012;12(20):4135. Available from: <http://xlink.rsc.org/?DOI=c2lc40570a>
183. Sethi P, Jyoti A, Swindell EP, Chan R, Langner UW, Feddock JM, et al. 3D tumor tissue analogs and their orthotopic implants for understanding tumor-targeting of microenvironment-responsive nanosized chemotherapy and radiation. *Nanomedicine Nanotechnology, Biol Med* [Internet]. 2015 Nov;11(8):2013–23. Available from: <https://linkinghub.elsevier.com/retrieve/pii/S1549963415001562>
184. Cui M, Naczynski DJ, Zevon M, Griffith CK, Sheihet L, Poventud-Fuentes I, et al. Multifunctional Albumin Nanoparticles As Combination Drug Carriers for Intra-Tumoral Chemotherapy. *Adv Healthc Mater* [Internet]. 2013 Sep;2(9):1236–45. Available from: <http://doi.wiley.com/10.1002/adhm.201200467>
185. Jiang Y, Lu H, Dag A, Hart-Smith G, Stenzel MH. Albumin–polymer conjugate nanoparticles and their interactions with prostate cancer cells in 2D and 3D culture: comparison between PMMA and PCL. *J Mater Chem B* [Internet]. 2016;4(11):2017–27. Available from: <http://xlink.rsc.org/?DOI=C5TB02576A>
186. Shen W, Wang H, Ling-hu Y, Lv J, Chang H, Cheng Y. Screening of efficient polymers for siRNA delivery in a library of hydrophobically modified polyethyleneimines. *J Mater Chem B* [Internet]. 2016;4(39):6468–74. Available from: <http://xlink.rsc.org/?DOI=C6TB01929C>
187. Du AW, Lu H, Stenzel M. Stabilization of Paclitaxel-Conjugated Micelles by Cross-Linking with Cystamine Compromises the Antitumor Effects against Two- and Three-Dimensional Tumor Cellular Models. *Mol Pharm* [Internet]. 2016 Nov 7;13(11):3648–56. Available from: <https://pubs.acs.org/doi/10.1021/acs.molpharmaceut.6b00410>
188. Kim TH, Mount CW, Gombotz WR, Pun SH. The delivery of doxorubicin to 3-D multicellular spheroids and tumors in a murine xenograft model using tumor-penetrating triblock polymeric micelles. *Biomaterials*. 2010;31(28):7386–97.
189. Goodman TT, Chen J, Matveev K, Pun SH. Spatio-temporal modeling of nanoparticle delivery to multicellular tumor spheroids. *Biotechnol Bioeng* [Internet]. 2008 Oct 1;101(2):388–99. Available from: <http://doi.wiley.com/10.1002/bit.21910>
190. LaBarbera D V, Reid BG, Yoo BH. The multicellular tumor spheroid model for high-throughput cancer drug discovery. *Expert Opin Drug Discov* [Internet]. 2012 Sep 12;7(9):819–30. Available from: <http://www.tandfonline.com/doi/full/10.1517/17460441.2012.708334>
191. Verbridge SS, Chakrabarti A, DelNero P, Kwee B, Varner JD, Stroock AD, et al. Physicochemical regulation of endothelial sprouting in a 3D microfluidic angiogenesis model. *J Biomed Mater Res Part A* [Internet]. 2013 Oct;101(10):2948–56. Available from: <http://doi.wiley.com/10.1002/jbm.a.34587>

192. Hardelauf H, Frimat J-P, Stewart JD, Schormann W, Chiang Y-Y, Lampen P, et al. Microarrays for the scalable production of metabolically relevant tumour spheroids: a tool for modulating chemosensitivity traits. *Lab Chip* [Internet]. 2011;11(3):419–28. Available from: <http://xlink.rsc.org/?DOI=C0LC00089B>
193. Morimoto Y, Hsiao AY, Takeuchi S. Point-, line-, and plane-shaped cellular constructs for 3D tissue assembly. *Adv Drug Deliv Rev* [Internet]. 2015 Dec;95:29–39. Available from: <https://linkinghub.elsevier.com/retrieve/pii/S0169409X15001982>
194. Cordey M, Limacher M, Kobel S, Taylor V, Lutolf MP. Enhancing the Reliability and Throughput of Neurosphere Culture on Hydrogel Microwell Arrays. *Stem Cells* [Internet]. 2008 Oct;26(10):2586–94. Available from: <http://doi.wiley.com/10.1634/stemcells.2008-0498>
195. Fukuda J, Khademhosseini A, Yeo Y, Yang X, Yeh J, Eng G, et al. Micromolding of photocrosslinkable chitosan hydrogel for spheroid microarray and co-cultures. *Biomaterials* [Internet]. 2006 Oct;27(30):5259–67. Available from: <https://linkinghub.elsevier.com/retrieve/pii/S0142961206004960>
196. Liu T, Kempson I, de Jonge M, Howard DL, Thierry B. Quantitative synchrotron X-ray fluorescence study of the penetration of transferrin-conjugated gold nanoparticles inside model tumour tissues. *Nanoscale* [Internet]. 2014;6(16):9774–82. Available from: <http://xlink.rsc.org/?DOI=C4NR02100B>
197. Ohta S, Hiramoto S, Amano Y, Sato M, Suzuki Y, Shinohara M, et al. Production of Cisplatin-Incorporating Hyaluronan Nanogels via Chelating Ligand–Metal Coordination. *Bioconjug Chem* [Internet]. 2016 Mar 16;27(3):504–8. Available from: <https://pubs.acs.org/doi/10.1021/acs.bioconjchem.5b00674>
198. Gaspar VM, Costa EC, Queiroz JA, Pichon C, Sousa F, Correia IJ. Folate-Targeted Multifunctional Amino Acid-Chitosan Nanoparticles for Improved Cancer Therapy. *Pharm Res* [Internet]. 2015 Feb 4;32(2):562–77. Available from: <http://link.springer.com/10.1007/s11095-014-1486-0>
199. Kang AR, Seo HI, Chung BG, Lee SH. Concave microwell array-mediated three-dimensional tumor model for screening anticancer drug-loaded nanoparticles. *Nanomedicine Nanotechnology, Biol Med* [Internet]. 2015;11(5):1153–61. Available from: <http://dx.doi.org/10.1016/j.nano.2015.02.009>
200. Gaspar VM, Baril P, Costa EC, de Melo-Diogo D, Foucher F, Queiroz JA, et al. Bioreducible poly(2-ethyl-2-oxazoline)–PLA–PEI–SS triblock copolymer micelles for co-delivery of DNA minicircles and Doxorubicin. *J Control Release* [Internet]. 2015 Sep;213:175–91. Available from: <https://linkinghub.elsevier.com/retrieve/pii/S0168365915300249>
201. Priwitaningrum DL, Blondé JBG, Sridhar A, van Baarlen J, Hennink WE, Storm G, et al. Tumor stroma-containing 3D spheroid arrays: A tool to study nanoparticle penetration. *J Control Release*. 2016;244:257–68.
202. Barata D, van Blitterswijk C, Habibovic P. High-throughput screening approaches and combinatorial development of biomaterials using microfluidics. *Acta Biomater* [Internet]. 2016 Apr;34:1–20. Available from: <https://linkinghub.elsevier.com/retrieve/pii/S1742706115301033>
203. Montanez-Sauri SI, Beebe DJ, Sung KE. Microscale screening systems for 3D cellular

- microenvironments: platforms, advances, and challenges. *Cell Mol Life Sci* [Internet]. 2015 Jan 2;72(2):237–49. Available from: <http://link.springer.com/10.1007/s00018-014-1738-5>
204. van Duinen V, Trietsch SJ, Joore J, Vulto P, Hankemeier T. Microfluidic 3D cell culture: from tools to tissue models. *Curr Opin Biotechnol* [Internet]. 2015 Dec;35:118–26. Available from: <https://linkinghub.elsevier.com/retrieve/pii/S0958166915000713>
 205. Esch MB, Smith AST, Prot J-M, Oleaga C, Hickman JJ, Shuler ML. How multi-organ microdevices can help foster drug development. *Adv Drug Deliv Rev* [Internet]. 2014 Apr;69–70:158–69. Available from: <https://linkinghub.elsevier.com/retrieve/pii/S0169409X13002895>
 206. Ho WY, Yeap SK, Ho CL, Rahim RA, Alitheen NB. Development of Multicellular Tumor Spheroid (MCTS) Culture from Breast Cancer Cell and a High Throughput Screening Method Using the MTT Assay. Mehta K, editor. *PLoS One* [Internet]. 2012 Sep 6;7(9):e44640. Available from: <https://dx.plos.org/10.1371/journal.pone.0044640>
 207. Eilenberger C, Kratz SRA, Rothbauer M, Ehmoser E-K, Ertl P, Küpcü S. Optimized alamarBlue assay protocol for drug dose-response determination of 3D tumor spheroids. *MethodsX* [Internet]. 2018;5:781–7. Available from: <https://linkinghub.elsevier.com/retrieve/pii/S2215016118301183>
 208. Pignatta S, Orienti I, Falconi M, Teti G, Arienti C, Medri L, et al. Albumin nanocapsules containing fenretinide: pre-clinical evaluation of cytotoxic activity in experimental models of human non-small cell lung cancer. *Nanomedicine Nanotechnology, Biol Med* [Internet]. 2015 Feb;11(2):263–73. Available from: <https://linkinghub.elsevier.com/retrieve/pii/S1549963414005553>
 209. Wen Z, Liao Q, Hu Y, You L, Zhou L, Zhao Y. A spheroid-based 3-D culture model for pancreatic cancer drug testing, using the acid phosphatase assay. *Brazilian J Med Biol Res* [Internet]. 2013 Jul;46(7):634–42. Available from: http://www.scielo.br/scielo.php?script=sci_arttext&pid=S0100-879X2013000700634&lng=en&tlng=en
 210. Fraga D, Meulia T, Fenster S. Real-Time PCR. *Curr Protoc Essent Lab Tech* [Internet]. 2008 Jan 15;00(1). Available from: <https://onlinelibrary.wiley.com/doi/10.1002/9780470089941.et1003s00>
 211. Chen M-W, Yang S-T, Chien M-H, Hua K-T, Wu C-J, Hsiao SM, et al. The STAT3-miRNA-92-Wnt Signaling Pathway Regulates Spheroid Formation and Malignant Progression in Ovarian Cancer. *Cancer Res* [Internet]. 2017 Apr 15;77(8):1955–67. Available from: <http://cancerres.aacrjournals.org/lookup/doi/10.1158/0008-5472.CAN-16-1115>
 212. Barbone D, Van Dam L, Follo C, Jithesh P V., Zhang S-D, Richards WG, et al. Analysis of Gene Expression in 3D Spheroids Highlights a Survival Role for ASS1 in Mesothelioma. Ho M, editor. *PLoS One* [Internet]. 2016 Mar 16;11(3):e0150044. Available from: <https://dx.plos.org/10.1371/journal.pone.0150044>
 213. Ma HL, Jiang Q, Han S, Wu Y, Tomshine JC, Wang D, et al. Multicellular tumor spheroids as an in vivo-like tumor model for three-dimensional imaging of chemotherapeutic and nano material cellular penetration. *Mol Imaging*. 2012;11(6):487–98.
 214. Ivascu A, Kubbies M. Diversity of cell-mediated adhesions in breast cancer spheroids. *Int J Oncol* [Internet]. 2007 Dec;31(6):1403–13. Available from: <http://www.ncbi.nlm.nih.gov/pubmed/17982667>
 215. Khaitan D, Chandna S, Arya MB, Dwarakanath BS. Establishment and characterization of multicellular spheroids from a human glioma cell line; Implications for tumor therapy. *J Transl*

- Med [Internet]. 2006 Mar 2;4:12. Available from: <http://www.ncbi.nlm.nih.gov/pubmed/16509995>
216. Bell HS, Whittle IR, Walker M, Leaver HA, Wharton SB. The development of necrosis and apoptosis in glioma: experimental findings using spheroid culture systems*. *Neuropathol Appl Neurobiol* [Internet]. 2001 Aug;27(4):291–304. Available from: <http://doi.wiley.com/10.1046/j.0305-1846.2001.00319.x>
 217. Uroukov IS, Patton D. Optimizing environmental scanning electron microscopy of spheroidal reaggregated neuronal cultures. *Microsc Res Tech* [Internet]. 2008 Nov;71(11):792–801. Available from: <http://doi.wiley.com/10.1002/jemt.20621>
 218. Bussador do Amaral J, Shiniti Urabayashi M, Maria Machado-Santelli G. Cell death and lumen formation in spheroids of MCF-7 cells. *Cell Biol Int* [Internet]. 2010 Mar 1;34(3):267–74. Available from: <http://doi.wiley.com/10.1042/CBI20090024>
 219. Costa EC, Gaspar VM, Coutinho P, Correia IJ. Optimization of liquid overlay technique to formulate heterogenic 3D co-cultures models. *Biotechnol Bioeng* [Internet]. 2014 Aug;111(8):1672–85. Available from: <http://doi.wiley.com/10.1002/bit.25210>
 220. Huang K, Ma H, Liu J, Huo S, Kumar A, Wei T, et al. Size-Dependent Localization and Penetration of Ultrasmall Gold Nanoparticles in Cancer Cells, Multicellular Spheroids, and Tumors in Vivo. *ACS Nano* [Internet]. 2012 May 22;6(5):4483–93. Available from: <https://pubs.acs.org/doi/10.1021/nn301282m>
 221. Ivanov DP, Parker TL, Walker DA, Alexander C, Ashford MB, Gellert PR, et al. In vitro co-culture model of medulloblastoma and human neural stem cells for drug delivery assessment. *J Biotechnol* [Internet]. 2015 Jul;205:3–13. Available from: <https://linkinghub.elsevier.com/retrieve/pii/S0168165615000115>
 222. Mikhail AS, Eetezadi S, Allen C. Multicellular Tumor Spheroids for Evaluation of Cytotoxicity and Tumor Growth Inhibitory Effects of Nanomedicines In Vitro: A Comparison of Docetaxel-Loaded Block Copolymer Micelles and Taxotere®. He X, editor. *PLoS One* [Internet]. 2013 Apr 23;8(4):e62630. Available from: <https://dx.plos.org/10.1371/journal.pone.0062630>
 223. Cheng G, Tse J, Jain RK, Munn LL. Micro-Environmental Mechanical Stress Controls Tumor Spheroid Size and Morphology by Suppressing Proliferation and Inducing Apoptosis in Cancer Cells. Blagosklonny M V., editor. *PLoS One* [Internet]. 2009 Feb 27;4(2):e4632. Available from: <https://dx.plos.org/10.1371/journal.pone.0004632>
 224. Yeon S-E, No DY, Lee S-H, Nam SW, Oh I-H, Lee J, et al. Application of Concave Microwells to Pancreatic Tumor Spheroids Enabling Anticancer Drug Evaluation in a Clinically Relevant Drug Resistance Model. Munshi HG, editor. *PLoS One* [Internet]. 2013 Sep 10;8(9):e73345. Available from: <https://dx.plos.org/10.1371/journal.pone.0073345>
 225. Correa de Sampaio P, Auslaender D, Krubasik D, Failla AV, Skepper JN, Murphy G, et al. A Heterogeneous In Vitro Three Dimensional Model of Tumour-Stroma Interactions Regulating Sprouting Angiogenesis. Gullberg D, editor. *PLoS One* [Internet]. 2012 Feb 20;7(2):e30753. Available from: <https://dx.plos.org/10.1371/journal.pone.0030753>
 226. Pettee KM, Dvorak KM, Nestor-Kalinoski AL, Eisenmann KM. An mDia2/ROCK Signaling Axis

- Regulates Invasive Egress from Epithelial Ovarian Cancer Spheroids. Aspenstrom P, editor. PLoS One [Internet]. 2014 Feb 28;9(2):e90371. Available from: <https://dx.plos.org/10.1371/journal.pone.0090371>
227. Wei B, Han X-Y, Qi C-L, Zhang S, Zheng Z-H, Huang Y, et al. Coaction of Spheroid-Derived Stem-Like Cells and Endothelial Progenitor Cells Promotes Development of Colon Cancer. Camussi G, editor. PLoS One [Internet]. 2012 Jun 26;7(6):e39069. Available from: <https://dx.plos.org/10.1371/journal.pone.0039069>
228. ERGUVEN M, BILIR A, YAZIHAN N, KORKMAZ S, AKTAS E, OVALIOGLU C, et al. Imatinib mesylate decreases the cytotoxic effect of roscovitine on human glioblastoma cells in vitro and the role of midkine. *Oncol Lett* [Internet]. 2012 Jan;3(1):200–8. Available from: <https://www.spandidos-publications.com/10.3892/ol.2011.434>
229. Kosheleva N V., Efremov YM, Shavkuta BS, Zurina IM, Zhang D, Zhang Y, et al. Cell spheroid fusion: beyond liquid drops model. *Sci Rep* [Internet]. 2020 Dec 28;10(1):12614. Available from: <http://www.nature.com/articles/s41598-020-69540-8>
230. Christie C, Molina S, Gonzales J, Berg K, Nair RK, Huynh K, et al. Synergistic chemotherapy by combined moderate hyperthermia and photochemical internalization. *Biomed Opt Express*. 2016;7(4):1240.
231. Kelm JM, Timmins NE, Brown CJ, Fussenegger M, Nielsen LK. Method for generation of homogeneous multicellular tumor spheroids applicable to a wide variety of cell types. *Biotechnol Bioeng*. 2003;83(2):173–80.
232. Celli JP, Rizvi I, Blanden AR, Massodi I, Glidden MD, Pogue BW, et al. An imaging-based platform for high-content, quantitative evaluation of therapeutic response in 3D tumour models. *Sci Rep* [Internet]. 2015 May 17;4(1):3751. Available from: <http://www.nature.com/articles/srep03751>
233. Verveer PJ, Swoger J, Pampaloni F, Greger K, Marcello M, Stelzer EHK. High-resolution three-dimensional imaging of large specimens with light sheet–based microscopy. *Nat Methods* [Internet]. 2007 Apr 4;4(4):311–3. Available from: <http://www.nature.com/articles/nmeth1017>
234. Lorenzo C, Frongia C, Jorand R, Fehrenbach J, Weiss P, Maandhui A, et al. Live cell division dynamics monitoring in 3D large spheroid tumor models using light sheet microscopy. *Cell Div* [Internet]. 2011;6(1):22. Available from: <http://celldiv.biomedcentral.com/articles/10.1186/1747-1028-6-22>
235. Pampaloni F, Ansari N, Stelzer EHK. High-resolution deep imaging of live cellular spheroids with light-sheet-based fluorescence microscopy. *Cell Tissue Res* [Internet]. 2013 Apr 27;352(1):161–77. Available from: <http://link.springer.com/10.1007/s00441-013-1589-7>
236. Helmchen F, Denk W. Deep tissue two-photon microscopy. *Nat Methods* [Internet]. 2005 Dec 18;2(12):932–40. Available from: <http://www.nature.com/articles/nmeth818>
237. Victora GD, Schwickert TA, Fooksman DR, Kamphorst AO, Meyer-Hermann M, Dustin ML, et al. Germinal Center Dynamics Revealed by Multiphoton Microscopy with a Photoactivatable Fluorescent Reporter. *Cell* [Internet]. 2010 Nov;143(4):592–605. Available from: <https://linkinghub.elsevier.com/retrieve/pii/S0092867410012365>
238. Weiswald L-B, Guinebretière J-M, Richon S, Bellet D, Saubaméa B, Dangles-Marie V. In situ protein expression in tumour spheres: development of an immunostaining protocol for confocal

- microscopy. *BMC Cancer* [Internet]. 2010 Dec 22;10(1):106. Available from: <http://bmccancer.biomedcentral.com/articles/10.1186/1471-2407-10-106>
239. Ingeson-Carlsson C, Martinez-Monleon A, Nilsson M. Differential effects of MAPK pathway inhibitors on migration and invasiveness of BRAFV600E mutant thyroid cancer cells in 2D and 3D culture. *Exp Cell Res* [Internet]. 2015 Nov;338(2):127–35. Available from: <https://linkinghub.elsevier.com/retrieve/pii/S0014482715300665>
240. Richardson DS, Lichtman JW. Clarifying Tissue Clearing. *Cell* [Internet]. 2015 Jul;162(2):246–57. Available from: <https://linkinghub.elsevier.com/retrieve/pii/S0092867415008375>
241. Keereweer S, Van Driel PBAA, Snoeks TJA, Kerrebijn JDF, Baatenburg de Jong RJ, Vahrmeijer AL, et al. Optical Image-Guided Cancer Surgery: Challenges and Limitations. *Clin Cancer Res* [Internet]. 2013 Jul 15;19(14):3745–54. Available from: <http://clincancerres.aacrjournals.org/lookup/doi/10.1158/1078-0432.CCR-12-3598>
242. Vidi P-A, Bissell MJ, Lelièvre SA. Three-Dimensional Culture of Human Breast Epithelial Cells: The How and the Why. In 2012. p. 193–219. Available from: http://link.springer.com/10.1007/978-1-62703-125-7_13
243. Langenbach F, Berr K, Naujoks C, Hassel A, Hentschel M, Deprich R, et al. Generation and differentiation of microtissues from multipotent precursor cells for use in tissue engineering. *Nat Protoc* [Internet]. 2011 Nov 13;6(11):1726–35. Available from: <http://www.nature.com/articles/nprot.2011.394>
244. Costa EC, Silva DN, Moreira AF, Correia IJ. Optical clearing methods: An overview of the techniques used for the imaging of 3D spheroids. *Biotechnol Bioeng*. 2019;116(10):2742–63.
245. Seo J, Choe M, Kim S-Y. Clearing and Labeling Techniques for Large-Scale Biological Tissues. *Mol Cells* [Internet]. 2016 Jun 30;39(6):439–46. Available from: <http://www.molcells.org/journal/view.html?doi=10.14348/molcells.2016.0088>
246. Costa EC, Silva DN, Moreira AF, Correia IJ. Optical clearing methods: An overview of the techniques used for the imaging of 3D spheroids. *Biotechnol Bioeng* [Internet]. 2019;116(10):2742–63. Available from: <https://doi.org/10.1002/bit.27105>
247. Sofias AM, Toner YC, Meerwaldt AE, van Leent MMT, Soultanidis G, Elschot M, et al. Tumor Targeting by α v β 3 -Integrin-Specific Lipid Nanoparticles Occurs via Phagocyte Hitchhiking. *ACS Nano* [Internet]. 2020 Jul 28;14(7):7832–46. Available from: <https://pubs.acs.org/doi/10.1021/acsnano.9b08693>
248. Shah NB, Vercellotti GM, White JG, Fegan A, Wagner CR, Bischof JC. Blood–Nanoparticle Interactions and in Vivo Biodistribution: Impact of Surface PEG and Ligand Properties. *Mol Pharm* [Internet]. 2012 Aug 6;9(8):2146–55. Available from: <https://pubs.acs.org/doi/10.1021/mp200626j>
249. Campbell F, Bos FL, Sieber S, Arias-Alpizar G, Koch BE, Huwyler J, et al. Directing Nanoparticle Biodistribution through Evasion and Exploitation of Stab2-Dependent Nanoparticle Uptake. *ACS Nano* [Internet]. 2018 Mar 27;12(3):2138–50. Available from: <https://pubs.acs.org/doi/10.1021/acsnano.7b06995>
250. Hayashi Y, Takamiya M, Jensen PB, Ojea-Jiménez I, Claude H, Antony C, et al. Differential

- Nanoparticle Sequestration by Macrophages and Scavenger Endothelial Cells Visualized in Vivo in Real-Time and at Ultrastructural Resolution. *ACS Nano* [Internet]. 2020 Feb 25;14(2):1665–81. Available from: <https://pubs.acs.org/doi/10.1021/acsnano.9b07233>
251. Miao L, Huang L. Exploring the Tumor Microenvironment with Nanoparticles. In 2015. p. 193–226. Available from: http://link.springer.com/10.1007/978-3-319-16555-4_9
 252. Lee H, Fonge H, Hoang B, Reilly RM, Allen C. The Effects of Particle Size and Molecular Targeting on the Intratumoral and Subcellular Distribution of Polymeric Nanoparticles. *Mol Pharm* [Internet]. 2010 Aug 2;7(4):1195–208. Available from: <https://pubs.acs.org/doi/10.1021/mp100038h>
 253. Donahue ND, Acar H, Wilhelm S. Concepts of nanoparticle cellular uptake, intracellular trafficking, and kinetics in nanomedicine. *Adv Drug Deliv Rev* [Internet]. 2019;143:68–96. Available from: <https://doi.org/10.1016/j.addr.2019.04.008>
 254. de Lázaro I, Mooney DJ. Obstacles and opportunities in a forward vision for cancer nanomedicine. *Nat Mater* [Internet]. 2021 Jul 5; Available from: <http://www.nature.com/articles/s41563-021-01047-7>
 255. Rollerova E, Mlynarcikova AB, Tulinska J, Ed GT. Safety of Nanomedicine: Neuroendocrine Disrupting Potential of Nanoparticles and Neurodegeneration. *Front Nanomedicine*. 2017;(August):239–62.
 256. Fontana F, Ezazi NZ, Tahir N, Santos HA. Cell–Nanoparticle Interactions: Toxicity and Safety Issues. In: *Characterization of Pharmaceutical Nano and Microsystems* [Internet]. Wiley; 2021. p. 207–42. Available from: <https://onlinelibrary.wiley.com/doi/10.1002/9781119414018.ch6>
 257. Behzadi S, Serpooshan V, Tao W, Hamaly MA, Alkawareek MY, Dreaden EC, et al. Cellular uptake of nanoparticles: Journey inside the cell. *Chem Soc Rev* [Internet]. 2017;46(14):4218–44. Available from: <http://dx.doi.org/10.1039/C6CS00636A>
 258. Zhao F, Zhao Y, Liu Y, Chang X, Chen C, Zhao Y. Cellular Uptake, Intracellular Trafficking, and Cytotoxicity of Nanomaterials. *Small* [Internet]. 2011 May 23;7(10):1322–37. Available from: <http://doi.wiley.com/10.1002/smll.201100001>
 259. Cartiera MS, Johnson KM, Rajendran V, Caplan MJ, Saltzman WM. The uptake and intracellular fate of PLGA nanoparticles in epithelial cells. *Biomaterials* [Internet]. 2009 May;30(14):2790–8. Available from: <https://linkinghub.elsevier.com/retrieve/pii/S014296120900115X>
 260. Huotari J, Helenius A. Endosome maturation. *EMBO J* [Internet]. 2011 Aug 31;30(17):3481–500. Available from: <http://emboj.embopress.org/cgi/doi/10.1038/emboj.2011.286>
 261. Millard M, Yakavets I, Zorin V, Kulmukhamedova A, Marchal S, Bezdetsnaya L. Drug delivery to solid tumors: the predictive value of the multicellular tumor spheroid model for nanomedicine screening. *Int J Nanomedicine*. 2017 Oct;Volume 12:7993–8007.
 262. Woodcroft BJ, Hammond L, Stow JL, Hamilton NA. Automated organelle-based colocalization in whole-cell imaging. *Cytom Part A* [Internet]. 2009 Nov;75A(11):941–50. Available from: <http://doi.wiley.com/10.1002/cyto.a.20786>
 263. Dunn KW, Kamocka MM, McDonald JH. A practical guide to evaluating colocalization in biological microscopy. *Am J Physiol - Cell Physiol*. 2011;300(4):723–42.

264. BOLTE S, CORDELIÈRES FP. A guided tour into subcellular colocalization analysis in light microscopy. *J Microsc* [Internet]. 2006 Dec;224(3):213–32. Available from: <http://doi.wiley.com/10.1111/j.1365-2818.2006.01706.x>
265. Behzadi S, Serpooshan V, Tao W, Hamaly MA, Alkawareek MY, Dreaden EC, et al. Cellular uptake of nanoparticles: Journey inside the cell. *Chem Soc Rev*. 2017;46(14):4218–44.
266. Minchinton AI, Tannock IF. Drug penetration in solid tumours. *Nat Rev Cancer*. 2006;6(8):583–92.
267. Lazzari G, Vinciguerra D, Balasso A, Nicolas V, Goudin N, Garfa-Traore M, et al. Light sheet fluorescence microscopy versus confocal microscopy: in quest of a suitable tool to assess drug and nanomedicine penetration into multicellular tumor spheroids. *Eur J Pharm Biopharm* [Internet]. 2019 Sep;142:195–203. Available from: <https://linkinghub.elsevier.com/retrieve/pii/S0939641119303017>
268. Däster S, Amatruda N, Calabrese D, Ivanek R, Turrini E, Drosner RA, et al. Induction of hypoxia and necrosis in multicellular tumor spheroids is associated with resistance to chemotherapy treatment. *Oncotarget* [Internet]. 2017 Jan 3;8(1):1725–36. Available from: <https://www.oncotarget.com/lookup/doi/10.18632/oncotarget.13857>
269. Shield K, Ackland ML, Ahmed N, Rice GE. Multicellular spheroids in ovarian cancer metastases: Biology and pathology. *Gynecol Oncol* [Internet]. 2009 Apr;113(1):143–8. Available from: <http://www.ncbi.nlm.nih.gov/pubmed/19135710>
270. Vadivelu R, Kamble H, Shiddiky M, Nguyen N-T. Microfluidic Technology for the Generation of Cell Spheroids and Their Applications. *Micromachines* [Internet]. 2017 Mar 23;8(4):94. Available from: <http://www.mdpi.com/2072-666X/8/4/94>
271. Zoetemelk M, Rausch M, Colin DJ, Dormond O, Nowak-Sliwinska P. Short-term 3D culture systems of various complexity for treatment optimization of colorectal carcinoma. *Sci Rep* [Internet]. 2019 Dec 8;9(1):7103. Available from: <http://www.nature.com/articles/s41598-019-42836-0>
272. Brüningk SC, Rivens I, Box C, Oelfke U, ter Haar G. 3D tumour spheroids for the prediction of the effects of radiation and hyperthermia treatments. *Sci Rep*. 2020;10(1):1–13.
273. Shaheen S, Ahmed M, Lorenzi F, Nateri AS. Spheroid-Formation (Colonosphere) Assay for in Vitro Assessment and Expansion of Stem Cells in Colon Cancer. *Stem Cell Rev Reports* [Internet]. 2016 Aug 20;12(4):492–9. Available from: <http://link.springer.com/10.1007/s12015-016-9664-6>
274. Lux F, Mignot A, Mowat P, Louis C, Dufort S, Bernhard C, et al. Ultrasmall Rigid Particles as Multimodal Probes for Medical Applications. *Angew Chemie Int Ed* [Internet]. 2011 Dec 16;50(51):12299–303. Available from: <https://onlinelibrary.wiley.com/doi/10.1002/anie.201104104>
275. Dentamaro M, Lux F, Vander Elst L, Dauguet N, Montante S, Moussaron A, et al. Chemical and in vitro characterizations of a promising bimodal AGuIX probe able to target apoptotic cells for applications in MRI and optical imaging. *Contrast Media Mol Imaging* [Internet]. 2016 Sep;11(5):381–95. Available from: <https://onlinelibrary.wiley.com/doi/10.1002/cmml.1702>
276. Sancey L, Kotb S, Truillet C, Appaix F, Marais A, Thomas E, et al. Long-term in Vivo clearance of gadolinium-based AGuIX nanoparticles and their biocompatibility after systemic injection. *ACS Nano*. 2015;9(3):2477–88.

277. Morlieras J, Dufort S, Sancey L, Truillet C, Mignot A, Rossetti F, et al. Functionalization of Small Rigid Platforms with Cyclic RGD Peptides for Targeting Tumors Overexpressing $\alpha v \beta 3$ -Integrins. *Bioconjug Chem* [Internet]. 2013 Sep 18;24(9):1584–97. Available from: <https://pubs.acs.org/doi/10.1021/bc4002097>
278. Hama H, Kurokawa H, Kawano H, Ando R, Shimogori T, Noda H, et al. Scale: a chemical approach for fluorescence imaging and reconstruction of transparent mouse brain. *Nat Neurosci* [Internet]. 2011 Nov 30;14(11):1481–8. Available from: <http://www.nature.com/articles/nn.2928>
279. Ke M-T, Fujimoto S, Imai T. SeeDB: a simple and morphology-preserving optical clearing agent for neuronal circuit reconstruction. *Nat Neurosci* [Internet]. 2013 Aug 23;16(8):1154–61. Available from: <http://www.nature.com/articles/nn.3447>
280. Staudt T, Lang MC, Medda R, Engelhardt J, Hell SW. 2,2'-Thiodiethanol: A new water soluble mounting medium for high resolution optical microscopy. *Microsc Res Tech* [Internet]. 2007 Jan;70(1):1–9. Available from: <http://doi.wiley.com/10.1002/jemt.20396>
281. Boutin ME, Hoffman-Kim D. Application and Assessment of Optical Clearing Methods for Imaging of Tissue-Engineered Neural Stem Cell Spheres. *Tissue Eng Part C Methods* [Internet]. 2015 Mar;21(3):292–302. Available from: <https://www.liebertpub.com/doi/10.1089/ten.tec.2014.0296>
282. Masson A, Escande P, Frongia C, Clouvel G, Ducommun B, Lorenzo C. High-resolution in-depth imaging of optically cleared thick samples using an adaptive SPIM. *Sci Rep* [Internet]. 2015 Dec 18;5(1):16898. Available from: <http://www.nature.com/articles/srep16898>
283. Silva Santisteban T, Rabajania O, Kalinina I, Robinson S, Meier M. Rapid spheroid clearing on a microfluidic chip. *Lab Chip*. 2018 Dec;18(1):153–61.
284. Ahmed A, Goodarzi S, Frindel C, Recher G, Riviere C, Rousseau D. Clearing spheroids for 3D fluorescent microscopy combining safe and soft chemicals with deep convolutional neural network. *bioRxiv* [Internet]. 2021; Available from: <https://www.biorxiv.org/content/10.1101/2021.01.31.428996v1>
285. Motto-Ros, V., Gardette, V., Sancey, L., Leprince, M., Genty, D., Roux, S., ... & Pelascini F. LIBS-Based Imaging: Recent Advances and Future Directions. *Spectroscopy*. 2020;35.
286. Duret D, Grassin A, Henry M, Jacquet T, Thoreau F, Denis-Quanquin S, et al. "Polymultivalent" Polymer–Peptide Cluster Conjugates for an Enhanced Targeting of Cells Expressing $\alpha v \beta 3$ Integrins. *Bioconjug Chem* [Internet]. 2017 Sep 20;28(9):2241–5. Available from: <https://pubs.acs.org/doi/10.1021/acs.bioconjchem.7b00362>
287. Banik BL, Fattahi P, Brown JL. Polymeric nanoparticles: the future of nanomedicine. *Wiley Interdiscip Rev Nanomedicine Nanobiotechnology* [Internet]. 2016 Mar;8(2):271–99. Available from: <https://onlinelibrary.wiley.com/doi/10.1002/wnan.1364>
288. Bort G, Lux F, Dufort S, Crémillieux Y, Verry C, Tillement O. EPR-mediated tumor targeting using ultrasmall-hybrid nanoparticles: From animal to human with theranostic AGuIX nanoparticles. *Theranostics*. 2020;10(3):1319–31.
289. Verry C, Dufort S, Lemasson B, Grand S, Pietras J, Troprès I, et al. Targeting brain metastases with ultrasmall theranostic nanoparticles, a first-in-human trial from an MRI perspective. *Sci Adv*. 2020;6(29).

290. Franken NAP, Rodermond HM, Stap J, Haveman J, van Bree C. Clonogenic assay of cells in vitro. *Nat Protoc.* 2006;1(5):2315–9.
291. Siegel RL, Miller KD, Jemal A. Cancer statistics, 2018. *CA Cancer J Clin* [Internet]. 2018 Jan;68(1):7–30. Available from: <http://doi.wiley.com/10.3322/caac.21442>
292. Sung H, Ferlay J, Siegel RL, Laversanne M, Soerjomataram I, Jemal A, et al. Global Cancer Statistics 2020: GLOBOCAN Estimates of Incidence and Mortality Worldwide for 36 Cancers in 185 Countries. *CA Cancer J Clin* [Internet]. 2021 May 4;71(3):209–49. Available from: <https://onlinelibrary.wiley.com/doi/10.3322/caac.21660>
293. Roeder F, Meldolesi E, Gerum S, Valentini V, Rödel C. Recent advances in (chemo-)radiation therapy for rectal cancer: a comprehensive review. *Radiat Oncol* [Internet]. 2020;15(1):1–21. Available from: <https://doi.org/10.1186/s13014-020-01695-0>
294. Bae SM, Park SJ, Choi M, Song M, Cho YE, Do EJ, et al. PSP1, a Phosphatidylserine-Recognizing Peptide, Is Useful for Visualizing Radiation-Induced Apoptosis in Colorectal Cancer In Vitro and In Vivo. *Transl Oncol* [Internet]. 2018;11(4):1044–52. Available from: <https://doi.org/10.1016/j.tranon.2018.06.008>
295. De Felice F, Crocetti D, Maiuri V, Parisi M, Marampon F, Izzo L, et al. Locally Advanced Rectal Cancer: Treatment Approach in Elderly Patients. *Curr Treat Options Oncol.* 2020;21(1):1–12.
296. Zhao F, Wang J, Yu H, Cheng X, Li X, Zhu X, et al. Neoadjuvant radiotherapy improves overall survival for T3/4N+M0 rectal cancer patients: a population-based study of 20300 patients. *Radiat Oncol* [Internet]. 2020 Dec 27;15(1):49. Available from: <https://ro-journal.biomedcentral.com/articles/10.1186/s13014-020-01497-4>
297. Antognelli C, Palumbo I, Piattoni S, Calzuola M, Del Papa B, Talesa VN, et al. Exploring the radiosensitizing potential of AZD8931: a pilot study on the human LoVo colorectal cancer cell line. *Int J Radiat Biol* [Internet]. 2020 Nov 1;96(11):1504–12. Available from: <https://www.tandfonline.com/doi/full/10.1080/09553002.2020.1820610>
298. Tam SY, Wu VWC. A review on the special radiotherapy techniques of colorectal cancer. *Front Oncol.* 2019;9(APR):1–9.
299. Kim MS, Lee E-J, Kim J-W, Chung US, Koh W-G, Keum KC, et al. Gold nanoparticles enhance anti-tumor effect of radiotherapy to hypoxic tumor. *Radiat Oncol J* [Internet]. 2016 Sep 30;34(3):230–8. Available from: <http://www.e-roj.org/journal/view.php?doi=10.3857/roj.2016.01788>
300. Le Duc G, Miladi I, Alric C, Mowat P, Bräuer-Krisch E, Bouchet A, et al. Toward an Image-Guided Microbeam Radiation Therapy Using Gadolinium-Based Nanoparticles. *ACS Nano* [Internet]. 2011 Dec 27;5(12):9566–74. Available from: <https://pubs.acs.org/doi/10.1021/nn202797h>
301. Bonvalot S, Le Pechoux C, De Baere T, Kantor G, Buy X, Stoeckle E, et al. First-in-Human Study Testing a New Radioenhancer Using Nanoparticles (NBTXR3) Activated by Radiation Therapy in Patients with Locally Advanced Soft Tissue Sarcomas. *Clin Cancer Res* [Internet]. 2017 Feb 15;23(4):908–17. Available from: <http://clincancerres.aacrjournals.org/lookup/doi/10.1158/1078-0432.CCR-16-1297>
302. Porcel E, Liehn S, Remita H, Usami N, Kobayashi K, Furusawa Y, et al. Platinum nanoparticles: a promising material for future cancer therapy? *Nanotechnology* [Internet]. 2010 Feb

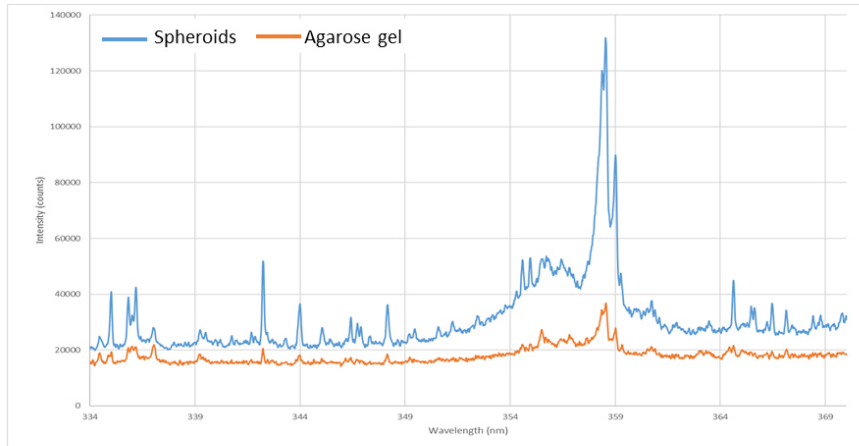
26;21(8):085103. Available from: <https://iopscience.iop.org/article/10.1088/0957-4484/21/8/085103>

303. Laurent G, Bernhard C, Dufort S, Jiménez Sánchez G, Bazzi R, Boschetti F, et al. Minor changes in the macrocyclic ligands but major consequences on the efficiency of gold nanoparticles designed for radiosensitization. *Nanoscale* [Internet]. 2016;8(23):12054–65. Available from: <http://xlink.rsc.org/?DOI=C6NR01228K>
304. Detappe A, Thomas E, Tibbitt MW, Kunjachan S, Zavidij O, Parnandi N, et al. Ultrasmall Silica-Based Bismuth Gadolinium Nanoparticles for Dual Magnetic Resonance–Computed Tomography Image Guided Radiation Therapy. *Nano Lett* [Internet]. 2017 Mar 8;17(3):1733–40. Available from: <https://pubs.acs.org/doi/10.1021/acs.nanolett.6b05055>
305. Rima W, Sancey L, Aloy MT, Armandy E, Alcantara GB, Epicier T, et al. Internalization pathways into cancer cells of gadolinium-based radiosensitizing nanoparticles. *Biomaterials* [Internet]. 2013;34(1):181–95. Available from: <http://dx.doi.org/10.1016/j.biomaterials.2012.09.029>
306. Phillips WT, Bao A, Brenner AJ, Goins BA. Image-guided interventional therapy for cancer with radiotherapeutic nanoparticles. *Adv Drug Deliv Rev*. 2014;76(1):39–59.
307. Sharma H, Mishra PK, Talegaonkar S, Vaidya B. Metal nanoparticles: a theranostic nanotool against cancer. *Drug Discov Today* [Internet]. 2015 Sep;20(9):1143–51. Available from: <https://linkinghub.elsevier.com/retrieve/pii/S1359644615001993>
308. Patra B, Chen Y-H, Peng C-C, Lin S-C, Lee C-H, Tung Y-C. A microfluidic device for uniform-sized cell spheroids formation, culture, harvesting and flow cytometry analysis. *Biomicrofluidics* [Internet]. 2013 Sep;7(5):054114. Available from: <http://aip.scitation.org/doi/10.1063/1.4824480>
309. McMillan KS, McCluskey AG, Sorensen A, Boyd M, Zagnoni M. Emulsion technologies for multicellular tumour spheroid radiation assays. *Analyst* [Internet]. 2016;141(1):100–10. Available from: <http://xlink.rsc.org/?DOI=C5AN01382H>
310. Kerr DJ, Wheldon TE, Hydns S, Kaye SB. Cytotoxic drug penetration studies in multicellular tumour spheroids. *Xenobiotica* [Internet]. 1988 Jan 30;18(6):641–8. Available from: <http://www.tandfonline.com/doi/full/10.3109/00498258809041702>
311. Awwad HK. *Radiation Oncology: Radiobiological and Physiological Perspectives* [Internet]. Dordrecht: Springer Netherlands; 1990. Available from: <http://link.springer.com/10.1007/978-94-015-7865-3>
312. Al-Ramadan A, Mortensen AC, Carlsson J, Nestor M V. Analysis of radiation effects in two irradiated tumor spheroid models. *Oncol Lett*. 2018;15(3):3008–16.
313. Patra B, Lafontaine J, Bavoux M, Zerouali K, Glory A, Ahanj M, et al. On-chip combined radiotherapy and chemotherapy testing on soft-tissue sarcoma spheroids to study cell death using flow cytometry and clonogenic assay. *Sci Rep*. 2019;9(1):1–9.
314. Wishart G, Gupta P, Schettino G, Nisbet A, Velliou E. 3D Tissue Models As Tools for Radiotherapy Screening for Pancreatic Cancer. *Br J Radiol*. 2021;94(1120):20201397.
315. Whitmore GF, Till JE. Quantitation of Cellular Radiobiological Responses. *Annu Rev Nucl Sci* [Internet]. 1964 Dec;14(1):347–74. Available from: <http://www.annualreviews.org/doi/10.1146/annurev.ns.14.120164.002023>

316. Al-Assar O, Demiciorglu F, Lunardi S, Gaspar-Carvalho MM, McKenna WG, Muschel RM, et al. Contextual regulation of pancreatic cancer stem cell phenotype and radioresistance by pancreatic stellate cells. *Radiother Oncol* [Internet]. 2014 May;111(2):243–51. Available from: <https://linkinghub.elsevier.com/retrieve/pii/S016781401400139X>
317. Longati P, Jia X, Eimer J, Wagman A, Witt M-R, Rehnmark S, et al. 3D pancreatic carcinoma spheroids induce a matrix-rich, chemoresistant phenotype offering a better model for drug testing. *BMC Cancer* [Internet]. 2013 Dec 27;13(1):95. Available from: <http://bmccancer.biomedcentral.com/articles/10.1186/1471-2407-13-95>
318. Le Duc G, Roux S, Paruta-Tuarez A, Dufort S, Brauer E, Marais A, et al. Advantages of gadolinium based ultrasmall nanoparticles vs molecular gadolinium chelates for radiotherapy guided by MRI for glioma treatment. *Cancer Nanotechnol*. 2014;5(1):1–14.
319. Goodarzi S, Prunet A, Rossetti F, Bort G, Tillement O, Porcel E, et al. Quantifying nanotherapeutic penetration using a hydrogel-based microsystem as a new 3D in vitro platform . *Lab Chip* [Internet]. 2021;21(13):2495–510. Available from: <http://dx.doi.org/10.1039/D1LC00192B>
320. Robert Grimes D, Partridge M. A mechanistic investigation of the oxygen fixation hypothesis and oxygen enhancement ratio. *Biomed Phys Eng Express* [Internet]. 2015 Dec 4;1(4):045209. Available from: <https://iopscience.iop.org/article/10.1088/2057-1976/1/4/045209>
321. Maury P, Porcel E, Mau A, Lux F, Tillement O, Mahou P, et al. Rapid Evaluation of Novel Therapeutic Strategies Using a 3D Collagen-Based Tissue-Like Model. *Front Bioeng Biotechnol* [Internet]. 2021 Feb 16;9. Available from: <https://www.frontiersin.org/articles/10.3389/fbioe.2021.574035/full>

APPENDIX I

Figure 1.



Detection of Gadolinium in spheroids and agarose using LIBS

APPENDIX II

Clearing spheroids for 3D fluorescent microscopy: combining safe and soft chemicals with deep convolutional neural network

Ali Ahmad^{1,2}, Saba Goodarzi³, Carole Frindel², Gaëlle Recher⁴, Charlotte Riviere^{3,5}, David Rousseau^{1,*},

1 Laboratoire Angevin de Recherche en Ingénierie des Systèmes (LARIS), UMR INRAE IRHS, Université d'Angers, Angers, 49000, France

2 Centre de Recherche en Acquisition et Traitement de l'Image pour la Santé (CREATIS), CNRS UMR 5220 – INSERM U1206, Université Lyon 1, Insa de Lyon, Villeurbanne, 69100, France

3 Univ Lyon, Université Claude Bernard Lyon 1, CNRS UMR-5306, Institut Lumière Matière, F-69622, Villeurbanne, 69100, France

4 BioImaging & OptoFluidics, LP2N, CNRS UMR5298, IOGS, Université de Bordeaux, Talence, F-33400, France

5 Institut Universitaire de France (IUF), France

* david.rousseau@univ-angers.fr

Abstract

In life sciences, there are increasing interest in 3D culture models to better reproduce the 3D environment encountered in-vivo. Imaging of such 3D culture models is instrumental for drug discovery, but face several issues before its use becomes widespread. Extensive microscopic investigation of these 3D cell models faces the challenge of light penetration in depth in opaque biological tissues. To overcome this limit, diverse clearing techniques have emerged over the past decades. However, it is not straightforward to choose the best clearing protocols, and assess quantitatively their clearing efficiency. Focusing on spheroids, we propose a combination of fast and cost-effective clearing procedure for such medium-sized samples. A generic method with local contrast metrics and deep convolutional neural network-based segmentation of nuclei is proposed to quantify the efficiency of clearing. We challenged this method by testing the possibility to transfer segmentation knowledge from a clearing protocol to another. The later results support the pertinence of training deep learning algorithms on cleared samples to further use the segmentation pipeline on non-cleared ones. This second step of the protocol gives access to digital clearing possibilities applicable to live and high-throughput optical imaging.

Introduction

Spheroids are three-dimensional (3D), heterogeneous aggregates of proliferating, quiescent and necrotic in vitro cell culture systems [1]. They have gained increasing interest in drug screening because of their ability to closely mimic the main features of physiological cell to cell and cell to matrix contacts as in in vivo human solid tumors [2, 3]. Because of the standardization of their production, spheroids became a model of choice in the context of the 3R (replace, reduce, refine) notably for

high-throughput drug screening [4,5]. Yet, the experimental readouts are often quantitative, between each size-controlled spheroid, but fail at providing insights in regards with single-cell information within the spheroid itself, due to its lack of amenability for in-depth microscopy. One main challenge is the visualization of spheroids via fluorescence imaging due to the light scattering inducing limited depth penetration in such opaque structure and therefore low data analysis performance at a single-cell level [6,7]. One solution to enhance visualization of fluorescently-labelled spheroids is to use optical clearing techniques, which improve in-depth imaging and allow high quality image acquisition and high-throughput image analysis. The rough principle of optical clearing is to uniformise the optical index within the 3D structure, so as to minimise diffraction. One of the option is to remove the lipids that contribute to light scattering effects, or, to replace water by a solution closer to the lipid refractive index [8–13]. So far, assessment of the quality of clearing in 3D spheroids has been performed with local quality metrics such as signal to noise ratio (SNR) and contrast to noise ratio (CNR) [14–16]. However, it is not straight-forward to relate local metrics with final quantitative measures of interest. We not only propose to revisit the assessment of clearing quality in such a perspective, but we also provide an assessment based on segmentation metrics.

Final quantitative measures for high-throughput image analysis of spheroids mostly rely on whole-spheroid fluorescent measures, size analysis and matrix invasion as an indicator of drug anti metastatic effects [17–22]. These metrics provide useful macroscopic quantitative information but do not provide enough biological details at single cell level for assessing therapy responses nor quantitative analysis such as cell counting and aggregation studies, and also no characteristics over time such as growth ratio and proliferation ratio. To overcome these limitations, individual cell nuclei segmentation methods have been developed for 2D and 3D spheroid images [23–30]. State-of-the-art methods for cell nuclei segmentation in microscopy are currently the deep learning-based methods. Also, a specific interest of the deep learning-based approach, by contrast with a standard image processing pipeline composed of denoising step [31] followed by a segmentation step [32,33], is to offer an end-to-end learning process where all the pipeline is optimized at the same time. Several architectures were developed to segment nuclei by integrating two or more channels in the output of deep learning architecture or by applying post processing methods to the predicted segmentation maps to enhance segmentation quality [34–40]. Deep learning methods were applied to segment entire spheroids of different sizes, shapes, and illumination conditions [41] and also to segment nuclei of 3D spheroid images [42]. In these closely related work, only one clearing method was investigated. By contrast in this article we propose, with a deep learning perspective, a protocol to compare clearing methods for the segmentation of nuclei in spheroids under 3D fluorescence microscopy.

A scheme of the operating pipeline of the article is provided in Figure 1. We compare clearing protocols RapiClear and Glycerol (Figure 1.A) to non cleared samples (Control). The two clearing methods investigated have been chosen for their simplicity and non-toxicity. Both RapiClear [43] and Glycerol [15] have already been reported as fast and cost-effective yet efficient clearing procedures, for medium-sized samples such as organoids and spheroids of few hundreds of micrometers. First, we assess the clearing quality of spheroid images acquired with confocal fluorescence microscopy with the conventional local metrics such as signal to noise ratio (SNR) and contrast to noise ratio (CNR) (Figure 1.B). Then, we use deep learning segmentation methods to assess the quality of the clearing (Figure 1.C,D). Finally, we investigate the possibility of digital clearing of non-cleared data with cleared data models via transfer learning and the transferability of knowledge from a clearing protocol to another (Figure 1.E). In this manuscript, we show that using a simple deep learning strategy, it is possible to get

reliable segmented images even for images with low intensity and low signal-to-noise ratio. Also, we demonstrate the segmentation knowledge transferability from cleared samples to native tissues for fast digital-clearing of living specimens on the fly.

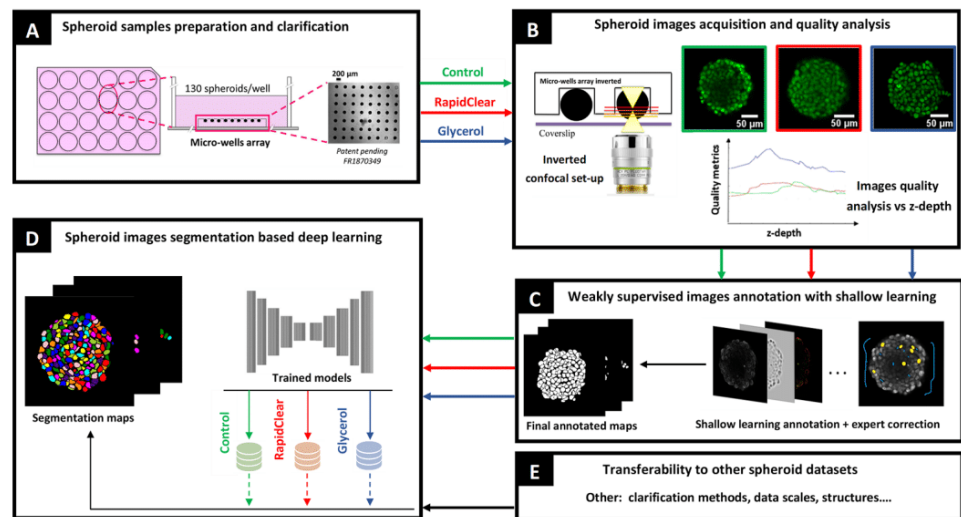


Fig 1. Protocol pipeline: (A) Spheroid samples are cultured in micro-well arrays. Control are the non cleared samples and others are clarified with two distinct clearing methods RapiClear and Glycerol. (B) Then, spheroid images acquired with a confocal microscope are analyzed for quality assessment along z-depth. (C) A dataset of images for each clarification method is annotated using shallow learning and corrected by an expert. (D) Finally, deep learning models are trained with the annotated data sets and the three segmentation models trained on RapiClear, Control and Glycerol are tested for (E) data transferability on various clarification methods.

Results and Discussion

Comparison of clearing methods with local metrics

We assessed the efficiency of RapiClear and Glycerol clearing protocols on image quality by comparing their datasets with non cleared datasets (Control) using image local quality metrics evaluation. This was quantitatively evaluated in depth on the 3D spheroid stacks (z-depth) based on the computation of various local metrics using patches cropped from the center of the spheroid signal in each slice (see SI Figures 1.A). The used metrics were the signal to noise ratio (SNR) (Equation 1) and the contrast to noise ratio (CNR) calculated by two ways: from Bhattacharyya coefficient (BC) (Equation 2) and from Fisher ratio (FR) (Equation 3). Figure 2 shows the xz planes at the center of spheroids and the xy planes at selected depth (from 70% to 100% of maximum diameter, corresponding to the range of depth where the three conditions can be compared) also the mean and the standard deviation (std) of the normalized average intensity (average I/I_{max}) evolution and of the computed local metrics from three spheroids for each Control, RapiClear and Glycerol conditions. Visual qualitative inspection of the xz and xy planes of spheroids are provided in Fig 2.A,B. Quantitative evaluation of image quality (Fig 2.C) shows the degradation of image with depth z.

Concerning intensities, an important drop is recorded for all clearing methods. This drop is more pronounced in the non cleared (control) spheroids. The intensity evolutions with depth are similar for RapiClear and Glycerol. SNR and FR metrics appear almost constant for the three investigated clearing conditions while BC shows global degradation along depth z . For the three metrics SNR, FR and BC, Glycerol shows significantly better values by comparison with RapiClear and Control. However, it is uneasy to produce a secured prediction of the effect of clearing along z with local metrics. This is why it was important also to confront what would be found with conventional local metrics with a machine learning perspective.

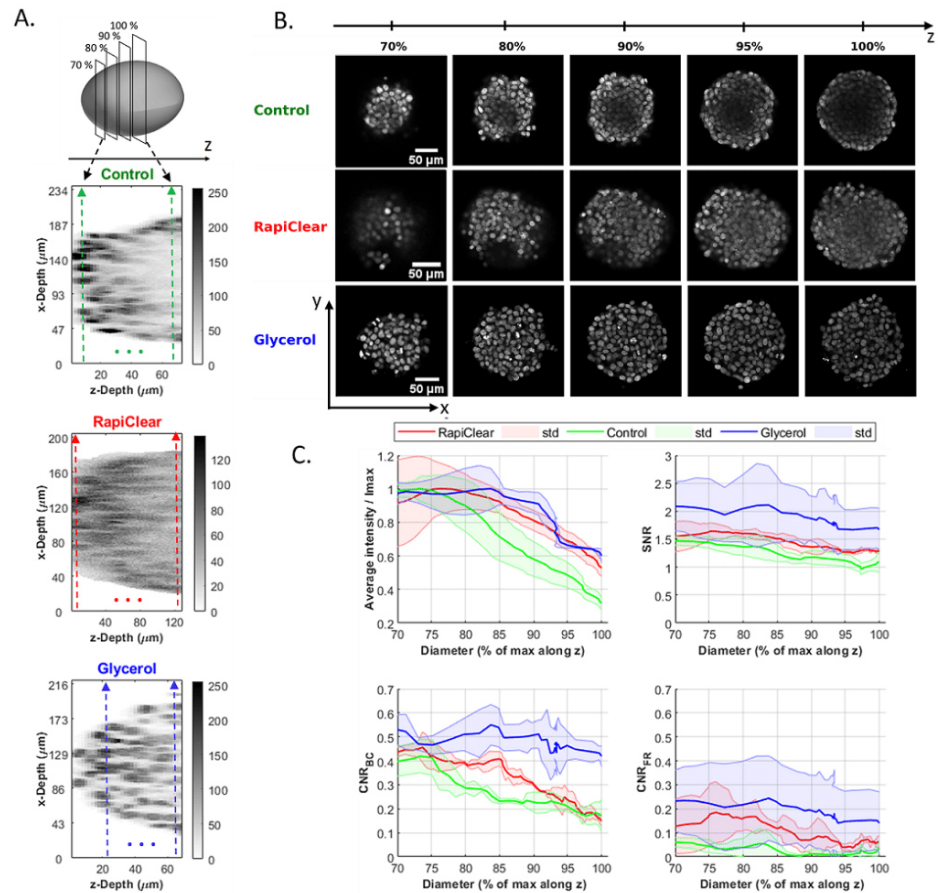


Fig 2. Image quality analysis function of the depth (z) defined as the percentage of the maximum diameter for the datasets produced with Control, RapiClear and Glycerol clarification methods. Slices with 100% of diameter are considered as the center of the 3D spheroids. **(A)** Illustration of the xz slices. Colored dashed lines correspond to the location (in μm) of the slices xy with 70% and 100% of maximum diameter. **(B)** Visualization of test images (xy slices) normalized in depths (z) and used to evaluate segmentation performance for each clarification method. **(C)** The mean and standard deviation (std) of the average intensity, SNR, CNR_{BC} by Battacharayya and CNR_{FR} by Fisher ratio computed for 3 spheroids for each clarification method and plotted as a function of the percentage of maximum diameter.

Spheroid 2D images segmentation

We used deep learning segmentation methods to characterize the quality of spheroid clearing protocols. Several segmentation methods such as Unet, Dist and Stardist, associated with post-processing steps based on dynamic morphology reconstruction and watershed algorithm (DM) were applied to the test images of Figure 2.B produced from the tested clearing conditions. We used the F1-score to quantify the quality of segmentation as a pixel wise metric and the aggregated Jaccard Index (AJI) as an object wise metric. We tested the segmentation efficiency for two cases: (i) when test images and pre-trained segmentation models are from the same clearing method and (ii) in a cross way taking test images from a clearing condition and using pre-trained model from another. Table 1 shows the mean values and the standard deviations (std) of the F1-score and AJI computed for test images located at 70, 80, 90, 95 and 100% of maximum diameter along z.

Interestingly, in accordance with the observation recorded by the local quality metrics, Glycerol clearing protocol provides the best segmentation performance in all tested configurations (Table 1.C-3). In addition, it is remarkable that Glycerol segmentation model is also powerful to segment data sets from Control or from RapiClear clearing when segmentation method is properly chosen (Table 1.A-3,B-3). It is also striking to note that segmentation results of Control and RapiClear test images gives higher F1-score and AJI values with segmentation models trained on Glycerol than with models trained on their data. As shown in Fig. 3.A, these average results are almost stationary along z for all clearing methods tested (also see qualitative illustration of the final segmentation in Figure 3.B and SI Figures 2 and 3.A). This demonstrates that the local evolution in intensity or SNR shown in Figure 2 do not necessarily correlate with the segmentation performances.

Segmentation models transferability to other data sets

Finally, we tested the transferability from cleared datasets to another datasets by segmenting test images from another clearing methods, another structure and also another imaging system using pre-trained segmentation models of Control, RapiClear and Glycerol. For this study, we used colorectal carcinoma HCT-116 cell lines test images cleared with TDE and acquired with a laser scan confocal system (Nikon). Also, we selected two datasets from the literature such as Breast carcinoma T47D cells cleared with ScaleS method and acquired with a spinning disk confocal system (Opera Phenix) [23] and colorectal carcinoma HCT-116 cell line cleared with CUBIC method and acquired with a light-sheet fluorescence (LSF) microscope [44]. Table 1.D,E,F shows the mean and standard deviation of computed F1-score and AJI segmentation metrics for each test images produced from TDE, ScaleS and CUBIC clearing methods and segmented with the Control, RapiClear and Glycerol pre-trained models. The segmentation results are high for both TDE and ScaleS (see Table 1 and Figure 4.A). Similarly to what was found for RapiClear and Control, Glycerol appears, for both TDE and ScaleS also, as the best method to train on to benefit from transfer learning. This experiment clearly proves the feasibility of information transferability by digital clearing from clearing method to another acquired with the same imaging system but with different structure and data scale. Contrariwise, CUBIC dataset acquired with light-sheet fluorescence (LSF) microscopy and presenting very different contrast and artefacts shows low performance. This experiment points the limit of data transferability by digital clearing (see Figure 4.B and SI Figures 3.B and 4 for qualitative illustration of final segmentation maps). Figure 5.A illustrates the qualitative interest of digital clearing available at the output of neural networks when the best segmentation neural network (Dist segmentation) is trained on the best

Test data	Segmentation models	F1-score \pm std			AJI \pm std				
		<i>Unet</i>	<i>Dist</i>	<i>Stardist</i>	<i>Unet</i>	<i>Unet+DM</i>	<i>Dist</i>	<i>Dist + DM</i>	<i>Stardist</i>
Control (A)	Control (1)	0.85 ± 0.01	0.85 ± 0.01	0.84 ± 0.01	0.07 ± 0.06	0.51 ± 0.03	0.26 ± 0.05	0.52 ± 0.03	0.59 ± 0.03
	RapiClear (2)	0.84 ± 0.02	0.85 ± 0.01	0.72 ± 0.04	0.14 ± 0.03	0.52 ± 0.05	0.16 ± 0.03	0.52 ± 0.03	0.42 ± 0.07
	Glycerol (3)	0.86 ± 0.02	0.86 ± 0.01	0.84 ± 0.02	0.01 ± 0.01	0.57 ± 0.05	0.06 ± 0.04	0.55 ± 0.02	0.55 ± 0.06
RapiClear (B)	Control (1)	0.82 ± 0.01	0.83 ± 0.01	0.81 ± 0.01	0.03 ± 0.02	0.41 ± 0.02	0.07 ± 0.03	0.47 ± 0.05	0.52 ± 0.03
	RapiClear (2)	0.83 ± 0.01	0.84 ± 0.01	0.76 ± 0.03	0.11 ± 0.09	0.46 ± 0.04	0.08 ± 0.04	0.48 ± 0.02	0.43 ± 0.06
	Glycerol (3)	0.83 ± 0.03	0.83 ± 0.02	0.80 ± 0.03	0.01 ± 0.01	0.46 ± 0.02	0.03 ± 0.01	0.47 ± 0.03	0.49 ± 0.03
Glycerol (C)	Control (1)	0.89 ± 0.01	0.89 ± 0.01	0.89 ± 0.01	0.29 ± 0.01	0.63 ± 0.01	0.46 ± 0.06	0.64 ± 0.03	0.68 ± 0.02
	RapiClear (2)	0.88 ± 0.01	0.87 ± 0.01	0.78 ± 0.02	0.40 ± 0.07	0.63 ± 0.03	0.46 ± 0.04	0.62 ± 0.02	0.51 ± 0.03
	Glycerol (3)	0.91 ± 0.01	0.91 ± 0.01	0.90 ± 0.01	0.34 ± 0.07	0.70 ± 0.02	0.47 ± 0.05	0.71 ± 0.02	0.70 ± 0.02
TDE (D)	Control (1)	0.88 ± 0.01	0.88 ± 0.02	0.84 ± 0.02	0.02 ± 0.01	0.44 ± 0.07	0.06 ± 0.05	0.56 ± 0.05	0.59 ± 0.04
	RapiClear (2)	0.89 ± 0.01	0.89 ± 0.02	0.78 ± 0.02	0.08 ± 0.04	0.60 ± 0.01	0.09 ± 0.04	0.60 ± 0.02	0.52 ± 0.06
	Glycerol (3)	0.90 ± 0.02	0.89 ± 0.03	0.84 ± 0.02	0.02 ± 0.02	0.39 ± 0.05	0.02 ± 0.02	0.54 ± 0.02	0.58 ± 0.04
ScaleS (E)	Control (1)	0.85 ± 0.03	0.86 ± 0.03	0.83 ± 0.03	0.29 ± 0.13	0.54 ± 0.03	0.39 ± 0.1	0.59 ± 0.05	0.62 ± 0.05
	RapiClear (2)	0.83 ± 0.06	0.85 ± 0.05	0.77 ± 0.06	0.22 ± 0.1	0.58 ± 0.03	0.26 ± 0.13	0.58 ± 0.06	0.50 ± 0.06
	Glycerol (3)	0.87 ± 0.03	0.85 ± 0.03	0.85 ± 0.03	0.12 ± 0.07	0.57 ± 0.04	0.14 ± 0.11	0.56 ± 0.05	0.63 ± 0.03
CUBIC (F)	Control (1)	0.68 ± 0.002	0.69 ± 0.03	0.24 ± 0.04	0.003 ± 0.001	0.33 ± 0.04	0.004 ± 0.001	0.16 ± 0.04	0.07 ± 0.02
	RapiClear (2)	0.66 ± 0.01	0.63 ± 0.02	0.42 ± 0.02	0.003 ± 0.001	0.23 ± 0.03	0.003 ± 0.001	0.19 ± 0.02	0.11 ± 0.001
	Glycerol (3)	0.58 ± 0.01	0.58 ± 0.01	0.26 ± 0.04	0.002 ± 0.001	0.23 ± 0.04	0.002 ± 0.001	0.16 ± 0.01	0.06 ± 0.01

Table 1. Mean and standard deviation of the computed segmentation metric (F1-score, AJI) for five test images produced from Control, RapiClear and Glycerol. Tests are realized in cross way between the segmentation models (A,B and C). And also for five test images produced from TDE, ScaleS and CUBIC to test data transferability from a clearing protocol to another clearing protocol (D, E and F). Various segmentation methods are used. The bold values are best segmentation model for each clearing method datasets. Except for Cubic clearing method where all methods provide low performance, Glycerol appears as the best method on which one should train the deep learning models in order to benefit from digital clearing.

clearing method (Glycerol) and applied to uncleared data or cleared with RapiClear. It is obvious with Fig. 5.A that the intensity attenuation recorded with local metrics along z can be compensated with the deep neural network thanks to digital clearing. As shown in Fig. 5.B in comparison with ground truth, a significant improvement of the counting of cells along z is brought by training on images obtained with the best clearing method while applying the model directly on control or on a less efficient clearing method. This opens also the possibility of an efficient post-segmentation 3D reconstruction of full spheroids (see SI Figure 5 and SI videos).

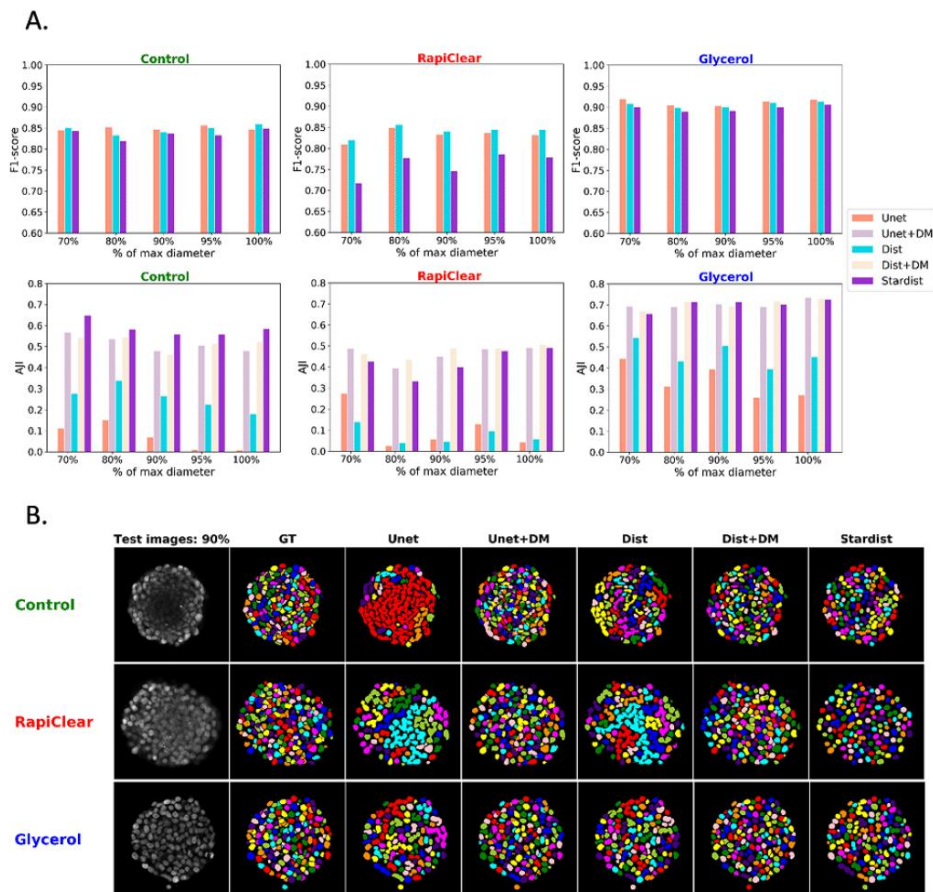


Fig 3. Segmentation results as a function of depths (z). **(A)** Quantitative segmentation results (F1-score, AJI) for the five test images taken at depth ranging from 70, 80, 90, 95 and 100% defined as the percentage of maximum diameter. Segmentation methods are trained and tested on the same clearing method. **(B)** Qualitative illustration of the final segmentation of the slices at 90% of maximum diameter produced from Control, RapiClear and Glycerol clearing methods.

Conclusion

In this report, we have investigated the interest of a deep learning perspective for the comparison of clearing methods in fluorescence microscopy. This was illustrated for a task of nuclei segmentation in spheroids under 3D fluorescent microscopy. The best clearing method identified with conventional local metric follows the performance of state-of-the-art deep learning based segmentation methods. However, because the training datasets include images from various depth, no real influence of depth was observed on segmentation performance contrarily to what was found with local metric. This demonstrates that local metric can be used to select an optimal clearing method but that final performances can be made invariant to the remaining noise thanks to adequate machine learning strategies.

We specially tested the interest of transfer learning in this context. We investigated the interest to train on one clearing condition and to test on another. The best

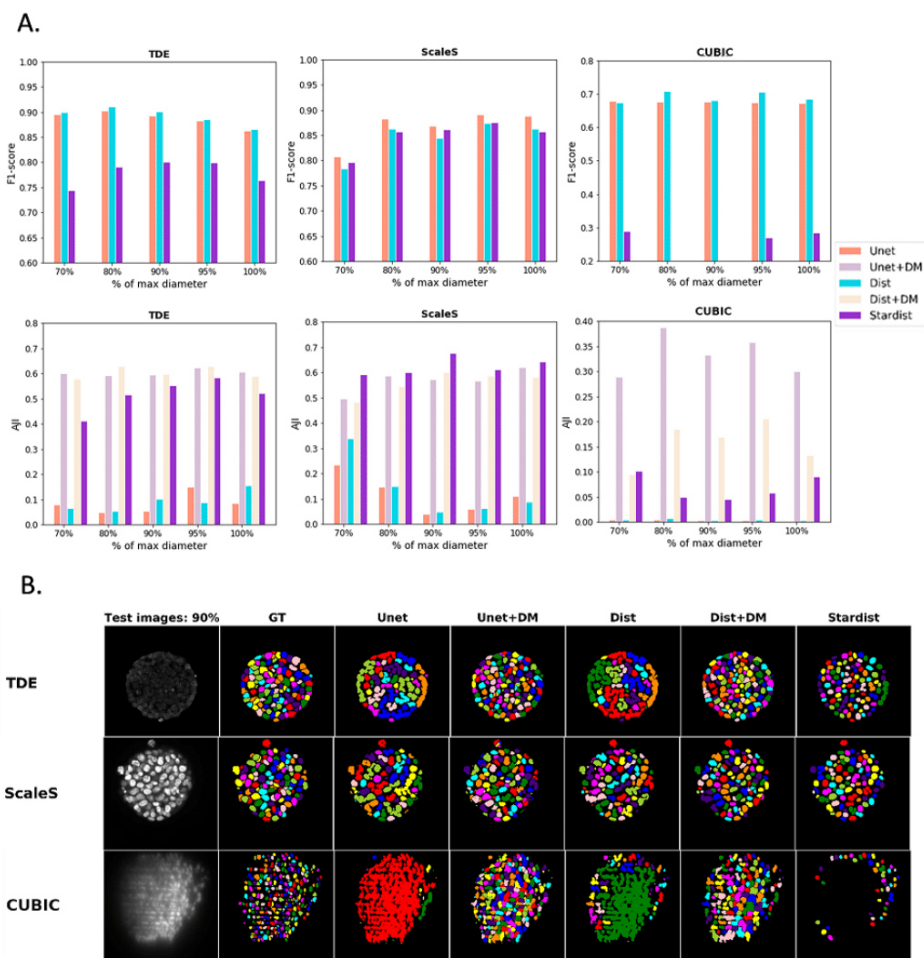


Fig 4. Data transferability assessment: segmentation results as a function of depths (z) defined as the percentage of maximum diameter. **(A)** Quantitative segmentation results (F1-score, AJI) for the five test images produced from TDE, ScaleS and CUBIC clearing methods and segmented using the RapiClear, Glycerol and Control segmentation models respectively. **(B)** Qualitative illustration of the final segmentation results for the slices at 90% of maximum diameter.

segmentation method was also found to be the one which gave the best transfer results. This is specially interesting when the test images are produced in uncleared conditions. Training a model on the best cleared conditions enable to perform segmentation of nuclei in non cleared conditions with enhanced performances. This opens the way to digital clearing of the samples. Annotated cleared images of high quality produced with time consuming protocols could enable anyone to denoise images acquired with much simpler protocols. For this reason we release our annotated data set publicly as pointed in section S1 Dataset.

These results could be extended in various directions. The inference of the proposed segmentation approach is very fast (around 2 minutes for a stack of 41 slices of 40 Mbs with a processor Intel Core i7-6700HQ CPU @ 2.60 GHz). It can be easily used for on the fly segmentation during acquisition for fixed samples, as well as for live imaging (for

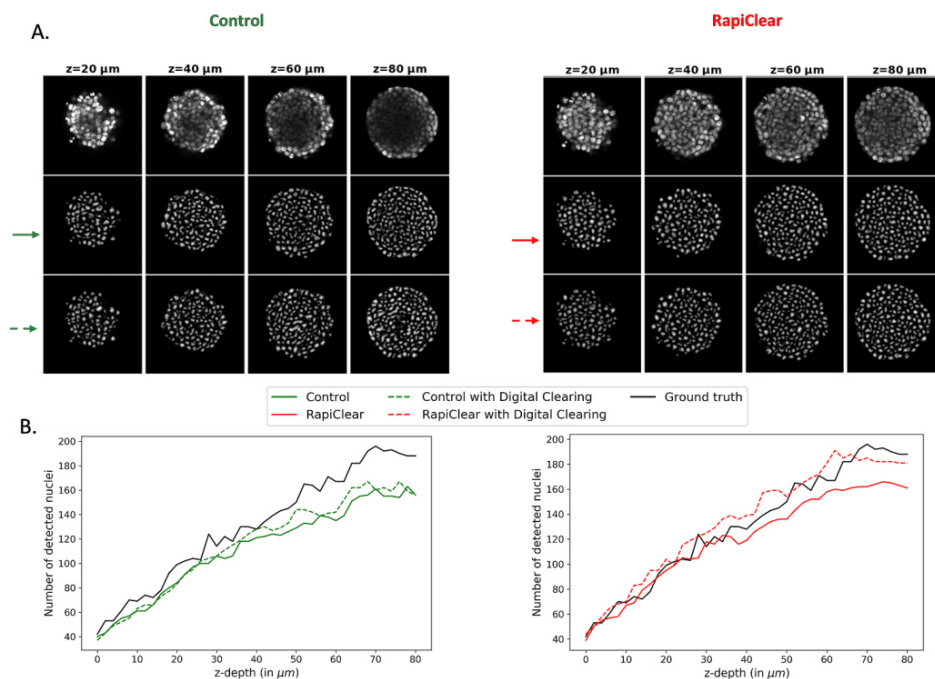


Fig 5. Digital clearing effect analysis. **(A)** Slices of non cleared spheroid (control) and same spheroid cleared with RapiClear are illustrated function of z-depth (μm). The predicted distance maps at the output of Unet architecture for Dist segmentation method computed for the slices with control model (green solid line) and RapiClear model (red solid line) and also with digital clearing via glycerol model (green and red dashed lines). **(B)** Number of detected nuclei computed after Dist segmentation function of the depth z in μm for the same non cleared and cleared spheroid before and after digital clearing. Ground truth in black solid line corresponds to a manual counting by an expert.

experiments where samples are acquired over extended time-period [tens of hours], but with rather long time intervals [higher than 10 min]). By bringing such single cell metrics directly available to the user, it opens up promising applications to screen therapeutics drugs within 3D environment closer to in-vivo. Colorectal cancer spheroids were used here as an example. The method is also readily available for organoids that have emerged as very powerful in vitro models to mimic various normal and pathological situations [45,46]. The method can also be easily extended to the segmentation of other biological structures of interest, such as the overall cell shapes, as long as the manually segmented datasets is implemented. Other clarification methods specially optimized for thick samples [15,47–49] could then be also tested with the same global approach presented in this article. The most promising result lay in the possibility of digital clearing. In this study we performed it, for a first demonstration, by training directly on the best clearing method. Variants could be considered like style transfer [50,51] or domain adaptation to further improve the digital clearing of the samples. Also, we demonstrated the possibility of digital clearing by transfer learning even when the two microscopes used are not strictly identical. This calls for a systematic quantitative study to assess the robustness of this finding with microscopes of various resolutions and aberrations.

Materials and Methods

190

We present the details of all the steps described in the graphical abstract of Figure 1.

191

Sample preparation and image acquisition

192

Cell lines and cell culture

193

Colorectal carcinoma cell line HCT-116 were used in this study. Cells were cultured in DMEM-GlutaMAX, supplemented with 10% of Heat-Inactivated Fetal Bovine Serum (FBS; Sigma, St. Louis, Missouri, US), 100 units / 100 μ g of penicillin / streptomycin and passaged every 3-4 days.

194

195

196

197

Agarose-based micro-systems

198

The micro-systems consist of arrays of 130 micro-wells of 200 μ m in diameter and height. They are used to create 130 reproducible spheroids per condition. This micro-system was produced by moulding agarose (Standard Agarose, 2% w/v) on PDMS molds created by photolithography process. A patent has been deposited for this process (FR 1870349).

199

200

201

202

203

Spheroid formation

204

Cells were seeded in each 24 wells-plate containing microsystems at a density of $1, 2 \cdot 10^5$ cells/mL, 1 mL per well. They were placed under orbital agitation (160 rpm) for 2 hours in the incubator (37° C, 5% CO₂) to increase cell sedimentation inside each micro-well. After 2 hours, the wells were rinsed with warm culture medium (3 \times) to get rid of cells that were out of the micro-wells. The 24 well-plate containing the microsystems were then kept in the incubator. Multicellular Tumor Spheroids (MCTs) are formed within 1 day and are used at Day 5 in this study.

205

206

207

208

209

210

211

Immunostaining

212

At day 5, cells were washed 3 times with warmed PBS for 5 min, followed by paraformaldehyde fixation (3.7% in PBS) for 20 minutes. All wells were then washed with PBS/3% BSA (3 \times 5 min), permeabilized with 0.5% Triton for 20 min, and rinsed again with PBS/ 3% BSA (3x 5 min). To stain nucleus, NucGreen Dead 488 ReadyProbes Reagent were used (Invitrogen R37109, 2 drops/mL , i.e. 2 drops per wells, 4 hours at room temperature). The samples were washed with PBS (1 \times 10 min) and kept protected from light in PBS at 4°C until image acquisition. Such non-cleared samples were either imaged directly (Control), or further processed with different clearing methods, described below.

213

214

215

216

217

218

219

220

221

Clarification

222

Different clarification techniques were used. For RapiClear-clarified samples, the microwells were incubated in RapiClear 1.52 solution (sunjinlab) overnight, then transferred in 0.5 mm Ispacer (sunjinlab, 2 spacers) and immersed in 35 μ L of fresh RapiClear solution. Sealing was achieved using an additional sticky Ispacer and a coverslip. For Glycerol-clarified samples, the microwells were incubated in a 80% glycerol solution in PBS (v/v) overnight, then transferred in 0.5 mm Ispacer (sunjinlab, 2 spacers) and immersed in 35 μ L of fresh 80% glycerol solution. The chemical compound 2,2'-thiodiethanol (TDE) was also tested in this study, following the procedure described in [52]. Briefly, the microwells were first incubated in a 20% TDE

223

224

225

226

227

228

229

230

231

solution in PBS (v/v) for 1 hour, then transferred in a 47% TDE solution in PBS (v/v) for 2 hours. The microwells were finally transferred in 0.5 mm Ispacer (sunjinlab, 2 spacers) and immersed in 35 μL of fresh 47% TDE/PBS solution. For ScaleS and CUBIC clarification methods, we used existing dataset of the literature described in [23, 44].

Image acquisition

A pile of z-stacks images of 1024×1024 pixels in xy was acquired using a classical confocal set-up. RapiClear images were acquired with Leica SP5 in resonant mode, a 20x dry objective lens (NA=0.7) is used with a pixel scale of 0.2 μm in xy and z-step 1 μm . Control, Glycerol and TDE images are acquired with Nikon A1Rplus using a 20x water immersion objective lens (NA=0.7) with a pixel scale of 0.243 μm in xy and z-step 2 μm . A 488 nm line of an Argon Laser was used to detect NucGreen. Note that, all 2D spheroid images were normalized to have zero mean and variance equal one to compensate for intensity variation before models training process.

Dataset annotation

Ground truth annotation was performed in semi-automatic way using the interactive learning and segmentation toolkit (Ilastik) [53] based on shallow learning followed by expert correction (Figure 1.c). 2D frames from the beginning, middle and the end of 3D image stacks belonging to each clearing condition were selected for exhaustive representation of instances and clearing effects on image depths. Pixel wise classification mode was used then to generate primary segmentation maps. The filters used in the segmentation step were intensity, edge and textural filters with various kernel sizes ranging from 0.7 pixel to 10 pixels in order to represent the smallest and largest details of the transition between the nuclei and the background (36 filters). Then, we applied the batch processing to segment all 2D data set images. Finally, a manual correction step produced by an expert was applied to the segmentation maps. The overall amount of annotated 2D images was 57 for each clearing conditions. Datasets were then split into 47 for training, 5 for validation and 5 for testing. The total number of cell nuclei was around 10000 for each condition dataset.

3D spheroid images of various thicknesses were normalized in z-depth by considering the slice with the largest diameter as the center of spheroid. Diameter of each spheroid slice was computed from the binarized maximum intensity projection of the 3D volume on y-axis. The percentage of diameter was derived then for each slice according to the maximum diameter value. Based on this normalization method, and for a fair comparison between the protocols, we considered slices of depths ranging from 70% to 100% of maximum diameter (Figure 2A). It is to be noticed that this limited range of depth causes no loss of information since spheroid are isotropic samples. The missing part of the spheroids are similar to the first half.

Image quality assessment based local metrics

We first assess locally the quality of spheroid images according to z-depth by using statistical metrics are the signal to noise ratio (SNR) and the contrast to noise ratio (CNR) calculated by two ways: Bhattacharyya coefficient (BC) and Fisher ratio (FR) defined as

$$SNR = \frac{\mu_{signal}}{\sigma_{noise}} \quad (1)$$

$$CNR_{BC} = 1 - \sum_{X=1}^{255} \sqrt{p_d(X) \cdot q_d(X)} \quad (2)$$

$$CNR_{FR} = \frac{(\mu_{signal} - \mu_{noise})^2}{V_{signal} + V_{noise}} \quad (3)$$

where, μ_{signal} , $p_d(X)$ and V_{signal} are the mean intensity of the signal, the probability of a signal intensity value X and the variance of the signal respectively. Also, μ_{noise} , $q_d(X)$, V_{noise} , and σ_{noise} are the mean intensity of the noise, the probability of a noise intensity value X , the variance and the standard deviation of the noise respectively (see SI Figure 1). We computed also the normalized average intensity (average I/Imax) in each image slice to illustrate the change in intensity along the depths. All these factors were computed for three spheroids from each clearing condition.

Deep learning segmentation methods

To assess the quality of clearing, we tested a set of state-of-the-art segmentation methods based on deep learning that were used for 2D spheroid images segmentation (Figure 1.D). They are briefly presented in this subsection.

U-Net

We used the reference segmentation network UNet [54] to predict 2 output classes (Cell nuclei and background). We simplified the architecture by reducing the number of feature channels. We use 5 blocks for contracting and expansive paths, each consisting of 2 convolutional layers with 4.2^n ($n = 2, 3, 4, 5, 6$) filters of size 3×3 and ReLU activation function. For the output probability map (\hat{y}), we use a single-channel convolutional layer with sigmoid activation function (see SI Figure 6.A). The total number of trainable parameters was 2,158,417 optimized by using the Adam optimizer [55] and the training hyper-parameters are: *batch size* = 1, *epochs* = 33 and the learning rate $lr = 1e^{-3}$. The final segmentation map was computed by thresholding the probability map by a threshold value α that was optimized on validation data set for each condition. The optimization process is described later in the same section.

Post processing based Dynamic Morphology (DM)

The same U-Net architecture described previously was applied to predict the probability map (\hat{y}) followed by a post processing step based on dynamic morphology [56] and watershed algorithm [57]. This combination was used in histopathology images segmentation to separate touching nuclei [58] that are considered as one object after thresholding the probability map. Briefly, the post processing step was based mainly on the hypothesis that the posterior probability at the border of the touching nuclei was systematically lower than in the putative center of the nucleus, and that the nuclei centers correspond to local maximum intensity in the image. The significant drop of the signal between nuclei center and the border was defined by morphological dynamics as the following: Let LM be a local maximum of the U-Net probability map output \hat{y} . LM represents a cell nuclei if along all paths P connecting LM with some higher maximum LM' , the decrease in \hat{y} is at least λ

$$\min_{\substack{P=(LM, \dots, LM') \\ \hat{y}(LM') > \hat{y}(LM)}} \{ \max_{x \in P} [\hat{y}(LM) - \hat{y}(x)] \} > \lambda \quad (4)$$

where x is a pixel at (i, j) coordinates and λ is a free parameter optimized for each clearing method (see SI Figure 6.B). The final segmentation map was then obtained by applying watershed transformation to the inverted probability map seeded from the maxima that fulfill this criterion.

Dist

315

The problem in high nuclei density 2D spheroid images is that the touching and overlapping nuclei are segmented as one object. Several works were proposed to solve this problem by predicting both the object and their contours [59,60]. Others proposed to focus the attention of the model on the core of the nuclei by predicting an eroded version of the annotation as centers correspond to the ultimate erosion of the ground truth [61,62]. In our work and unlike pixel-wise binary classification used previously, we follow the proposed work in [37] and we turned 2D spheroid images classification to a regression problem by predicting the distance maps (\hat{d}) that focus on the center of nuclei (see SI Figure 6.A). Therefore, for each pixel $x = (i, j)$ of the annotated spheroid binary image (y), with $y(x) > 0$, we assign a distance transform (D_c) representing the distance to the closest background pixel $x_b = [i_b, j_b]$. Here, we used the Chebyshev distance defined as,

$$D_c = \max(|i_b - i|, |j_b - j|) . \quad (5)$$

The Dist model is based on the same U-Net architecture described before. The same training hyper-parameters were used to predict distance maps. Only sigmoid output function was replaced with ReLU function at the output channel since the predicted values are higher than 1. The final binary segmentation map was then obtained by thresholding the distance output maps \hat{d} . The threshold value denoted β was also optimized for RapiClear, Control and Glycerol clearing methods. Finally, the post processing step described before was also applied to the predicted maps to enhance the final segmentation after optimizing the parameter λ for each clearing method.

Stardist: Star-convex polygons

336

Star-convex polygons (Stardist) is one of the robust widely used algorithms for cells detection and segmentation in 2D microscopy images [36]. It consists in predicting a star-convex polygon for each cell nuclei pixel $x = [i, j]$ by regressing the distances $\{r_{i,j}^k\}_{k=1}^\eta$ of the pixel to the boundary of the nuclei to which belong, along a set of optimized number of radial directions η with equidistant angles. Also, separately, the algorithm predicts probability map ($p_{i,j}$) for each pixel x as the normalized Euclidean distance to the nearest background pixel $x_b = [i_b, j_b]$ (see SI Figure 6.A). Given such polygon candidates with their associated nuclei probabilities, a non-maximum suppression (NMS) was performed to reach the final set of polygons, each representing a cell nuclei. Stardist was mainly based on Unet architecture with 3 blocks for contracting and expansive paths, each consisting of 2 convolutional layers with $32 \cdot 2^n$ ($n = 0, 1, 2$) filters of size 3×3 , and an additional layer of 128 3×3 filters added after the final Unet feature layer to avoid that the subsequent two output layers have to fight over features. The activation functions between layers are ReLU and the total number of trainable parameters was approximately 1.4 million parameters. The output layers of the architecture consist of a single-channel convolutional layer with sigmoid activation for the nuclei probability output and the polygon distance output layer has as many channels as there are radial directions η and do not use an additional activation function. We used Stardist in our study to segment cell nuclei inside 2D spheroid images. For the three conditions datasets, the training stage was performed with the following primary hyper parameters: *batch size* = 1, *epochs* = 400 and the learning rate $lr = 0.3e^{-3}$. After that, the best training model that minimized the loss functions (Equations 6, 7) was selected for each condition. So, based on this criterion the hyper parameters for the selected models of RapiClear, Control and Glycerol datasets were (*epochs* = 317, $lr = 0.75e^{-4}$), (*epochs* = 282, $lr = 1.5e^{-4}$) and (*epochs* = 380, $lr = 0.75e^{-4}$) respectively. As in the previously described segmentation methods, the

parameters: number of rays η , threshold α of the nuclei probability map and threshold of the non-maximum suppression τ , were optimized for each data set.

Training loss functions and segmentation evaluation metrics

Loss function

The purpose of loss function in a deep learning training stage model is to quantify the difference between predictions and ground truths for steering the training of the network. In our work, we used two commonly used loss functions the binary cross entropy (*BCE*) and the mean squared error (*MSE*) for classification and regression problem respectively. The *BCE* for binary classification (nuclei and background) was defined as

$$BCE(y, \hat{y}) = \frac{-1}{M} \sum_{m=1}^M y_m \cdot \log(\hat{y}_m) + (1 - y_m) \cdot \log(1 - \hat{y}_m) \quad (6)$$

and *MSE* for distance map prediction was defined as,

$$MSE(d, \hat{d}) = \frac{-1}{M} \sum_{m=1}^M (d_m - \hat{d}_m)^2 \quad (7)$$

where M is the 1D output map size, \hat{y}_m and \hat{d}_m are the m -th scalar values in the output predicted maps, y_m and d_m the corresponding target values of probability maps and distance maps respectively.

Evaluation metrics

To evaluate the performance of spheroid images segmentation and to be able to quantitatively compare between the transferability of segmentation models trained on clarification method to other clearing protocols, we used the pixel wise-metric F1-score [63] for segmentation evaluation and also the Aggregated Jaccard Index (AJI) [61] as an object-wise metric for touching nuclei splitting evaluation. The F1 measure is defined as the harmonic mean between recall and precision at the pixel level and it was computed as

$$F1\text{-score} = 2 \cdot \frac{Precision \times Recall}{Precision + Recall} \quad (8)$$

with the $Precision = \frac{TP}{TP+FP}$ and $Recall = \frac{TP}{TP+FN}$, where TP , FP and FN are the true positive, false positive and false negative respectively.

The AJI is an extension of the global Jaccard index, where every ground truth nucleus is first matched to one detected nucleus by maximizing the Jaccard index. The AJI corresponds then to the ratio of the sums of the cardinals of intersection and union of these matched components respectively. In addition, all detected components that do not matched were added to the denominator. More formally [37], AJI can be defined as,

$$AJI = \frac{\sum_{i=1}^L |G_i \cap S_k^*(i)|}{\sum_{i=1}^L |G_i \cup S_k^*(i)| + \sum_{l \in U} |S_l|} \quad (9)$$

where G_i is a nucleus ground truth of L nuclei in an image, S is all the detected nuclei, $S_k^*(i)$ is the segmented nucleus associated with G_i that maximizes the Jaccard index, i.e. $S_k^*(i) = \operatorname{argmax}_k \frac{|G_i \cap S_k|}{|G_i \cup S_k|}$ and U is the set of indices of detected nuclei that have not been assigned to any ground truth.

Parameter Optimization

395

One important step in supervised learning with deep learning is the hyperparameters fine tuning. This optimization step was applied to validation data set to maximize the segmentation metrics such as F1-score, AJI or Jaccard index for Stardist segmentation method. In our work, threshold of the probability maps α , threshold of predicted distance maps β , the h-minima value λ of the dynamic morphology reconstruction post processing step, the numbers of rays of the star-convex polygons η and threshold τ of the non-maximum suppression (nms) were optimized empirically by varying each parameter between a range of values (see SI Figure 7). Then, the value that maximized a segmentation metric were selected for each segmentation method depending on the RapiClear, Control and Glycerol segmentation models as shown in Table 2.

396
397
398
399
400
401
402
403
404
405

Parameters	Segmentation methods	Ranges	Metrics	Segmentation models		
				<i>Control</i>	<i>RapiClear</i>	<i>Glycerol</i>
α	Unet	$\alpha \in [0 \ 1]$	F1-score	0.5	0.6	0.4
	Stardist	$\alpha \in [0.3 \ 0.7]$	Jaccard index	0.6	0.4	0.5
β	Dist	$\beta \in [0 \ 2]$	F1-score	1.1	1.2	0.6
λ	Unet + DM	$\lambda \in [0 \ 20]$	AJI	8	7	2
	Dist + DM			2	1	1
η	Stardist	$\eta \in 2^i, i \in [2 \ 8]$	F1-score	64		
τ		$\tau \in [0.3 \ 0.5]$	Jaccard index	0.4	0.3	0.4

Table 2. Parameters optimization step. Various thresholds were optimized for each used segmentation method between a range of tested values. The value of threshold that maximized a metric was selected.

Transfer learning

406

We used transfer learning [64] methodology in our study to transfer knowledge gained from training segmentation model on a dataset from a clarification condition and apply the pre-trained model to segment images clarified from other conditions. This was done by brute transfer of the weights in the neural network without fine tuning.

407
408
409
410

Supporting information

411

S1 Fig. Supplementary Figures 1,2,3,4,5 and 6

412

S1 Datasets and Videos. Datasets availability and 3D spheroids reconstruction videos. Annotated data sets used during the current study are available and supplementary videos of 3D reconstructed spheroids for Control (non cleared), RapiClear and Glycerol cleared samples are available in the following repository: <https://uabox.univ-angers.fr/index.php/s/6myuGGs0JO94M8D>.

413
414
415
416
417

Acknowledgments

418

Ali Ahmad gratefully acknowledges project EU H2020 FET Open, PROCHIP, Chromatin organization PROFiling with high-throughput super-resolution microscopy on a CHIP, grant agreement no. 801336 (<https://pro-chip.eu/>) for funding his PhD. The authors also thank the GdR ImaBio for financial support to the organisation of a deep learning hackathon which contributed to the initiation of this study.

419
420
421
422
423

Author contributions statement

424

A.A. and D.R. conceived of and designed the experiments. S.G., G.R. and C.R prepared and acquired the spheroid samples. A.A. annotated the data used in the experiments. A.A conceived and developed image quality assessment and image segmentation based on deep learning algorithms. A.A., D.R. G.R. and C.R analysed the data and the results. All authors contributed to the redaction of the manuscript and approved the final version. D.R. and C.F. supervised the PROCHIP project.

425

426

427

428

429

430

References

1. Sutherland RM. Cell and environment interactions in tumor microregions: the multicell spheroid model. *Science*. 1988;240(4849):177–184.
2. Nunes AS, Barros AS, Costa EC, Moreira AF, Correia IJ. 3D tumor spheroids as in vitro models to mimic in vivo human solid tumors resistance to therapeutic drugs. *Biotechnology and bioengineering*. 2019;116(1):206–226.
3. Mittler F, Obeid P, Rulina AV, Hagnet V, Gidrol X, Balakirev MY. High-content monitoring of drug effects in a 3D spheroid model. *Frontiers in oncology*. 2017;7:293.
4. Langhans SA. Three-dimensional in vitro cell culture models in drug discovery and drug repositioning. *Frontiers in pharmacology*. 2018;9:6.
5. Edmondson R, Broglie JJ, Adcock AF, Yang L. Three-dimensional cell culture systems and their applications in drug discovery and cell-based biosensors. *Assay and drug development technologies*. 2014;12(4):207–218.
6. Booi TH, Price LS, Danen EH. 3D cell-based assays for drug screens: challenges in imaging, image analysis, and high-content analysis. *SLAS DISCOVERY: Advancing Life Sciences R&D*. 2019;24(6):615–627.
7. Mehta G, Hsiao AY, Ingram M, Luker GD, Takayama S. Opportunities and challenges for use of tumor spheroids as models to test drug delivery and efficacy. *Journal of controlled release*. 2012;164(2):192–204.
8. Dekkers JF, Alieva M, Wellens LM, Ariese HC, Jamieson PR, Vonk AM, et al. High-resolution 3D imaging of fixed and cleared organoids. *Nature protocols*. 2019;14(6):1756.
9. Silvestri L, Costantini I, Sacconi L, Pavone FS. Clearing of fixed tissue: a review from a microscopist's perspective. *Journal of biomedical optics*. 2016;21(8):081205.
10. Chen YY, Silva PN, Syed AM, Sindhvani S, Rocheleau JV, Chan WC. Clarifying intact 3D tissues on a microfluidic chip for high-throughput structural analysis. *Proceedings of the National Academy of Sciences*. 2016;113(52):14915–14920.
11. Santisteban TS, Rabajania O, Kalinina I, Robinson S, Meier M. Rapid spheroid clearing on a microfluidic chip. *Lab on a Chip*. 2018;18(1):153–161.
12. Costa EC, Silva DN, Moreira AF, Correia IJ. Optical clearing methods: An overview of the techniques used for the imaging of 3D spheroids. *Biotechnology and bioengineering*. 2019;116(10):2742–2763.

13. Oliveira LMC, Tuchin VV. The Optical Clearing Method: A New Tool for Clinical Practice and Biomedical Engineering. Springer Nature; 2019.
14. Boutin ME, Hoffman-Kim D. Application and assessment of optical clearing methods for imaging of tissue-engineered neural stem cell spheres. *Tissue Engineering Part C: Methods*. 2015;21(3):292–302.
15. Nürnberg E, Vitacolonna M, Klicks J, von Molitor E, Cesetti T, Keller F, et al. Routine Optical Clearing of 3D-Cell Cultures: Simplicity Forward. *Frontiers in Molecular Biosciences*. 2020;7:20.
16. Wan P, Zhu J, Xu J, Li Y, Yu T, Zhu D. Evaluation of seven optical clearing methods in mouse brain. *Neurophotonics*. 2018;5(3):035007.
17. Sirenko O, Mitlo T, Hesley J, Luke S, Owens W, Cromwell EF. High-content assays for characterizing the viability and morphology of 3D cancer spheroid cultures. *Assay and drug development technologies*. 2015;13(7):402–414.
18. Chan LLY, Cribbes S, Kessel S, McMenemy S, Qiu J. A high-throughput 3D tumor spheroid screening method for drug discovery using imaging cytometry; 2017.
19. Ekert JE, Johnson K, Strake B, Pardinas J, Jarantow S, Perkinson R, et al. Three-dimensional lung tumor microenvironment modulates therapeutic compound responsiveness in vitro—implication for drug development. *PloS one*. 2014;9(3):e92248.
20. Chen W, Wong C, Vosburgh E, Levine AJ, Foran DJ, Xu EY. High-throughput image analysis of tumor spheroids: a user-friendly software application to measure the size of spheroids automatically and accurately. *Journal of Visualized Experiments (JoVE)*. 2014;(89):e51639.
21. Vinci M, Gowan S, Boxall F, Patterson L, Zimmermann M, Lomas C, et al. Advances in establishment and analysis of three-dimensional tumor spheroid-based functional assays for target validation and drug evaluation. *BMC biology*. 2012;10(1):29.
22. Aleshli H, Mosis F, Thomson C, Hamrud E, Wiseman E, Gentleman E, et al. An integrated pipeline for high-throughput screening and profiling of spheroids using simple live image analysis of frame to frame variations. *Methods*. 2020;.
23. Boutin ME, Voss TC, Titus SA, Cruz-Gutierrez K, Michael S, Ferrer M. A high-throughput imaging and nuclear segmentation analysis protocol for cleared 3D culture models. *Scientific reports*. 2018;8(1):1–14.
24. Mathew B, Schmitz A, Muñoz-Descalzo S, Ansari N, Pampaloni F, Stelzer EH, et al. Robust and automated three-dimensional segmentation of densely packed cell nuclei in different biological specimens with Lines-of-Sight decomposition. *BMC bioinformatics*. 2015;16(1):187.
25. Barbier M, Jaensch S, Cornelissen F, Vidic S, Gjerde K, de Hoogt R, et al. Ellipsoid segmentation model for analyzing light-attenuated 3D confocal image stacks of fluorescent multi-cellular spheroids. *PloS one*. 2016;11(6):e0156942.
26. Dunn KW, Fu C, Ho DJ, Lee S, Han S, Salama P, et al. DeepSynth: Three-dimensional nuclear segmentation of biological images using neural networks trained with synthetic data. *Scientific reports*. 2019;9(1):1–15.

27. Tasnadi EA, Toth T, Kovacs M, Diosdi A, Pampaloni F, Molnar J, et al. 3D-Cell-Annotator: an open-source active surface tool for single-cell segmentation in 3D microscopy images. *Bioinformatics*. 2020;36(9):2948–2949.
28. Piccinini F, Balassa T, Carbonaro A, Diosdi A, Toth T, Moshkov N, et al. Software tools for 3D nuclei segmentation and quantitative analysis in multicellular aggregates. *Computational and Structural Biotechnology Journal*. 2020;.
29. Kovac B, Fehrenbach J, Guillaume L, Weiss P. FitEllipsoid: a fast supervised ellipsoid segmentation plugin. *BMC bioinformatics*. 2019;20(1):1–8.
30. Schmitz A, Fischer SC, Mattheyer C, Pampaloni F, Stelzer EH. Multiscale image analysis reveals structural heterogeneity of the cell microenvironment in homotypic spheroids. *Scientific reports*. 2017;7(1):1–13.
31. Goyal B, Dogra A, Agrawal S, Sohi B, Sharma A. Image denoising review: From classical to state-of-the-art approaches. *Information Fusion*. 2020;55:220–244.
32. Xing F, Yang L. Robust nucleus/cell detection and segmentation in digital pathology and microscopy images: a comprehensive review. *IEEE reviews in biomedical engineering*. 2016;9:234–263.
33. Toyoshima Y, Tokunaga T, Hirose O, Kanamori M, Teramoto T, Jang MS, et al. Accurate automatic detection of densely distributed cell nuclei in 3D space. *PLoS computational biology*. 2016;12(6):e1004970.
34. Weigert M, Schmidt U, Haase R, Sugawara K, Myers G. Star-convex polyhedra for 3d object detection and segmentation in microscopy. In: *The IEEE Winter Conference on Applications of Computer Vision*; 2020. p. 3666–3673.
35. Xie L, Qi J, Pan L, Wali S. Integrating deep convolutional neural networks with marker-controlled watershed for overlapping nuclei segmentation in histopathology images. *Neurocomputing*. 2020;376:166–179.
36. Schmidt U, Weigert M, Broaddus C, Myers G. Cell detection with star-convex polygons. In: *International Conference on Medical Image Computing and Computer-Assisted Intervention*. Springer; 2018. p. 265–273.
37. Naylor P, Laé M, Reyat F, Walter T. Segmentation of nuclei in histopathology images by deep regression of the distance map. *IEEE transactions on medical imaging*. 2018;38(2):448–459.
38. Jung H, Lodhi B, Kang J. An automatic nuclei segmentation method based on deep convolutional neural networks for histopathology images. *BMC Biomedical Engineering*. 2019;1(1):24.
39. Jimenez-Carretero D, Abrishami V, Fernández-de Manuel L, Palacios I, Quílez-Álvarez A, Díez-Sánchez A, et al. Tox_ (R) CNN: Deep learning-based nuclei profiling tool for drug toxicity screening. *PLoS computational biology*. 2018;14(11):e1006238.
40. Yang L, Ghosh RP, Franklin JM, Chen S, You C, Narayan RR, et al. NuSeT: A deep learning tool for reliably separating and analyzing crowded cells. *PLoS computational biology*. 2020;16(9):e1008193.

41. Kecheril Sadanandan S, Karlsson J, Wahlby C. Spheroid segmentation using multiscale deep adversarial networks. In: Proceedings of the IEEE International Conference on Computer Vision Workshops; 2017. p. 36–41.
42. Khoshdeli M, Winkelmaier G, Parvin B. Multilayer Encoder-Decoder Network for 3D Nuclear Segmentation in Spheroid Models of Human Mammary Epithelial Cell Lines. In: Proceedings of the IEEE Conference on Computer Vision and Pattern Recognition Workshops; 2018. p. 2239–2245.
43. Tan SH, Swathi Y, Tan S, Goh J, Seishima R, Murakami K, et al. AQP5 enriches for stem cells and cancer origins in the distal stomach. *Nature*. 2020;578(7795):437–443.
44. Masson A, Escande P, Frongia C, Clouvel G, Ducommun B, Lorenzo C. High-resolution in-depth imaging of optically cleared thick samples using an adaptive SPIM. *Scientific reports*. 2015;5:16898.
45. Drost J, Clevers H. Organoids in cancer research. *Nature Reviews Cancer*. 2018;18(7):407–418.
46. Dutta D, Heo I, Clevers H. Disease modeling in stem cell-derived 3D organoid systems. *Trends in molecular medicine*. 2017;23(5):393–410.
47. Lai HM, Liu AKL, Ng HHM, Goldfinger MH, Chau TW, DeFelice J, et al. Next generation histology methods for three-dimensional imaging of fresh and archival human brain tissues. *Nature communications*. 2018;9(1):1–12.
48. Li W, Germain RN, Gerner MY. Multiplex, quantitative cellular analysis in large tissue volumes with clearing-enhanced 3D microscopy (Ce3D). *Proceedings of the National Academy of Sciences*. 2017;114(35):E7321–E7330.
49. Zhu J, Yu T, Li Y, Xu J, Qi Y, Yao Y, et al. MACS: Rapid Aqueous Clearing System for 3D Mapping of Intact Organs. *Advanced Science*. 2020;7(8):1903185.
50. Hollandi R, Szkalicity A, Toth T, Tasnadi E, Molnar C, Mathe B, et al. nucleAIzer: A parameter-free deep learning framework for nucleus segmentation using image style transfer. *Cell Systems*. 2020;.
51. Cho H, Lim S, Choi G, Min H. Neural stain-style transfer learning using gan for histopathological images. *arXiv preprint arXiv:171008543*. 2017;.
52. Costantini I, Ghobril JP, Di Giovanna AP, Mascaro ALA, Silvestri L, Müllenbroich MC, et al. A versatile clearing agent for multi-modal brain imaging. *Scientific reports*. 2015;5:9808.
53. Berg S, Kutra D, Kroeger T, Straehle CN, Kausler BX, Haubold C, et al. ilastik: interactive machine learning for (bio)image analysis. *Nature Methods*. 2019; p. 1–7.
54. Ronneberger O, Fischer P, Brox T. U-net: Convolutional networks for biomedical image segmentation. In: *International Conference on Medical image computing and computer-assisted intervention*. Springer; 2015. p. 234–241.
55. Kingma DP, Ba J. Adam: A method for stochastic optimization. *arXiv preprint arXiv:14126980*. 2014;.
56. Grimaud M. New measure of contrast: the dynamics. In: *Image Algebra and Morphological Image Processing III*. vol. 1769. International Society for Optics and Photonics; 1992. p. 292–305.

57. Beucher S, Meyer F. The morphological approach to segmentation: the watershed transformation. *Mathematical morphology in image processing*. 1993;34:433–481.
58. Naylor P, Laé M, Reyat F, Walter T. Nuclei segmentation in histopathology images using deep neural networks. In: *2017 IEEE 14th international symposium on biomedical imaging (ISBI 2017)*. IEEE; 2017. p. 933–936.
59. Kumar N, Verma R, Sharma S, Bhargava S, Vahadane A, Sethi A. A dataset and a technique for generalized nuclear segmentation for computational pathology. *IEEE transactions on medical imaging*. 2017;36(7):1550–1560.
60. Van Valen DA, Kudo T, Lane KM, Macklin DN, Quach NT, DeFelice MM, et al. Deep learning automates the quantitative analysis of individual cells in live-cell imaging experiments. *PLoS computational biology*. 2016;12(11).
61. Kumar N, Verma R, Arora A, Kumar A, Gupta S, Sethi A, et al. Convolutional neural networks for prostate cancer recurrence prediction. In: *Medical Imaging 2017: Digital Pathology*. vol. 10140. International Society for Optics and Photonics; 2017. p. 101400H.
62. Sirinukunwattana K, Raza SEA, Tsang YW, Snead DR, Cree IA, Rajpoot NM. Locality sensitive deep learning for detection and classification of nuclei in routine colon cancer histology images. *IEEE transactions on medical imaging*. 2016;35(5):1196–1206.
63. Chinchor N, Sundheim BM. MUC-5 evaluation metrics. In: *Fifth Message Understanding Conference (MUC-5): Proceedings of a Conference Held in Baltimore, Maryland, August 25-27, 1993*; 1993.
64. Pan SJ, Yang Q. A survey on transfer learning. *IEEE Transactions on knowledge and data engineering*. 2009;22(10):1345–1359.

